DEFORMATION STUDIES OF $\gamma+\alpha_2$ TITANIUM ALUMINIDES PROCESSED THROUGH REACTION SYNTHESIS

A THESIS

Submitted in partial fulfilment of the requirements for the award of the degree

of

DOCTOR OF PHILOSOPHY

in

METALLURGICAL AND MATERIALS ENGINEERING

by

ROHIT KUMAR GUPTA

DEPARTMENT OF METALLURGICAL AND MATERIALS ENGINEERING
INDIAN INSTITUTE OF TECHNOLOGY ROORKEE
ROORKEE - 247 667 (INDIA)

JUNE, 2011

INDIAN INSTITUTE OF TECHNOLOGY ROORKEE
ROORKEE

CANDIDATE'S DECLARATION

I hereby certify that the work which is being presented in the thesis entitled **"DEFORMATION STUDIES OF $\gamma+\alpha_2$ TITANIUM ALUMINIDES PROCESSED THROUGH REACTION SYNTHESIS"** in partial fulfilment of the requirement for the award of the Degree of Doctor of Philosophy and submitted in the Department of Metallurgical and Materials Engineering of the Indian Institute of Technology Roorkee, Roorkee is an authentic record of my own work carried out during a period from January 2008 to June 2011 under the supervision of Dr. (Mrs.) Vijaya Agarwala, Professor, Department of Metallurgical and Materials Engineering, Indian Institute of Technology Roorkee, Roorkee, India and Dr. Bhanu Pant, Head, Material Processing Division, Vikram Sarabhai Space Centre, ISRO, Trivandrum, India and Dr. P. P. Sinha, Dy. Director, Vikram Sarabhai Space Centre, ISRO, Trivandrum, India.

The matter presented in this thesis has not been submitted by me for the award of any other degree of this or any other Institute.

(ROHIT KUMAR GUPTA)

This is to certify that the above statement made by the candidate is correct to the best of our knowledge.

(P. P. Sinha)
Supervisor

(Bhanu Pant)
Supervisor

(Vijaya Agarwala)
Supervisor

Dated: 27/5/11

The Ph.D. Viva-Voce examination of **ROHIT KUMAR GUPTA**, Research Scholar, has been held on 17/10/11

Signature of Supervisors

Signature of External Examiner

ABSTRACT

Gamma Ti aluminde has been an important aerospace material due to its high temperature properties and lower density as compared to other high temperature materials. However, it has poor ductility at room temperature, which limits it processing and application. The alloy has been extensively studied and several methods have been applied to bring this class of alloy to industrial application. Alloy design and process design both were equally attempted and limited success have been reported. In the area of alloy design, Ti48Al with small addition of Cr, Nb and B has been noted to be promising and in the area of process design, reaction synthesis (RS) alongwith isothermal working is found to be a potential option.

Considering all these, a base alloy (Ti48Al2Cr2Nb, at%) has been selected and studied in the present work. The alloy has been modified with small addition of boron and Ni-P coated boron (0.1 at%) to obtain the benefit of microstructural refinement.

RS was selected to obtain uniform and homogenous alloy as compared to ingot metallurgy route. Effect of Ti particle size is included in the work by selecting two different sizes of particles. This study is attempted to understand the effect of particle size on reaction synthesis, homogenization and subsequent processing, through microstructure development. Calorimetry study has been carried out using non-isothermal differential scanning calorimetry (DSC) of various combinations of powder mixtures to examine the reaction of titanium aluminide formation. Reaction temperatures were noted to optimize the RS process parameters and phases formed due to transformation were analyzed.

Deformation studies of the developed alloys were carried out through isothermal and near isothermal working under vacuum and ambient atmosphere. Hot isothermal compression tests at different strain rates and at different temperatures were conducted to evaluate the flow stress and to study the deformation behaviour of the alloys. Processing maps and constitutive equations were developed using hot isothermal compression test data. Finally, heat treatment response of all the deformed samples were studied to obtain lamellar microstructures through a designed heat treatment cycle based on the understanding of phase transformations. Characterization of the alloys was carried out through X-ray diffraction, optical microscopy, Scanning electron microscopy with EDAX and elemental mapping, Transmission electron microscopy, microhardness, hardness etc.

The proposed studies are worked out considering the following points:

1. The base composition is chosen as Ti- 48Al, at.% (Ti-48Al) based on extensive literature review, which has revealed that alloys of engineering interest are centered around this composition due to best combination of mechanical properties. Addition of Cr and Nb are made to obtain Ti-Al-Cr-Nb alloy. Further, minor addition of B and Ni-P coated B is studied.
2. There are only a few studies reported for reaction kinetics of non-stoichiometric composition of binary alloys, however, no study is reported for multicomponent alloy of engineering importance i.e. for Ti-48Al 2Cr2Nb (at%) and with small addition of boron. So, basic study of exothermic reaction kinetics is proposed to be conducted on the designed compositions, using differential scanning calorimetry (DSC) technique.
3. Reaction synthesis process of titanium aluminide formation shall be studied for the designed alloy compositions to understand the mechanism of reaction. It includes variation in chemistry with respect to boron and coated boron addition and also with variation in particle sizes of titanium powder (predominant element).
4. An experimental set up was designed and fabricated to study reaction hot pressing under vacuum conditions. This set-up consists of- (i) furnace with loading arrangement with provision for vacuum (vacuum hot press) and (ii) suitable dies and punches for hot pressing experiments. This set-up is such that, it can be placed in the vacuum hot press where pre-determined loads can be applied at specified temperature.
5. Homogenization is to be carried out in the α-γ phase field of binary Ti-Al phase diagram to achieve uniformity in composition as well as to obtain Ti rich phases like TiAl and Ti_3Al from Al_3Ti formed during reaction synthesis.
6. Deformation studies through isothermal pressing/ forging with controlled strain rate are to be done to understand the mechanical behaviour of alloy at different temperatures and loading conditions.
7. Heat treatment is to be incorporated on the deformed samples to study the response of reaction synthesized plus deformed alloys to obtain desired microstructure.
8. Evaluation of alloy needs to be carried out on the samples obtained from different processing stages to understand the progress of phase transformation, element distribution, densification, microstructural changes etc.

9. Based on present study, the process technology to produce titanium aluminide of useful compositions is to be established. Processing of aluminides of these compositions is to be attempted using RS route followed by near conventional forming methods.

The thesis has been organized in different chapters as follows:

(Chapter-1: Introduction) In this chapter, the importance of Ti aluminide is introduced giving brief description of developments, their properties, advantages, and limitations. This chapter also presents briefly about various processing techniques and challenges in realization of products. Scope of the present work has also been defined.

(Chapter-2: Literature Review) This chapter contains extensive literature review on types of aluminides of interest their crystal structures, alloying additions, properties, microstructures, processing techniques, deformation behaviour, phase transformations, heat treatment, applications etc. and identifies gaps of information. This chapter also reviews studies on calorimetry to understand the aluminide formation reactions. All these lead to formulation of problem for undertaking the present research work.

(Chapter-3: Problem Formulation) Based on the extensive literature review, the problem for the present work is defined and the gaps of information found in the area of synthesis and deformation studies of $\gamma+\alpha_2$ titanium aluminides is identified.

(Chapter-4: Experimental Details) Experimental details including raw materials used, experimental set-up, equipments used, process parameters followed during reaction synthesis, secondary processing and characterization methods used are presented in this chapter.

(Chapter-5: Non-isothermal DSC studies) In this chapter, reaction kinetics studies of Ti-aluminide compositions of binary (Ti48Al, at%), ternary (Ti48Al2Cr and Ti48Al2Nb) and quaternary (Ti48Al2Cr2Nb) alloy powder mixture have been carried out through non-isothermal differential scanning calorimetry (DSC) experiments. DSC was conducted at four heating rates i.e. 10, 20, 30 and 40^0C/min. Formation of Al_3Ti phase alongwith Ti rich phases like, Al_2Ti and AlTi was confirmed through X-ray diffraction (XRD). Change in reaction enthalpy of ternary and quaternary alloys from the binary alloy is observed due to addition of Cr, Nb and B and also with change in heating rates.

Onset temperatures of reaction for all the alloys are found to be just occurring after endothermic peak of Al melting. It indicates triggering of exothermic reaction due to melting of aluminium. Onset temperatures, completion temperatures and peak temperatures of different alloys at different heating rates were observed and discussed.

Small additions of Cr, Nb, B to binary alloy is found to have important effect on reaction enthalpy, activation energy and phase transformation mechanisms. It is observed that alloying additions bring down the enthalpy and activation energy. The application of Johnson – Mehl – Avrami equation to the kinetics of exothermic reaction of Ti-aluminide formation yielded different activation energies (E) from 169.5 to 234.4 kJ/ mol. The value of Avrami parameter 'n' is calculated for exothermic reaction and is found to be in the range of 0.946 to 4.62 for various alloys. Reaction mechanisms are found to be different for different composition. Effect of particle size of Ti has been observed in changing the enthalpy, reaction temperatures and reaction transformation mechanisms. Similarly, role of Ni-P coating over boron has been observed in diminishing the reaction kinetics of the alloy.

Thus DSC studies are found to be not only useful in obtaining the kinetic parameters for the reaction, but, also in selecting the optimum parameters for reaction synthesis (RS) on the basis of onset temperature, completion temperature, enthalpy etc. It also indicated the point of application of pressure in the pressure assisted RS, to obtain desired phase transformation with densification.

(Chapter-6: Reaction synthesis studies) This chapter contains results and discussion on reaction synthesis of variants of Ti-48Al-4 (Cr, Nb, B) alloy. Analysis of results of density evaluation, phases present, elemental distribution and hardness measurement for various processing stages is presented.

Five alloys (A1-A5) have been made through reaction synthesis process using optimum parameters. Nominal chemistry of alloys are found to be A1-Ti48Al2Cr2Nb, A2-Ti48Al2Cr2Nb0.1B, A3-Ti48Al2Cr2Nb0.1B, A4-Ti48Al2Cr2Nb0.1B, A5-Ti48Al2Cr2Nb0.1B, where A3 and A5 contains Ni-P coated boron. And, Ti particle size of alloy A1-A3 is higher (200μm) whereas it is lower (50μm) in alloys A4-A5. Only minor loss of alloying elements (1-2%) has been observed in reaction synthesis (RS) due to spillage of viscous reaction products. Chemistry of the alloys are found to be within the aimed composition. Gas content was found to be higher, which can be partly due to processing/

handling environment and partly due to purity of initial powder. However, alloy products near to full density have been achieved.

Reaction synthesized samples were homogenized at 1250^{0}C for different soaking times (12-20 hrs.) depending on the alloys. Stable phases like TiAl and Ti_3Al are observed in the homogenized samples. Microstructures consisting of lamellar (γ plus α_2) and γ grains has been observed for different alloys through optical microscopy, SEM and TEM.

Average Vickers hardness values for alloys produced by RS are found to be 138-180Hv (in RS condition) and 160-240 Hv (in homogenized condition) for various alloys. Homogenized alloys have shown transformation ($\alpha+\gamma$ to α) temperature ~1400^{0}C through DSC.

Significant effect of boron addition (0.1 at%) and Ni-P coated boron addition on reaction synthesis characteristics are not found. However, it has been noted that it inhibits grain coarsening during homogenization. Effect of Ti particle size on reaction synthesis is clearly seen by the presence of Ti rich aluminides (TiAl) in the RS stage itself.

(Chapter-7: Deformation studies-I, Hot working and Flow curve) In this chapter, results of hot working of different alloys are discussed. Deformation behaviour of alloys has been studied in detail through hot isothermal compression tests.

Hot isostatic pressing (under argon), hot isothermal pressing (under vacuum) and hot near isothermal forging (ambient atmosphere) has been carried out in the temperature range of 1200-1350^{0}C. Hot isothermal compression testing of selected three alloys were conducted at temperature ranging from 750-1250^{0}C and with strain rate of 0.001 to 0.1/ sec under vacuum. Surface crack/ cracking in the tested specimens are observed when strain rate is high (0.1/ sec) and temperature is low (750-850^{0}C). Peak flow stress is found to decrease with increase in temperature and decrease in strain rate.

Stress-strain curve have been divided into three stages, flow hardening, steady state stage and flow softening stage. Most of the alloys have shown wider steady state stage in case the alloys deformed between 950-1150^{0}C at slower strain rates (<0.01/ sec.). Hot workability maps based on observations of hot compression tested samples, also show this range of temperature and strain rate as a safe zone for deformation.

Microstructures of all the alloys are found to be refined after hot deformation. Microstructure of boron free alloy showed two phase (α_2 and γ), whereas boron containing alloys showed lamellar structure alongwith single phase γ.

Alloys made with smaller size of Ti particle showed relatively finer microstructure than the alloys made with larger size of Ti particles. Lamellar volume fraction in boron containing alloys is found to be significantly high >40%. Also, interlamellar spacing is higher for deformed samples deformed at higher temperature and slow strain rates and vice versa. Interlamellar spacing has been found to be varying between 0.5-2μm depending on the rate of loading. Presence of twins has been noted in alloy deformed with relatively higher strain rates (through pack forging and open die forging). DRX grains content (10-50%) of size (5-20μm) is found on the samples deformed at different temperature and strain rates. It grows with increasing temperature and decreasing strain rate and vice versa in isothermal working. It is present at the boundaries of primary grains. Lamellae orientation difference within the grain is noted, which indicates multiple nucleation sites along the grain boundary for lamellar phase transformation. Dynamic recrystallization is found to be the restoration processes of γ-TiAl base alloys during high temperature deformation.

Microhardness of single phase is found to be between 520 to 668Hv, of recrystallized grains is 214 to 380Hv and of lamellar packets is from 388 to 497Hv. On an average lamellar phase has microhardness of ~430Hv.

(Chapter-8: Deformation studies-II: hot workability, development and validation of constitutive equations) In this chapter, deformation behaviour of TiAl alloys based on macroscopic determination approach of flow stress has been discussed. Zones corresponding to flow instabilities has been identified. It is noted that flow instabilities are either due to lower temperature where formation of microcracks leads to premature failure of material or due to flow softening.

Power efficiency maps, contour maps and processing maps have been generated using hot isothermal compression tested data. DRX domain is found to be in the temperature and strain rate regime of 950-1150^{0}C and 10^{-1}-10^{-2}/sec respectively, which is in the homologous temperature range of 0.7-0.8. Superplastic domain is found to be in this temperature range with slower strain rates. However, temperature of superplastic zone is found to be 950-1050^{0}C, showing role of boron in lowering the superplastic temperature domain.

Safe working range for boron free alloy is found to be wider as compared to boron containing alloys. This zone is found to be decreasing with increasing strain. However, this effect is different for different alloys. It is more pronounced in the case of boron containing alloys.

Strain rate sensitivity (m) is found to be upto 0.55 for boron free alloy and upto 0.9 for boron containing alloys, depending on strain rates and temperature. 'm' is also found to be varying with strain, mainly at low strain level and at higher strain level. At intermediate strain change in m is marginal. Activation energy for deformation of boron free alloy is found to be 335 kJ/ mole and of boron containing alloy is 387.5 kJ/ mole. Zener-Holloman parameter is found to have very close linearity with the peak stress. Prediction of flow stress through generated constitutive equations is found to be more precise in sound deformation regime i.e. 950-1050^{0}C range at 0.01/ sec. strain rate. Universal applicability of equation is also noted at 950^{0}C at intermediate strain rates. For the present TiAl alloys, recrystallized grain size (D_{DRX}), is found to be related to deformation temperature and strain rate as '$\ln D_{DRX} = 3.26-0.052\ln Z$ '(for boron free alloy) and as '$\ln D_{DRX} = 4.27-0.084\ln Z$' (for boron containing alloy).

(Chapter-9: Response to heat treatment) This chapter discusses about the heat treatment cycle implemented in deformed alloys. Heat treatment cycle is designed and carried out to obtain refined fully lamellar microstructure. Fast cooling from just above α transus followed by reheating and soaking at two phase region is followed. Hardness of the alloys is found to vary between 284 to 355Hv in heat treated condition. Higher hardness for boron containing alloys is observed.

Microstructure after heat treatment in most of the cases is seen to be lamellar type. However, minor variation in morphology of lamellar microstructure is observed from alloy to alloy. As quenched alloy microstructure showed feathery structure with fine lamellar colonies.

Lamellar colony size of boron free alloy is found to be relatively higher (100-300μm) than boron containing alloys (75-200μm). In open die forged and heat treated sample, many localized phenomenon like presence of serrated lamellar boundaries, lamellae resembling bamboo-clusters boundary (zig-zag uneven boundary), small isolated lamellar colony, straight cross boundary, secondary lamellar colony, localized lamellae coarsening, differential lamellae, discontinuous coarsening, bending of lamellae etc. are seen.

In double annealing treatment presence of γ phase is observed. It indicates single annealing cycle is insufficient to nucleate γ precipitate and if this cycle is repeated γ phase can be obtained with desired volume fraction. In double annealing lamellar spacing and colony size is found to be similar to single annealing.

(Chapter-10: Conclusions) This chapter covers the conclusions drawn from this work on synthesis and deformation behaviour of $\gamma+\alpha_2$ aluminide alloy compositions with respect to reaction kinetics, densification, homogeneity, phase transformation, deformation behaviour, heat treatment response and mechanical properties.

ACKNOWLEDGEMENT

I derive esteemed pleasure in expressing my deep sense of gratitude to Prof. Vijaya Agarwala of IIT Roorkee, Dr. Bhanu Pant and Dr. P.P. Sinha of VSSC Trivandrum for suggesting me the problem, supervising the work and being a source of inspiration at each stage of this investigation. I am deeply indebted to them for their inspiring guidance, meticulous attention, constructive criticism and giving new shape to this work. The completion of this thesis has been possible, only due to their intellectual support.

I express my sincere thanks to Prof. R.C. Agarwala, IITR, who helped me to understand reaction kinetics and various types of phase transformation. I am grateful to Dr. Rama, NIH Roorkee for guiding me in the area of soft computing. I express my deep sense of gratitude to Shri P. Ramkumar, DGM, MPA (VSSC) who has been providing me constant technical, moral and managerial support during the work. I thank Dr. Appa Rao, DMRL for HIP facility support. I express my sincere gratitude to Prof. G.V.S. Sastry and Dr. Manna of Metallurgy Dept., IT-BHU for TEM support and technical discussions.

Shri K. Sreekumar and Dr. S. C. Sharma has been constantly inspiring and providing necessary guidance. I am very much grateful to them. I am thankful to Shri R. Suresh Kumar, Shri Samuel, Shri A.K. Shukla of VSSC for extending support with vacuum hot press, Shri A. K. Saini of IIC (IITR), Dr. P. Ramesh Narayanan, Shri A.K. Jha, Shri Sushant, Ms. Swathi, Shri V.M.J. Sharma, Shri Sudershan Rao of MMG, VSSC for characterization, Shri Jacob Phillip, Shri G. Radhakrishnan, Shri V. Rajesh, Shri Suresh, Shri Ravish, Shri Jose, Shri Johnson for specimen preparation through EDM and necessary workshop facility. I am thankful to Dr. S.V.S. Narayan Murty for deformation related studies and technical discussions.

The work could not have been completed without my two dear colleagues Shri V. Anil Kumar and Shri M. K. Karthikeyan of MPA, VSSC and my dear friend Shri Sachin Tyagi (PhD, IITR) who were always with me to share all types of technical and managerial problems during the entire course of my work. I am thankful to them. I also thank all the laboratory staff members of Deptt. of MME, IIT Roorkee, MMG (VSSC) and IFF (VSSC) who directly or indirectly extended their co-operation for completion of this work. I am grateful especially to Shri S.D. Sharma (TEM lab, IITR), Shri Anjaneya (TEM lab, IT-BHU), Shri Sharma (OM lab, IITR), Smt. Dhanya (OM lab, MCD, VSSC) for their co-operation.

It would not have been possible to complete successfully my thesis without the invaluable inspirations and constant encouragement of my friends Lalmoni, S.K. Singh, Niraj Nayan, Manoj Agrawal, Vinod, Dr. N. K. Prasad (IT-BHU). I am thankful to all of them.

I wish to express my sincere indebtedness to my grand parents, parents, parents' in-law, brother and sisters, whose deep affection and silent inspiration have always guided me towards success. Throughout the course of work, my dear wife Smt. Shachi and daughter Nidhhi have been with me wholeheartedly and I would not have been able to complete this onerous task without their proactive support and encouragement. Last but not the least, I am thankful to THE ALMIGHTY for giving me the inspiration and strength to undertake this work and sustaining through the course of the work to bring it to a meaningful conclusion.

June, 2011 **Rohit Kumar Gupta**

CONTENTS

LIST OF FIGURES

LIST OF TABLES

NOMENCLATURE

α	The reacted fraction
β	The heating rate
ρ	Density
σ	Stress
C	Compliance factor
DSC	Differential scanning calorimetry
E	The activation energy of the reaction
m	Rate of densification parameter
n	Avrami parameter (in reaction kinetics)
P	Pressure during RS
Ω	Porosity
R	The gas constant, 8.3143 J/ mol/ K
RHP	Reaction hot pressing
RS	Reaction synthesis
SHS	Self propagating high temperature synthesis
T	The absolute temperature
t	Time
TLPS	Transient liquid phase sintering
m	Strain rate sensitivity
η	Power efficiency
ζ	Instability criteria
ε	strain
σ	stress
σ_p	peak stress
$\dot{\varepsilon}$	Strain rate
Hp	HIPed

Af	Open die forged (air forged)
If	Isothermal forged
Z	Zener-Holloman parameter
Q	Activation energy (of deformation)
n	strain hardening exponent (in deformation)
D	Grain diameter (size)
A1-A5 (in italic font)	Five different alloys
DRX	Dynamic recrystallization

Chapter-1

INTRODUCTION

In the era of economical and interplanetary aerospace missions, advanced materials play prominent role, especially for high temperature applications. Large numbers of high temperature materials have been studied in the recent years and researchers have proposed many potential materials for specific purposes. However, selection of material for aerospace systems is very critical, which experiences very complex environments. It is equally true for increasing demand of energy efficient systems in automotive industries also, to reduce CO/ CO_2 emissions. All these requirements are guided by high temperature strength with lower weight.

Gamma Titanium aluminides are envisaged as a potential candidate for high temperature applications in aerospace and automobile industries. This belongs to the class of ordered intermetallics, which has excellent modulus and strength retention at elevated temperatures coupled with low density and good high temperature oxidation resistance. Study on this class of material began in 1950's, however major attention was not focused until the mid 1970's when research programme was initiated by U.S. Air Force Materials Laboratory *[1]*. This research program and subsequent work conducted in 1980's recommended Ti48Al (at%) with minor addition of alloying elements like V, Mn, C, etc. *[2-4]*. Subsequently, addition of Cr and Nb was also reported to improve the ductility and oxidation resistance of the alloy *[1, 5]*. In 1993, General Electric conducted successful engine tests on a full-set wheel of gamma titanium aluminide blades, which improved overall confidence in the material *[1, 2]*. Noting its importance, research and development work picked-up in the subsequent years in the area of alloy design, microstructure d esign, properties evaluation and characterizations for fatigue and creep applications in aerospace and automobile sectors. However, limitations for widespread applications of these materials were noted due to poor room temperature ductility, low fracture toughness, fast fatigue crack growth rates and lower oxidation resistance above 800^0C. Further, mechanical properties were linked to chemistry and microstructure and trade-off between properties like fracture toughness and ductility was suggested *[1, 6]* to tap the potential of alloy.

Process selection for fabrication of Ti aluminide components was another major challenge and several processes were attempted. Primary ingot through ingot metallurgy

route as well as powder metallurgy was evaluated [5, 7-9]. Difficulties in secondary processing were also reported [10-14]. Recently, processing method of Plansee AG for titanium aluminide sheets through patented 'Advanced Sheet Rolling Process (ASRP)' has been reported. Sheets (foils) of thickness down to 150μm have been rolled *[15]*. Simultaneously, processing to realize useful components for aerospace and automobile applications have also been attempted by several agencies *[16-21]*.

Today, it is highly convincing that gamma titanium aluminides hold excellent properties for high temperature applications. However, challenges and problems cited above are not resolved fully and studies on this material are being continued to make it suitable for conventional processes. The present work is undertaken with an aim to study the processing of alloys with Ti-48Al (at%), through near conventional methods using powder metallurgy (PM) route. The purpose of this research is to process and characterize this potential candidate material and to provide a better understanding of synthesis and mechanical behaviour of alloys with minor addition of alloying elements in gamma Ti aluminide. The objective of the present work is to study the processing aspects of $\gamma+\alpha_2$ based alloys and to obtain a combination of parameters for processing through near conventional methods. It is also intended to use these alloys is aerospace systems.

In the present work, firstly a base alloy (Ti48Al2Cr2Nb, at%) has been selected on the basis of properties and prospective applications in aerospace and automobile. Reaction synthesis (RS) was selected to obtain uniformity with respect to composition. Selected alloy and its variants with respect to Ti particle size and boron addition were made through RS process. Effect of Ti particle size is included in the work by selecting two different sizes of particles i.e. smaller particle size (50μm average) and larger particle size (200μm average). This study is attempted to understand the effect of particle size on reaction synthesis, homogenization and subsequent processing, through microstructure development.

Calorimetry study has been carried out using non-isothermal differential scanning calorimetry (DSC) of various combinations of powder mixtures to examine the mechanism of titanium aluminide formation through exothermic reaction. Phases formed due to transformation were analysed through X-ray diffraction (XRD) of DSC samples. Reaction temperatures were noted to optimize the RS process parameters.

Deformation studies of the developed alloys were carried out through isothermal and near isothermal working under vacuum and ambient atmosphere. Hot isothermal compression tests at different strain rates and at different temperatures were conducted to evaluate the flow

stress and to study the deformation behaviour of the all oys. Processing maps and constitutive equations were developed using hot isothermal compression test data. Finally, h eat treatment response of all the deformed samples was studied to obtain lamellar microstructures through a designed heat treatment cycle based on the understanding of phase transformations. Characterization of the alloys was carried out through X-ray diffraction, optical microscopy, electron microscopy, microhardness, hardness etc.

Chapter-2

LITERATURE REVIEW

2.1 INTRODUCTION

Intermetallic compounds are defined as solid materials containing two or more metallic elements, with optionally one or more non metallic elements, whose crystal structure is same as that of the other constituents. Under this definition Electron compounds (or Hume-Rothery compounds) and Laves phases are included. These are ordered compounds, where atoms tend to occupy specific lattice sites as compared to solid solution alloys that have constituent atoms at random lattice sites. The driving force for such an arrangement is the greater strength of dissimilar atomic (A-B) bonds as compared to similar atomic (A-A or B-B) bonds *[22]*.

Intermetallics have been in use for a very long time starting from 2500 BC as cementation, dental amalgam, magnets etc. Its history has been outlined by several researchers *[23, 24]*. Presently, large systems of intermetallics are envisaged for various applications ranging from thermo-structural, electromagnetic to chemical/electrochemical applications. Specifically, aluminides of nickel, iron and titanium are in the advanced stage of development for different types of thermo-structural applications in aerospace, automobile and energy industries *[16, 20, 25, 26]*.

Amongst aluminides of nickel, iron and titanium, the density of Ti aluminides is lowest. It is about half of the superalloys. These aluminides possess higher specific modulus and specific strengths at elevated temperatures *[16, 20, 27]*. Ti aluminides of industrial importance are mainly γ (TiAl) based aluminides (γ aluminides) and α_2 (Ti_3Al) based aluminides (α_2 aluminides). The strength retention in the α_2 aluminides is upto a temperature of 700^0C whereas γ aluminides retain strength upto 1000^0C. Among these two, γ titanium aluminides are more attractive due to relatively lower density and better high temperature properties. The most important γ Ti-aluminides are the two-phase alloys based on Ti_3Al and TiAl with aluminum content ranging from 36 to 50 atomic percent, as shown in Fig. 2.1 *[28]*.

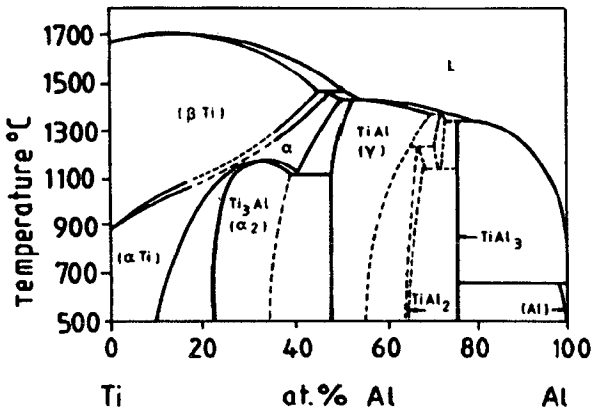

Fig. 2.1: Ti -Al phase diagram *[28]*

Reviews on applications and properties of these titanium aluminides have been comprehensively presented by several researchers *[29-31]*. Application of γ titanium aluminides are envisaged as turbine blades, turbine rotor discs, fins, nozzle fins and automobile rotor discs *[16-21]*. In fact, Mitsubishi is already using γ titanium aluminide turbocharger rotors in commercial automobiles since 1999 *[20, 21]*. The alloy has also received tremendous attention from aerospace sector as well *[18]*. Some of the components used in various industries are shown in Fig. 2.2.

Present work is focused on two phase $\gamma+\alpha_2$ alloys and the same have been reviewed in this chapter. A brief comparison of these alloys with some high temperature materials is presented in Table 2.1. Regarding thermal properties, it has been reported to have lower thermal expansion and higher specific heat as compared to Ni based alloys and Ti alloys whereas thermal conductivity is comparable to superalloys and is higher than Ti alloy *[32]*.

The ordered structure of aluminides that make them useful for high temperature applications renders them brittle at ambient temperature *[16, 22]*. The inherent brittle nature of aluminides has necessitated development of new alloys and processing routes to achieve the required form and shapes. Alloy developments have been focused mainly on binary alloy composition of Ti 44-50Al (at%) due to higher ductility *[17]* with small additions of Cr, V, Mn to further improve the ductility of the alloy. In the processing area, different processing techniques have been evolved for the intermetallics over the years like casting *[20, 21, 33-37]*, powder metallurgy (PM) routes *[38-40]*, mechanical alloying *[41-46]* and reaction synthesis *[47-50]* etc. A detailed review of various processing techniques and current status of intermetallics has been presented by Yamaguchi et al. and has also been described in detail by Zhao and Westbrook *[25, 51]*.

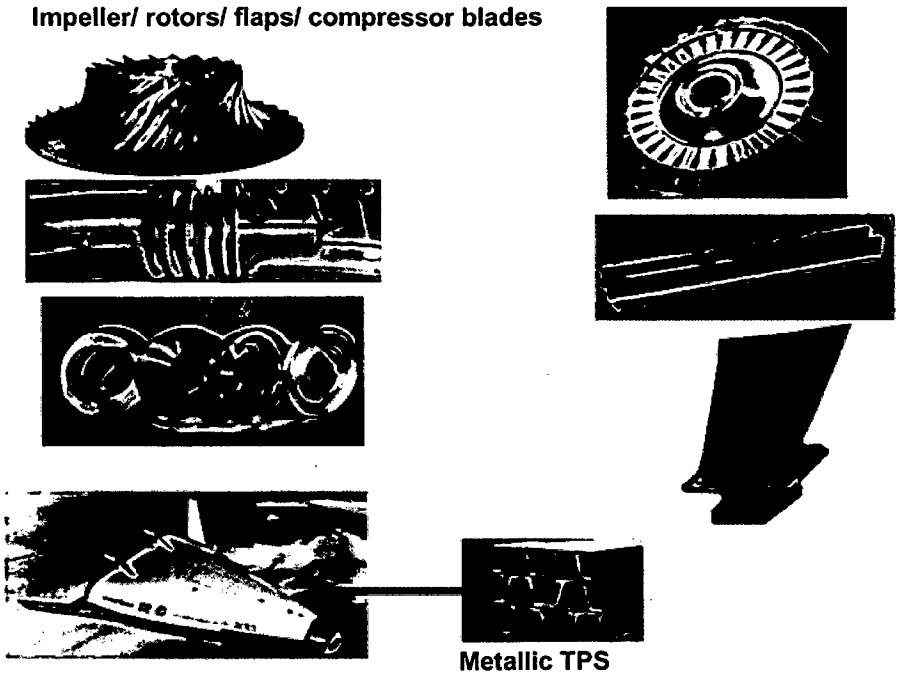

Fig. 2.2: Components of Ti aluminides used in various industries

Another important property required for using the alloy at elevated temperature is, high temperature oxidation resistance, which is reported to be poor and need of improvement has been noted. Since, it depends on the formation of protective alumina scale that in turn depends on the activity of aluminum in the alloy *[52-55]*, efforts have been made in this direction by alloying additions of Nb, W and Mo (as low as 1-2 at%). Considering the poor ductility and poor oxidation resistance of the alloy, Cr and Nb both have been added to binary alloy (Ti 44-50 Al), which has led to development of most notable γ-alloy Ti-48Al-2Cr-2Nb *[56-57]*.

Much success with respect to improvement in ductility could not be achieved even with very specialized processes. Therefore, in spite of having good properties, the alloy has been limited to some specific applications only. To fulfill the aim of present work, a thorough literature review on various aspects of primary processing, secondary processing (mechanical working) and deformation mechanisms have been conducted. Literature on various heat treatment cycles to obtain desired microstructures and properties have also been included. Physical metallurgy of the alloy and effect of alloying addition to binary γ titanium aluminide alloy has been reviewed to have better understanding in designing experimental work.

Table 2.1: Properties of important aluminides and superalloys *[16, 24]*

Type	M. P. °C	Density gm/cc	0.2% YS MPa	Modulus GPa	Oxidation resistance	Usable temperature °C
Ti_3Al	1600	4.2	700-900	145	Poor	700
TiAl	1460	3.8	400-650	176	Fair	900
Fe_3Al	1540	6.7	385-392	141	Good	750
FeAl	1250	5.6	360-380	261	Good	750
Ni_3Al	1390	7.5	250-500	179	Good	750
NiAl	1640	5.9	250-475	294	Good	750
Superalloy (Ni base)	1380	8.3	850-900	206	Good	650

2.2 IMPORTANT Ti ALUMINIDES

2.2.1 Ti_3Al (α_2 TITANIUM ALUMINIDE)

Ti_3Al (α_2) phase has a wide composition range from 22 to 39 atomic percent aluminium (Fig. 2.1) and is stable upto about 1090°C *[58]* for stoichimetric composition Ti-25 Al (at%). It has hexagonal ordered DO_{19} crystal structure as shown in Fig. 2.3. The density of Ti_3Al is 4.2 gm/cc and the density of Ti_3Al based alloys is in the range of 4.1 to 4.7 gm/cc *[24, 58]*.

Unalloyed Ti_3Al is brittle and has no workability at low temperatures upto 600^0C *[24]*. Various alloys have been developed to enhance strength and ductility by alloying with elements like Mo, V, Nb etc. and by controlling the microstructure *[59]*. Typical alloy compositions of engineering significance are Ti-24Al-11Nb, Ti-25Al-17Nb, Ti-25Al-17Nb-1Mo *[58]* and Ti-25Al-10Nb-3V- 1Mo [60]. These alloys have combination of substantially higher strength and toughness *[59, 61]*.

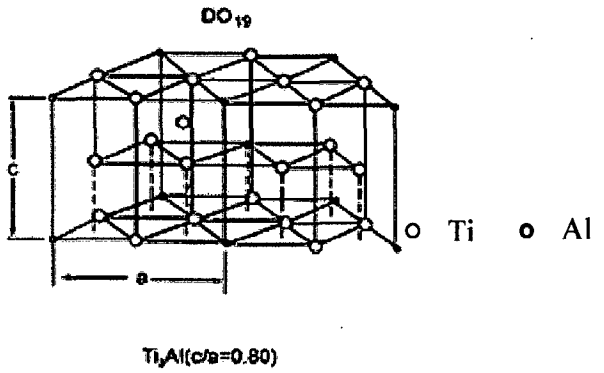

Fig. 2.3: Ordered DO_{19} crystal structure of Ti_3Al

2.2.2 TiAl (γ TITANIUM ALUMINIDE)

The γ TiAl phase has ordered face centered tetragonal $L1_0$ structure (Fig. 2.4) with a composition range of 49-66 Al (at%). It remains ordered upto its melting point of 1440^{0}C *[17]*. Single phase γ TiAl is completely brittle at room temperature. Room temperature ductility of γ TiAl based on two phase ($\gamma+\alpha_2$) alloy is higher at around Ti-48Al (at%) *[17]*, therefore studies have been focused in two phase region of binary phase diagram i.e. Ti 44-50 Al (at%). The density of TiAl is 3.4 gm/cc and the density of TiAl–based alloys is in the range of 3.4 to 3.9 gm/cc *[24, 58]*.

However, ductility of binary alloy is insufficient for further processing and applications. Therefore, various methods like alloy addition, controlled processing, heat treatment etc. are applied to get optimum combination of strength and ductility. Alloying additions in the range of 1 to 10 at% are used among Cr, V, Mn, Nb, Ta, W and Mo for γ Ti aluminides *[58]*.

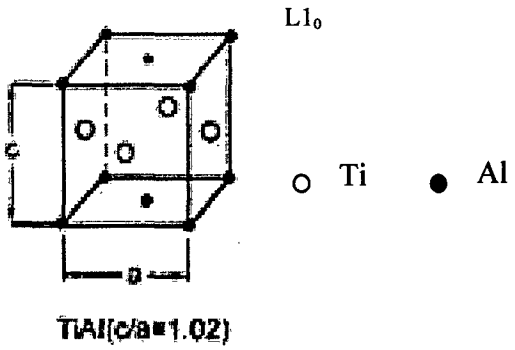

Fig. 2.4: Ordered $L1_0$ crystal structure of TiAl

2.2.3 IMPORTANCE OF γ-Ti ALUMINIDES AND ITS APPLICATIONS

There are at least three major pay off areas for γ Ti aluminides in advanced turbine engines and other aerospace systems like thermal protection systems:

(a) γ-TiAl has a higher specific stiffness as compared to structural materials commonly used in aircraft engines. Generally, stiffness is valuable whenever clearances are concerned, such as frames, seal supports, cases, linings etc.

(b) The good creep resistance of advanced γ-TiAl based alloys in the temperature range of 600 to 650^{0}C enables it to substitute Ni based alloys (twice the density as γ-TiAl alloys) for certain applications like turbine blades, turbine rotor discs etc.

(c) The high fire resistance of γ-TiAl based alloys (nearly as resistant as Ni based alloys) may enable the substitution of heavy and expensive fire-resistant Ti based alloy components. Skin panel structures in regions that experience temperatures below 800^0C for reusable launch vehicles has been suggested with gamma titanium aluminides.

Besides aerospace applications, worldwide interest is focused on automotive engine applications also. Exhaust engine valves appear to be an ideal application for γ Ti alloys. There are three major benefits, which could be exploited by the use of lightweight engine valves namely, a) higher fuel economy, b) better performance and c) reduced noise and vibration. In the processing area, casting and reactive sintering are the extensively used processing methods for actual component fabrication *[20, 62-64]*.

Further, studies and development and characterization of gamma aluminides are being carried out in various countries e.g. in the USA *[16, 65-67]*, in Japan *[20, 21, 51, 68, 69]*, in Great Britain *[70-73]*, Russia *[74-80]*, Poland *[81-83]*, Germany *[24, 84, 85]* and India *[50, 87-91]* to achieve better combination of properties.

2.3 PHYSICAL METALLURGY OF γ TiAl

2.3.1 PHASE TRANSFORMATIONS

Two phase ($\gamma+\alpha_2$) alloys of practical importance in aerospace and automobile lies in the composition range of 38-50Al (at%) in binary Ti-Al system. These two ordered intermetallic phases coexist in equilibrium at temperatures below 1000^0C. The lattice parameter of DO_{19} structure of α_2 phase (with 38 at.% Al) and of $L1_0$ structure of γ phase (with 48 at.% Al) are:

α_2: a= 0.57 nm; c= 0.46 nm; c/a = 0.803

γ: a= 0.40 nm; c=0.408 nm; c/a = 1.020

The axial ratio of tetragonal unit cell of the γ phase being very close to unity, the structure of the γ phase can be approximated to be cubic and the transformation between the α_2 and γ structures can be considered as that between an ordered hcp (ordered α) and an ordered cubic structure. The near perfect lattice matching between the close packed planes of α_2 and γ phases controls the morphology of the $\gamma+\alpha_2$ structure. A strict orientation relation between α_2 and γ is invariably maintained in the lamellar $\gamma+\alpha_2$ structure, which has been revealed from the diffraction pattern, as shown in Fig. 2.5 *[91]*.

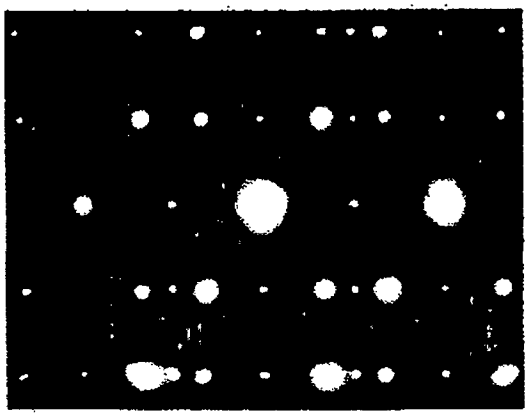

Fig. 2.5: Diffraction pattern of α_2 and γ lamellar structure *[91]*

From the binary Ti-Al phase diagram, covering 35-50Al (at%) (Fig. 2.6) *[91]* transformation pathways of α_2 and the γ phases can be seen, which evolve through one of the pathways listed in Fig. 2.6 for 5 different binary alloys.

2.3.2 MECHANISMS OF PHASE FORMATIONS

It has been reported that, all types of transformations are affected by cooling rate from the heat treatment temperatures and the kinetics is strongly influenced by the Al content, by the amount of beta stabilizer and grain size *[92-97]*. Hu and Botten (2002) *[92]* has experimentally investigated the continuous cooling transformation (CCT) curve for a typical industrial alloy Ti46Al2Cr2Nb1B (Fig. 2.7) using different cooling rates from 1450^0C (β phase field). Mechanisms of various types of microstructure development have been proposed by several workers, which are briefly discussed here.

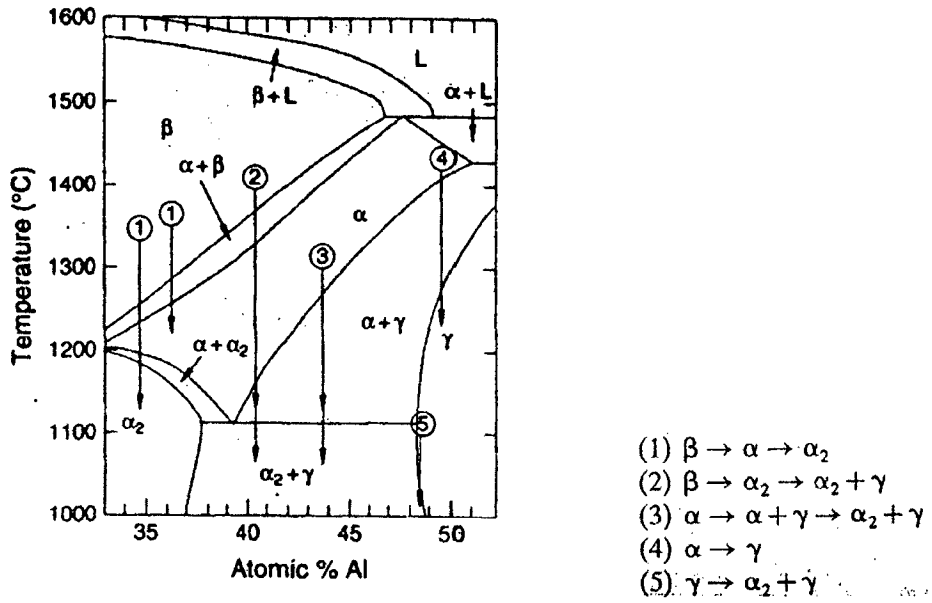

Fig. 2.6: Ti-Al binary phase diagram showing formation of various phases at different temperatures and compositions in the range of 35-50 (at%) *[91]*.

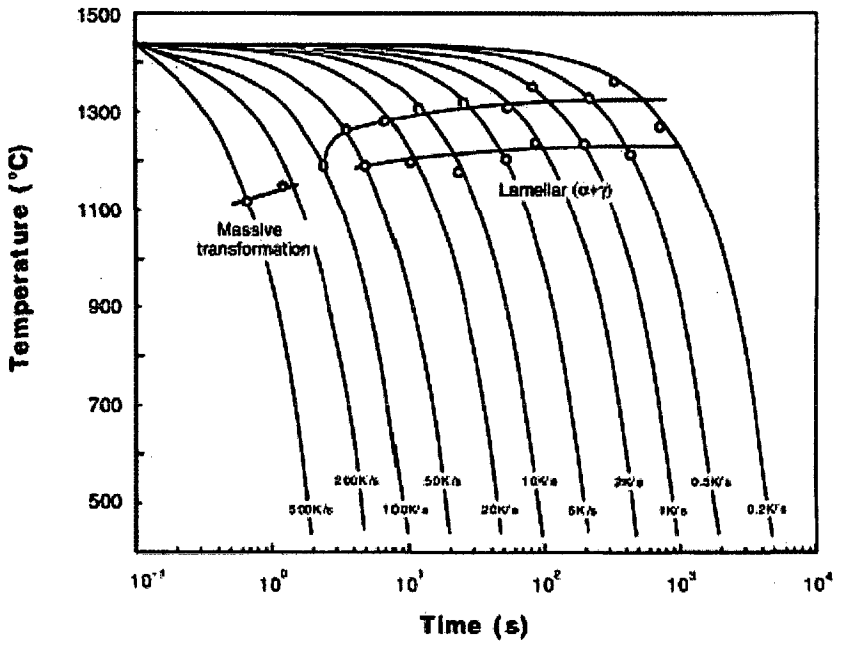

Fig. 2.7: CCT curve of Ti 46Al 2Cr 2Nb 1B *[92]*

2.3.2.1 Formation of Lamellar Structure

The mechanism of formation of lamellar structure has been different from eutectoid reaction. In this alloy, lamellar structure is the result of precipitation of γ lamellae in either a disordered α or in ordered α_2 matrix. Its formation starts with pre nucleation stage where stacking faults are introduced through propagation of Shockley partials in either the hexagonal disordered α or ordered α_2 matrix, which results in change in the crystal structure *[98]*. It has been proposed by Denquin and Naka *[99]* that, longitudinal and lateral growth of the lamellar precipitates occurs through 'terrace-ledge-kink' mechanism, which corresponds to the transfer of atoms onto ledge-kinks ensuring the composition change involved in the lamellar structure formation.

The ordering process, which assumes the existence of a metastable lamellar fcc phase, consists of a nucleation of orientation variants at a number of separate sites followed by independent growth of the variants on those sites in this metastable phase. Finally independent growth of the variants and encountering of two adjacent lamellae leads to the formation of twin boundaries (TBs), pseudo-twin boundaries (PTBs), ordered domain boundaries (ODBs) or anti phase boundaries (APBs), if the stacking sequence of two lamellae is different. Further, coupling of ODBs/ APBs with the other boundaries of lamellar structure results in mixed boundaries (MBs) *[99]*. Subsequently, the growth of the lamellar γ phase slows down and can stop with a gradually decreasing solute supersaturation in the matrix, reducing the driving force for ledge movement.

2.3.2.2 Formation of Secondary Lamellar Structure

Modification of primary lamellar structure has also been reported in the processing, which is found to be due to discontinuous coarsening of primary lamellar structure *[100-101]*. It occurs behind the migrating α or α_2 grain boundary and the resulting secondary γ lamellae remain inside the initial grain of the primary lamellar structure almost parallel to the primary γ lamellae. However, the secondary lamellae become much coarser, and the boundaries between the two phases α_2 and γ are less regular, although the orientation relationship between these two phases is the same as that observed in the primary lamellar structure. Optical microscopy reveals the development of discontinuous coarsening at both sides of a grain boundary ('double –seam' development) *[102]*.

The discontinuous coarsening reaction starts during the formation of the primary lamellar structure leading to the formation of serrated grain boundaries. It is due to a

change in the matrix composition as well as in the volume fraction of γ and α_2 phases of the lamellar structure. Thickening of these lamellae during the growth stage is provided by solute supersaturation, which slows down with the decrease of solute supersaturation similar to termination of primary lamellae growth. If grain boundaries possess sufficient mobility, dissolution of primary lamellae and its reprecipitation has also been suggested as another type of growth process. All the above phenomena can be seen in the microstructures presented in Fig. 2.8.

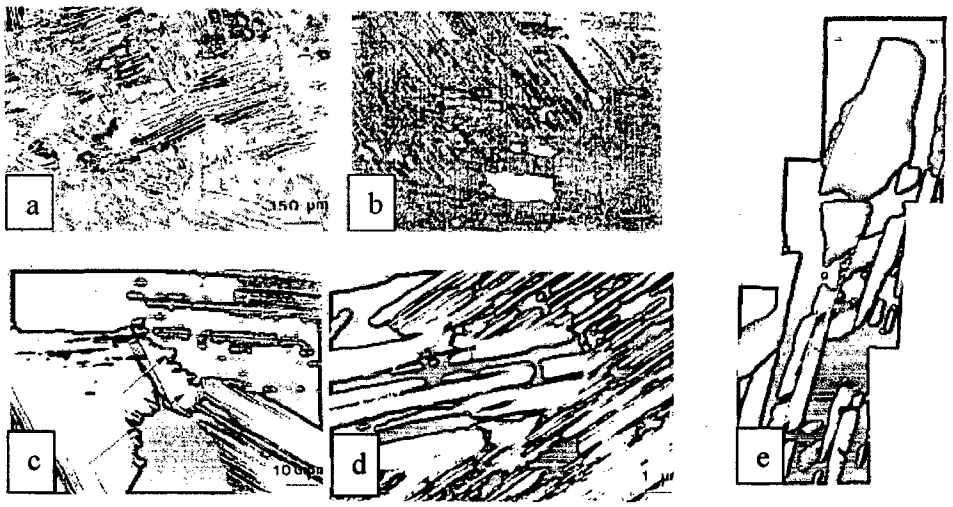

Fig. 2.8: Discontinuous coarsening in Ti 46 Al alloy, (a) homogenized for 72 hrs at 1150^0C, (b) double seam structure (24 hrs at 1150^0C), (c) cooled from 1400^0C to 1250^0C then oil quenched (discontinuous coarsening of primary lamellar structure), (d) TEM micrograph showing serrated grain boundary, (e) Various stages of discontinuous coarsening (1150^0C for 24 hrs.) showing irregular secondary lamellar structure *[102].*

After discontinuous coarsening, the two phases α_2 and γ keep the same orientation relationship as that observed in the primary lamellar structure, but their interfaces are much more irregular. Such an irregularity indicates that the formation process of the secondary lamellar structure (discontinuous coarsening) is different from that of primary lamellar structure. Secondary γ lamellae formed just behind the moving grain boundary maintain lattice continuity; this suggests an epitaxial character of the process. Re-precipitation occurs on the extremity of a pre-existing primary lamella with a direct solute transfer from grain boundary. In such case, there is no apparent role of Shockley partials.

2.3.2.3 Formation of Massive Structure

Formation of other phases and microstructures like massive, feathery, Widmanstatten etc. has also been confirmed in TiAl alloys (Fig. 2.9) *[103-112]*. These phases are more specific in experimental conditions. As the cooling rate from the α phase increases, the formation of the lamellar structure is replaced by massive transformed γ (γ_m) regions, which has large number of faulted domains. Various types of defects are found to be present in these domains. Stacking faults lying on {111} planes, act as nucleation sites for the micro twins. From the crystallographic point of view, the apparent absence of any simple orientation relationship between the parent α phase and the γ_m phase as well as the irregular and curved character of various interfaces, particularly between the parent and product phases suggest that γ_m does not form simply through a homogeneous shear on specific planes, typical of the martensite transformation.

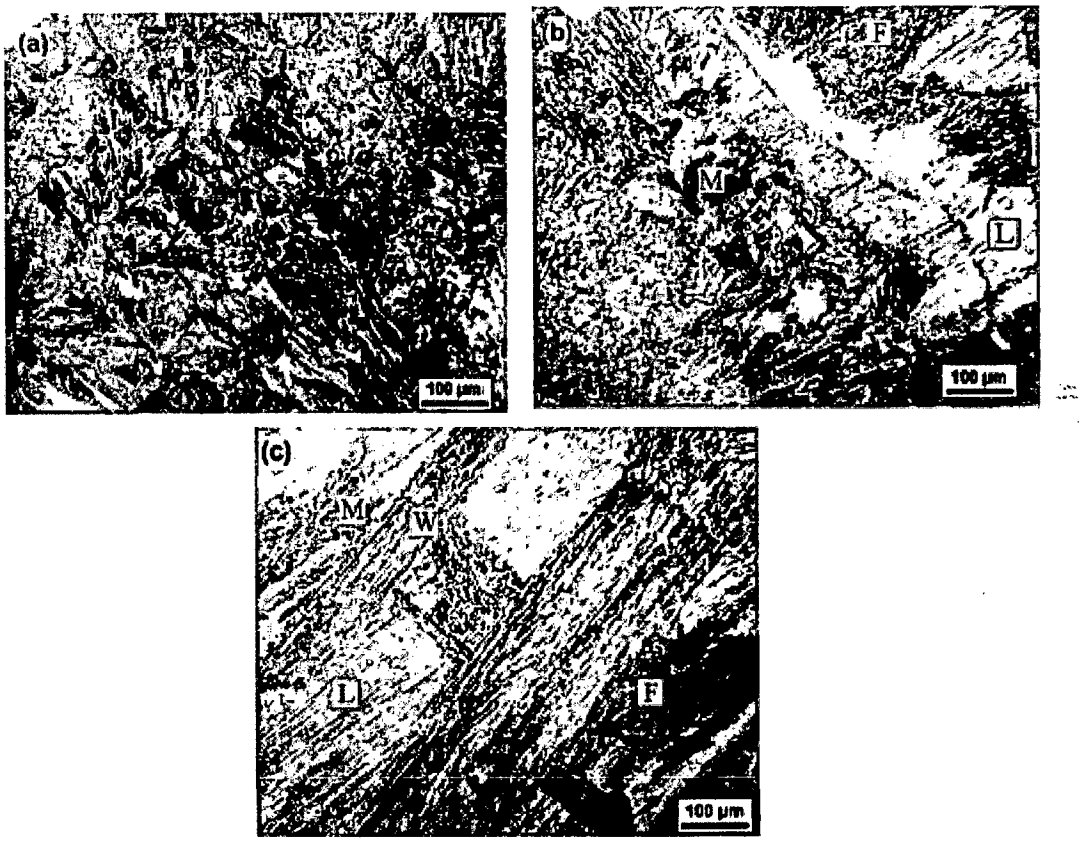

Fig. 2.9: Optical microstructures in continuously cooled Ti46Al8Nb from 1360^{0}C (α phase), (a) fully massive γ obtained at cooling rate of 1800^{0}C s^{-1}, (b) a mixture of massive γ+ feathery+ lamellar microstructures obtained at a cooling rate of 25^{0}C s^{-1} (c) a mixture of feathery+ Widmanstatten + lamellar microstructures obtained at a cooling rate of 10^{0}C s^{-1} (M, F, W and L stand for massive, feathery, Widmanstatten and lamellar microstructure) *[112]*

As per the proposed mechanism, the nucleation of γ_m phase takes place at grain boundaries by forming a low energy highly coherent interface with at least one of the matrix grains. The γ_m nuclei growth is achieved by thermally activated jumps of individual atoms across an incoherent α/γ interface. Then ordering takes place by two probable methods. The first one involves the direct α to γ transformation. In this process, ordered domains and antiphase domains can be formed through a random character of atomic transfer (Ti or Al) resulting in the arrival of atoms at different positions of the lattice. The second one involves the existence of a metastable disordered fcc type phase followed by an ordering reaction at numerous sites, and the encountering of two growing domains leads to the formation of 'ordered domain boundaries' (ODBs) or 'antiphase boundaries' (APBs). Also, the twinning due to a transformation induced stress concentration leads to the formation of twin and pseudo-twin related domains.

2.3.3 ALLOYING ADDITIONS IN TWO PHASE γ Ti ALUMINIDE

It is noted that, with increasing temperature and decreasing aluminum content with small amount of α_2 phase, the ductility increases and is significantly more ductile than single-phase (γ) alloys *[17, 113]*. This has been due to the increase in activities of the slip and twining *[114]* and according to Tsujimoto and Hashimoto *[115]*, the strong covalent bond existing in γ TiAl would evolve towards a metallic bonding when the amount of aluminum diminishes. Accordingly, alloys are designed to obtain the benefit of maximum ductility in binary composition and also alloying elements are added to further improve the ductility. The role of third alloying element like Cr, V, Mn and Ni to the two-phase binary alloy is to improve ductility, whereas elements like Nb and Ta have been reported to improve oxidation resistance *[58]*. Further, the oxidation resistance improves with the addition of small amount of phosphorus *[116, 117]* also.

Several mechanisms have been proposed on the improvement in ductility of aluminides due to alloying additions. Addition of W, V, Mn and Cr helps in reducing the grain size *[115, 118]*, which improves the ductility. Another factor for higher ductility is attributed to reduction in covalency of Ti-Al bond because atoms of ternary elements replace Ti and Al atoms in the ordered lattice *[66, 119]*. It is reported that, Zr, Nb and Hf occupy Ti sites, while Ga, Sn, Fe and Ni occupy the Al sites. V, Cr and Mn may occupy either the Ti or Al sites depending on ratio of Ti/ Al and also on the concentration of alloying elements *[120, 121]*.

Role of interstitial elements like C, O and N on TiAl has been studied by several workers *[122-123]*. It is reported that grain size is reduced by small addition of carbon. Room temperature yield strength of alloy increases with the addition of carbon, nitrogen and oxygen. Similarly, small addition of boron has significant effect in improving ductility of TiAl alloys through grain refinement. Effect of small addition of boron on microstructure can be observed from Fig. 2.10 *[124]*. It improves the strength at room temperature and at high temperatures as well *[125, 126]*. However, excess boron is harmful to ductility due to formation of TiB_2 brittle phase. Functions of different alloying elements have been summarized and are presented in Table 2.2 *[124-138]*.

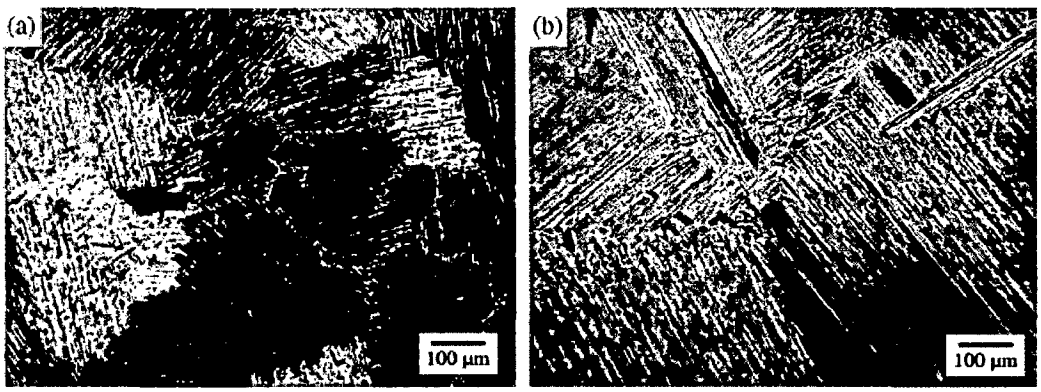

Fig. 2.10: Optical micrograph illustrating grain refinement in a TiAl based alloy by boron addition (a) Ti48Al2Cr2Nb1B, (b) Ti48Al2Cr2Nb *[124]*

Alloying elements such as silicon and tungsten have been reported to enhance creep resistance. But their individual role remains to be specific. Excess carbon >1000 wt. ppm also results in precipitation of Ti_2AlC, improving creep resistance *[139]*.

Further, for adequate oxidation resistance and creep resistance at high temperatures, alloying with one or more elements like Nb, W, Mo and Ta has been suggested *[17]*, which promote Al_2O_3 formation *[54]* and tend to substitute titanium atoms and enhance diffusivity of aluminum atoms leading to the formation of a continuous Al_2O_3 layer. The oxidation resistance of the γ Ti aluminides and its composites can be improved marginally by the addition of alloying elements such as Nb, Mo and W and impurities like Cl and P *[140]*.

Alloying elements have been grouped into three groups based on their specific role in mechanical properties of the alloy. Appropriate addition of element combination of these groups designated as X_1, X_2 and X_3 depends on the relation Ti–(45–49)Al–(1–3)X_1–(1–4)X_2–(0.1–1)X_3 are added to two-phase ($\gamma+\alpha_2$) alloys for optimum ductility, oxidation resistance and creep strength.

Taking into account the specific role of alloying elements various types of TiAl alloys have been formulated and studied. Some of the mostly studied alloys are described here based on their time of development.

First generation alloy [139]: Ti–47Al–1V–0.3C has improved ductility and creep strength.

Second generation alloy [141, 142]: Ti–48Al–2(Cr or Mn)–2Nb have improved oxidation behavior. The alloy Ti–48Al–2Cr–2Nb and the alloy Ti–46.2Al–2Cr–3Nb–0.2N has been further studied and proposed.

Third generation alloys [143-145]: These have been developed with an aim to refine the microstructure. Alloys were studied with various elements including B, C, Si and O. At this time, progress has been made in controlling and evaluating microstructures produced through wrought processing in different alloys such as Ti–(45–49)Al–(0–3)(Cr, Mn, V)–(0–5)B–(0.05–0.3)Si. According to Naka et al. *[145]*, the addition of refractory alloying elements, such as Re and W improves creep strength. This has led to the formulation and study of the alloy composed of Ti–46.6Al–2Re–0.8Si.

2.3.4 BRITTLE TO DUCTILE TRANSITION

Brittle to ductile transition state of material is very important for processing and application of alloys. Process parameters, application environments and temperature are accordingly selected to avoid brittle regime.

For TiAl, the brittle–ductile transition occurs at 827°C and below it the mobility of dislocations is very low *[146]* and therefore the alloy is brittle. However, alloyed TiAl has shown improvement in ductility after 700°C indicating brittle to ductile transition near to this temperature. For TiAl alloys, below 700°C, the stress vs. strain behaviour is characterized by work hardening followed by sudden decrease in stress i.e. failure. Deformation in lower temperature regime <700°C, only pseudo plasticity is observed owing to microcrack formation instead of plastic deformation. Therefore, it is proposed that, brittle-ductile transition takes place between 600-700°C *[147]*. However, it also depends on alloy composition and microstructure *[148-150]*.

Table 2.2: Function of different alloying elements *[30, 127-138]*

Group	Alloy	Amount (at%)	Function & Mechanism	References
X_1	Mn	1-3	Doubles material's room temperature (RT) ductility *by* activating twining deformation in γ based alloys	*127*
	Cr	1-3	Doubles material's RT ductility *by* intrinsic microstructural changes, in particular, in decreasing the tetragonality (c/a ratio) and unit-cell volume of the $L1_0$ γ-TiAl phase, weakening the directional TiAl covalent bonding, reducing the volume fraction of the α_2-Ti_3Al phase and refining the grain size.	*128, 129*
	Mo	1.5	Improves tensile ductility more effectively then addition of Cr or Mn	*30*
X_2	Nb	at least 2%	Do not increase ductility of Ti-48Al alloys. Very effective in improving oxidation resistance and strength.	
X_3	C	0.1–1	Improves creep resistance	
	N	0.1–1	Improves creep resistance	
	Si	Small %	Some improvements in oxidation and creep resistance. Even in low amounts, it brittles alloy during the preparation of the ingot by melting or thermomechanical processing	
	W	0.1-1	Improves creep resistance in temperature range 550–850°C. Increases oxidation resistance and strength but lowers room temperature ductility. It prevents dislocation motion and limits twinning deformation during tensile test	*130-133*
	B	Small %	Improves ductility through grain refinement. Improves strength at room temperature and high temperature by forming fine intermetallic particles at the grain boundaries	*134-138*

An anomalous (positive) temperature dependence of yield strength (σ_y) is also observed in compression tested single crystal along the c-axis (Fig. 2.11) *[151]*, in Ti, TiAl and Ti_3Al. This hardening is beneficial for high temperature property differentiating these materials from most fcc metals which soften rapidly as temperature rises. For titanium, this

may be related to a change in the deformation mode that occurs by twinning at low temperature and by slip along <c + a> directions at high temperature. In Ti_3Al, the anomalous yield stress behavior is attributed to the low mobility of edge super-dislocations; twinning is not observed in this compound. For single γ-TiAl phase, the origins of the flow stress anomaly is due to partly by the specific core structures of dislocations. Whereas, in $TiAl_3$, the temperature dependence of σ_y is monotonous.

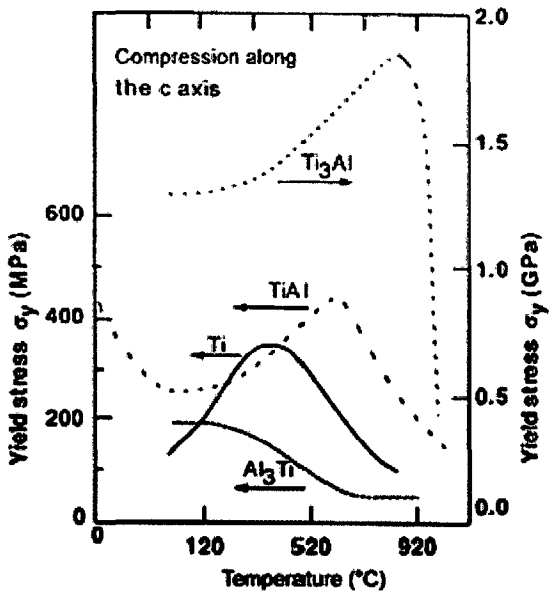

Fig. 2.11: Temperature dependence of the compressive yield stress of Ti and titanium aluminide single crystals *[151]*

2.4 DEFORMATION BEHAVIOUR OF γ -TiAl

2.4.1 FLOW BEHAVIOUR

γ TiAl based two phase (γ+α_2) alloy has been studied by Dhams *[147]* and reported that it behaves plastically above 700^{0}C and upto maximum stress, work hardening takes place (Fig. 2.12). Having reached the peak stress, the material softens to a stable flow stress. Increasing temperature leads to decreased strength as well as to a reduced peak strain. The difference between the peak stress and minimum stress in high temperature regime >700^{0}C is found to be in the range of 100MPa.

It has been reported that, hard and easy mode of deformation can occur in TiAl with lamellar structure. The strength of TiAl with lamellar structure is thought to be related to the

hard mode of deformation, i.e. shear deformation across the lamellar boundaries, and its ductility is associated with the easy mode of deformation, i.e. the shear deformation parallel to the lamellar boundaries *[114]*.

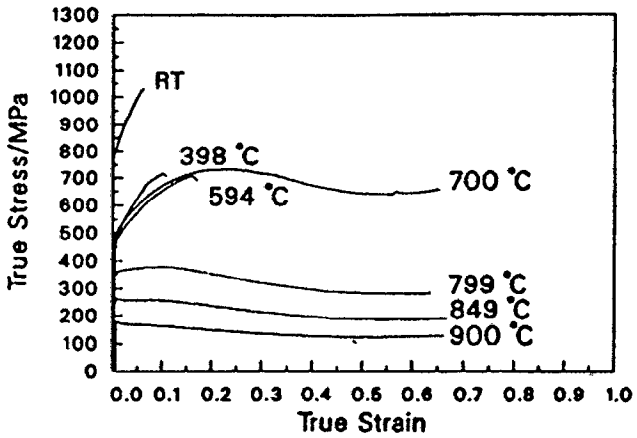

Fig. 2.12: True stress vs. true strain at various temperatures of cold extruded and HIPed alloy *[147]*

During tension at low strain rates, the alloy is susceptible to colony or grain boundary sliding (GBS), which leads to a high elongation. As the elongation increases, the shape of α_2 grain remains essentially unchanged with a sharp and straight boundary, but γ grain is soft compared to α_2. Thus the misfit strains of these phases, accompanied by the strain incompatibility of lamellar colonies and γ grain, results in cavity formation. Many cavities are formed not only at γ/ lamella and γ/γ boundaries, but also at γ/α_2 under extensive deformation. At the final stage of deformation intensive pore formation also occurs, ultimately leading to fracture *[152]*. This can be avoided through proper design of deformation process under isothermal working *[153]*.

2.4.2 HIGH TEMPERATURE DEFORMATION MECHANISMS

The initial investigation of deformation of $L1_0$ type compounds began with AuCu compound. The existence of super dislocations in $L1_0$ structure and its asymmetric array of partial dislocations were predicted *[154-155]*. Such change in deformation properties with temperature is due to evolution of dislocation structure. TiAl has a $L1_0$ structure and its axial ratio c/a is close to unity (c/a = 1.02). Therefore, its unit cell may be considered as cubic, but

its tetragonality remains. However, TiAl has not shown any transformation into fcc structure upon disordering because of its ordered state upto the melting temperature. Therefore, it is anticipated that its slip system, dislocation structure and deformation behaviour should be anisotropic and different from those of $L1_2$ structure as well as fcc metals all the way to elevated temperatures.

During the initial stage of deformation, dislocations are generated and multiplied; bowing and tangling of the dislocations contribute to work hardening of the material. Although dislocation climb also occurs, the aforementioned features are the dominant microstructural changes during the initial stage of deformation. These provide sufficient dislocation barriers necessary for the hardening. It is reported that such dislocation network is a result of massive cross-slip during deformation. Such cross-slip was noted as thermally assisted in overcoming the Peierls force barrier. Therefore, it has been assumed that, high Peierls stress in $L1_0$ TiAl requires high activation energy for such cross-slip. Cross-slip of <101> dislocations onto other {111} planes at 600^0C in TiAl has been reported *[156, 157]* and also there is evidence that APB between two dissociated superpartials lies in a {100} plane instead of a {111} plane. Dislocation-dislocation pinning was also reported in this temperature range.

Deformation of TiAl and its alloys above 800^0C shows a rapid decline in strength probably due to lattice softening and dislocation annihilation. Dislocations responsible for hardening are found to disappear at higher temperature and long and stretched dislocations were observed at higher temperature deformation as compared to shorter dislocations at lower temperature deformation. Dislocations no longer look tangled and curled at this temperature indicating that the hardening structures have disappeared. It is also noted that ($L1_0$) titanium aluminides have a positive deviation of yield stress at high temperatures and the maximum is centered between 600^0C and 800^0C depending upon the deformation orientation and their slip mode *[156-157]*.

The special aspect of high temperature deformation is that the effect of diffusion is pronounced *[158]*. The dislocation can climb as well as glide so that recovery due to dislocation rearrangement and pair annihilation proceed quickly. For polycrystalline materials, recrystallization, grain boundary sliding and migration also occur. The controlling mechanisms can vary with test condition. During tension at $1X10^{-3}s^{-1}$, the deformation rate is

sufficiently high, and the effect of diffusion on deformation may be small. At the decreased strain rate, the dislocation climb process frequently accompanies the grain matrix deformation, because the dislocation pile-ups at grain boundaries can climb easily at high temperatures, thereby relieving the stress concentration. The strain rate dependence of flow stress is always considered to occur when a dislocation can surmount obstacles by a thermally activated process, so the stress-strain data obey a single-logarithm linear relationship. In this state, grain boundary sliding and migration also occur, showing the necking and grain elongation *[152]*.

It is reported that PM alloy responded to dynamic recrystallization (DRX) more readily at 950^0C than 1050^0C, resulting in a finer grain structure. Recrystallization is again a diffusion controlled process, sometimes requiring a high level of deformation to build strain within the matrix. If sufficient time is not allowed for diffusion to take place, recrystallization may not take place *[159]*. A typical example of deformed microstructure is presented in Fig. 2.13 showing dynamic recrystallization at moderate strain and twining at high strain.

In another observation on dislocation study while carrying out tensile creep test, Rong et al. (1998) *[160]* reported the evolution of dislocation networks. Both ordinary dislocations, superdislocations and twining were observed for the specimens tested at relatively higher strain rate than creep. Such twin boundaries act as barriers to dislocation movement. At the grain boundaries and subgrain boundaries, dislocation concentration was found to be much higher than inside the grains/ subgrains *[160]*.

2.5 MICROSTRUCTURE AND MECHANICAL PROPERTIES OF γ TiAl

It has been shown that the microstructure strongly affects the mechanical properties. Many studies have been carried out to establish relationship between microstructures and mechanical properties. It is observed that the duplex structure at the heat treatment temperature retards the grain growth of γ-phase due to the presence of α_2 phase *[66]*. The duplex structure has superior strength and ductility, while the transformed structure possesses higher fracture toughness *[17]*. The effect of microstructural features like large grain size on mechanical properties has been studied *[26, 143, 161, 162]*.

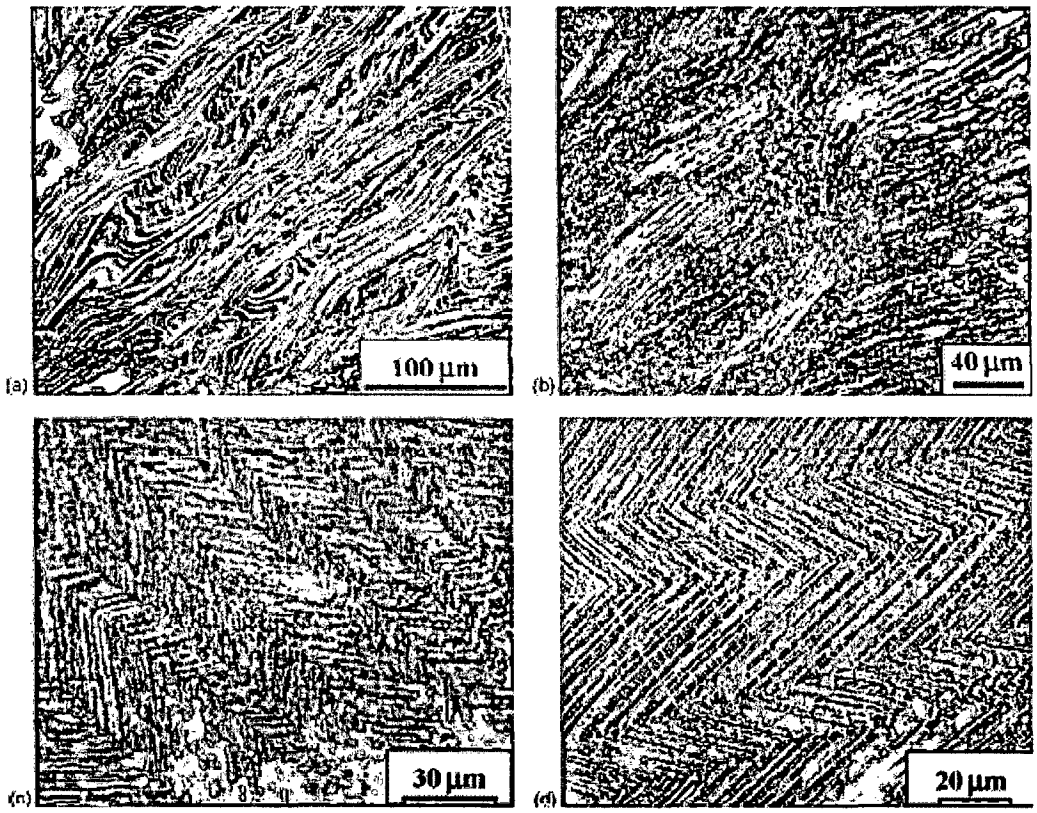

Fig. 2.13: Microstructure of deformed sample with fully lamellar structure, (a and b) Remnant $\alpha_2 + \gamma$ lamellar grains surrounded by fine dynamically recrystallized grains in the regions with true strain of 0.3 and 1, respectively, (c and d) A twinned $\alpha_2 + \gamma$ lamellar grain in a region with a true strain of 0.9 (optical and back scattered electron images respectively) *[161]*

The hot working and fracture are studied and correlated to the grain size of γ aluminides by Seetharaman and Semiatin *[163]*, and room temperature mechanical properties have been correlated to grain size by Imayev et al. *[165]* and Salishchev et al. *[78]*. Substantial increase in strength was observed when the grain size was decreased. Similarly, ductility first increases with decreasing grain size till the grain size of 8 µm then decreases with further decrease in grain size for TiAl. Optimum microstructures for desired properties are discussed in following sections and also summarized in Table 2.3.

2.5.1 MICROSTRUCTURES FOR IMPROVED DUCTILITY

It is noted that duplex structure exhibits higher ductility than the lamellar structure. The reason for improved ductility of duplex structure is because of fine grain size and presence of α_2 in the structure. The later effect is more potent because α_2 phase scavenges oxygen from γ phase and modifies deformation structure of γ rendering the alloy ductile *[66]*. Denquin *[165]* has shown that a difference in the α_2 phase composition exists between Ti–48Al and Ti–46Al alloys for similar heat treatments and microstructures. Furthermore, in γ TiAl alloys, none of the phases are cubic: hence, the crystalline order does not contribute to the ductility. However, it seems that even a low volume fraction of the α_2 phase traps interstitial impurities and thereby improves ductility.

2.5.2 MICROSTRUCTURES FOR HARDNESS/ STRENGTH

Wang and Dahms *[166]* have reported highest hardness for lamellar microstructure. The hardness values for γ, α_2 and lamellar (γ plus α_2) phases were found to be 269±51, 455±33, 468±24 Hv respectively. The microhardness values for gamma grains (single phase) are lesser than the lamellar regions due to presence of harder Ti_3Al phase in lamellar regions of both as-cast and duplex structures *[166, 167]*. Tensile strength of TiAl alloys varies between 190 to 380 MPa depending on the condition of the material.

Desired grain size can be obtained by heat treatments. For each type of microstructure, the yield stress and the grain size are related by the Hall–Petch relation *[139]*. Within a class of microstructure, both tensile strength and ductility decreases as the grain size increases. The tensile strength of near lamellar and totally lamellar microstructure with grain size ranging between 100 and 300μm is similar to that of materials formed of a duplex microstructure. The near lamellar material with 100μm grain size shows an optimum combination of tensile strength (nearly 700MPa) and of ductility superior to 2.0%.

2.5.3 MICROSTRUCTURES FOR HIGHER FRACTURE TOUGHNESS

Lamellar structure has the best fracture toughness in comparison to duplex and single γ phase structures as shown in Fig. 2.14 *[17]*. Higher fracture toughness of lamellar structure is attributed to composite toughening effect *[168]* where deformation blunting and interface debonding requires higher energy for fracture. This microstructure exhibits remarkably increased values of fracture toughness ranging from 20 to 30MPam$^{1/2}$ *[169]*. For totally lamellar coarse grains, the value of K_{IC} at 800°C is upto 35MPam$^{1/2}$ *[170]*. Toughness is

improved by a microstructure of coarse grains formed of lamellae, both the geometry of grains and the structure of interfaces marked by a strong anisotropy indicate high toughness of the material *[171]*.

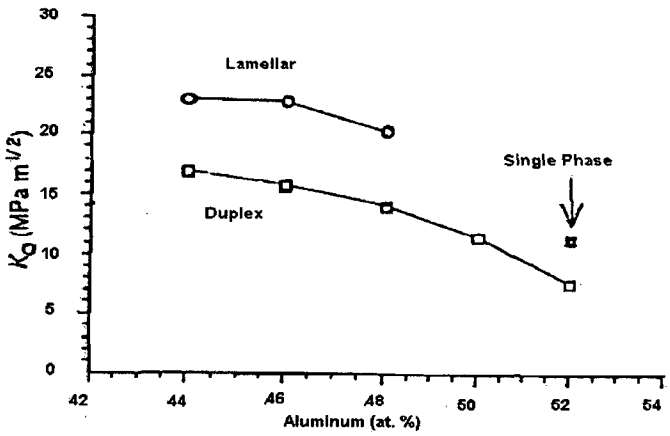

Fig. 2.14: Fracture toughness of γ-TiAl (Ti48Al) for various microstructures and Al content *[17]*

The toughness also depends on grain size; for a lamellar microstructure, the toughness increases with increase in grains size up to 500μm but it becomes independent for coarser grains. However, in a lamellar grain, if spacing between lamellae is superior to 10μm, the toughness of this type of microstructure is similar to that of duplex microstructure (10MPam$^{1/2}$). This shows that a lamellar structure with higher spacing between lamellae behaves as fine grained material by losing the anisotropy in deformation *[148, 149]*. The toughness K_{IC} of a fully lamellar microstructure with a small grain size (17 MPam$^{1/2}$) is much higher than that for duplex lamellar microstructure (10MPam$^{1/2}$) *[148, 149]*. For a lamellar microstructure, a Hall–Petch-type relation has been established between toughness and lamellar spacing $K = K_0 + k\lambda^{-1/2}$ by Kim, where K_0 is the intrinsic toughness, k is constant and λ the lamellar spacing *[148, 170]*.

2.5.4 MICROSTRUCTURES FOR HIGHER CREEP STRENGTH

The lamellar structure has superior creep strength than duplex structure *[172]*. The main cause for superior creep properties for lamellar structure is thought to be larger grain size *[17]*. And best structure for creep properties below 760^{0}C is duplex while fully transformed (lamellar) structure is optimum for higher toughness and creep strength above 760^{0}C. Creep resistance of lamellar microstructures is superior to the other microstructures is

also due to the α_2 laths acting as reinforcements *[130, 173]*. In fact the creep rate of the alloy Ti–48Al–2Cr–2Nb in air at 760°C and under a stress of 105MPa is 4×10^{-7} h^{-1}, whereas that of the duplex microstructure is 3.3×10^{-5} h^{-1}.

2.5.5 MICROSTRUCTURES FOR OPTIMUM PROPERTIES

The influence of microstructure on room temperature properties of a two-phase γ alloy (Ti-47Al-1Cr-2.5Nb) is presented in Fig 2.15 *[148]*. In short, properties of the alloy are explained with mainly three types of microstructures.

- Duplex Microstructure: The duplex microstructure characterized by fine grains presents the best tensile elongation combined with a reasonable strength (curves E and F of Fig. 2.15). Investigations on deformation modes within γ and α_2 phases have shown that sufficient mobility of dislocations are activated in γ phase but not in the α_2 phase *[174, 175]*. The toughness K_{IC} of this type of microstructure is ranged between 10 and 16MPam$^{1/2}$; the absence of crack growth resistance behavior in duplex structures is observed at least up to 600°C and is due to the lack of bridging ligaments *[148]*.
- Near lamellar microstructure (curve D of Fig. 2.15) has a high strength with an average ductility.
- Fully $\gamma+\alpha_2$ lamellar microstructures generally exhibit poor ductility and lower room temperature strength. These properties may be improved by reducing the fully lamellar grain size (curves A, B and C of Fig. 2.15) through innovative heat treatments and thermomechanical processing.

Based on microstructure type, comparison of properties of as-cast structure with duplex and with fully lamellar structures in γ-titanium aluminide is presented in Table 2.3 *[168, 176]*.

2.6 PRIMARY PROCESSING OF Ti ALUMINIDES

The major problem of poor ductility has been overcome by alloying additions, composition and microstructure control in γ alloys. Tensile ductility of 1 to 3% has been achieved at room temperature *[17]*. However, this level of ductility is insufficient for conventional mechanical working processes. Therefore, efforts were made to work the alloy through selection of processing methods and to obtain optimum processing conditions. Several innovative methods have been employed for intermetallics and composites of different systems [177-217]. This section discusses various processing methods used for realizing Ti aluminides billets/ ingots.

Table 2.3: Parameters for optimum microstructure and specific properties *[168, 176]*

Property	Conditions	Beneficial microstructural feature	Optimal
Strength	< 760^{0}C	Small grains Lamellar structure	Duplex
Ductility	< 760^{0}C	$\gamma/\ \alpha_2$ ratio	Duplex
Toughness	All temperatures	Lamellar structure	Fully transformed
Creep and rupture	< 650^{0}C > 650^{0}C	Small grains Lamellar structure Large grains Lamellar structure	Duplex Fully transformed
High cycle fatigue	> 250 MPa (at 760^{0}C)	Small grains Lamellar structure	Duplex

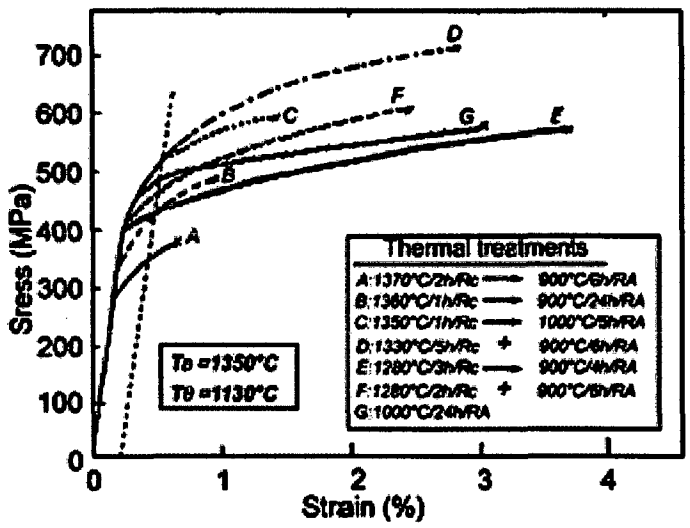

Fig. 2.15: Room temperature tensile properties of a two-phase γ alloy (Ti–47Al–1Cr–1V–2.5Nb) in various post-forging heat treatment conditions *[148.]*

2.6.1 FABRICATION OF BILLET/ INGOTS

2.6.1.1 Ingot Metallurgy (IM)

The aluminides of potential interest have composition of 44-50 at% Al, which solidify through peritectic reaction (α + Liquid $\rightarrow$ γ) as seen in the phase diagram (Fig. 2.1). It results in heavy segregation and non–uniform structures *[7, 8]*, which makes cast alloys weaker and less ductile even though these alloys contain elements like Cr, V and Mn, for enhancing the ductility *[177]*. For thin walled castings, the additions of Ni, Fe and B have been reported to increase castability *[62]*. Higher strength casting alloys based on higher Nb have already been developed and successfully used *[20, 21, 27, 62]*.

2.6.1.2 Rapid Solidification

Rapid solidification process utilizes cooling rates of more than 10^3 $^0Cs^{-1}$ from liquid phase, which results in significant undercooling of the melt and leads to several metastable phases *[178, 179]*. Rapid solidification has been used to avoid heavily segregated peritectic solidification structure resulting in homogeneous structures *[131, 180]*. This route also results in finer structures with more homogeneity and with metastable phases which may pave the way for more ductile alloys *[181, 182]*. However, there is a risk of contamination during processing by rapid solidification *[183]* and processing of thicker sections is also difficult.

2.6.1.3 Polysynthetically Twinned (PST) Crystal Growth

Two phase aluminides containing α_2 and γ with very special microstructure and striking mechanical properties have been produced by using a special crystal growth technique *[184]*. In zone melting furnace, PST crystals with single set of lamellae are grown with controlled growth rate. For example, the alloy with 49.3 at.% Al consists of one or two lamellar grains which are composed of lamellae of the major constituents TiAl and of the secondary phase Ti_3Al. Since, numerous thin twin lamellae are contained in the major constituent γ phase, these crystals have been named polysynthetically twinned (PST) crystals from which the analogy is drawn with phenomenon 'polysynthetic twinning'. It is often observed in mineral crystals *[51]*.

This microstructure gives rise to a mechanical behavior which depends sensitively on the orientation of the crystal with respect to the loading direction. There is a hard deformation mode with shearing across the lamella boundaries and an easy mode with shearing parallel of the lamella boundaries. The later allows tensile elongations upto 20% at room temperature.

Lamellar microstructural features and its properties such as microstructural characterization, deformation, fracture toughness and macroscopic flow behavior have been extensively studied by making the best use of the fact that the PST crystal is a single crystal of the fully lamellar polycrystalline alloy. Literature on evaluation of PST aluminides is available for fatigue properties *[185]*, characterization of lamellar interfaces and segregations *[186]* and microstructural stability under creep conditions for these aluminides *[187]*. Most of the properties are observed to be sensitive to the relative orientation of the lamellae in PST titanium aluminides.

2.6.1.4 Powder Metallurgy (PM)

Difficulties associated with IM route are elemental segregation, elemental loss, non-homogenous structures, cracking and requirement of secondary working to produce useful parts. Hence, powder metallurgy (PM) route is useful for processing of these materials, which results in a product with fine grains and uniform elemental distribution *[5, 9]*. Also, need to go through secondary working is resolved in PM route leading to near-net shape (NNS) processing *[5, 188]*. PM approaches are based on pre-alloyed and elemental-powder to achieve near net shapes in gamma titanium aluminides. Mechanical alloying (MA) is an important PM method to produce aluminide powders *[189]*. Synthesis of Al_3Ti from elemental powders by MA has been investigated by Srinivasan et al. *[190]* while Christman and Jain *[191]* have reported that bulk quantities of nano phase Ti_3Al-Nb can be produced by MA technique. The main drawback of MA process is difficulty of secondary consolidation as the powders are in heavily worked condition.

In pre-alloyed route, very high pressures are required for consolidation and interstitial contamination is a major issue. Pre-alloyed PM route also poses problems of coarse grains, cracking and porosity. However, comparable microstructures and properties to wrought products have been achieved through hot isostatic pressing *[192]*.

Elemental PM route is attractive for intermetallics since the above-mentioned problems are less encountered in this process. Reaction synthesis (RS) process is a promising technique, which uses elemental powders, and alloys are made with an added advantage of heat of reaction during consolidation. It is an attractive method for producing aluminides. This process has been applied in the present work for billet realization and it is described in detail in subsequent section (2.7).

2.7 SELF–PROPAGATING HIGH-TEMPERATURE SYNTHESIS (SHS)/ REACTION SYNTHESIS (RS) PROCESS

In addition to advantages of PM processing, SHS processes is beneficial due to simplicity of the process, low energy requirements, possibility of obtaining high purity products, simultaneous formation and densification and near-net shape processing. Product can be further processed as well. As suggested by Rawers and Wrzeninski *[63]*, this process can be termed as reactive sintering instead of SHS because the entire powder compact is heated up so that the SHS reaction occurs throughout the sample at the same time.

Besides the advantages, some limitation also lies in the process. Especially difficulty in control of reaction, loss of shape due to melting and swelling, resulting in high levels of porosity etc. Therefore, processing window, in terms of tooling temperature, heating time and ram speed for successful pressing is found to be very small. Also, it is suggested that aluminides formed in this way would undergo additional or simultaneous application of pressure to reduce the porosity *[193]*.

This process has been extensively reviewed by several researchers *[194-196]*. There have been number of efforts to synthesize nickel and titanium aluminides through SHS and its variants such as combustion synthesis *[197]*, reactive hot pressing *[5, 63, 198]*, reactive hot isostatic pressing *[199]*, XD^{TM} process *[200]* etc. Dense and ductile intermetallic alloys based on Ni_3Al have been produced through reaction synthesis *[199, 201-203]*. Iron aluminide has been synthesized by Gedevanishvili et al. through pressure-less RS process *[204]*. In these studies with optimized particle size, heating rate and atmosphere, product of more than 95% density have been achieved. Various researchers have worked on reaction synthesis of TiAl *[205-206]*. However, these RS studies have been mostly limited to binary stoichiometric compositions. Limited effort has been made on RS processing of Ti48Al2Cr2Nb alloy *[17, 50, 87]* from the γ titanium aluminide family that is of interest for aerospace and automobile applications.

High thermodynamic stability of the intermetallic compound is the driving force for the SHS reaction. Free energy of formation of titanium aluminides of interest is shown in Table 2.4 *[207]*.

Table 2.4: Free energy of formation of three titanium aluminides *[207]*

Intermetallic Compound	Ti_3Al	TiAl	$TiAl_3$
Free Energy of Formation (kJ/ mole)	-39	-69	-39

Another important RS process is microwave RS, which can result in better intermetallic products as the heating rates involved are high during microwave heating *[208]*. In Ti-Al system, swelling takes place for pressure-less reaction synthesis due to imbalance in solubility. The solid solubility ratio for Al-Ti system is very poor (0.003 at.%) *[206]*. However, use of pressure during reaction sintering can lead to dense products in Ti-Al system and has been used to produce near net shape gamma TiAl *[5, 63, 64, 198, 209]*. Thin foils of 50 μm thickness from reaction extruded TiAl have been realized, which is an achievement for inherently difficult to roll intermetallics *[210]*.

2.7.1 TRANSIENT LIQUID PHASE SINTERRING (TLPS)

Reactive sintering is basically derived from transient liquid phase sintering. It is characterized by large heat liberation due to a reaction between the constituent powders. When a liquid forms in the compact, rapid compound formation begins, with liquid flow into the pores. It densifies due to simultaneous sintering and reaction. During the reaction, grain growth and solidification occurs due to rapid diffusion in the transient liquid *[211]*.

The requirements for TLPS include mutual solubility between the components. The liquid must wet the solid and have high diffusion rate for the solid. The solubility ratio necessary for the liquid to be transient induces swelling during heating to the sintering temperature. Swelling is common during heating because of the required solubility of constituent in the base, especially if intermediate compounds form between the constituents *[195, 211]*. The process depends on particle sizes, amount of additive, heating rate and maximum temperature. The densification depends on the amount of liquid formed and the length of time the liquid exists. Typically, the liquid lasts for only a few minutes, thus pore refilling does not occur and large pores result. However, if the liquid persists, then densification will follow.

Heating rate is very important in transient liquid phase sintering. During heating, diffusional homogenization leads to pore formation by a Kirkendall effect. The amount of swelling increases with the amount of interdiffusion, thus, more swelling is seen with slower heating rates. More liquid is formed with faster heating. Often swelling reaction is most intense just prior to the liquid formation temperature and is not due to trapped gas in the pores *[199, 211]*. Faster heating rates, use of small particle sizes and lower additive contents give superior density. The compact viscosity is another factor, which increases with time because of decreased quantity of liquid and thus densification process slows down rapidly.

2.7.2 REACTION SYNTHESIS (RS) PROCESS

Similar to TLPS, the process involves a transient liquid for small duration and in small amount depending on process parameters, which control the sintering characteristics. German has extensively reviewed the reactive sintering and effect of various process parameters on swelling and shrinkage (Table 2.5) *[211]*. Role of important process parameters for RS and for TLPS processes are described below:

2.7.2.1 Particle Size

The densification associated with TLPS depends on the amount of liquid formed and length of time the liquid exists. Too much liquid generates large pores due to spreading and penetration of the melt away from the additive particle sites. Alternately, too little liquid leads to minimal densification. In systems like Ti-Al imbalanced diffusivities between Ti and Al, lead to swelling because of porosity generated due to Kirekendall effect *[205, 208]*. Therefore, an optimum particle size is a must for pressure-less RS process as shown by Bose et al. *[201]*. For swelling systems, small particle sizes and rapid heating rates result in best densification *[211]*.

2.7.2.2 Heating Rate

During heating, diffusional homogenization in solid state leads to pore formation due to Kirkendall effect and this in turn lead to swelling *[211]*. The solid-state compound formation can also inhibit subsequent interdiffusion and hence, leads to less densification for slower heating rates. Whereas, faster heating rate leads to more amount of liquid formation and less amount of solid state diffusion. This results in minimum formation of transient phases and also reaction proceeds towards Ti rich aluminide formations *[216]*.

2.7.2.3 Sintering Atmosphere

Bose et al. have studied the effect of sintering atmosphere in Ni_3Al *[201]*. They concluded that heating rates do not have significant effect on densification while sintering under vacuum. However, high heating rates are necessary to obtain dense products in case of sintering in argon and hydrogen atmospheres. Amongst two gas atmospheres, hydrogen results in better densification as it has more solubility in elements like Ni and Al, which provides opportunity for other gases to escape even after the pores have been sealed during densification.

Table 2.5: Variables for liquid phase sintering *[211]*

Variable	Factor favours swelling	Factor favours shrinkage
Solubility Ratio	Low	High
Particle size	Coarse	Fine
Green density	High	Low
Amount of liquid	Small	Large
Contact angle	Large	Small
Heating rate	Low	High
Atmosphere	Insoluble	Soluble
Powder porosity	Low	High

2.7.2.4 Sintering Time

Generally, duration of sintering is not a major parameter because the process is based on exothermic heat production leading to intermetallic formation and densification which is not controlled by diffusion process.

2.7.2.5 Sintering Temperature

For the reaction synthesis process, primary requirement is the initiation of exothermic reaction between constituent elemental powders *[202, 211]*. The temperature is selected for a composition AB as shown in Fig. 2.16, which causes an exothermic reaction to initiate and leads to simultaneous compound formation and densification aided by the presence of a liquid for a short time *[211]*. In aluminides, the RS temperature is close to melting point of aluminum and exothermic heat during RS leads to melting of aluminum for a short time and densification is achieved *[202]*.

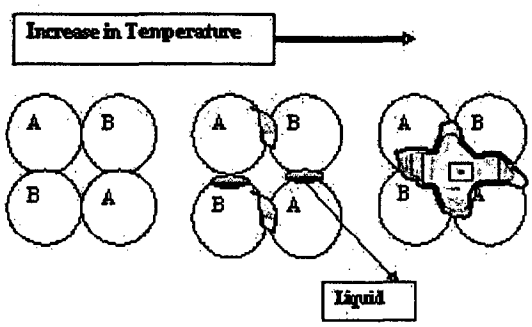

Fig. 2.16: Schematic diagram of reactive sintering to obtain compound AB from A and B powders.

2.7.2.5.1 External Pressure

Use of external pressure during TLPS and RS helps in densification and pore collapse *[208, 218]*. The liquid that is transient in nature cannot sustain a shear stress and lubricates sliding particles as induced by external stress. Shrinkage rate $d(\Delta L/L_0)/dt$ related to applied stress (σ) in the final stages of sintering has been given by Kingery et al. *[218]* as;

$$d(\Delta L/L_0)/dt = B\sigma^n \exp[-Q/(kT)]/G^3 \qquad (2.1)$$

where, B is a material constant, n stress exponent (~1 for most of systems), Q is activation energy for diffusion, T is absolute temperature, G is grain size and k is the Boltzmann's constant. Thus, for higher σ and lower G, better densification is achieved.

Relatively small pressures of the order of 40 MPa have shown to make significant change in sintering behavior *[188]*. Nishimura et al. have demonstrated that use of uniaxial compressive stress of about 50 MPa results in near full density product *[202]*. With pressure-assisted RS process, effect of particle size, sintering atmosphere and initial green density on the densification is quite small due to enhanced inter-particle contact achieved owing to better capillary force during the process *[202, 211]*. The densification effect of pressure is higher for transient liquid process like RS as compared to normal sintering process (involving no liquid formation) *[218]*. Near full density aluminides have been obtained by pressure-assisted processes *[5, 63, 199, 200, 202]*. In case of pressure-assisted RS process, heating rate affects the densification by way of changing the kinetics of the process *[64]*.

It has been reported that, liquid phase sintering exhibits sufficient internal force through liquid capillary action on the particulate solid that external forces are not required. The magnitude of capillary force is equivalent to very large external pressures. With the formation of liquid there is rapid initial densification due to capillary force. The elimination of porosity occurs as the system minimizes its surface energy. During rearrangement, the compact responds as a viscous solid to the capillary action and elimination of porosity increases the viscosity. As a consequence the densification rate continuously decreases. Usually finer particles give better rearrangement. Full density is possible by rearrangement if enough liquid is formed. Kinetics of rearrangement are initially fast, as the densification process becomes slow, solubility and diffusivity effects become dominant. Small grains have a higher solubility than coarse grains. The grain shape is also altered by diffusion to allow tighter packing of the grains. This process of grain accommodation leads to pore elimination *[211]*.

However, an external pressure during liquid phase sintering aids densification and pore collapse. The liquid can not sustain a shear stress, thus, it lubricates particle sliding as induced by an external stress. As a consequence, an external stress eliminates pores and inhomogeneous regions which are otherwise stable in some liquid phase sintered material. With an external stress, rearrangement processes play a larger role in densification. It directly supplements the capillary force. Depending on the particle sizes, the applied stress significant increase in capillary force is possible. The effect of pressure is more pronounced with coarser particle sizes since the capillary force is inversely proportional to the grain size. Thus an increase in the particle size gives a greater relative effect from the applied stress *[199, 211]*. As the pressure increases the particle size effect becomes smaller.

2.7.3 PROPERTIES OF REACTION SYNTHESIZED (RS) ALUMINIDES

Mechanical properties of γ-TiAl produced through RS were evaluated using transverse rupture stress test *[63]*, Vickers hardness *[98]* and tensile tests *[5, 64]*. A comparison of creep properties for RS TiAl alloy with conventional cast alloy has indicated that steady state creep resistance is equal or better in RS processed material *[5]*.

High temperature X-ray diffraction phase studies provide information on phases present at high temperature *[83]*. Hot hardness measurement of Ti-46.6Al-1.4Mn-2Mo alloy produced by RS technique has been carried out by Lee et al. *[64]* and they found the hardness to be varying between 25 to 35 Rc from room temperature to 1270^{0}C as shown in Fig. 2.17. It has been reported by Lee et al. *[64]* that higher heating rates during RS reduces porosity and increases the content of TiAl and Ti_3Al phases in γ titanium aluminide.

2.8 MECHANICAL WORKING AND HEAT TREATMENT

Microstructures of TiAl products play a significant role in their mechanical properties, which can be optimized through mechanical working and heat treatment. Significant attempts have been made by researchers to study hot deformation of aluminides *[10-14, 78, 79, 219]*. It is found that, major challenge of the wrought processing is to break down the coarse and segregated structure of the cast ingots. Similarly, P/M products were also found to be difficult to work due to brittle nature. Hot workability of aluminides has been studied extensively *[220-222]*. Safe working zone (temperature and strain rate) has been identified. Accordingly, most of the researchers followed isothermal working process.

2.8.1 ISOTHERMAL PRESSING

Isothermal deformation is an effective method of increasing the utilization factor of materials. The prevention of abrupt cooling and reducing the deformation rate under isothermal conditions lead to an increase in plasticity and reduction of flow stress. It is beneficial for brittle materials as reviewed by Huang and Chesnutt *[17]*. Due to inherent brittleness, isothermal forging is recommended for secondary processing of aluminides and in the absence of it, canned non-isothermal forging or canned extrusion process are adopted *[26]*. Scientists at the Institute for Metal Superplasticity Problems, Russia have developed a dynamic recrystallization process based on repeated isothermal forging at progressively low temperatures *[75-79]*. This process has resulted in fine grained aluminides which sustain large deformations without cracking. A typical example of isothermal forged alloy microstructure of Ti aluminide *[223]* is presented in Fig. 2.18, showing flow of lamellar structure (in case of 30% reduction) and recrystallization (in case of 80% reduction).

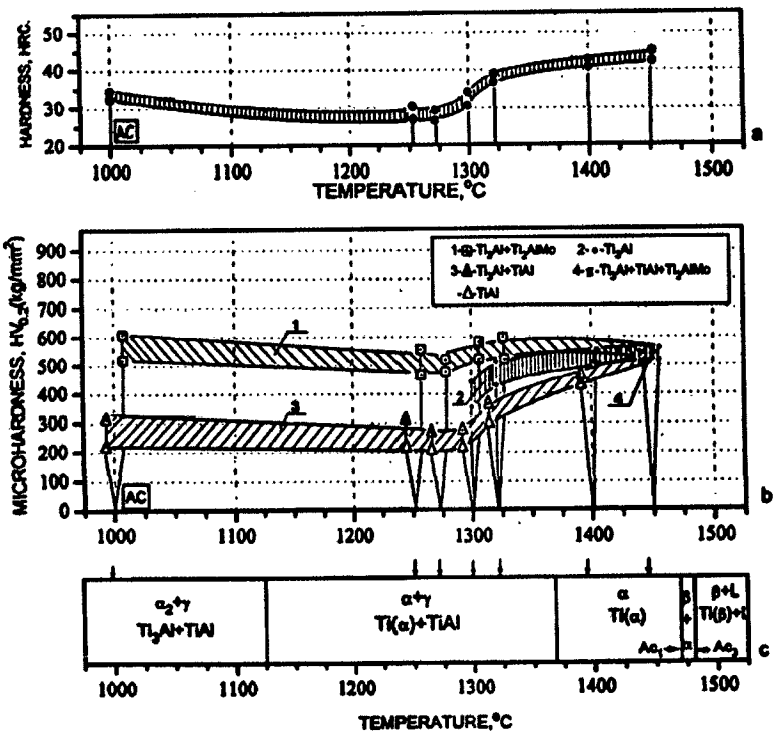

Fig. 2.17: Rockwell hardness of RS processed gamma TiAl and micro-hardness of constituent phases in this material [64]

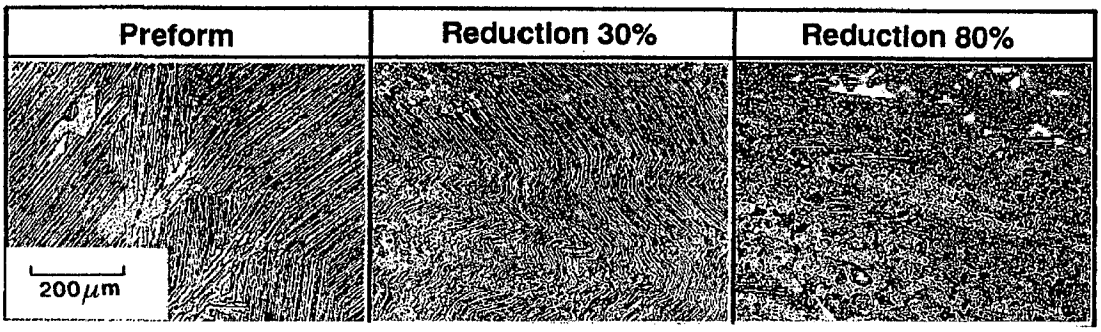

Fig. 2.18: Microstructure of TiAl isothermally forged at 1150^{0}C *[223]*

2.8.2 PACK ROLLING

Pack rolling process has been studied as an alternative method for rolling "difficult to form" materials. By packing or canning heat losses are minimized and near isothermal working condition has been maintained. Process and packing is schematically shown in Fig. 2.19. Thin sheets and foils of aluminides have been realized by this technique *[26, 31, 224-226]*.

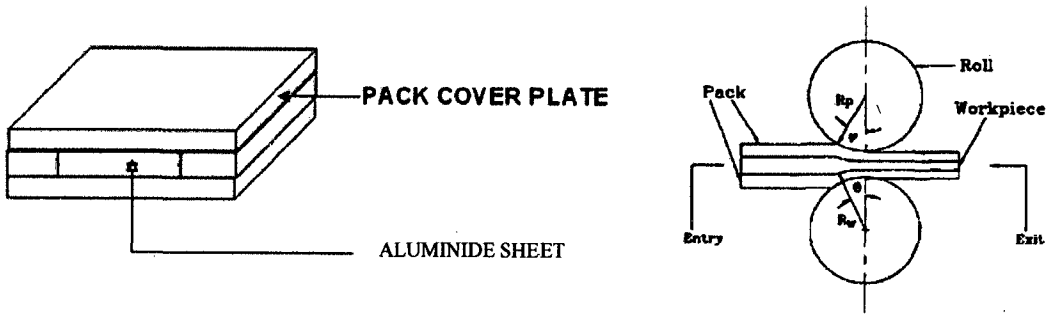

Fig. 2.19: Ti aluminide packing and pack rolling process

2.8.3 HEAT TREATMENT AND MICROSTRUCTURE EVOLUTION

Heat treatment of aluminides has been carried out at different temperatures to obtain desired microstructures through solid state transformations. Such microstructures can be final microstructures in component or a precursor to the final microstructure. Various heat treatments can be accordingly designed to achieve desired microstructures. Wang et al. successfully refined the coarse lamellar microstructure of 500μm to10 μm by rapid heat treatment *[227]*. Seetharaman and Semiatin, varied the heating temperatures to obtain various combination of mechanical properties and microstructures in rolled sheet *[228]*. By varying

the cooling rate from α transus temperature, various types of microstructures were obtained by Beschliesser et al. *[229]*. Imayev et al. studied the change in mechanical properties of aluminides through themomechanical processing *[230]*. Recently, Clemens et al., Bravo et al. and Wang et al. studied stepped heat treatments and obtained different types of microstructures and various combinations of mechanical properties *[231-233]*. It is found that most of the studies are carried out by varying the heating temperature, time and cooling rate. It is noted that, cooling rate has very prominent role in modifying the morphology of microstructure. As discussed in section 2.3.2, about the various modes of solid state phase transformation and in section 2.5 about the requirement of microstructures for various properties, it is important to understand the design of heat treatment to achieve such phase transformations in industrial practice.

Although massive gamma has not been used as a microstructure in service, it has been used as a precursor for the formation of microstructures. Thus, heat treatments of massive gamma have been used to refine the microstructures in cast alloys, which are normally very difficult to refine without thermo-mechanical processing *[112, 234-237]*. By heat treating massive gamma at temperatures above/ close to the α transus for a very short time, fine α grains can be obtained. Those small α grains will, on subsequent cooling, transform into small lamellar colonies *[234-236]*. If the massive γ is heat treated in the α+γ two phase field, α plates will precipitate on all {111} planes of massive γ to form fine microstructures *[235-239]*. It is also reported that, microstructural refinement based on massive γ can lead to improvement in properties, especially room temperature ductility *[112, 240]*. But, a high cooling rate commonly required for massive transformation can lead to fracture in brittle alloys and also it is difficult to achieve in large samples. Therefore, studies have been attempted to reduce the quench cracking by quenching the samples below massive transformation temperature but above the ductile to brittle temperature using a salt bath also known that, alloys with different compositions have different responses to continuous cooling, therefore, it is necessary to apply the heat treatment within the massive transformation regime for that alloy. It is reported that, all the alloys may not be suitable for massive transformation since in some alloys the massive transformation regime is either too narrow or is shifted to very high cooling rate, which is not practicable.

Examining the CCT curve in TiAl alloys (Fig. 2.7), it can be divided into the different regions and accordingly desired type of microstructure can be obtained by controlling the cooling rates. To avoid brittle cracking in the billets due to faster cooling

rate and also to achieve the optimum microstructure (refined duplex) for higher ductility, use of alloying additions which can help in obtaining the desired microstructures at relatively slower cooling rate is a better option. Experimental results show that the massive regime varies significantly with alloy composition and heavy elements like Nb and Ta can effectively extend the massive regime to low cooling rate side. This is due to low diffusivity of these alloying elements in TiAl alloys, which suppresses the formation of diffusion related feathery/ lamellar transformation, allowing massive transformation to occur. It is also noted that Ta has a greater effect than Nb in extending the massive regime to low cooling rate side of TiAl alloys, which leads to possibility to develop alloys able to undergo massive transformation during air cooling in large sized sample *[112, 241-244]*. Microstructure (Fig. 2.20) of less Nb containing alloy and high Nb containing alloy obtained through air cooling from 1350^{0}C to room temperature and from 1360^{0}C to intermediate temperature (below massive transformation temperature) followed by air cooling to room temperature respectively, clearly reveals similarity. Stepped cooling was carried out in (Fig. 2.20b) to avoid quench cracking *[245]*. Microstructural variation with distinct change in morphology of structure can be seen when cooling rate has large difference by using different cooling media (Fig. 2.21 and 2.22) *[135, 246]*.

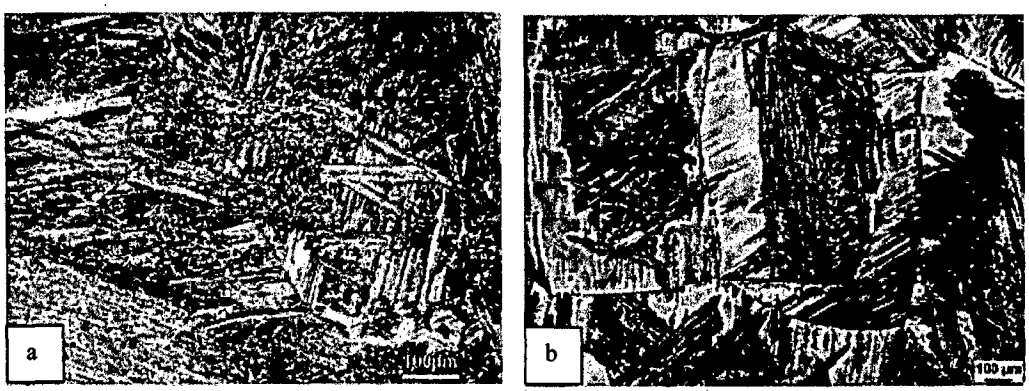

Fig. 2.20: Optical microstructures of (a) Ti47Al2Nb1W1Mn0.2Si alloy after heat treatment at 1350^{0}C/ 1h/AC and (b) Ti46Al8Nb after a heat treatment of 1360^{0}C/ 1h quenched in fluidized bed at 620^{0}C/5min/AC *[245]*

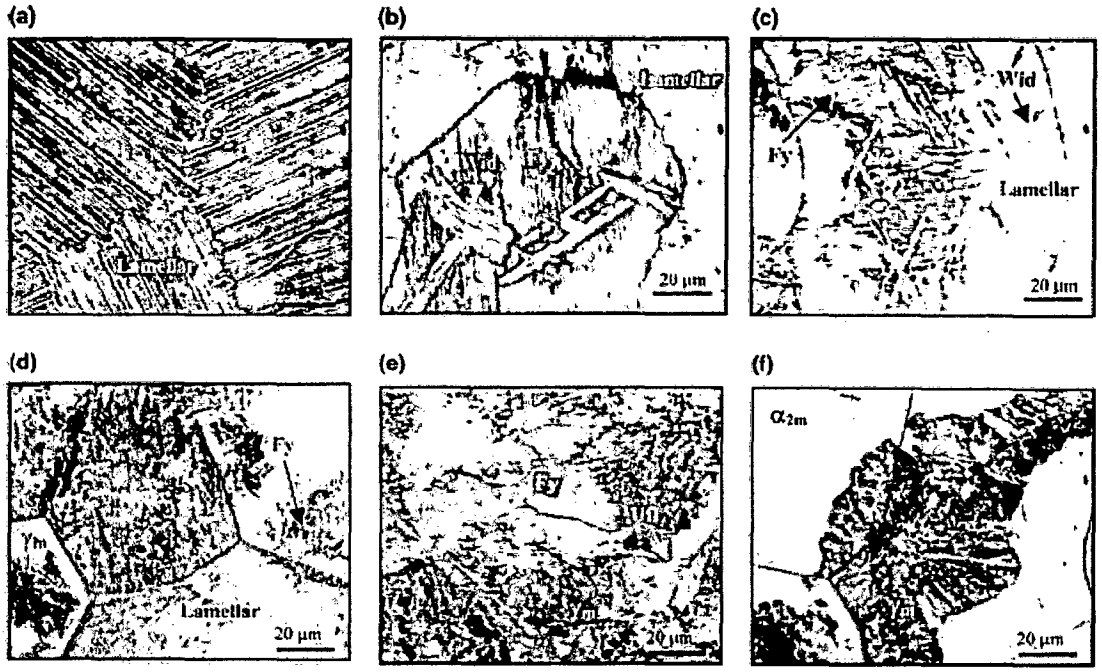

Fig. 2.21: Optical micrographs of heat treated Ti46.8Al1.7Cr1.8Nb (at%) alloy at 1380^{0}Cfor 30 min and then (a) furnace cooled, (b) air cooled, (c) sand cooled, (d) oil quenched, (e) water quenched and (f) ice water quenched *[246]*

Heat treatment temperature also has distinct role in final microstructure of the alloy. Effect of continuous cooling at relatively lower cooling rate ranges of 5-50^{0}C/ min (Fig. 2.23) shows change in lamellar structure morphology of grains and also size and spacing of lamellae. Microstructural characterization of as-cast Ti–48Al–2V studied by Sujata et al. *[247]* and studies conducted by Novoselova et al. *[248]* concluded that the grain size of the lamellar structure gets refined with increasing cooling rate and decreasing holding time at heat treatment temperature (Fig. 2.23). Further, Fig. 2.24 clearly reveals the change in lamellar structure spacing and morphology due to heat temperature even at the same cooling rate *[35]*.

Some of the important microstructures obtained through different temperature treatment are summarized as per the heating temperatures. They are classified into four groups designated as near γ, duplex, nearly lamellar and fully lamellar microstructures according to heat treatments made at temperatures such as T_2, T_3, T_4 and T_5 (Fig. 2.25) *[134]*:

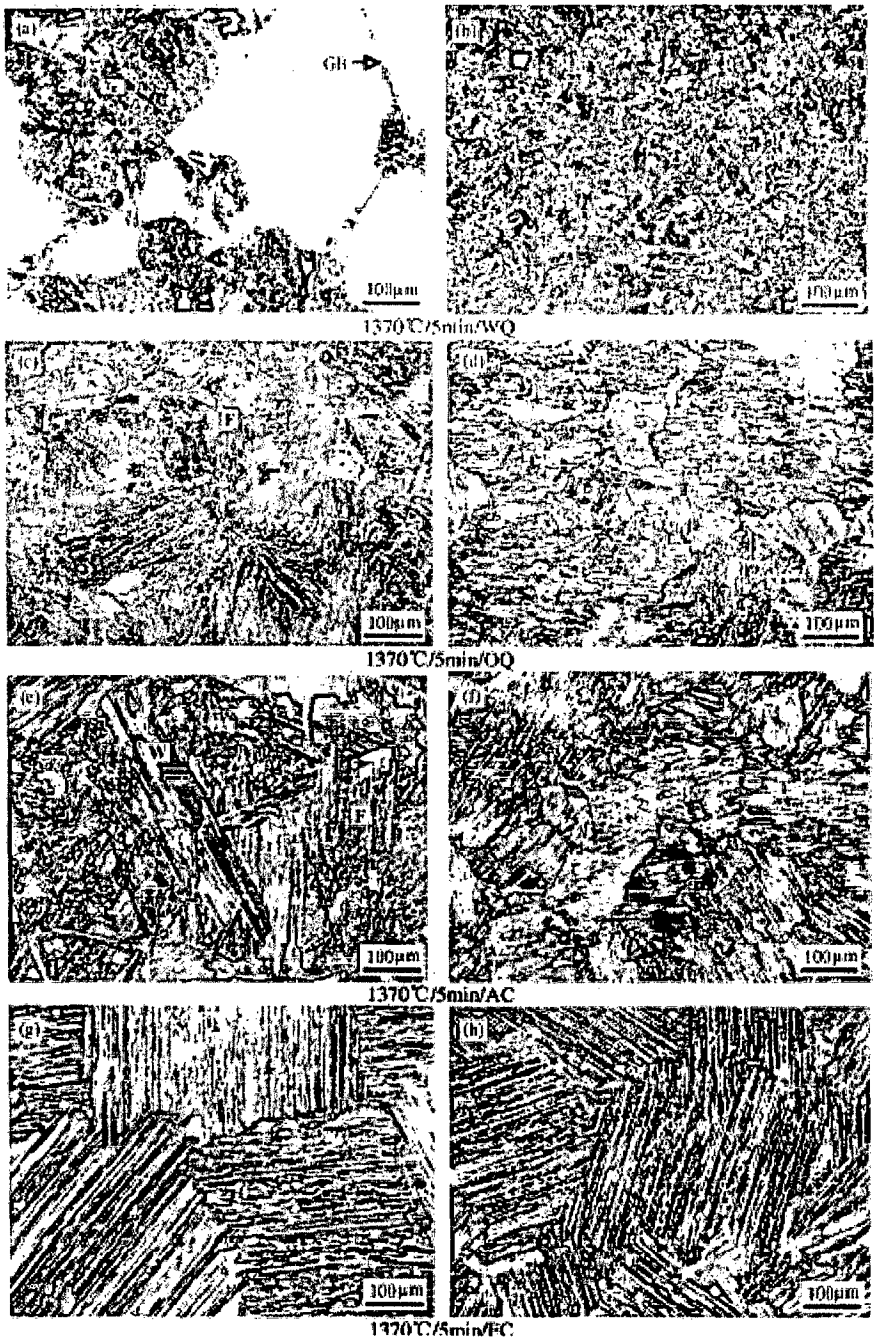

Fig. 2.22: Optical microstructure of A (a, c, e, g) and B (b, d, f, h) alloys cooled by water quenching (a, b), oil quenching (c, d), air cooling (e, f) and furnace cooling (g, h) after being treated at 1370^0C for 5 min (F-Feathery structure, W-widmansttaten structure, GB-grain boundary) *[135]*

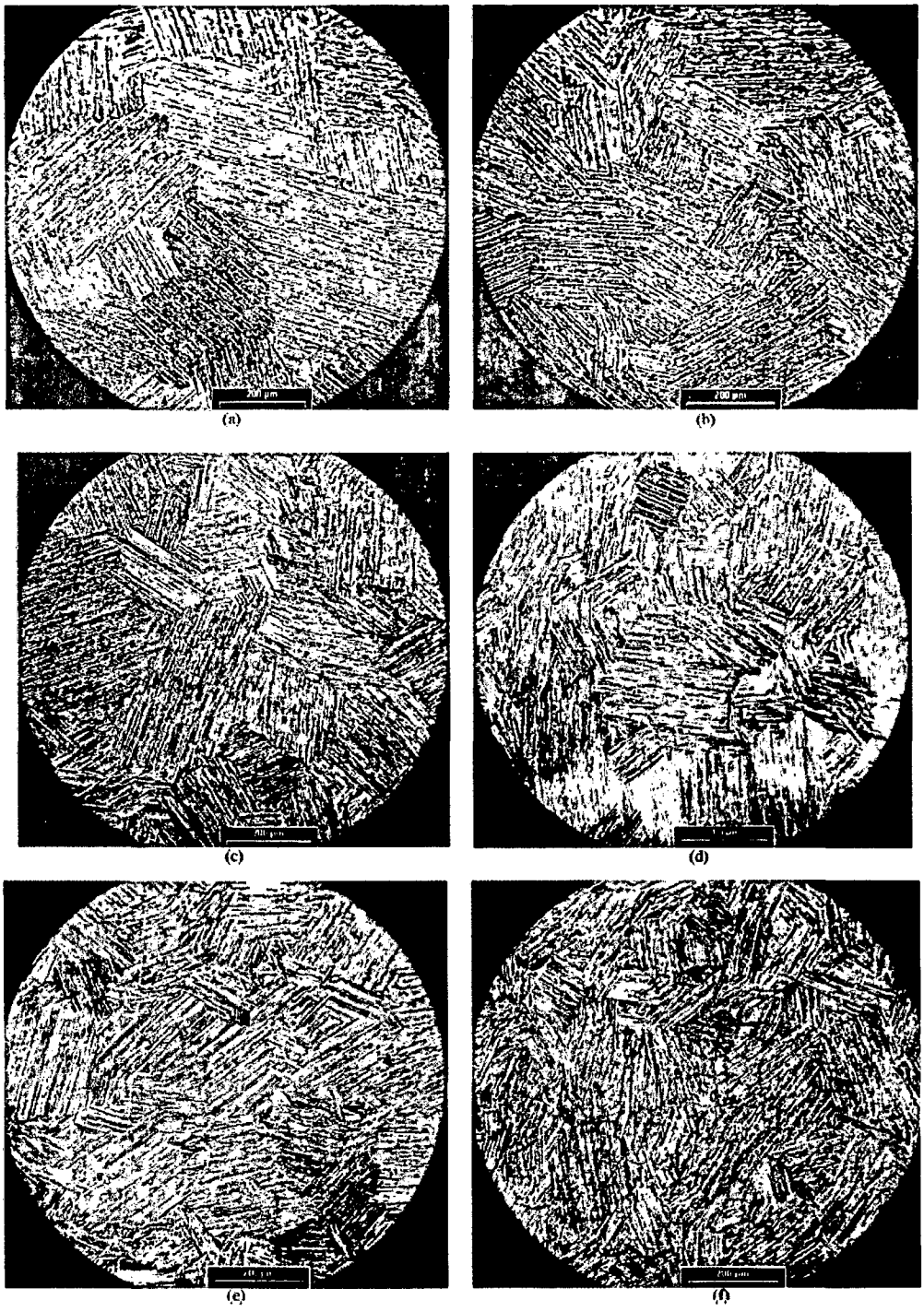

Fig. 2.23: Optical micrographs showing fully lamellar structure of Ti46Al1.9Cr3Nb alloy after continuous cooling from 1450^{0}C with different rates: (a) 5^{0}C/ min, (b) 10^{0}C/ min, (c) 20^{0}C/ min, (d) 30^{0}C/ min, (e) 40^{0}C/ min, (f) 50^{0}C/ min *[248]*

- *Near γ microstructure* (termed 'NG') It is obtained by hot working and subsequent heat-treatment at a temperature slightly below or above the eutectoid on (~1125°C). A high volume fraction of γ phase is formed. This microstructure is generally non-uniform, consisting of coarse γ grains and stringers of fine γ grains pinned by α_2 particles (Fig. 2.26 a).
- *Duplex microstructure* (termed 'D') – D is produced by hot working at about 1200°C in the (α + γ) phase field. It is composed of the γ grains and lamellae colonies (Fig. 2.26b), and a few small α_2 precipitates in γ grains.
- *Near lamellar microstructure* (termed 'NL') –NL consists of coarse α lamellar grains as the main constituent and minor amounts of fine γ grains. It is obtained by thermal treatment at T_4.
- Fully *lamellar microstructure* (termed 'FL') – The totally lamellar microstructure is obtained after a treatment at T_5 (Fig. 2.26c).

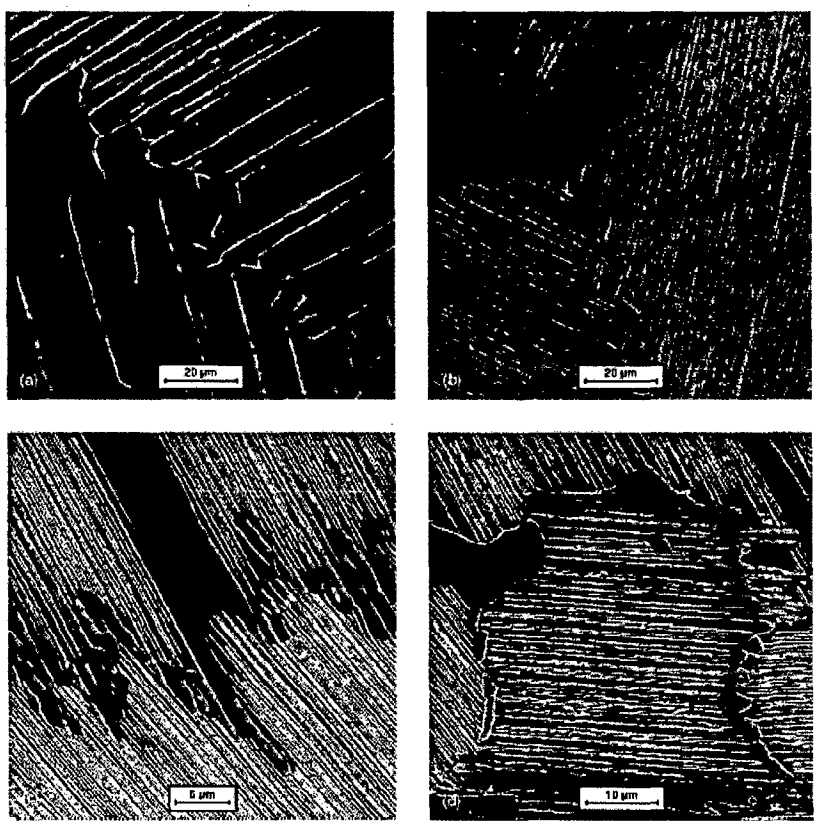

Fig. 2.24: Microstructure of specimens annealed at 1280°C (a and b) and 1130°C (c and d), then water quenched (a and c), furnace cooled (b and d) *[35]*

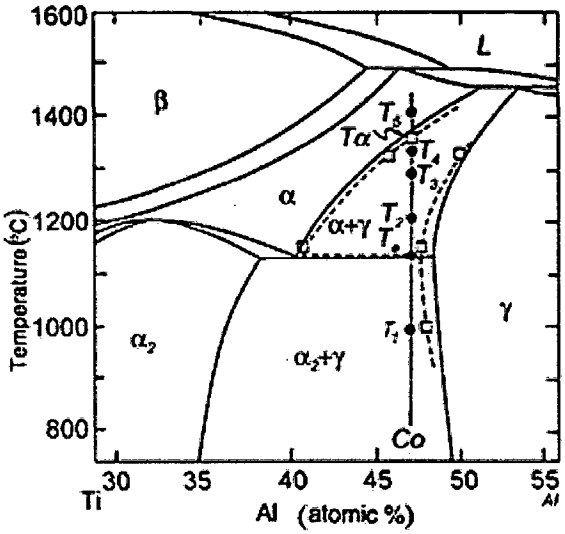

Fig. 2.25: Section of the Ti-Al phase diagram; C_0 Composition (Ti-48Al) line is shown with typical heat treatment temperatures *[134]*

Fig. 2.26: Microstructures of forged Ti–47Al–1V–1Cr–2.5Nb two-phase γ alloy after the following heat treatments (a) T_2, (b) T_3 and (c) T_5 *[134]*

2.9 CALORIMETRY STUDIES OF γ TiAl

There are many studies relating to development of various intermetallics through RS as described in Section 2.7. However, very little work has been reported *[249-256]* on the study of kinetics of the exothermic reaction that is responsible for compound formation from elemental powders. However, there is no literature available on the reaction kinetic study of non-stoichiometric compositions which are of practical interest such as Ti- 48Al2Cr2Nb composition.

Mathematical modeling and differential scanning calorimetry (DSC) have been used to determine the activation energy for the formation of stoichiometric Al_3Ti, Ni_3Al *[252, 253]* from elemental powders. Both isothermal and non isothermal methods have been used for calculation of the activation energy with fraction transformed using the following equations *[253]*:

$f(\alpha) = kt = A \exp(-E/RT)$ [isothermal kinetics] (2.2) and

$\ln(d\alpha/dt) = k\, g(\alpha)$ (2.3) thereby

$\ln[(d\alpha/dt)/g(\alpha)] = -E/RT + \ln A$ [non isothermal kinetics] (2.4)

where, α : the reacted fraction, t : time, T : the absolute temperature, R : the gas constant = 8.3143 J/mol/K, E : the activation energy, A : the pre–exponential factor

The activation energies have been reported to be 483 and 283 kJ/mole for Al_3Ti and Ni_3Al respectively *[252]*. However, the activation energy for the exothermic reaction is dependent on the reaction temperature as shown by Wang et al. for Al_3Ti formation. They obtained activation energy value for Al_3Ti as 149 kJ/mole in the reaction temperature range of 690^{0}C to 740^{0}C and 517 kJ/mole in the temperature range of 740^{0}C to 900^{0}C *[253]*.

Several methods have been attempted to study reaction kinetics and mechanisms of self propagating high temperature synthesis (SHS) processes *[257-263]*. High temperature thermoanalytical methods (such as DTA, DSC, etc.) have been preferred due to their advantages on experimental easiness with large data generation ability. In thermo-analytical methods, either temperature of the system is maintained constant (isothermal) or heating rate of sample is kept constant where temperature of the system varies (non-isothermal). Among these two, non-isothermal method is preferred for systems like Ti-aluminide where heat is generated due to exothermic reaction and where maintenance of isothermal condition is difficult.

Chapter-3

PROBLEM FORMULATION

Titanium aluminides belong to the class of ordered intermetallics, which are in advanced stage of development for aerospace applications as rotating parts and thermo-structural members of future launch vehicles. However, main concern for these materials has been the difficulty to produce them into useful shapes by conventional process route due to lower ductility of alloy. In view of this, processing of gamma titanium aluminides through alternate routes has been explored. Amongst various processes, reaction synthesis (RS) has recently received a lot of attention by academicians/ researchers as well as aerospace/ automobile industries. Only limited work on RS processing and characterization of important titanium aluminide alloy Ti48Al *[17, 50, 87]* is reported. Further study on RS processing as well as deformation behaviour of RS processed Ti aluminide alloy is required to establish a better understanding towards practical processing and application. Hence, the present work is taken up to study the two phase gamma titanium aluminide alongwith alloying additions, considering the prospective applications of gamma titanium aluminides in the space programmes. Accordingly, the main focus of the study is made on reaction synthesis of Ti48Al2Cr2Nb alloy with minor (0.1 %) addition of boron (with and without Ni-P coating) and on their deformation behaviours.

Ti48Al (at%) alloy has important engineering interest and hence this basic composition is selected for the study. In this system, addition of Cr enhances the ductility while Nb addition is reported to improve the oxidation and creep resistance and B addition leads to grain refinement. So, such alloying additions are incorporated to obtain Ti46-48Al2Cr2Nb alloys. The summary of experimental tasks planned in the proposed study is shown in the form of a flow chart as shown in Fig. 3.1.

The details of the proposed study are worked out considering the following points:

1. The base composition is chosen as Ti- 48Al, at.% (Ti-48Al) based on extensive literature review, which has revealed that alloys of engineering interest are centered around this composition due to best combination of mechanical properties. Additions of Cr and Nb are made to obtain Ti-Al-Cr-Nb alloy. Further, minor addition of B and Ni-P coated B is planned and studied due to its important benefits as noted in section 2.33.

2. There are only few studies reported on reaction kinetics for non-stoichiometric composition of binary alloys, however, no study is reported for multicomponent alloy of engineering importance i.e. for Ti-48Al 2Cr2Nb (at%) and with small addition of boron. So, basic study of exothermic reaction kinetics is proposed to be conducted on the designed compositions, using differential scanning calorimetry (DSC) technique.
3. An experimental set up is designed and fabricated to study reaction hot pressing under vacuum conditions. This set-up consists of- (i) furnace with loading arrangement with provision for vacuum and (ii) suitable dies and punches for hot pressing experiments. This set-up is such that, it can be placed in the vacuum hot press where pre-determined loads can be applied at specified temperature.
4. Reaction synthesis process of titanium aluminide formation is studied for the designed alloy compositions to understand the mechanism of reaction. It includes variation in chemistry with respect to boron and Ni-P coated boron addition and also with variation in particle sizes of titanium powder (which is predominant element).
5. Homogenization is planned in the α-γ phase field of binary Ti-Al phase diagram to achieve uniformity in composition as well as to obtain Ti rich phases like TiAl and Ti_3Al from Al_3Ti phase formed during reaction synthesis.
6. Deformation studies through isothermal pressing/ forging are carried out to understand the mechanical behaviour of alloy at different temperatures and loading conditions. Further, hot isothermal compression test of different alloys made through reaction synthesis is conducted at different temperatures and at different strain rates using Gleeble thermomechanical simulator.
7. Heat treatment is incorporated on the deformed samples to study the response of alloy with respect to microstructure development. Efforts shall be to obtain lamellar structure, which is suggested for high temperature applications (creep resistance/ stress rupture properties) for aerospace systems.
8. Evaluation of alloy is carried out on the samples obtained from different processing stages to understand the progress of phase transformation, element distribution, densification, microstructural changes etc.
9. Processing of aluminides of these compositions is attempted for the first time through the present work using RS route followed by deformation studies employing near conventional deformation methods.
10. The metallurgical tools proposed to be used for elemental and phase analysis are XRD, OM, SEM and TEM. Hardness measurement at various stages is to be carried out.

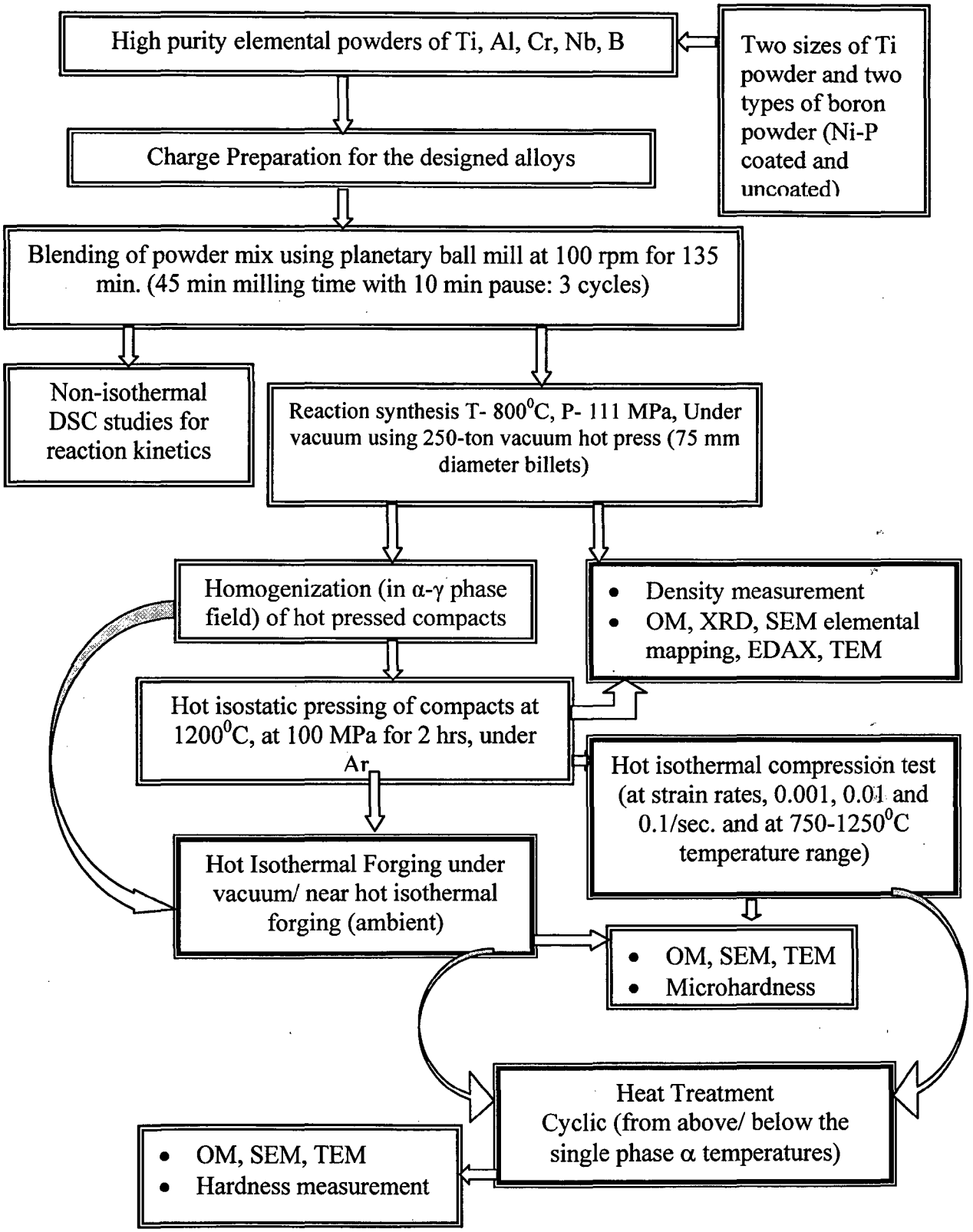

Fig. 3.1: Flow chart for experimentation on gamma titanium aluminides

Chapter-4

EXPERIMENTAL DETAILS

4.1 INTRODUCTION

As stated earlier, two phase alloys of Ti-48Al (at%) composition consisting of γ and α_2 phases are of practical interest, as these exhibit higher ductility in binary system and alloying with 2-4 at% Cr, V, Mn, Nb etc. enhances the ductility. Optimization of overall high temperature performance with certain minimum ductility requirement has resulted in development of an alloy Ti48Al2Cr2Nb *[17, 56-58]*. Experimental plan was systematically made to achieve the objective of present work covering the study on effect of particle sizes, boron addition and deformation behaviour, which has not been specifically reported for Ti48AlCrNb system.

In the present work, initially reaction kinetics study has been carried out through differential scanning calorimetry (DSC) experimentation for better understanding of the reaction mechanisms and to derive process parameters for reaction synthesis. Then reaction synthesis (RS) of Ti aluminides was carried out with minor additions of boron. Also, addition of boron has been made after coating it with Ni-P by electroless technique. Extensive deformation studies have been carried out under near isothermal and isothermal conditions in vacuum as well as in ambient atmosphere. Heat treatment was carried out on the deformed material to obtain the desired microstructure. Thorough evaluation of material was conducted at various stages. The complete processing was carried out in simple and adaptable way considering the technological restraints and requirements. Flow chart of experimental process is presented in Fig. 4.1.

4.2 RAW MATERIAL (POWDER) FOR REACTION SYNTHESIS

The specification of fine, high purity titanium, aluminum, chromium and niobium powders used for RS is given in Table 4.1. Average particle size was specified by the powder supplier, which was verified by random measurement of ~20 particles under SEM.

SEM photographs showing the morphology of elemental powders seen through Philips XL-30 scanning electron microscope is included in Fig. 4.2. Coating of boron powder particles were carried out using alkaline electroless bath process as followed for several material *[264]*. Ni-P coating on boron particles were confirmed through EDS analysis using

FESEM (FEI QUANTA 200F, USA) equipped with EDS (EDAX, USA) facility. Morphology of boron powder particle alongwith coating and EDS is presented in Fig. 4.3. Coating thickness was estimated through process control (coating time) and verified through increase in weight after coating of boron powder.

Table 4.1: Specification of elemental powders used in alloy development

Element	Particle size (average)	Purity (%)	Make
Titanium	200μm and 50μm	99.5%	Sumitomo Sitix of Amagasaki Alfa Aesar
Aluminium	24μm	99.0%	Metal Powder Company, India
Chromium	150μm	99.5%	Aldrich
Niobium	200μm	99.8%	Shanghai Jiangxi Metals Company
Boron	10μm	(>99.5%	Changsha Asian economic company

4.3 BLENDING OF POWDERS

The elemental powders were weighed in a precision balance of Sartorius, Austria make. Blending of elemental powders was carried out using P5 Planetary ball mill of Fritsch, German make. Agate jars and spherical balls were used for blending. Total 135 minutes of blending for a cycle was executed in the three segments namely, (1) 45 minutes running + 10 minutes pause, (2) 45 minutes running + 10 minutes pause (3) 45 minutes running. The blending was carried out at 100 rpm using balls to charge ratio of 4:1 (by weight) to achieve good blending.

4.4 REACTION SYNTHESIS

The experimental set–up shown in Fig. 4.4, was used for carrying out reaction synthesis experiments under vacuum. Vacuum hot press of 250 ton capacity of Veco make, was used where vacuum level of 10^{-4} mbar was achieved. Die and punch were made out of Inconel 718 alloy. 75 mm diameter of die cavity was used for powder pressing. Boron nitride coating (of thickness ~ 10 μm) was carried out manually (by spray method) on the inner walls of die and on the punch surface. After drying of die and punch, one kg of powder mixture was loaded into the hot pressing die. Alignment of the punch was checked by applying 1 ton

load in the cold condition. After checking the punch alignment the load was gradually raised to 5 ton level. Then furnace was switched on and load was applied as per the optimized loading cycle as shown in Fig. 4.5.

Heating cycle was designed considering the phase transformations which were observed during DSC studies. Fast heating to the reaction synthesis temperature or slow heating plus holding to reaction synthesis temperature are reported to minimize the Kirkendall porosity *[5, 211]*. Effect of heating rate with respect to reaction kinetics was also studied. Fast heating is not usually recommended from process control point of view. Therefore, heating rate of $\leq 10^{0}$C/ min was selected followed by hold at terminating temperature.

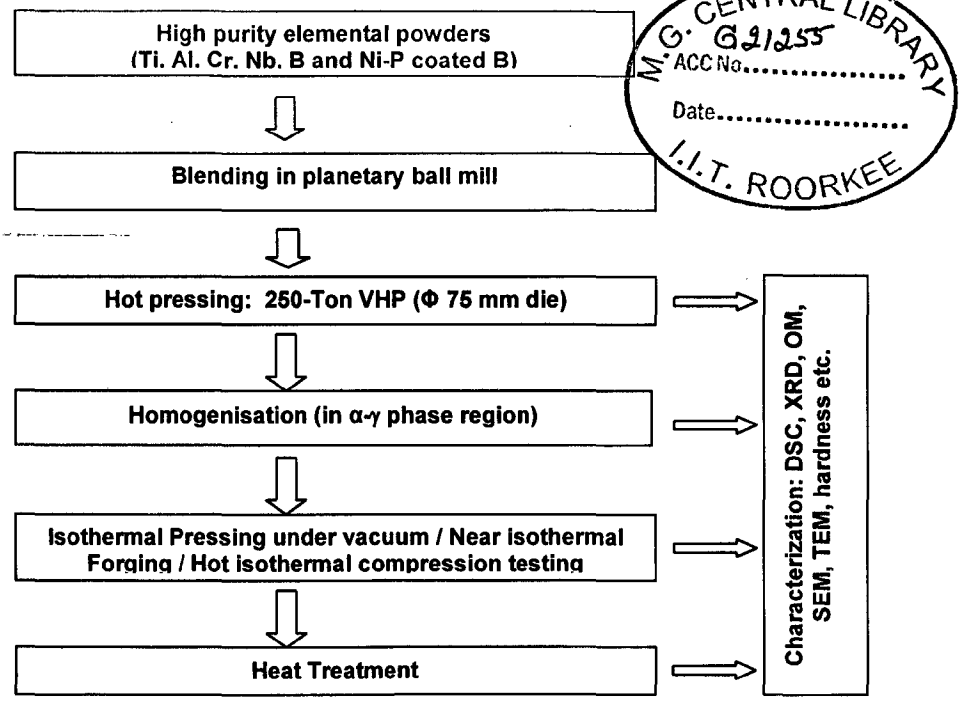

Fig. 4.1: Flow chart for development of Ti aluminide intermetallic flat products

Loading cycle was optimized after trial experiments to avoid squeezing out of liquid metal at higher temperature and to obtain the benefit of densification as well as phase transformation of heating cycle. Time was recorded at the start of the heating and at the time of reaching the set temperatures. Soaking time at the selected temperature was given as shown in Fig. 4.5. At the start of hot pressing furnace was switched off to avoid temperature rise due to dynamic process and friction between die-punch.

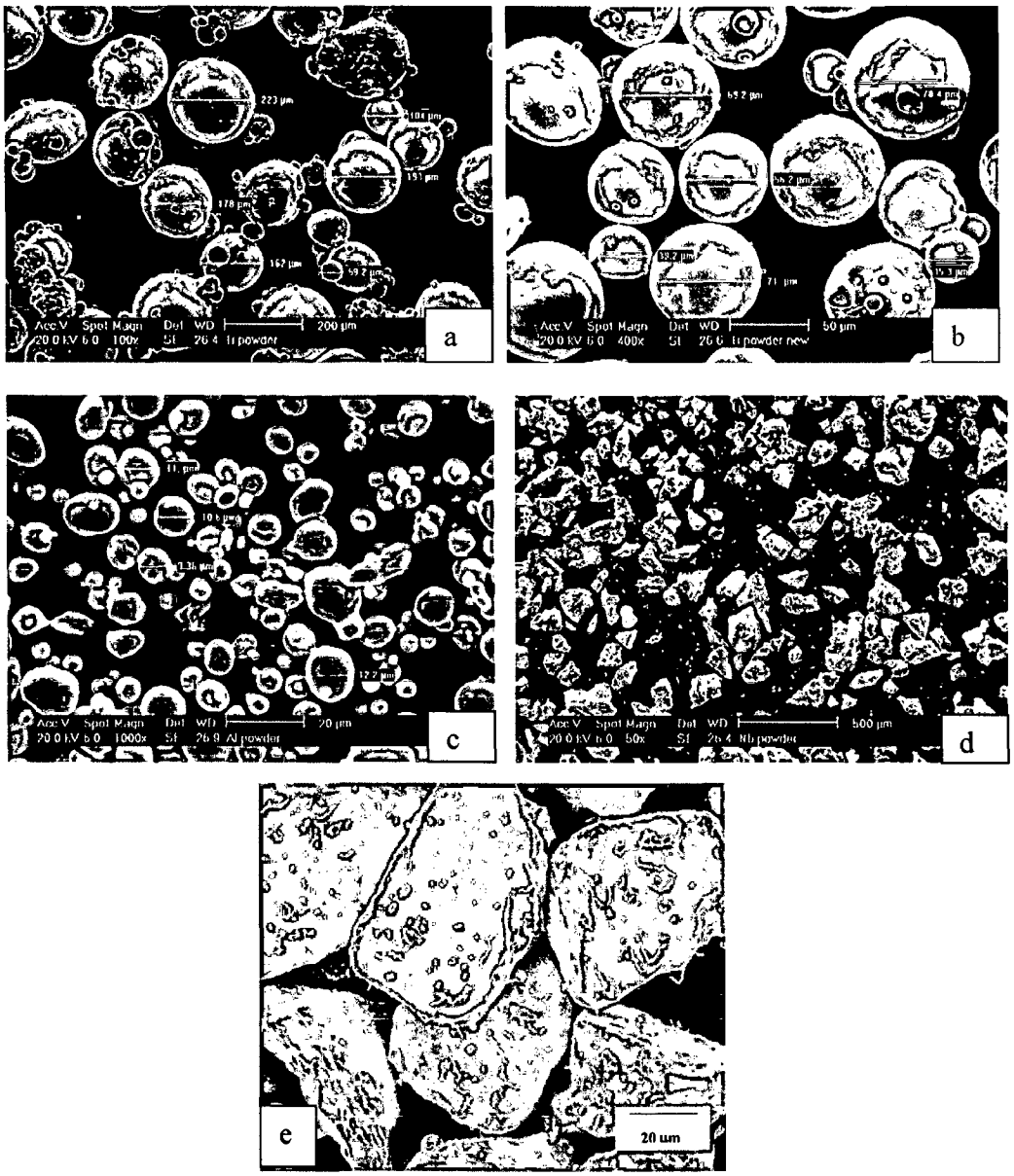

Fig. 4.2: SEM photomicrographs of the powders, (a) Ti coarse particle, (b) Ti fine particle (c) Al, (d) Nb and (e) Cr.

Constant load was applied for 30 min and then the load was released. Vacuum of better than 10^{-3}mbar was maintained in the furnace till the furnace was cooled to 300^0C. Hot pressed billets were carefully removed by pressing in reverse direction in cold condition using smaller punch in a 500-ton hydraulic press.

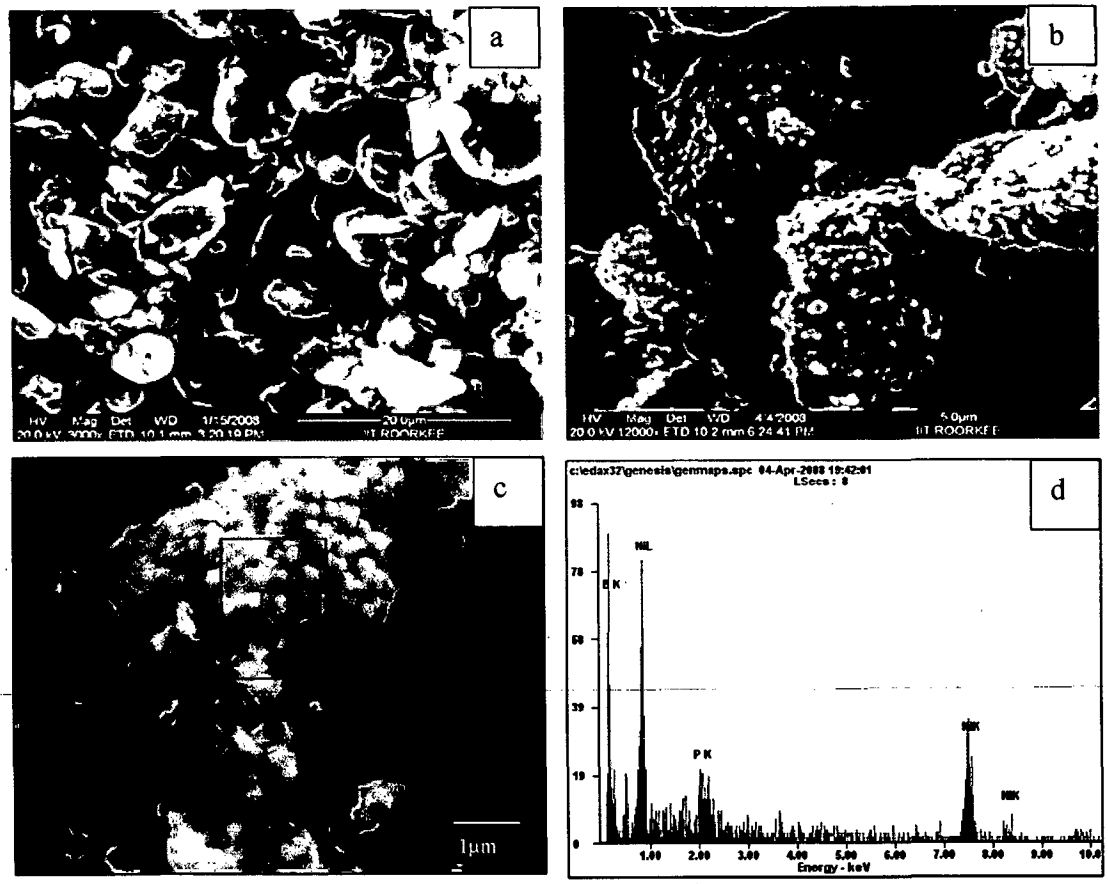

Fig. 4.3: FESEM photomicrographs of boron powders: (a) Uncoated boron, (b) Coated Boron (coating seen as layer of Ni-P nano globules), (c) magnified view of coated boron, (d) EDS of selected area of coated boron particle of Fig. 4.3c

4.5 HOMOGENIZING TREATMENT

Homogenization provides uniform distribution of microconstituents. However, in the present case, it is mainly used to transform the Al rich phase (Al_3Ti) formed during RS to Ti rich phase (Ti_3Al and TiAl). Homogenizing treatment of various hot pressed billets was carried out at a temperature of 1250^0C i.e. in the two-phase ($\alpha + \gamma$) phase field where each of the α and γ phases are approximately in equal proportion. Vacuum heat treatment furnace was used for this process. Different homogenizing times were imparted to billets (alloys) as per the optimized cycle (section 6.3) on the basis of microstructure and microhardness.

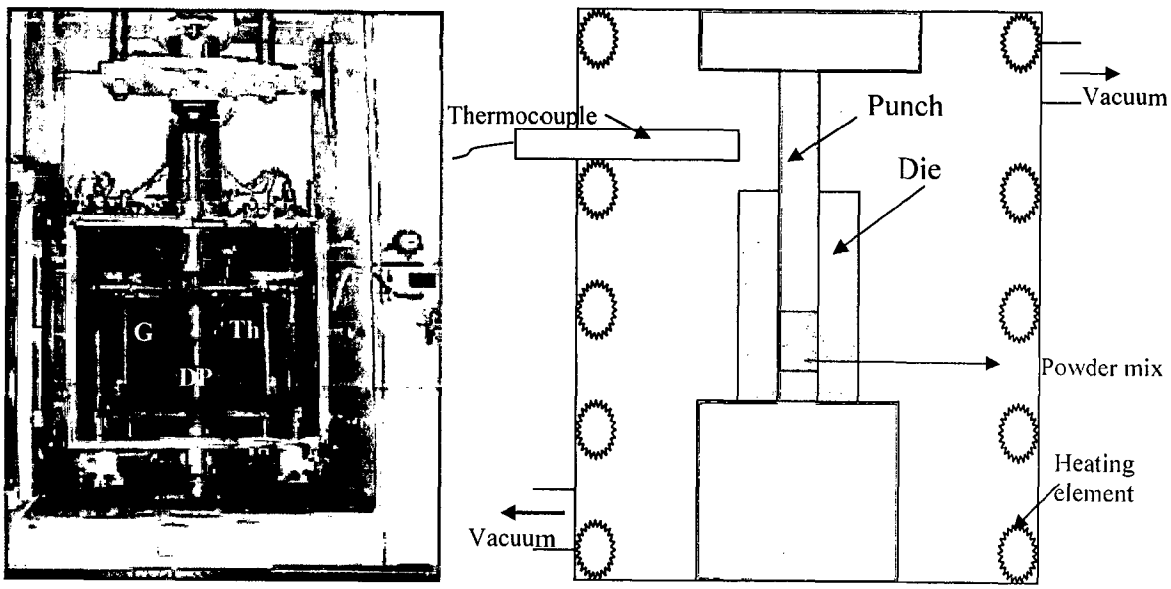

Th.: Thermocouple to monitor the die temperature, DP: Die and punch set-up loaded with the powder mix, G: Graphite heating elements

Fig. 4.4: (a) Photograph of the experimental setup for reaction hot pressing (RHP) in 250 ton vacuum hot press, (b) Schematic of the reaction hot pressing set-up.

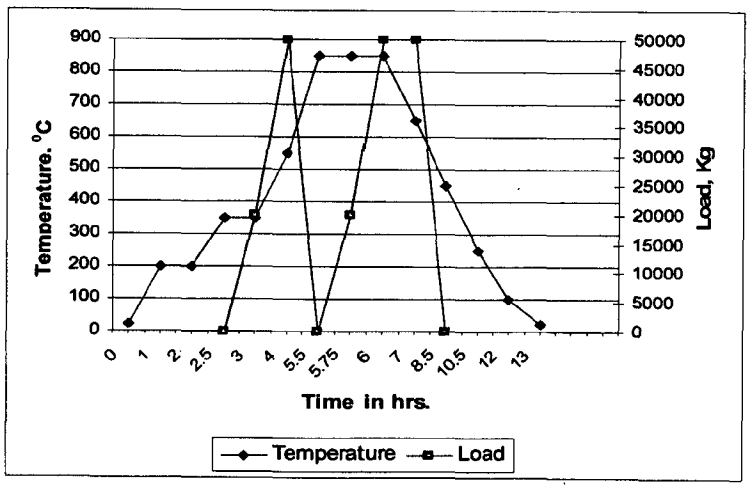

Fig. 4.5: Actual heating cycle and compaction cycle followed during reaction synthesis

4.6 HOT ISOSTATIC PRESSING

Hot isostatic pressing (HIP) was carried out to improve the densification of the billets of size ~ϕ75mmX 50mm. This process was carried out on reaction synthesized billets at 1200^0C under argon atmosphere with pressure of 120MPa. HIP of capacity 200MPa of EPSI, Sweden make was employed for pressing.

4.7 HOT ISOTHERMAL COMPRESSION

Hot compression test has decisive advantages like use of cylindrical specimen, easier to maintain constant true strain rate, convenient to measure adiabatic temperature rise, maintaining isothermal conditions etc. over the hot tensile and hot torsion test. Also, it simulates the primary metal working process (like forging). Therefore, compression test was selected for flow stress determination and hot deformation studies.

Hot isothermal compression was carried out on the hot isostatic pressed (HIP) alloy samples. Cylindrical specimens with height to diameter ratio of around 1.25-1.5 are used in compression testing. Specimens of size ϕ 8 mm X 10 mm length were made through electro discharge machine (EDM). Specimens were polished using lapping machine with emery papers and both the faces of the specimens were made parallel within 0.01 mm.

Compression was carried out on 3500C Gleeble thermomechanical simulator. Horizontal axial compression was used under vacuum. Test temperatures are selected in the homologous temperature range 0.6-0.8. It was carried out at three different strain rates (0.001, 0.01 and 0.1/sec.) and at different temperatures (750, 850, 950, 1050, 1150, 1250^0C). At each test temperature 1 minute soaking time is allowed for equilibrium of temperature before compressing the specimen to about half the initial height. Fifty percent compression was imparted on each specimen. True stress-strain data was obtained from the Gleeble 3500C system using software for conversion of load-stroke data. A photographic view of compression testing samples attached with the instrument is presented in Fig. 4.6.

Tested specimens were sectioned at the mid plane parallel to compression axis (Fig. 4.7) and the cut sections are prepared for metallographic examination. For examining the dynamically recrystallized (DRX) microstructures, the central region is selected while for observing cracking features, the bulge portion is viewed.

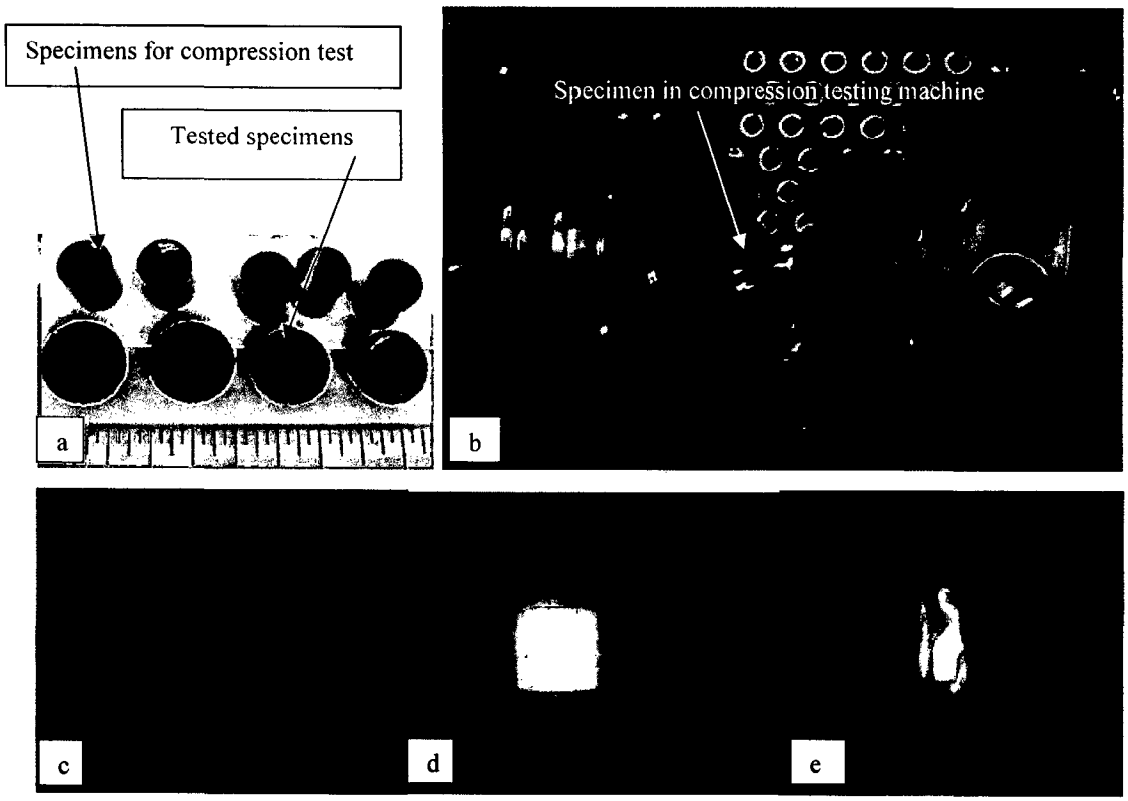

Fig. 4.6: Photographs showing, (a) Test specimen, (b) Test set-up (under vacuum), (c) heating in progress, (d) start of compression and (e) towards end of testing

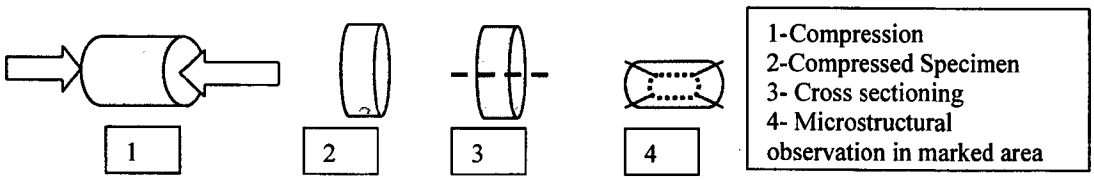

Fig. 4.7: Schematic diagram of hot isothermal compression testing and sampling for microstructural observation

4.8 HOT ISOTHERMAL FORGING

As a part of mechanical working, billets were forged in isothermal condition under vacuum at 1250^{0}C using 250 ton vacuum hot press. Forging was carried out using graphite die and punch limiting to the load of 20MPa. 50% deformation was imparted on the billet by upset forging.

4.9 HOT NEAR-ISOTHERMAL FORGING (OPEN DIE FORGING)

Considering the poor formability of material and to explore a more practical way of working, near isothermal forging was conducted. Forging was carried out at 1250^{0}C temperature in ambient atmosphere. High temperature soaking furnace with SiC heating element was used. Billets were charged at 400^{0}C and soaking of 1 hr was given. Upset forging was imparted on the billets using 500 ton hydraulic press. Forged billets were characterized. Similarly, pack forging was also carried out at same temperature, using Ti alloy as a packing material.

4.10 HEAT TREATMENT

After extensive literature review and reported phase transformations, a heat treatment cycle was designed with an aim to obtain fine lamellar microstructure. In designing the heat treatment cycle, transformation temperatures obtained through DSC studies were also taken into account. Designed heat treatment cycle (Fig. 4.8) was imparted on the hot compression tested samples and forged billet samples. High temperature soaking furnace with Molybdenum heating element having ±5^{0}C accuracy was used for heat treatment. Response to the heat treatment was studied through microstructural characterization and phase analysis.

4.11 DIFFERENTIAL SCANNING CALORIMETRY (DSC)

The reaction synthesis of aluminides of titanium-aluminum system is exothermic in nature and hence DSC is a suitable technique to study the reaction and kinetics of the process. For this reason, all the alloy compositions were subjected to non isothermal DSC analysis. Perkin-Elemer make heat flux differential scanning calorimeter was used, which gives output in microwatts. The DSC signal is derived from the temperature difference between the sample and an inert reference material by a predetermined linearization curve. The unit has a working range from ambient to 1400^{0}C and the equipment has facility for atmospheric control. Elemental powders of Ti, Al, Cr, Nb, B, Ni-P coated B etc. were thoroughly mixed in

specific ratio for different alloy compositions (section 5.2). Elemental powder mix weighing 10 mg was used for the DSC studies. Reaction was carried out under argon atmosphere at heating rates of 10, 20, 30 and 40^{0}C/min. The samples were heated upto 1400^{0}C.

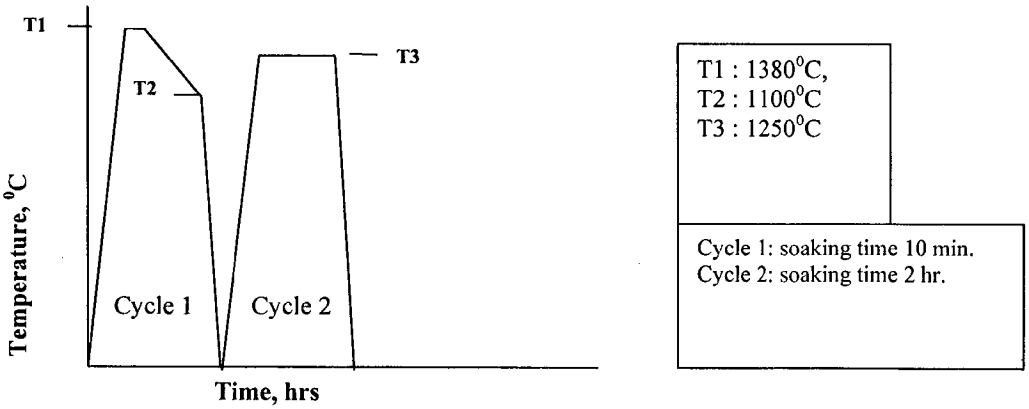

Fig. 4.8: Heat treatment cycle for Ti aluminide forged billet

For analysis of the DSC curve, baseline of the exotherm is constructed by drawing the tangents from the beginning and end points of the exotherm and drawing a straight line from the peak of the exotherm. Fractional areas of the exotherm were calculated at regular interval of temperatures to obtain the conversion fraction (α) i.e. fraction transformed.

Onset and completion temperature of aluminide formation reaction and exothermic heat release alongwith peak temperature was obtained from DSC curves. Activation energy for Ti-aluminide reaction is calculated and kinetic parameter 'n' was obtained using the Johnson–Mehl–Avrami (JMA) equation. Reaction mechanisms has been proposed in accordance with kinetic parameter 'n' values following the Criedo and Ortega criterion. Powder mixture was characterized through X-ray diffraction (XRD) to identify the formation of different phases during reaction.

4.12 CHARACTERISATION

Chemical composition of homogenized billets was analyzed through X-ray fluorescence (XRF) and inductively coupled plasma-optical emission spectroscopy (ICP-OES) methods. As–pressed, homogenized, hot isostatic pressed, isothermal forged, near

isothermal forged and heat treated samples were characterized for density and microstructure. Analysis of the phases present in various stages of processing was carried out using X-ray diffraction (XRD), Scanning Electron Microscopy (SEM), SEM elemental mapping, optical microscopy (OM), Transmission Electron Microscopy (TEM) and Energy dispersive analysis through X-ray (EDAX). Kroll's reagent was used for etching of specimens for OM observations. Vickers hardness was also measured for various samples. These characterization methods are described in the following paragraphs.

4.12.1 *CHEMICAL ANALYSIS*

Reaction synthesized and vacuum homogenized billets were analyzed for chemical compositions through XRF and ICP methods. This was carried out to confirm the actual composition of the alloys for further processing. PW 2400 Phillips make for XRF and Perkin Elmer Optima 4300V instrument was used for ICP. Gas analysis, nitrogen and oxygen was carried out using Leco make PC436 and hydrogen was analyzed through Leco make RH 504 instrument.

4.12.2 DENSITY MEASUREMENT

The density was measured using Archimedes principle and density measurement kit available with Sartorius balance. The weight of sample in air (W_a) was measured followed by weight of sample in water (W_w) and density was calculated using the following relation.

$$\rho = W_a / W_a - W_w$$

4.12.3 X-RAY DIFFRACTION

X-ray diffraction analyses of samples were conducted to identify various phases present in different conditions. The solid sample of approximately 25 mm diameter was used after cleaning the surface for any oxide layer by 1/0 emery paper. Similarly, powder mixture (after DSC) was also subjected to XRD. PANalytical X-ray instrument was used in the angle range of 5-100° with Cu K_α target and with a current of 20 mA at accelerating voltage of 35 kV.

The intensity of diffracted beam was plotted on a graphical chart at a chart speed of 1cm/min and at the goniometer speed of 1°/ cm. Peaks of different phases present in samples were identified using XRD X'Pert HighScore Plus software.

Chapter-5

NON ISOTHERMAL DSC STUDIES AND PHASE TRANSFORMATIONS

5.1 INTRODUCTION

As an alternate to ingot metallurgy route, aluminides are synthesized through reaction synthesis (RS) route wherein the exothermic heat of reaction of elemental powders is utilized to achieve compound formation. This powder metallurgy route is getting lot of attention globally due to the attractive characteristics of the process. It includes (i) absence of elemental loss/ cracking/ elemental segregation as prevalent in ingot metallurgy/ pre-alloyed powder metallurgy (PM) route, (ii) use of cheaper elemental powders as compared to pre-alloyed powder used in other PM route, (iii) use of desired fine grained powders (iv) simple process and with the use of moderate pressures, it is possible to achieve high density near-net-shape (NNS) products.

The exothermic reaction during RS process starts at specific temperature, which has important role in obtaining the desired phase and density in the final product. Reaction temperature and phase formation also varies with heating rates. It can be determined through differential scanning calorimetry experiments of powder samples. It has been reported that, the trialuminide of Ti, i.e. $TiAl_3$ is the first phase to form and this phase governs the transformation of other Ti rich aluminides *[249]*. It is also reported that, $TiAl_3$ forms at the expense of the pre-existing Ti_3Al or TiAl phases in the presence of excess aluminium. It indicates its kinetic and the thermodynamic stability *[265, 266]*.

Other investigations also revealed that desired phase of γ-TiAl was formed in the Ti/Al multilayer after the $TiAl_3$ phase reached a certain thickness and if all the aluminium was consumed *[249, 265, 266]*, indicating that γ-TiAl was the second phase to form in the Ti aluminide system, followed by the formation of α_2-Ti_3Al and $TiAl_2$ which grew together with $TiAl_3$ and γ-TiAl. In general, it can be inferred that, all these sequence of intermetallic phase formation is governed not only by the thermodynamics of the alloy system but also by the kinetics of the reaction process. Especially in the early stage of the phase reaction, which results in phase selection in the intermetallic formation process *[267]*. Therefore, analysis of kinetics of aluminide formation is very important for selection of optimum reaction

conditions during sintering of powder compacts such that the synthesis process can be made to go to its completion/partial completion depending on the requirement. This study also helps in obtaining the required heating temperature and heating rate for the reaction.

It has been reported that, kinetic steps involved in the formation of the aluminide include the two important factors (a) exothermic chemical reaction at the Ti/liquid Al interface leading to the formation of $TiAl_3$ and (b) flow of fragmented particles away from the reaction interface due to thermal currents inside liquid Al. Where, in step (a), for continuous chemical reaction to occur, supply of aluminium to the reaction site by diffusion through the already formed $TiAl_3$ is essential. This is possible only by diffusion of aluminium through $TiAl_3$ to the Ti/TiAl interface. In view of this, activation energy for the formation of $TiAl_3$ is equal to the sum of activation energies for chemical reaction between Ti and Al and for diffusion of Al/ Ti through the $TiAl_3$ layer *[249]*. Therefore, activation energy of $TiAl_3$ formation has also been discussed in the present work, which provides sufficient indication of reaction.

Reaction synthesis process can be pressure assisted as well as pressureless. For the pressure assisted RS, reaction kinetics is expected to be accelerated due to closer contact of reacting powders/ phases and so reaction kinetic study of pressureless system shall provide the input for both type of processes. Kinetics study of Ti aluminide system has been reported *[252, 253, 256]*. However it is either limited to binary system or carried out with solid state system *[249]*. Therefore, study of reaction kinetics of alloys under study is found to be essential, which shall provide guideline for selection of reaction synthesis parameters and also confirm the phase formation sequence.

Considering this, kinetic studies under pressureless condition have been selected for various combination of alloy powder mixture around the composition of Ti48Al. Thorough analysis of exothermic reaction in binary system and also with addition of specific alloying elements to binary system has been carried out. Attempt has been made to understand the mechanism of aluminide formation, where the exothermic reaction is the basis for aluminide formation.

Several methods have been attempted to study the reaction kinetics and mechanisms of self-propagating high temperature synthesis (SHS) processes *[257-263]*. High temperature thermoanalytical methods (such as DTA, DSC, etc.) have been preferred due to their advantages on experimental easiness with large data generation ability. In thermoanalytical methods, either temperature of the system is maintained constant (isothermal) or heating rate of sample is kept constant where temperature of the system varies (non-isothermal). Among

these two, non-isothermal method is preferred for systems like Ti-aluminide where heat is generated due to exothermic reaction and where maintenance of isothermal condition is difficult. The reaction kinetics for the formation of Al_3Ti phase using elemental powders has been studied *[252, 253]*. It has been shown that the reaction between elemental titanium and aluminum powders leads to formation of Al_3Ti *[256]* and a number of other intermetallic phases like Al_2Ti, AlTi etc. *[250]* alongwith unreacted elemental titanium.

In the present work, kinetics of reaction has been studied through analysis of non isothermal DSC at various heating rates. Activation energy and kinetic parameter 'n' for aluminide formation are obtained using the Johnson – Mehl – Avrami (JMA) equation.

5.2 REACTION ANALYSIS

The exothermic reaction between Al and Ti results in the formation of various phases like Al_3Ti, Al_2Ti, AlTi and $AlTi_3$ starting from aluminium rich side of the Ti-Al phase diagram *[250]*. The reaction kinetics is thus corresponding to overall reaction, resulting in various phases.

Eight different compositions of powder mixtures (*A1* to *A5* and *B1* to *B3*) were prepared for reaction kinetic studies which are presented in Table 5.1. The non-isothermal DSC curves obtained for a typical composition at heating rates of 10, 20, 30 and 40 ^{0}C/min are shown in Figs. 5.1 and 5.2. The heat release during exothermic reaction is calculated as the area under the DSC curve (at exothermic peak) for various heating rates.

Table 5.1: Samples (powder mixture) chemistry used for DSC studies.

Sample No. (powder chemistry No.)		Chemistry of mixed powder
Alloy Composition	*A1*	Ti48Al2Cr2Nb
	A2	Ti48Al2Cr2Nb0.1B
	A3	Ti48Al2Cr2Nb0.1B(Ni-P coated)
	*A4**	Ti48Al2Cr2Nb0.1B
	*A5**	Ti48Al2Cr2Nb0.1B(Ni-P coated)
Base Composition	*B1*	Ti48Al
	B2	Ti48Al2Cr
	B3	Ti48Al2Nb

* *A4* and *A5* has the same composition of *A2* and *A3* respectively with change in particle size of Ti (<50 μm) in place of (200 μm used in alloy *A1-A3*)

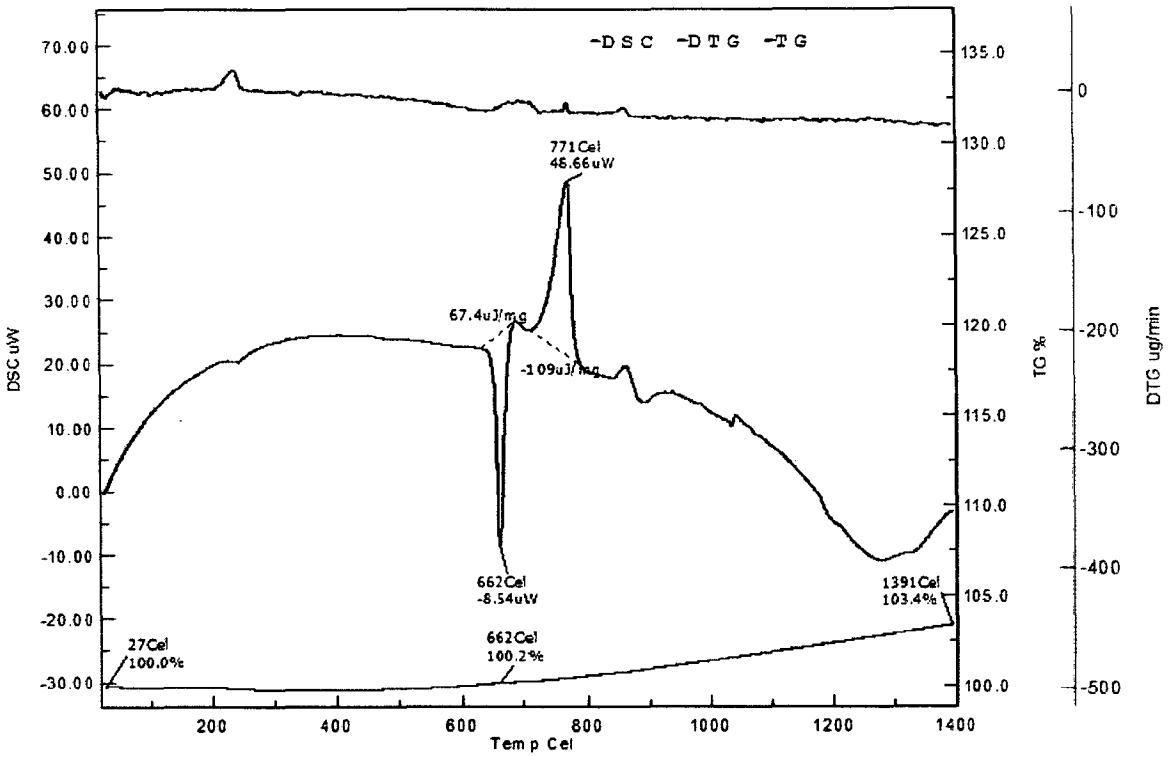

Fig. 5.1: DSC with TG and DTG of a typical alloy mixture *A5* at 20^0C/ min heating rate

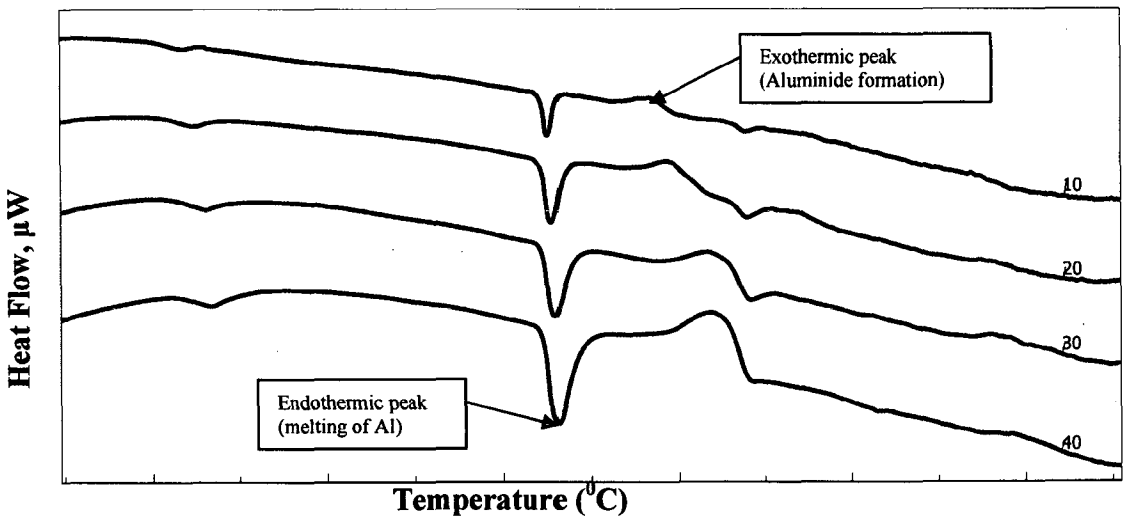

Fig. 5.2: DSC traces at different heating rates 10, 20, 30 and 40^0C/ min (indicated as 10, 20, 30, 40 in the plot respectively) for a typical alloy *A1*, showing the relative shift in reaction temperatures with heating rates (data presented in Table 5.2)

For all the compositions, DSC curves (heat flux vs. temperature plot) do not show any specific difference in characteristics except for the change in peak temperature and energy values. Only two major peaks are seen in each of the curves. One is endothermic peak i.e. for melting of aluminium powder (around 660^0C), where marginal increase in temperature with increase in heating rates is observed. It is because, at higher heating rates, thermal inertia shifts the endothermic peak temperature to higher side, since the time available for maintaining the equilibrium state are insufficient at lower heating rates. Another peak is exothermic for Ti-aluminide formation (around 800^0C), which starts after melting of Al *[253, 254]*. Duration of the exothermic reaction is considered to be very short, about 0.5sec.

Based on the experiments, Kim (1999) reported a sequence of reaction in the powder mixture *[5]*. During heating of the powder mixture, pure elemental powder particles of Al and Ti react in solid form. The extent of this solid reaction, however, depends on rate of heating. Slow heating provides for more time of reaction, resulting in a larger amount of transient phases. The compound form of the transient phases is mainly $TiAl_3$.

Variation in onset temperature, completion temperature, peak temperature and enthalpy of reaction for various alloys and at various heating rates were noted, which is presented in Table 5.2 and Fig. 5.3.

Table 5.2: Thermal properties during reaction in DSC of various powder compositions.

Sample No. (powder chemistry No.)	Heating rate, ^{0}C/min	Al_3Ti Reaction Temperature, ^{0}C			Al_3Ti Reaction Exothermic Enthalpy, J/gm	Endothermic temperatures, ^{0}C
		Onset	Completion	Peak		
A1	10	730	820	766	56.5	652
	20	750	920	788	49.1	655
	30	790	930	832	49.4	658
	40	740	950	837	99.7	662
A2	10	710	780	766	83.5	650
	20	720	800	784	86.6	653
	30	750	870	817	64.2	658
	40	700	870	831	123	661
A3	10	700	845	774	54.5	653
	20	710	830	800	51	658
	30	740	850	825	79.2	661
	40	750	860	839	79.7	664
A4	10	730	820	777	91.2	659
	20	740	870	807	109	663
	30	770	885	828	103	665
	40	772	900	845	196	669
A5	10	700	770	745	109	659
	20	710	800	771	112	662
	30	720	840	791	112	666
	40	730	855	805	110	669
B1	10	700	820	796	226	651
	20	710	920	829	224	656
	30	720	930	840	218	656
	40	730	980	850	253	661
B2	10	730	800	779	109	651
	20	745	840	805	108	654
	30	760	850	827	109.1	660
	40	780	850	844	112	663
B3	10	730	895	820	76	651
	20	740	930	860	85.5	658
	30	750	930	870	90	658
	40	760	940	876	95.4	663

For a particular alloy composition, the heat released at different heating rates is found to be varying. Two opposing factors i.e. diffusion time and temperature during reaction are responsible for variation in enthalpy at different heating rates. At lower heating rates, the time available for solid state diffusion will be more, whereas at higher heating rates the diffusion time available is less but the time required for reaching the reaction temperature shall be lower. Resultant of these two gives the extent of reaction in the form of net heat released in aluminide formation. Higher heating rates also result in the formation of relatively more amount of liquid aluminium, since the entire Al are available for melting. This is evident from the DSC traces shown in Fig. 5.2, where endotherm for aluminium melting is largest corresponding to the heating rate of 40^0C/min, which progressively becomes smaller for lower heating rates.

Higher temperature and presence of more amount of liquid aluminium result in increased exothermic reaction at 40^0C/min heating rate and accordingly the enthalpy changes. However, at intermediate heating rates both the factors have equal roles, so the heat released exhibits minor variation only. Enthalpy of formation of Al_3Ti is found to be higher than the one reported for binary system (~37 kJ/ mole for fine powders) *[28, 268, 269]*. This may be due to higher heating rates and non-isothermal calorimetry adopted in the present work, which has been done considering the practical aspects of reaction synthesis.

Aluminide formation is basically a three step process. First Ti and liquid aluminium reacts to form Al_3Ti, then thickening of this layer depends on interdiffusivity of Ti and Al through Al_3Ti layer and further reaction of Al_3Ti with Ti takes place to form Ti rich aluminides *[254, 270]*. Here, availability of reactant have important role in phase formation as well as heat evolution. It is observed that (Table 5.2), addition of alloying elements to binary alloy lowers the amount of heat released at all the heating rates for ternary as well as for quaternary alloys. This is attributed to formation of compound with aluminium lowering its availability for Ti aluminide reaction. For example, in presence of third elements, ternary compound formations are possible as reported by Jewett et al. *[251]* and this results in low availability of aluminium atoms for reaction. In case of ternary alloy containing Cr, complex compounds of Ti-Al-Cr forms *[251]*. Bohenkamp et al. *[271]* also reported that rate of phase formation of Ti aluminide based materials via reactive synthesis route decreases with Cr additions of as little as 2 at%. Although Ti-aluminde formation is lowered and correspondingly the exothermic heat of reaction, however, some amount of heat is added through ternary aluminide compound *[251]*. Therefore, net heat evolved is the result of all these reactions, which indicates that reaction for ternary compound formation is less

exothermic than the reaction for binary Ti aluminide formation and hence enthalpy is lower than binary alloy.

Similarly, ternary alloy with Nb also has important effect in exothermic reaction by modifying the diffusivity of Ti. Nb is reported as a slow diffuser in these compounds due to relatively large size (Nb atoms) and their preferred solubility on the Ti sublattice. Therefore, microalloying with Nb is expected to cause enhancement on self diffusion of Ti, whereas, heavy alloying by Nb enhances both Nb and Ti diffusion in ternary alloy with respect to binary alloy *[272]*. However, reduction in Ti activity due to presence of Nb was proposed by Kasahara et al. *[273]* and Meier et al. *[274]*, which results in relatively poor exothermic reactions and therefore lowering of exothermic enthalpy. Further, detailed data on the effect of simultaneous addition of Cr and Nb together on diffusivity of Ti and Al and correspondingly on exothermic reaction is not available. In the present work, large reduction in enthalpy of reaction as compared to binary/ ternary alloys at lower heating rates has been observed. It is clear from Table 5.2 that, factors responsible for change in enthalpy in ternary alloys are also operative for quaternary alloys and it may be acting cumulatively at lower heating rates (having more time for solid state diffusion) whereas it is not so at higher heating rate 40^0C/ min. It indicates that, some minimum diffusion time is required to have the effect of factors responsible for reduction in enthalpy of quaternary alloy, which is possible at 10, 20, 30^0C/ min heating rates.

Boron forms Ti_3B_4 and TiB_2 rather than monoborides according to the phase diagram of the Al-B-Ti system. To obtain the beneficial effect of boron, it is added in small amount. Accordingly, 0.1 % (at%) boron has been added in the present study. Effect of boron (0.1%) on exothermic enthalpy is clearly seen from the Table 5.2 and Fig. 5.3. It is observed that, enthalpy of alloy *A2* is higher than alloy *A1* indicating the contribution of boron in exothermic reaction, whereas enthalpy is lowered in case of alloy *A3*. But, significant contribution is noted in case of alloy *A4*, where alongwith boron, smaller size of Ti particles were used as compared to alloy *A2*. Further, significant change in enthalpy is not seen from alloy *A4* to alloy *A5*, where Ni-P coated boron was used. This indicates that, diminishing effect on enthalpy due to lack of contact of boron surface (because of coating) as seen in case of alloy *A3*, is not pronounced in case of alloy *A5*. This may be due to predominant effect of smaller size of Ti particles. Similar to alloys *A1* and *B1*, boron containing alloys *A2* and *A4* also show higher enthalpy at higher heating rate (40^0C/ min). However, such trend is not seen in case of alloys *A3* and *A5*, where coated boron has been added. This also indicates that coated boron is not participating completely in the exothermic reaction.

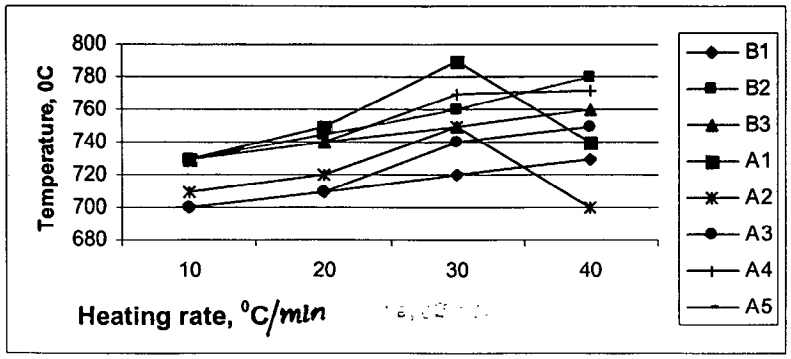

(a)

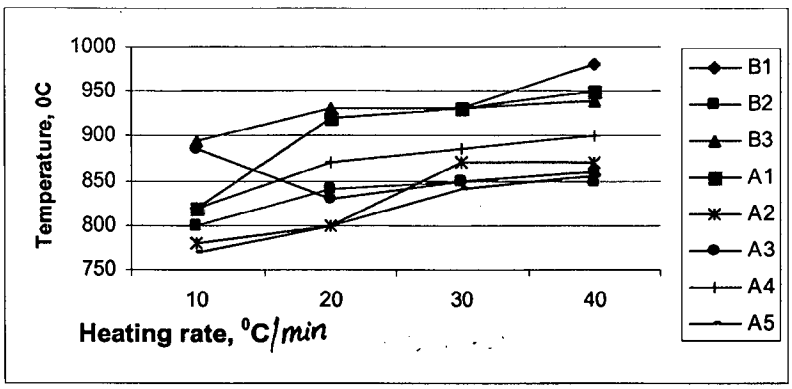

(b)

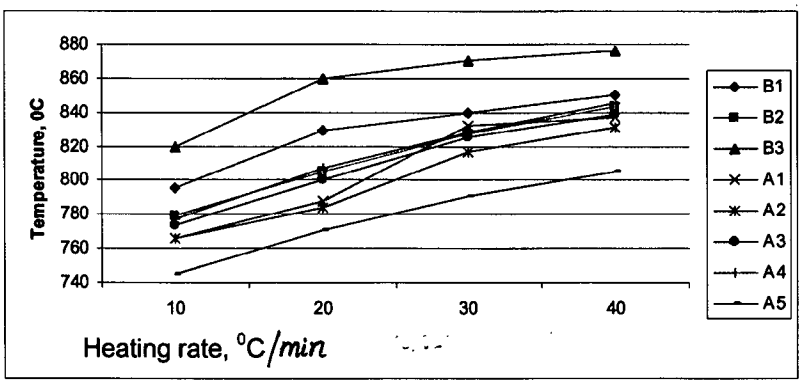

(c)

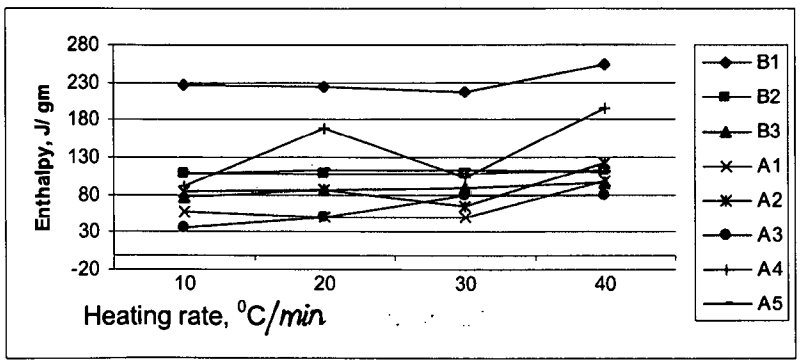

(d)

Fig. 5.3: Variation in Al_3Ti reaction temperatures and enthalpy for various alloy chemistry, (a) onset temperature, (b) completion temperature, (c) peak temperature, (d) enthalpy.

Onset temperature of reaction (Table 5.2) for all the alloys is found to be just after endothermic peak of aluminium melting. It indicates triggering of exothermic reaction due to melting of aluminium *[253]*. Exothermic reaction temperature for binary alloy is found to be in the similar temperature range as reported earlier *[256]*. Marginal difference in onset temperature and in enthalpy as compared to reported one *[256]* is due to difference in particle size of Ti *[255]*. Onset reaction temperatures in different alloys at lower heating rates are found to be nearly same with marginally high for ternary (B2, B3) and quaternary (*A1-A5*) alloys, indicating requirement of relatively higher temperature to initiate reaction in presence of alloying elements. Minor increase in onset temperature is noted for all the alloys with increase in heating rates. This is due to availability of less time for reactant to initiate reactions at higher heating rates, which enhances temperature to start the reaction. Exothermic completion temperature also varies marginally in similar way for various alloys and at different heating rates. For binary alloy, completion temperature is relatively higher than all the other alloys. It is because of higher heat released in binary alloy. In case of alloy containing boron *A2-A5*, there is no significant change in onset and completion temperature of reaction. This indicates, exothermic reaction of boron also takes place almost simultaneously alongwith aluminide formation after melting of aluminium. The same has been reported *[243, 275]*. Change in free energy for TiB_2 formation is marginally less as compared to aluminide reaction. So, it can be inferred that, boride formation and aluminide formation shall be almost simultaneously. Also, this level of boron is not affecting the reaction temperatures.

Peak temperature increases with increase in heating rates in all the cases. It is due to lesser time available at faster heating rates for the reaction to start and so reaction shifts towards higher temperature, so that increased activity of elements help to start the reaction. Peak temperature is marginally low for ternary and quaternary alloys as compared to binary alloy for the same heating rates. It is due to lower amount of heat release for ternary and quaternary alloys, which is insufficient to raise the temperature of ternary and quaternary alloys to the level of binary alloy. For boron containing alloys *A2-A5*, no significant change in peak temperatures were noted. This is also due to the same reasons as discussed for onset and completion temperatures.

From the above results and discussion, it is noted that, through alloying addition, reaction synthesis process becomes less energy efficient than binary alloy. As enthalpy becomes lower and accordingly peak temperature decreases in ternary and quaternary alloys.

It indicates that process need to be extended for relatively longer time to achieve secondary diffusion (of Ti to obtain Ti rich aluminides) and also longer homogenization is required as compared to binary alloy. It also indicates that higher heating rates of the range of 40^0C/min will result in better reaction where liquid formation is relatively higher helping in more vigorous reaction resulting in higher enthalpy. This can be attributed to the availability of less time for alloy compound formation and availability of more aluminium for aluminide reaction. This also helps to move the reaction forward towards second stage i.e. towards Ti rich aluminide formation, which requires less homogenization time in subsequent processing.

From the DSC studies it is clear about the onset temperature of reaction. This also indicates the point of application of pressure in the pressure assisted RS. It is assumed that application of pressure further increases the reaction kinetics through bringing the atoms nearer. It is to be noted that, pressure can be applied accordingly before onset of reaction or during reaction and/ or after reaction to obtain desired phase transformation with densification.

5.3 ACTIVATION ENERGY (E) AND KINETIC PARAMETER (n)

5.3.1 THEORETICAL BACKGROUND

Different models have been applied to study the reaction kinetics of phase transformation in various systems *[253-255, 276-278]*. Among various models, popular JMA model has been extensively used and its limitation for non-isothermal reaction kinetics of some specific systems has been reported *[277, 279]*. For Ti-aluminide system also, variants of JMA were studied *[253, 254]* and Wang T. et al. *[254]* reported only minor variation in activation energy calculated through different methods *[254, 255]*. Wang X. et al. also pointed out, since reaction synthesis occurs at relatively higher temperature (700-1000^0C), the kinetics obtained by non-isothermal method is found to be applicable *[253]*. Considering the above, JMA model has been applied in the present study, which provides sufficient indications on the kinetics of aluminium rich aluminide formation in various alloy systems under study.

The reaction rate of a solid-state transformation obeying JMA kinetic model can be written in the following form *[276]*;

$$d\alpha/dt = An\,(1-\alpha)[\ln 1/(1-\alpha)]^{(n-1)/n} \exp(-E/RT) \qquad (5.1)$$

where α : the reacted fraction, t : time, R : the gas constant = 8.3143 J/mol/K, β : the heating rate, T : the absolute temperature, Tm : maximum (peak) temperature, E : the activation energy, A : the pre–exponential factor and n is Avrami index parameter (depending on the nucleation mechanism and number of growth dimensions).

The above equation is differentiated and equated to zero ($d^2\alpha/dt^2 = 0$) for the maximum reaction rate at T_m temperature to obtain final equation as follows;

$$\ln \beta/T_m^2 = -E/RT_m + C1 \qquad (5.2)$$

where C1 is a constant.

For all the different heating rates, T_m is calculated from the DSC plots with the assumption that the peak of respective DSC plots for a particular heating rate (β) is the maximum reaction rate point. The plot for $\ln \beta/T_m^2$ versus $1/T_m$ is linear and the slope of this curve is used to calculate the activation energy E.

Integrating equation 5.1 and after taking double natural logarithm and using Doyle's approximation *[280]*;

$$\ln[\ln (1/1-\alpha)] = C2 - 1.05nE/RT \qquad (5.3)$$

where C 2 is a constant

Thus, slope of the '$\ln[\ln (1/1-\alpha)]$' versus '1/T' plot gives the value of 'nE'. Ratio of slopes of this plot and E (slope of plot for '$\ln \beta/T_m^2$' versus '$1/T_m$') would thus give the value of 'n' for the reaction under a particular heating rate.

The above model is for pressureless system. In case of pressure assisted system, all the kinetic parameters will change due to change in onset temperature, enthalpy etc. However, kinetics studied through DSC of pressureless powder mixture provides useful indications about the trend of reaction for pressure assisted system also. It is important to mention that, mainly two factors can be affected due to application of pressure in reaction synthesis. One is change in peak temperature (Tm), which is likely to increase due to closer contact of reactant resulting in higher and easy availability of reactant specifically at relatively higher heating rate i.e. 40^0C/ min (where minimum time will be there for compound formation due to diffusion). Second factor is the change in activation energy (E), which is likely to decrease, due to similar reasons and also due to presence of deformed/ refined powder particles (under application of pressure, metal powders shall deform and break). Decrease in E is an indication of low energy barrier for the reaction, which means early start of reaction. It means, the 'n' value is likely to increase due to decrease in E (from the JMA equations) helping in multidimensional nucleation/ growth of product phase.

Therefore, from the above discussion it is clear that DSC study of pressureless system is limiting condition of pressure assisted system from the point of view of progress of reaction.

5.3.2 DETERMINATION OF ACTIVATION ENERGY AND KINETIC PARAMETER

Using the non–isothermal kinetics as per equation 5.2, plot of '$\ln \beta/T_m^2$' versus '1/T' is obtained and is shown in Fig. 5.4. From the slope of this curve the activation energy for the reaction is calculated for Ti-aluminide formation in binary, ternary and quaternary alloys and is presented in Table 5.3. It has been observed that, activation energy of ternary and quaternary alloys is found to be lower than the binary alloy. It is due to change in diffusivity and activity of aluminium and titanium atoms *[6, 28, 16]*, which influences the activation of reaction. Formation of single phase TiAl (γ) in addition to Al_3Ti is also reported in presence of Cr, where diffusion of Ti in Al_3Ti takes place *[281]*. Similarly Nb favours formation of lamellar phase (Ti_3Al+TiAl, i.e. $\alpha_2+\gamma$) *[281]* alongwith Al_3Ti and additional diffusion of Ti in Al_3Ti and TiAl takes place. Simultaneous addition of these elements further decreased the activation energy. This indicates reaction proceeds further and formation of Ti rich aluminides (TiAl and Ti_3Al) is possible. It means, some amount of Ti rich phases may form due to presence of Cr and Nb. And, available Ti and aluminium atoms participate in reaction for Al_3Ti formation resulting in lower activation energy. Lowering of activation barrier due to presence of Cr and Nb can be explained as change in diffusivity and or activity of Ti and aluminium atoms in their presence and at that temperature *[254, 272-274]*.

In case of boron added alloys *A2* to *A5*, marginal change (decrease) in activation energy is noted. This indicates that, reaction has relatively lower energy barrier than alloy *A1*. Alloys with Ni-P coated boron (*A3* and *A5*) has higher activation energy than alloys having uncoated boron (*A2* and *A4*). It indicates that, Ni-P coating which comes in direct contact to the reaction interface diminishes the activity of reactants. Also, the alloy containing boron and with lower size Ti particles (alloy *A4*) have marginally higher activation energy than the alloy *A2*. This change (increase) in activation energy for smaller size Ti particles is found to be opposite to the expected lines and needs more experimentation to reach to a conclusion. Also the effect of agglomeration of particles (due to small size of particle) during reaction has not been considered. Although, all these data obtained were based on repeated experimentation; a series of experimentation with different particles sizes needs to be carried

out. However, the difference in activation energy between alloy *A2* and alloy *A4* is only marginal (8.86kJ/ mol), which can be considered within the experimental and calculation (model) error. Also, decrease in activation energy due to boron confirms the near simultaneous exothermic reaction of aluminide and boride formation where both are exothermic in nature and by decreasing activation energy, reaction needs to cross relatively lower energy barrier.

Several workers have reported the activation energy (E) of Al_3Ti formation in binary alloys. Large scattering in E values has been noted through different experimental conditions. Using isothermal kinetics, Wang (1994) *[253]* calculated E as 149kJ/ mol, whereas through non-isothermal method, it is found to be 517kJ/ mol. In another analysis, Ti-75Al (at%) experimentation having small Ti particles (39μm) in binary alloy, Wang X. et al. (2002) *[254]* has reported 170kJ/mole under non-isothermal condition. They also divided the reaction into steps and calculated E separately for each step. Finally, rate controlling step of this process is reported as interdiffusion between Ti and Al through $TiAl_3$ layer. Similarly, Ramos et al. (2005) also reported different E values through their thin film experimentation, where E values were ranging from 231-268 kJ/ mol. Increase in E values from 231 to 268kJ/mol was noted when nanometric layer thickness increased from 4nm to 200nm. It is to be noted that, activation energy for self diffusion of Ti is 302kJ/mol and for aluminium, it is only 142kJ/ mol. But, activation energy for aluminium diffusion in α-Ti is 328kJ/ mol *[244]*. In another study, Lucadamo et al. also reported E value as 171kJ/ mol for Al_3Ti formation *[266]*. Wang *[254]* reported activation energy for interdiffusion between Ti and Al through Al_3Ti layer as 180kJ/ mol and between Ti and Al_3Ti through TiAl and Ti_3Al as 206kJ/ mol. Activation energy obtained in the present work (Table 5.3) is found to be near to this range.

Activation energy for Ti-aluminide formation in binary alloy is found to be marginally higher than the activation energy data reported by other workers for Ti-aluminide formation through other processes *[249, 253, 254, 266, 279]*. It is due to larger size of Ti particles (used in the present work) where surface area available per unit volume is lower for the reaction. Similar observation was made by Wang et al. *[253]* on effect of size of particles on reaction kinetics. It also suggests change in mechanism of reaction.

For the binary alloy *B1*, activation energy is near to the work of Ramos *[270]* as reported for thin film and for alloy *A1-A5*, activation energies are near to the E value of Wang et al. *[253]* reported for high aluminium containing DSC work. This indicates, E value is

lower in presence of excess (sufficient) aluminium and the same has also been reported by Ramos et al *[270]*. Also, E values of alloys *A1-A5* is near (marginally high) to self diffusion of aluminium, indicating diffusivity of aluminium has the prime role in the reaction. This further shows that, most probable phase to form first can be aluminium rich compound Al_3Ti, since E for self diffusion of Ti is higher and until the entire aluminium is consumed, diffusion of Ti is limited. This also indicates that, higher homogenization time and temperature may be required to obtain Ti rich aluminide phases by diffusion of remaining Ti through aluminium rich aluminide phases, which is governed by diffusivity of Ti through the intermetallic layer.

Characteristics of the DSC peak (Figs. 5.1-5.2) represent transformation of phases as the reaction proceeds, which can be analyzed by the JMA model. Values of 'nE' are evaluated from 'ln[ln1/(1-α)]' vs. '1/T' plots based on the relationship depicted in equation 5.3. These plots are presented in Fig. 5.5 for various alloys with respective heating rates of 10, 20, 30 and 40 ^{0}C/min. The 'nE' values are obtained as the slope of the curves. It is observed that, mostly slopes decreases gradually as heating rates are increased and correspondingly 'n' value changes. The same observation has been reported by Joraid et al. (2005) *[277]*. The value of n is calculated through dividing this slope by activation energy. Value of kinetic parameter 'n' obtained for Ti-aluminide reaction is presented in Table-5.3. The mechanisms for these reactions can be derived in accordance with 'n' values *[265, 276]*. Calculated values of 'n' are not integers and showed a variation of 0.946 to 4.62, it means that formation of aluminide occurs by more than one mechanism. These values of 'n' may be accounted for the possibility of a combination of multi dimensional crystal growth with heterogeneous nucleation and or with homogenous nucleation.

Based on kinetic parameter 'n' for the alloys, it is grouped in two groups. In first group, kinetic parameter 'n' for binary and ternary alloy (TiAlNb) are found to be similar and is varying from 0.946 to 2.01 for various heating rates. Generally, it is higher for lower heating rates (10^{0}C/min) and lower at higher heating rates except for the alloy *A4*. Also, at intermediate heating rates 'n' values have small difference only, indicating transformation mechanisms at intermediate heating rates are similar. However, it is different at lower (10 ^{0}C/ min) and at higher (40 ^{0}C/ min) heating rates. In case of alloy *A4*, 'n' values do not show any definite trend or not varying significantly with respect to heating rates as compared to other alloys. This shows that, for smaller size Ti particles, transformation mechanisms are not dependent on heating rates, indicating reactants are getting converted to product phase in a

very short period by multidimensional growth where high heating rate of 40^0C/ min is sufficient. Conversely, it can also be explained that at lower heating rates of 10^0C/ min, the alloy has very fast multidimensional growth. This is all due to smaller size Ti particles, which participate in reaction with higher surface area. This effect is however not present in alloy *A5*, which may be due to presence of coated boron particle, diminishing the activity of the reactants at higher heating rates. Following the Criedo and Ortega criterion *[276]*, instantaneous nucleation and two dimensional growth for binary and ternary (TiAlNb) alloys at low heating rates and instantaneous nucleation and one dimensional growth for binary and ternary (TiAlNb) alloys at higher heating rates can be proposed. This value is found to be similar to the value found in Ti/Al thin films *[251, 282]*.

In second group, kinetic parameter 'n' for ternary (TiAlCr) and quaternary alloys (*A1-A5*) is similar and varying from 2.17 to 4.62 for various heating rates. In the JMA model, kinetic parameter (Avrami constant) 'n' has value of 2 (for constant number of nuclei) or 3 (for constant nucleation rate) for a two dimensional process. Ma and Thompson *[283]* modified the two dimensional process to a diffusion controlled thickening of the cylindrical nuclei in addition to the radial growth, where n= 2.5 or 3.5. Here also for ternary (TiAlCr) and quaternary alloys, n value is consistent with the modified model for a fixed nuclei population and a constant in-plane (two dimensional) growth and diffusion controlled growth in third dimension *[276, 283]*. It means that, reaction mechanisms are different for different compositions. Although 'n' values are marginally higher for ternary (TiAlNb) as compared to binary alloy, phase transformation mechanism has not changed due to addition of Nb (since 'n' values are between 1-2) whereas Cr addition has changed the transformation mechanisms towards multidimensional growth in ternary (TiAlCr) as well as in quaternary alloys (n is >2). This is in line with the activation energy data where decrease in activation energy is seen with Cr addition. It means addition of Cr and Nb to binary alloy has important effect on activation energy and phase transformation mechanisms, which may be through change in diffusivity and/ or activity of elements. Similarly, boron addition has increased the 'n' values in case of alloy *A2* and *A4*. Also, effect of Ni-P coated boron is clearly seen in 'n' values, where it is lower (in alloys *A3* and *A5*) than the uncoated boron containing alloys (*A2* and *A4*).

Table 5.3: Slopes of ln[ln 1/ (1-α)] versus 1/T plots and calculated n values

Alloy	Activation Energy, E	Slope, nE/R at different Heating Rate				n at different Heating Rate			
		10 °C/ min	20 °C/ min	30 °C/ min	40 °C/ min	10 °C/ min	20 °C/ min	30 °C/ min	40 °C/ min
A1	184	71.11	50.27	55.03	43.7	3.21	2.27	2.48	1.97
A2	169.5	94.29	78.83	61.8	47.14	4.62	3.86	3	2.31
A3	189.98	63.52	63.21	48.08	61.42	2.87	2.85	2.17	2.77
A4	178.36	72.37	63.52	67.58	77.59	3.37	2.96	3.14	3.61
A5	192.49	83.81	57.92	62.55	51.89	3.62	2.5	2.7	2.24
B1	234.4	63.18	31.03	29.64	26.69	2.0	1.1	1.05	0.946
B2	189.5	81.48	94.77	65.17	65.52	3.57	3.15	2.85	2.87
B3	222.4	53.79	32.2	32.6	37.08	2.01	1.2	1.2	1.38

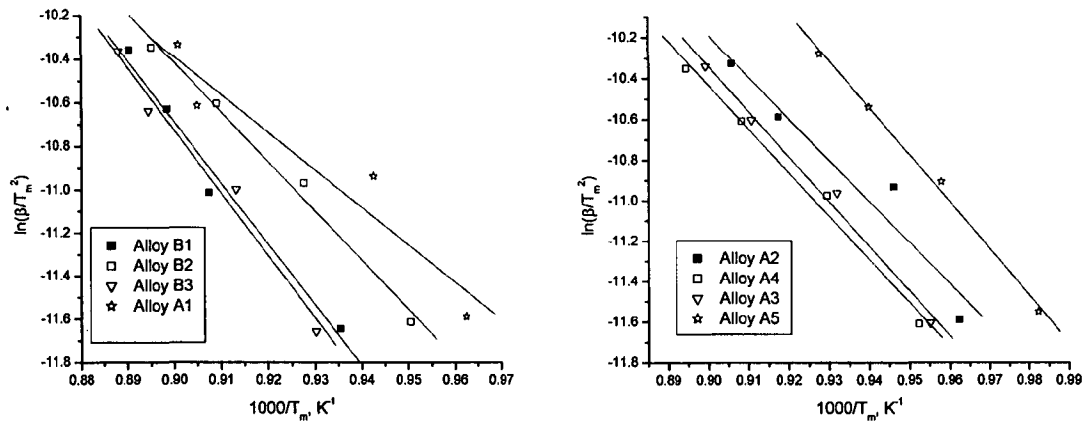

Fig. 5.4: Plot of ln β/T_m^2 versus 1/T obtained for various alloys at different heating rates 10, 20, 30 and 40^{0}C/ min.

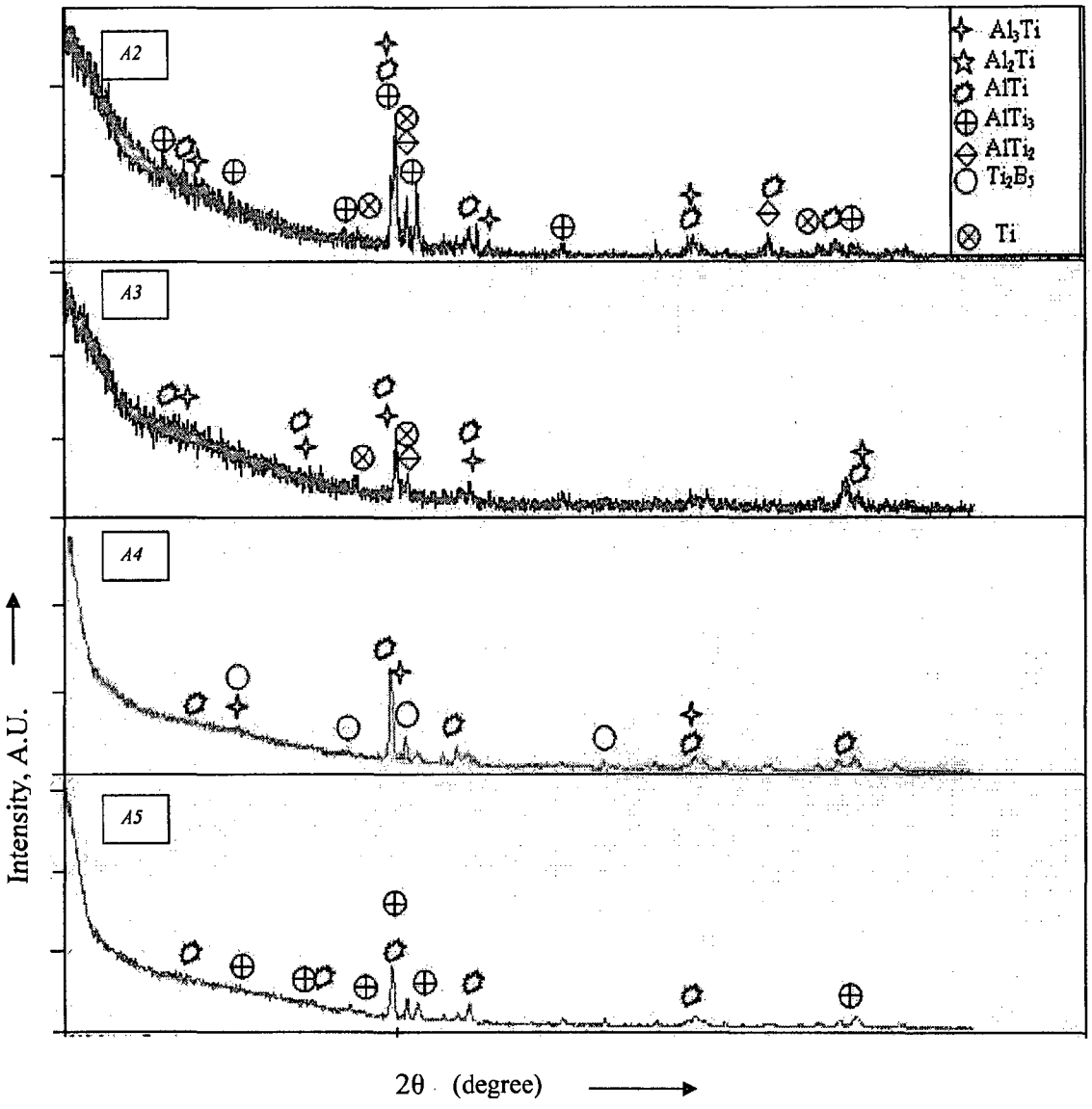

Fig. 5.6c: XRD pattern with corresponding peaks of DSC residue of various alloys

5.5 SUMMARY

Reaction kinetics studies of Ti-aluminide compositions of binary (Ti48Al, at%), ternary (Ti48Al2Cr and Ti48Al2Nb) and quaternary (Ti48Al2Cr2Nb) alloy powder mixture has been carried out through non-isothermal differential scanning calorimetry (DSC) experiments. DSC was conducted at four heating rates i.e. 10, 20, 30 and 40^0C/ min. Formation of Al_3Ti phase alongwith Ti rich phases like, Al_2Ti and AlTi was confirmed through X-ray diffraction (XRD). Change in reaction enthalpy of ternary and quaternary alloys from the binary alloy is observed due to addition of Cr, Nb and B and also with change in heating rates.

Onset temperature of reaction for all the alloys is found to be just after endothermic peak of aluminium melting. It indicates triggering of exothermic reaction due to melting of Al. Onset temperatures of different alloys at lower heating rates are found to be nearly same with marginally high for ternary (B2, B3) and quaternary (*A1-A5*) alloys. Minor increase in onset temperature is noted for all the alloys with increase in heating rates. Exothermic completion temperature also varies marginally in the similar way for various alloys and at different heating rates. Peak temperature is found to be increasing with increase in heating rates in all the cases. Peak temperature is marginally lower for ternary and quaternary alloys as compared to binary alloy for the same heating rates. Significant effect of boron of this level (0.1 at%) is not observed in the reaction temperatures.

Small additions of Cr, Nb, B to binary alloy is found to have important effect on reaction enthalpy, activation energy and phase transformation mechanisms. It is observed that alloying additions (Cr and Nb) brings down the enthalpy. However, addition of boron increases the enthalpy and use of smaller size Ti particle further increases the enthalpy. But diminishing effect of Cr and Nb on enthalpy from the binary alloy is not compensated by using 0.1 (at%) boron and also with use of smaller size Ti particle size.

The application of Johnson – Mehl – Avrami equation to the kinetics of exothermic reaction of Ti-aluminide formation yielded different activation energies (E) for different alloys ranging from 169.5 to 234.4 kJ/ mol. Activation energy is found to be lower for ternary and quaternary alloys than binary alloy. The value of Avrami parameter 'n' for exothermic reaction and is found to be in the range of 0.946 to 4.62 for various alloys. Reaction mechanisms are found to be different for different composition. Binary alloy *B1* and ternary alloy *B3* (TiAlNb) showed value of n <2 whereas ternary alloy *B2* (TiAlCr) and quaternary

alloys (*A1-A5*) showed value of n>2, indicating addition of Cr is helping additionally in multidimensional growth of reaction products.

Effect of particle size of Ti has been noted in changing the enthalpy, reaction temperatures and reaction transformation mechanisms. Similarly, role of Ni-P coating over boron has been observed in diminishing the reaction kinetics of the alloy. It is clear that, although alloying additions are bringing down the enthalpy, but helping in phase transformation by multidimensional growth and lowering of activation energy.

Thus DSC studies are not only useful in obtaining the kinetic parameters for the reaction but, it also provides parameters for reaction synthesis (RS) by showing onset temperature, completion temperature, enthalpy etc. It also indicates the point of application of pressure in the pressure assisted RS, where load can be applied before onset of reaction or during reaction and/ or after reaction to obtain desired phase transformation with densification.

Chapter-6

REACTION SYNTHESIS STUDIES

6.1 INTRODUCTION

Reaction synthesis (RS) process also known as reactive sintering, has been one of the important alternatives to melt route with respect to homogeneity and uniformity in the final product. It gives better uniformity in terms of composition and phases present, which results finer grain size product as compared to the ingot metallurgy route. This process is used for the alloy systems where exothermic reaction takes place among the alloy constituents and the same heat is utilized in propagating the reaction and compound formation. This process is suitable for Ti aluminide system and therefore, aluminides have been synthesized and studied through this method. Studies on RS of binary γ-TiAl have been extensively reported in literature *[63, 206, 209, 286]*, but only few studies on quaternary alloys are reported *[5, 17, 49]*. Limited study on RS of Ti-Al-Cr-Nb alloys have been carried out, which are of great engineering importance. Role of pressure before, after and during the reaction has not been specifically reported. Also, effect of particle size during reaction and finally on the product needs better understanding.

Alloying addition of Cr to two-phase binary titanium aluminides containing γ and α_2 phases enhances the ductility, whereas, Nb additions improve strength and oxidation resistance *[58]*. Both of these alloying elements have good solubility in both the γ and α_2 phases. However, Nb has more solubility in the two phases amongst the two elements and forms no intermetallic phases both with Ti and aluminium in small concentrations *[287]*. Further, it is reported that alloying addition of Nb enhances diffusivity of Ti in TiAl due to elastic distortion of the $L1_0$ structure caused by oversized Nb atoms *[288]*. The atomic sizes of Ti, Al, Cr and Nb are reported as 2.4861, 1.3607, 2.2701 and 3.2071 angstroms respectively *[289]*. High solubility and good diffusivity of Cr and Nb in γ and α_2 phases make them suitable for alloying additions and render the quaternary alloys amenable to reaction synthesis (RS).

In the present work, it has been attempted to study the gamma Ti aluminide alloy Ti48Al with Cr, and Nb through pressureless RS route (during reaction). However, pressure has been applied prior to reaction and after the reaction. In addition to base alloy (Ti48Al2Cr2Nb), 2 more alloys with addition of minor B and Ni-P coated B is made and with

two different particle size of Ti. In this way 4 variants of quaternary alloy Ti48Al2Cr2Nb has been studied through this process under similar processing conditions. Characterization of the RS products involve chemical analysis, density measurement, XRD, OM, SEM, EDAX/ elemental mapping, TEM, hardness and microhardness measurements.

6.2 REACTION SYNTHESIS

The parameters were derived from reaction kinetics study, experimental trials and reported literature *[64, 195-211]*. For finalization of RS parameters, trial experiments with simultaneous application of pressure (during reaction) were carried out, where heavy loss of material by spillage was observed. Therefore, cycle was modified to avoid the material loss. Accordingly, heating and loading cycle was designed, which is presented in experimentation section 4.4. Experiments were conducted with this cycle for 5 types of alloys to produce 75 mm diameter billets. The alloy composition of the RS experiments are presented in Table-6.1. In alloys A3 and A5, at% of boron was maintained as 0.1, and for compensating the amount of Ni-P additional amount was added. Content of Ni-P in the alloys was estimated to be <0.04 (at%), where Ni-P coating thickness was 150-200 nm. Photograph of a typical RS billet is presented in Fig. 6.1.

Table-6.1: Details of RS experiments of various alloys.

Alloy no.	Chemistry, at%
A1	Ti48Al2Cr2Nb
A2	Ti48Al2Cr2Nb0.1B
A3	Ti48Al2Cr2Nb0.1B(Ni-P coated)
*A4**	Ti48Al2Cr2Nb0.1B
*A5**	Ti48Al2Cr2Nb0.1B(Ni-P coated)

* *A4* and *A5* has the same composition of *A2* and *A3* respectively with change in particle size of Ti (<50 μm) in place of (~200 μm used in alloy *A1-A3*)

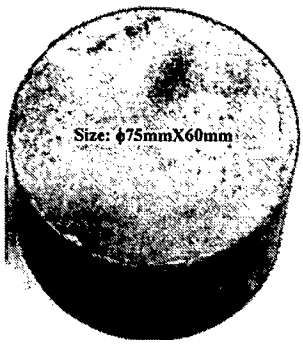

Fig. 6.1: Ti aluminide billet made through reaction synthesis process

Swelling of the compact was observed during reaction. When the load was removed at 550^0C to allow the reaction under no-load condition, level of the alloy compact was increased by 23-25 mm in a compact of 1 Kg. This observation was seen in all the experiments (alloy *A1-A3*). In case of alloy *A4* and *A5*, relatively less swelling/ expansion was observed (18-20 mm rise). This swelling is reported to be common in RS and is due to formation of compound where aluminium atoms diffuse towards Ti vacating the atomic sites of aluminium, which results in pore formation and shows as swelling *[199, 211]*. This is attributed to various factors like, heating rate, particle size, holding time etc. Swelling/ pore formation is not due to gas entrapment, since the reaction is taking place under vacuum condition *[211]*. Rise due to swelling in case of alloy *A4*, *A5* is found to be relatively less. It indicates that, smaller particles have better compaction, faster reaction product formation due to less diffusion distance *[201]*.

Process characteristics are found to be same for all the alloys and variation due to small change in chemistry from alloy *A1* to *A5* has not been observed. This indicates that, predominantly Ti and Al only play role in the RS process.

6.3 HOMOGENIZATION

Homogenization is carried out at elevated temperatures to obtain homogeneity in chemistry and desired Ti rich aluminide phases like γ and α_2. Homogenization parameter for different alloys (*A1-A5*) are found to be marginally different. It is due to presence of alloying elements and initial particle size of Ti. Homogenization is a solid state diffusion process which is affected by the type of alloying elements and distance of diffusion. Element like B retards the diffusion process *[134-138]* whereas Cr and Nb help in diffusion *[288]*. Larger

particle size of Ti needs longer time for homogenization. Accordingly, homogenization cycle has been studied for all the alloys on the basis of optical microscopy and scanning electron microscopy with EDAX. Final optimized cycle for various alloys is presented in Table 6.2.

Two step homogenization was decided based on DSC of RS billet samples (Fig. 6.2) showing some endothermic peak around 875^{0}C, which may be due to the presence of aluminium rich compounds or may be due to Ti phase transformation. Therefore, 850^{0}C soaking was used for 4 hrs and absence of such endothermic peak was confirmed. Second stage temperature was carried out to homogenize in two phase region where (α+γ) phases are nearly in equal proportion.

Table-6.2: Optimized homogenization cycle of various alloys.

Alloy	Homogenization cycle
A1	850^{0}C/ 4hrs.-F/c* cool +1250^{0}C/ 6 hrs-F/c cool +1250^{0}C/ 4 hrs-F/c cool
A2	850^{0}C/ 4hrs.-F/c cool +1250^{0}C/ 6 hrs-F/c cool+1250^{0}C/ (4+2) hrs-F/c cool
A3	850^{0}C/ 4hrs.-F/c cool +1250^{0}C/ 6 hrs-F/c cool+1250^{0}C/ (4+2) hrs-F/c cool
A4	850^{0}C/ 4hrs.-F/c cool +1250^{0}C/ 6 hrs-F/c cool+1250^{0}C/ 2 hrs-F/c cool
A5	850^{0}C/ 4hrs.-F/c cool +1250^{0}C/ 6 hrs-F/c cool+1250^{0}C/ 2 hrs-F/c cool

*F/c means furnace cooled

Although, homogenization treatment is reported to be carried out in single phase region of α, where all the aluminide phases transform to α phase *[290]*. However, in the present work, temperature of two phase region (α+γ) was selected to obtain more volume fraction of γ. At this temperature grain growth is also limited. Kinetics of homogenization study suggest that temperature and time is important to obtain complete homogenization and without any grain growth *[290]*. Gupta et al. on homogenization study of Al alloys demonstrated that grain size has important role in the selection of homogenization time and temperature, which follows Fick's laws of solid state diffusion *[291]*. Here also homogenization parameters depend on the intermetallics grains/ particle sizes. Therefore, philosophy of lower temperature and longer time was taken in the present study.

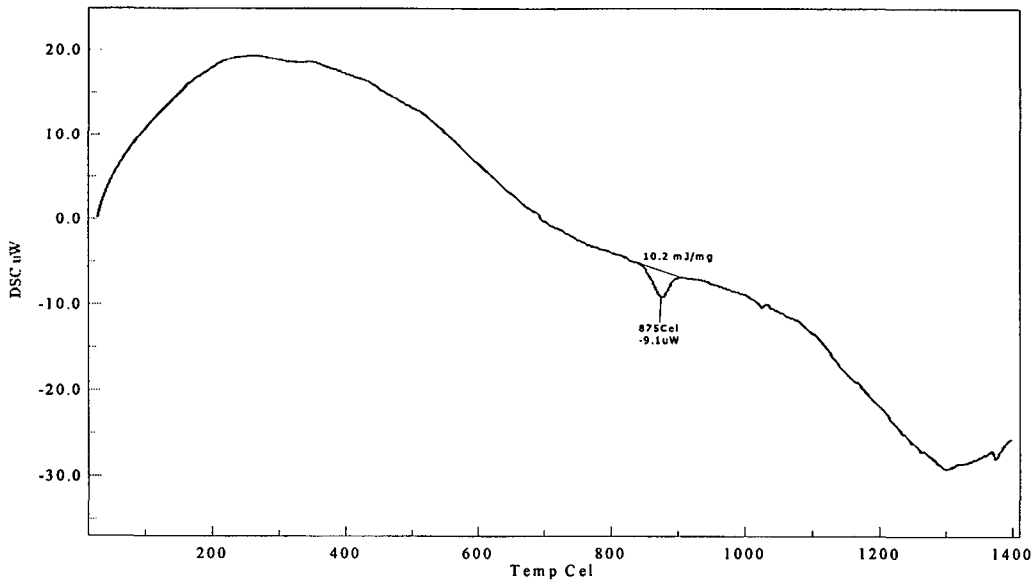

Fig. 6.2: DSC of Ti aluminide billet made through reaction synthesis process

It is observed that, alloys *A1-A3* having relatively coarser Ti particles took longer homogenization time as compared to alloy *A4-A5*. It is mainly due to the effect of Ti particle size used in RS. Also, boron containing alloys (*A2-A3*) took relatively more time in homogenization indicating the affect on the diffusivity of Al_3Ti/ Ti in the presence of boron or TiB_2 (which may form during reaction).

6.4 RESULTS

6.4.1 Chemical Analysis

Reaction synthesized and homogenized billets were analyzed for chemical composition using X-ray fluorescence (XRF) and Inductively coupled plasma optical emission spectroscopy (ICP-OES) methods. Although analyzed chemistry through these methods does not have any error, small (1-2%) variation from the analyzed content is possible, since it has been done with the assumption of total 100 as basis, ignoring boron content and gas content. Gas analysis was carried out through IR cell (for Oxygen) and through thermal conductivity cell (for Hydrogen and Nitrogen). Results of the analysis are shown in Table 6.3. Boron could not be analyzed by XRF due to its low atomic number.

Other methods used in the present work also could not provide accurate result due to its low content. Hence, its presence has been confirmed by XRD, TEM and EDAX. Loss of boron in processing is assumed to be insignificant since after RS it will be present in the form of compound. Similarly, content of Ni-P could not be analyzed due to its very small amount, and therefore, estimated weight of Ni-P (added to the alloy) has been considered as actual amount of Ni-P present in the alloy.

Table-6.3: Analyzed composition of various alloys on homogenized samples.

Sl. No.	Analyzed Chemistry, at%				Gas content, wt. ppm		
(Alloy)	Al	Cr	Nb	Ti (Balance)	H_2	O_2	N_2
A1	46.17	1.9	1.85	50.08	90-	2600-	169-
A2	46.69	1.95	1.89	49.47	100	3700	195
A3	46.4	1.98	1.85	49.77			
A4	46.26	1.89	1.87	49.98	120-	2500-	240-
A5	46.19	1.91	1.90	50.00	130	4100	250

As mentioned earlier, heavy loss of aluminium by spillage due to simultaneous application of pressure was noted in initial experiments. With modified cycle also, loss of aluminium is in the range of 1-2 at%, in addition to this, small amount of Cr and Nb loss is observed (Table 6.3). This can be attributed to the spilling of liquid during RS process. From the gas analysis (Table 6.3), it is observed that RS process under 10^{-4}mbar of vacuum level is insufficient to restrict the gas content to lower level. This level of gas content may lead to reduction in properties, especially ductility. Also, it is noted that gas content is marginally higher for alloys *A4-A5* as compared to alloys *A1-A3*. This may be due to the use of smaller Ti particles in RS process, which will have higher surface area to volume ratio and correspondingly higher reactivity during reaction, as well as gas pick-up.

6.4.2 Density Measurements

Theoretical density of each alloy was calculated based on analyzed chemistry of alloying element and with actual amount of Boron and Ni-P coated Boron added in the respective

alloy system. The density levels achieved for the alloys are presented in Table-6.4 and Fig. 6.3. Following formulae have been used for the calculation of theoretical density.

$100/\rho_{alloy}$= w_f. of Ti/ρ_{Ti}+w_f. of Al/ρ_{Al}+w_f. of Cr/ρ_{Cr}+w_f. of Nb/ρ_{Nb}+w_f. of B/ρ_B

(where ρ is density and w_f. is weight fraction)

Table-6.4: Density achieved for various alloys at different stages of processing.

Alloy no.	Processing stage	Density achieved gm/cc	Theoretical density	% of theoretical density
A1	RS	3.69	3.821	96.57
	Homogenized	3.70		96.83
	HIPed	3.736		97.77
A2	RS	3.71	3.794	97.78
	Homogenized	3.715		97.91
	HIPed	3.74		98.57
	Isothermal Forged	3.76		99.10
	Open forged	3.718		97.99
A3	RS	3.678	3.824	96.18
	Homogenized	3.69		96.49
	HIPed	3.78		98.84
	Isothermal Forged	3.792		99.16
	Open forged	3.76		98.32
A4	RS	3.82	3.827	99.81
	Homogenized	3.821		99.84
A5	RS	3.769	3.832	98.35
	Homogenized	3.77		98.38
	HIPed	3.822		99.73
	Open Forged	3.79		98.90

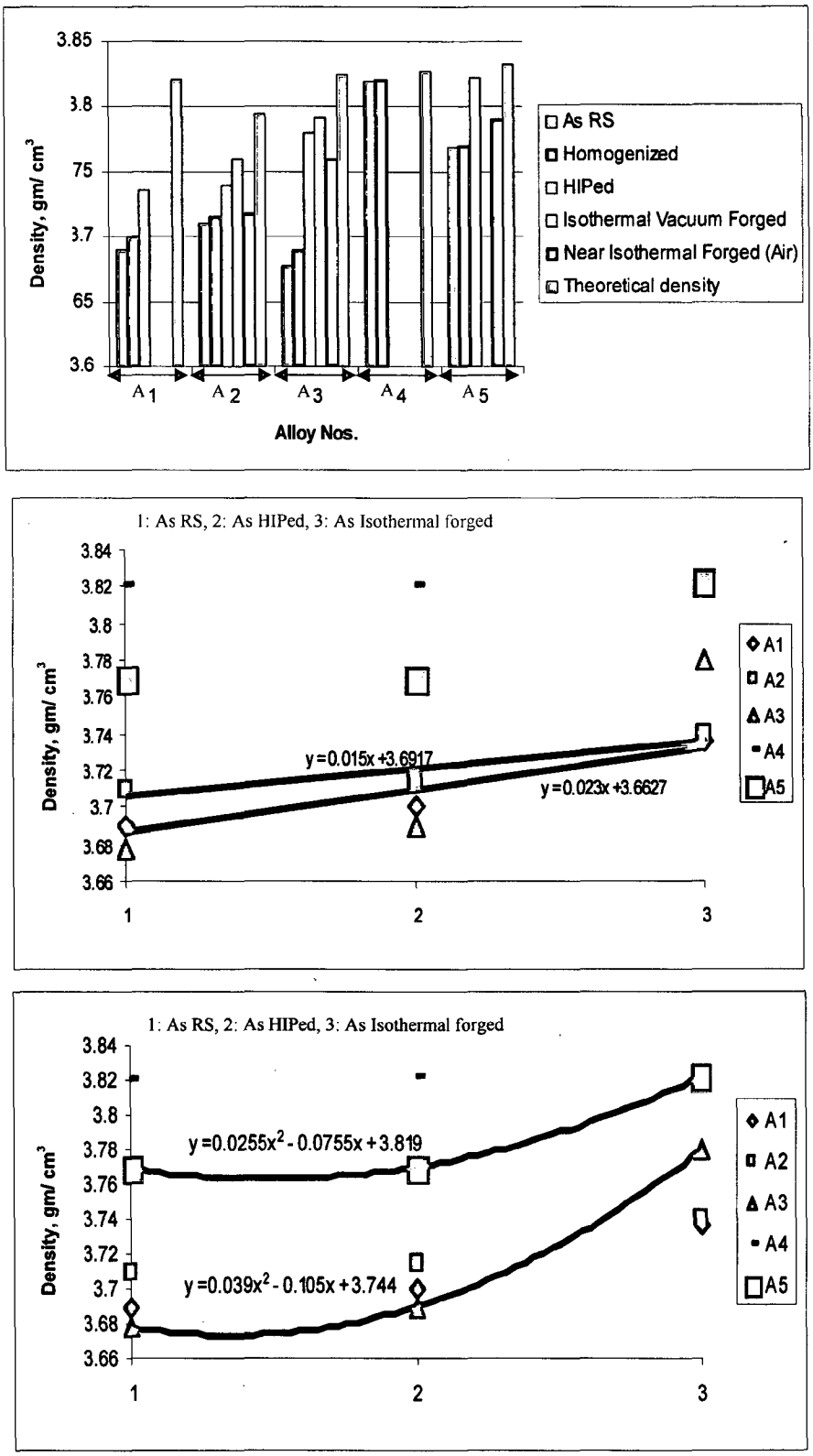

Fig. 6.3: Comparative view of density in various processing stages of alloys (*A1-A5*)

From Table 6.4, it is seen that, actual density varies in the range of 96.18 to 99.8% of theoretical density in various conditions. Density is found to be minimum in RS condition, which progressively increases after hot isostatic pressing and with hot isothermal forging. Density of alloys *A4-A5* is relatively higher than other alloys. It is due to use of smaller particles of Ti. Although, alloys *A4-A5* contain marginally higher gases (Table 6.2), however, Kirkendall porosity content may be relatively low due to the partial closure of such pores in RS process. This is due to increased diffusion distance in Ti particles, resulting in less content of elemental Ti (remaining) and more content of aluminides. Also, due to smaller Ti powder particles, interstices created by aluminium are compacted better during post RS pressure application.

Only marginal increase in density is seen after homogenization. This indicates, further porosity formation is not there from the existing RS condition. This also validates the concept of porosity generation through diffusion of Al (Kirkendall porosity), which is possible only in RS stage, where elemental Al is available. Significant increase in density after HIPing (under argon) and hot isothermal forging (under vacuum) is due to closure of existing pores at high temperature. This leads to density of various alloys approximately near to its theoretical density.

During ambient (near isothermal) forging (open die forging), it is noted that, surface gets oxidized. Although density was measured after removing oxide layers, but, total removal can not be ruled out due to uneven surface of forging. This may give rise to small decrease in density.

It is also observed that, alloy *A1* and *A2* follow linear relation with respect to reduction in porosity with hot isothermal working, alloy *A3* and *A5* follow polynomial relations. This change in behaviour from linear to polynomial indicates role of coating constituents (Ni/P) on boron, which may be helping to reduce the porosity at higher rates (polynomial rates) in subsequent forging. It is a unique observation and needs more experimentation to validate this phenomenon.

Thus improvement in density of alloys in subsequent processing indicates the densification tendency of the RS processed materials.

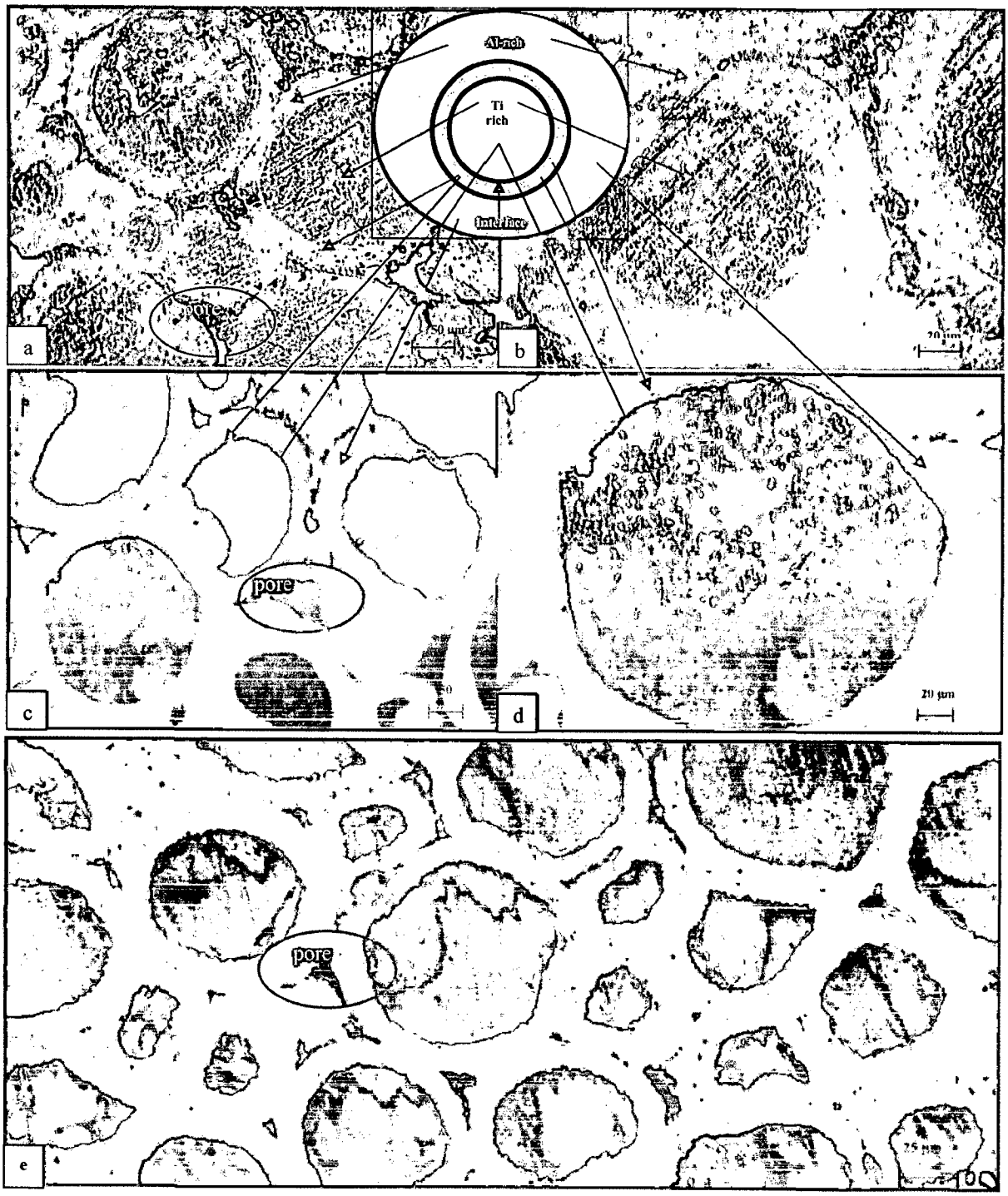

Fig. 6.4: Optical micrographs of a typical RS samples (with larger Ti particles, alloy *A3*) showing Ti-rich and Al-rich regions alongwith interface, (a-b) unetched specimen, (c-d) etched with Kroll's reagent, (e) RS sample with smaller Ti particles, Alloy *A5*.

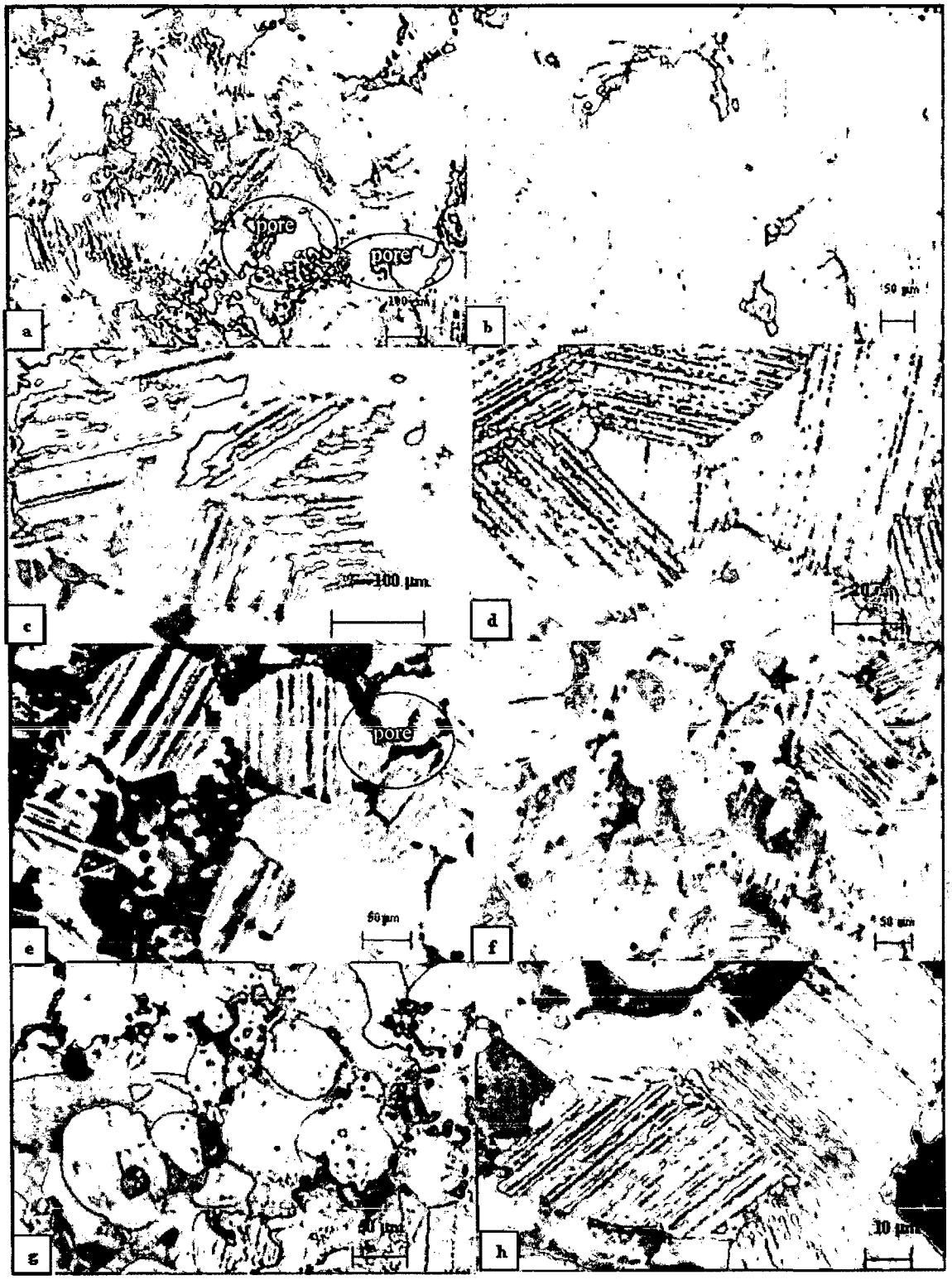

Fig. 6.5: Optical micrographs of a typical homogenized samples showing lamellar structure, (a-d) with larger Ti particles, alloy *A3* and (e-h) with smaller Ti particles, alloy *A5*

The optical micrographs of homogenized samples from the edges and from the center of the 75 mm diameter billets do not show any significant variation in the microstructure. Most of the samples show lamellar-phase regions with small γ-phase regions as shown in Fig. 6.5. This indicates some variation in elemental content within the sample. γ-phase rich regions result in the areas, where Ti is on the lower side, as presence of more aluminium in these regions stabilizes γ-phase, which can be clearly seen in Ti-Al phase diagram.

Also, grain sizes of homogenized alloys were seen to be clearly governed by the initial particle size of the Ti powder particles. Grain size of different alloys is presented in Table 6.6. This indicates, small amount of coarsening of grain size during homogenization treatment in case of alloy *A1*. Whereas alloys *A2* and *A3* retain the initial particle size of Ti, which can be attributed to the presence of boron and TiB_2 at the grain boundary, inhibiting the grain growth during homogenization. Alloys *A4* and *A5* also do not have any growth indicating the role of boron/ TiB_2 even at this level of addition. However, among the alloys uncoated boron containing alloys *A2* and *A4* shows no grain growth having lowest grain sizes against their initial particle sizes respectively.

Table 6.6: Grain size of homogenized alloys

Alloy	*A1*	*A2*	*A3*	*A4*	*A5*
Grain size, μm	220-240	170-180	180-200	35-40	45-50

6.4.4 SEM Elemental Mapping/ EDAX Point Analysis

The SEM elemental mapping results for the elements aluminum and Ti for RS alloy samples are included in Fig. 6.6. Distinct regions of Ti-rich and Al-rich phases are observed. It also indicates that diffusion of aluminium has occurred from the periphery of Ti particles and a layer of aluminium rich phase is formed at the periphery (Fig. 6.6). Presence of Cr atoms is seen to be uniformly distributed (Fig. 6.6). Nb atoms are found to be present in localized area, which is due to relatively larger size of Nb particles and low diffusivity of Nb. Distribution of boron in specific alloys is also found to be nearly uniform. A mixed image of elemental mapping (Fig. 6.7) clearly represents the distribution of various elements.

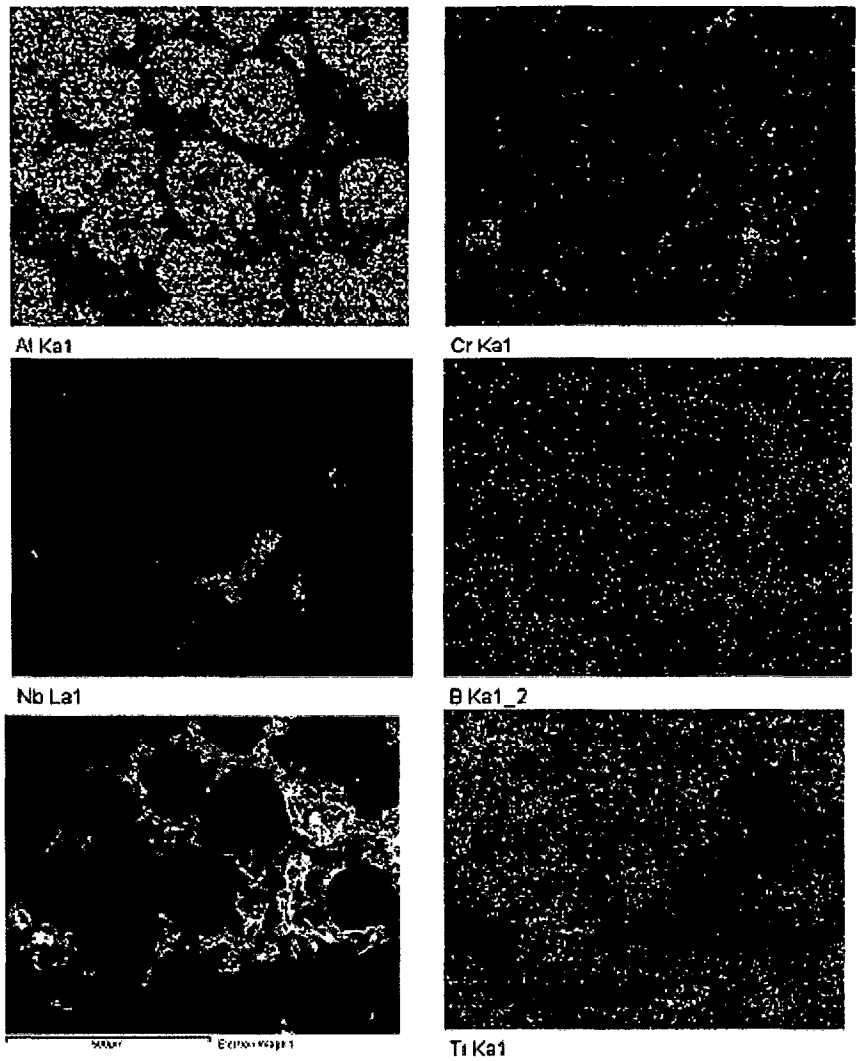

Fig. 6.6: SEM elemental mapping of a typical RS sample (*A2*) showing distribution of Ti, Al, Cr, Nb and B

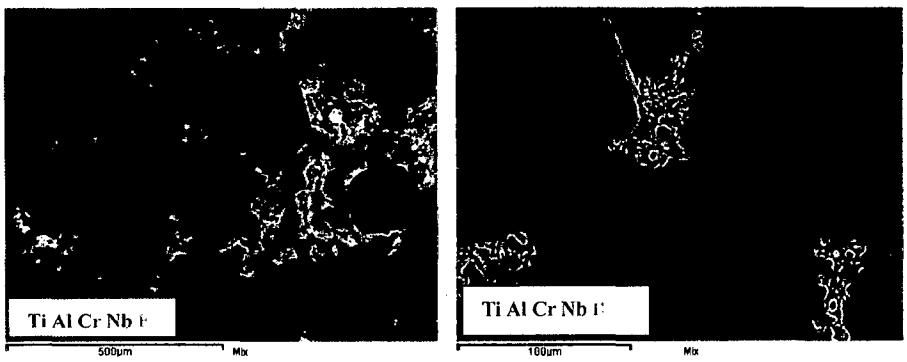

Fig. 6.7: Mixed image of SEM elemental mapping of a typical RS sample (*A2*) showing distribution of Ti, Al, Cr, Nb and B

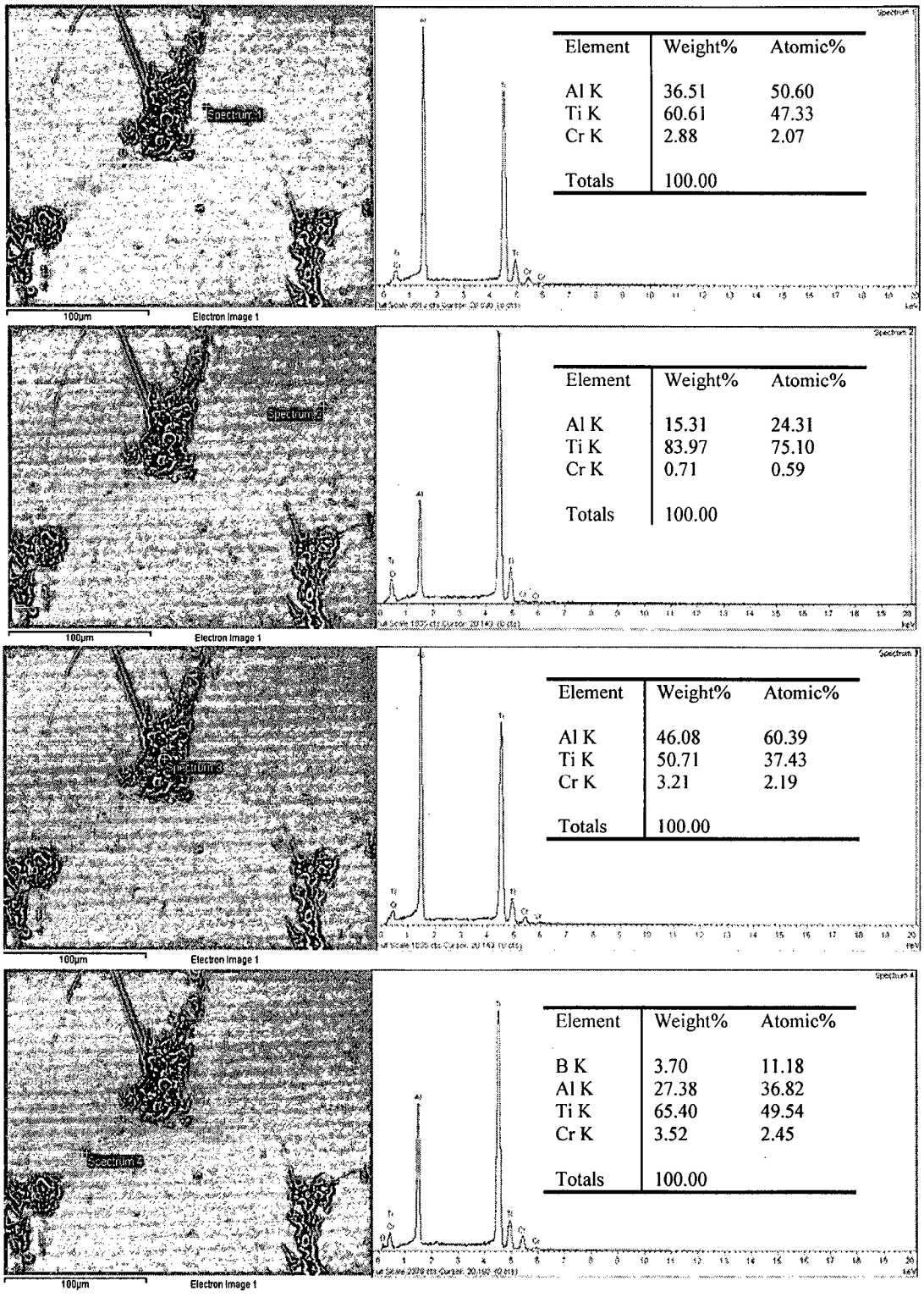

Fig. 6.8: SEM elemental mapping and EDAX of a typical RS sample (alloy *A2*) showing distribution of Ti, aluminium, Cr and B

Further, EDAX of reaction synthesized samples also confirmed the formation of aluminium rich annular rings on the Ti particles (Fig. 6.8) and limited diffusion of aluminium atoms to Ti particles. It has also shown the presence of Cr, whereas Nb atoms could not be observed. It means diffusion of Nb atoms has not been completed during reaction synthesis. This is due to relatively lower temperature of reaction synthesis for Nb diffusion and also larger sizes of Nb particles.

Elemental concentration at various regions of RS sample (Fig. 6.8) shows aluminium rich phases in the outer boundary of the Ti particles (Spectrum 3) and Ti rich phases in the inner boundary of Ti particles (Spectrum 2). Progressive diffusion of aluminum from the periphery of Ti particle can be clearly seen (Spectrum 1 and 3).

Elemental mapping of alloys (*A4-A5*) with smaller Ti particle sizes is presented in Fig. 6.9. It is observed that, diffusion of aluminium has taken place inside Ti particles. Presence of elemental Ti has been detected here also as observed in case of alloy *A1-A3*. Since reaction synthesis process parameters were same for these alloys also, extent of diffusion of aluminum is same according to Fick's law. However, since Ti particle size was smaller, remaining area in the Ti particle is less, where aluminium diffusion has not been detected. It means diffusion of Ti during further processing shall be taking lesser time in completing the homogenization (γ and α_2 aluminide formation).

Homogenization response of various alloys was observed to be in line with optical microscopy. The elemental mapping for the partially homogenized and completely homogenized sample is presented in Fig. 6.10-6.11 respectively. Typical microstructures of homogenized samples are presented in Fig. 6.12.

From Fig. 6.10, it is observed that, diffusion of Nb has not been completed, which is not seen in point analysis of sample. From the elemental mapping of RS alloy (Fig. 6.6.) and partially homogenized alloy (Fig. 6.10), it is clearly seen that, Ti, Al, Cr elements are uniformly distributed in later case and Nb atoms have started diffusing. But, for the same amount of time, alloy *A4-A5* shows completion of diffusion (Fig. 6.11). Homogenization is found to be completed in these alloys and presence of lamellar structure is noted (Fig. 6.10c-d), which is due to higher temperature exposure of the alloy during homogenization.

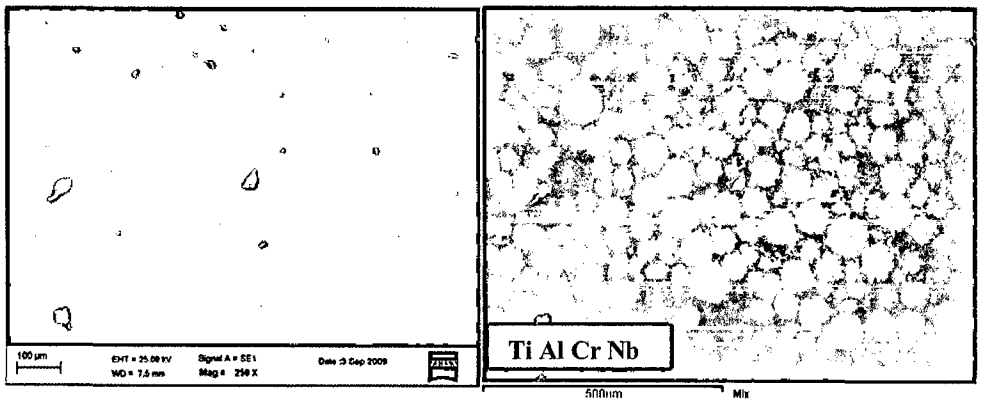

Fig. 6.9: SEM elemental mapping of a typical RS sample (of smaller Ti particle) showing distribution of Ti, aluminium, Cr, Nb and B

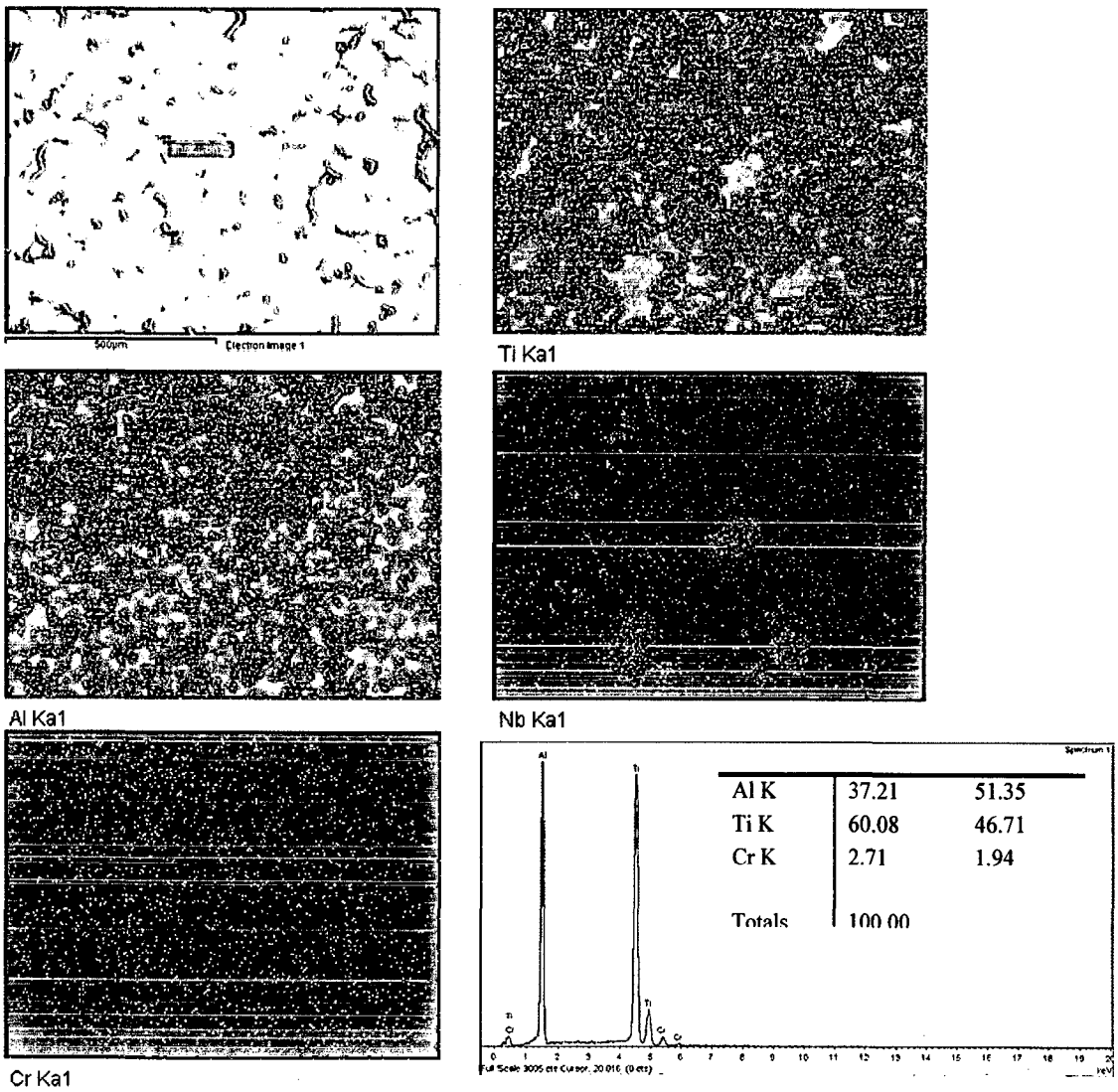

Fig. 6.10 : Elemental mapping with larger Ti particle size partially homogenized alloy (alloy *A1*)

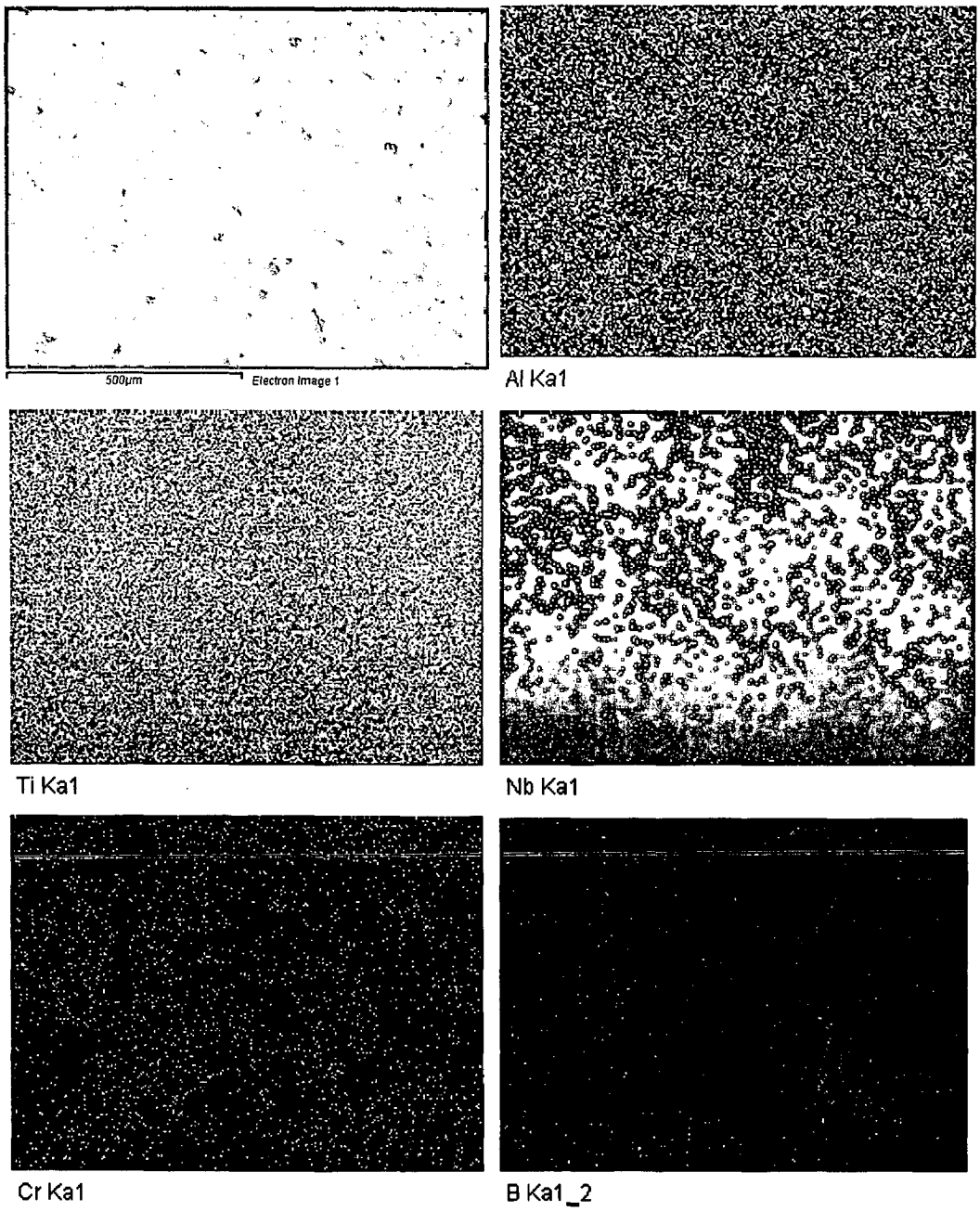

Fig. 6.11 : Elemental mapping with smaller Ti particle size homogenized alloy (alloy *A4*)

From Fig. 6.10, it is observed that, diffusion of Nb has not been completed, which is not seen in point analysis of sample. From the elemental mapping of RS alloy (Fig. 6.6.) and partially homogenized alloy (Fig. 6.10), it is clearly seen that, Ti, Al, Cr elements are uniformly distributed in later case and Nb atoms have started diffusing. But, for the same amount of time, alloy *A4-A5* shows completion of diffusion (Fig. 6.11). Homogenization is found to be completed in these alloys and presence of lamellar structure is noted (Fig. 6.12c-d), which is due to higher temperature exposure of the alloy during homogenization.

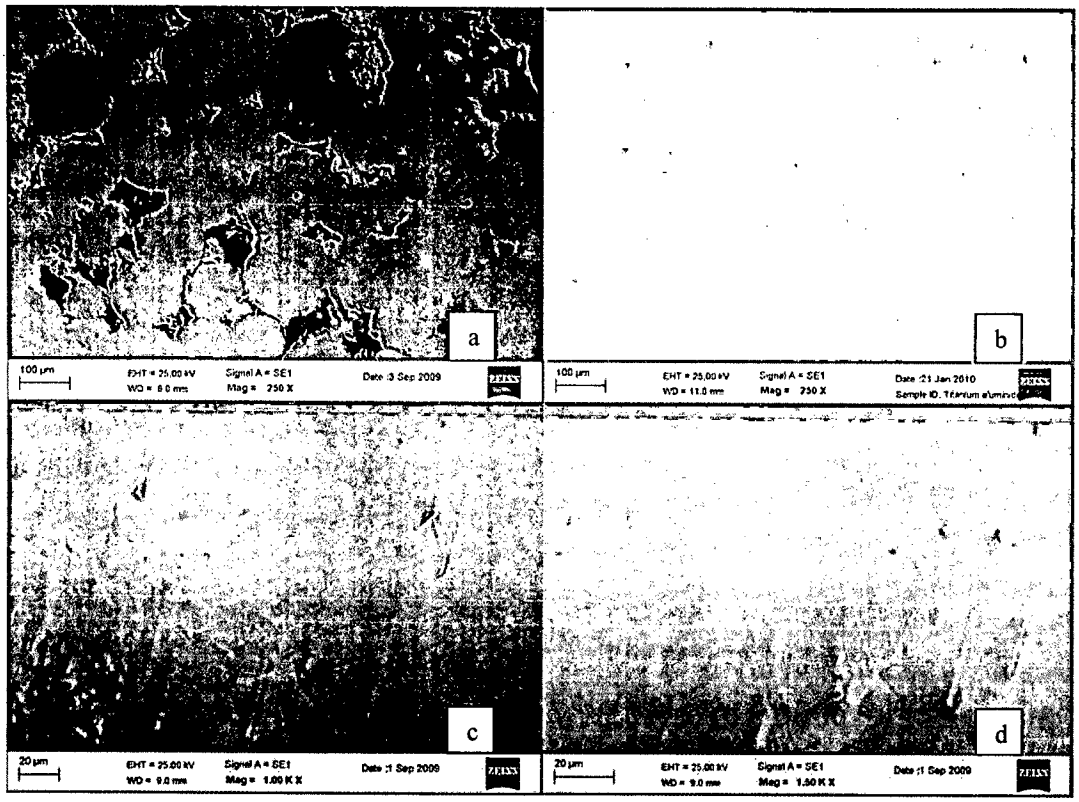

Fig. 6.12: Typical SEM photomicrograph of homogenized samples (a) with larger Ti particle (alloy *A2*), (b) with smaller particle size (alloy *A5*), (c&d) at higher magnification with larger particle size (alloy *A2*).

6.4.5 X-Ray Diffraction (XRD)

The XRD plots of typical RS and homogenized alloy samples are presented in Fig. 6.13-6.14. It is observed that, Al rich phases Al_3Ti and Ti rich phase TiAl alongwith unreacted Ti atoms are present in as reaction synthesized samples. Transient phases like Al_5Ti_2, Al_2Ti, Al_5Cr etc. are also present in some of the alloys. Weak peaks of Ni_2B compound was detected in XRD of RS alloy *A5*, indicating small content of this compound. Comparing the alloys *A1-A3* to *A4-A5* (smaller Ti particle) alloy, Ti rich Ti_3Al phase is also formed in the *A4-A5*, indicating reactions further move forward towards Ti rich phases. It is due to use of smaller size Ti particles, where diffusion distance required for aluminium is less in alloys *A4-A5*.

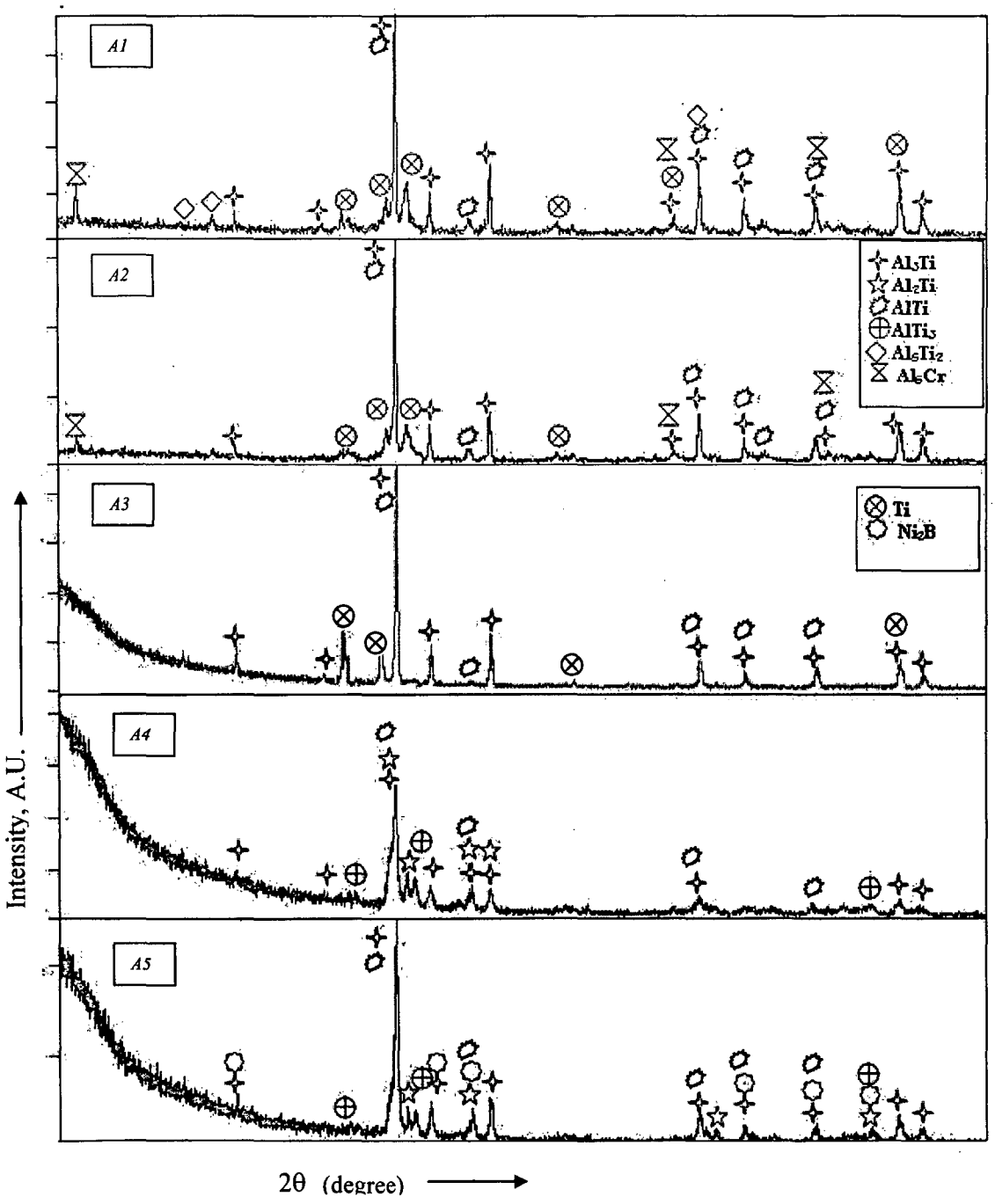

Fig. 6.13: XRD plot of RS billet samples, *A1, A2, A3, A4, A5* for respective alloys *A1-A5.*

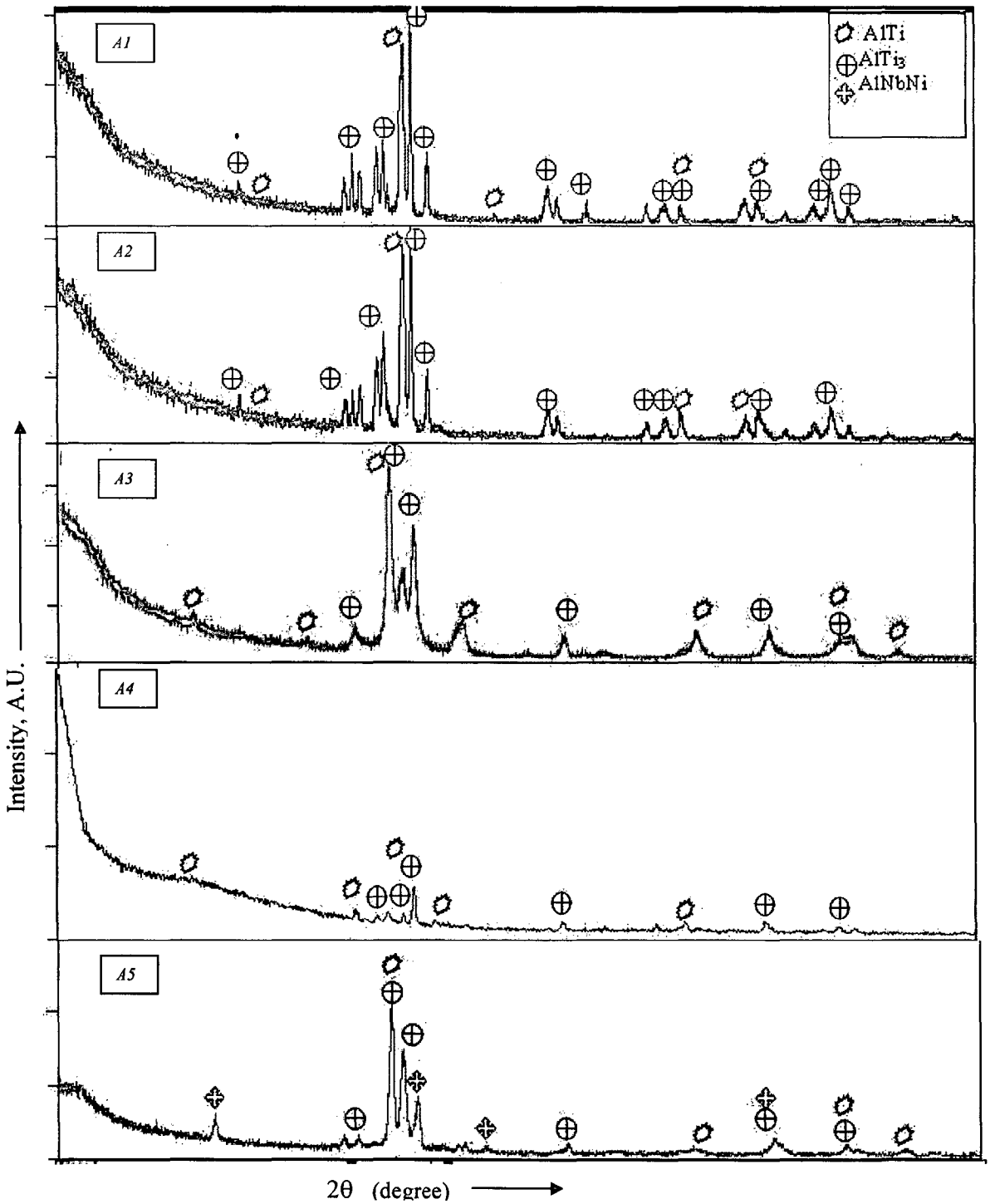

Fig. 6.14: XRD plot of homogenized billet samples, *A1, A2, A3, A4, A5* for respective alloys *A1-A5*

After homogenization, all the alloys have Ti rich aluminide phases Ti_3Al and TiAl only. Cr, Nb, Ni containing phases was not found in homogenization except weak peaks of AlNbNi (in alloy *A5*). It means either these elements are dissolved or present in compound form in very small content, below that possible to detect through XRD.

Table 6.7: Summary of phases in various alloys

Alloy	Process stage	Phases obtained through XRD
A1	As RS	Al_3Ti, Al_5Ti_2 , AlTi, Ti, Al_5Cr
	Homogenized	AlTi, $AlTi_3$
A2	As RS	Al_3Ti, AlTi, Ti, Al_5Cr
	Homogenized	AlTi, $AlTi_3$
A3	As RS	Al_3Ti, Ti, AlTi
	Homogenized	AlTi, $AlTi_3$
A4	As RS	Al_3Ti, $AlTi_3$, Al_2Ti, AlTi
	Homogenized	AlTi, $AlTi_3$
A5	As RS	$AlTi_3$, AlTi, Al_2Ti, Ni_2B
	Homogenized	AlNbNi, AlTi, $AlTi_3$

Based on the XRD analysis, it is seen that complete phase transformation occurs in two stages namely RS and homogenization. In the RS stage Al_3Ti forms which reacts with Ti and during homogenizing treatment it leads to formation of stable TiAl plus Ti_3Al phases. Thus, it is confirmed by XRD that, all the aluminum atoms have formed intermetallic compounds and free aluminium atom was not available after RS. Therefore, formation of γ and α_2 phases shall be possible by reaction between Al_3Ti and remaining Ti atoms. The phase formation sequences is schematically shown in Fig. 6.15, which explains formation of liquid aluminium envelope around the Ti-particle leading to Al_3Ti phase formation which gets homogenized and results in stable TiAl plus Ti_3Al phases. This is in line with earlier reported work *[87, 247, 262, 266]*.

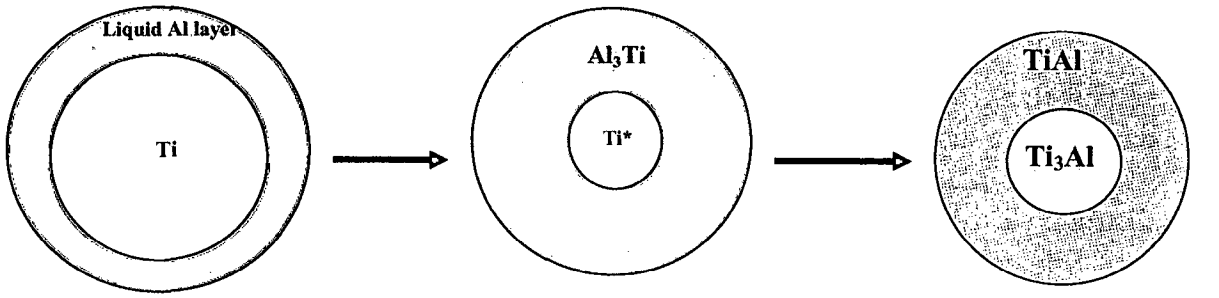

*small amount of Ti rich aluminides (TiAl and Ti_3Al)

Fig. 6.15: Schematic diagram showing various stages of phase formation in ternary and quaternary samples.

6.4.6 Transmission Electron Microscopy (TEM)

The TEM micrographs from two different regions of the reaction synthesized sample were observed (Fig. 6.16). The phases in the as–pressed samples are observed to be Al_3Ti, Ti, TiAl, Ti_3Al in alloy *A1* and additionally TiB_2 in boron containing alloys (*A2-A5*). This indicates that Ti rich phases may be simultaneously formed in RS, which are so small to be detected through XRD. SAD pattern of typical phases AlTi, Al Ti_3 and TiB_2 as seen in RS specimen is presented in Fig. 6.17.

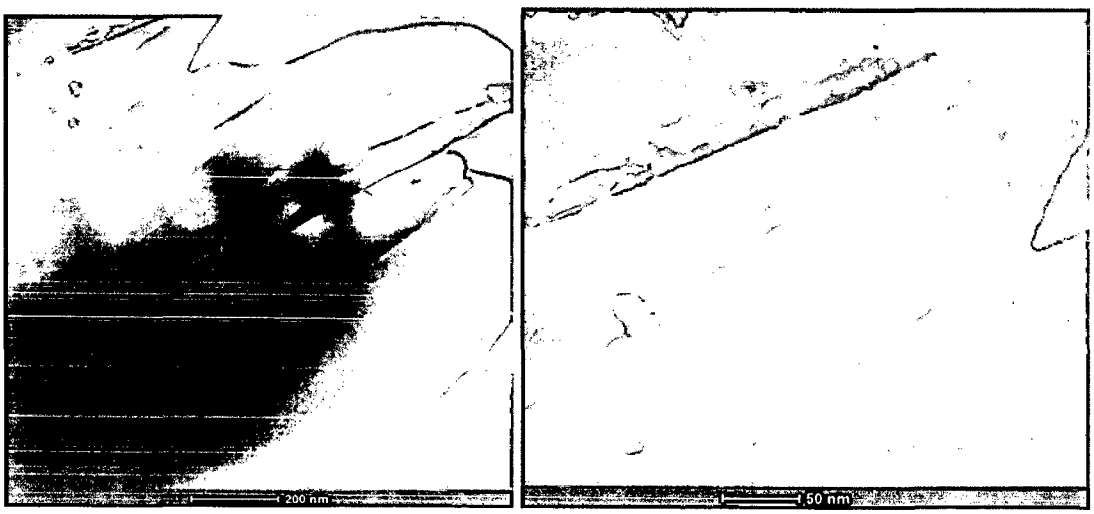

Fig.6.16: TEM micrograph of RS sample (alloy *A2*) from a region showing lamellar structures

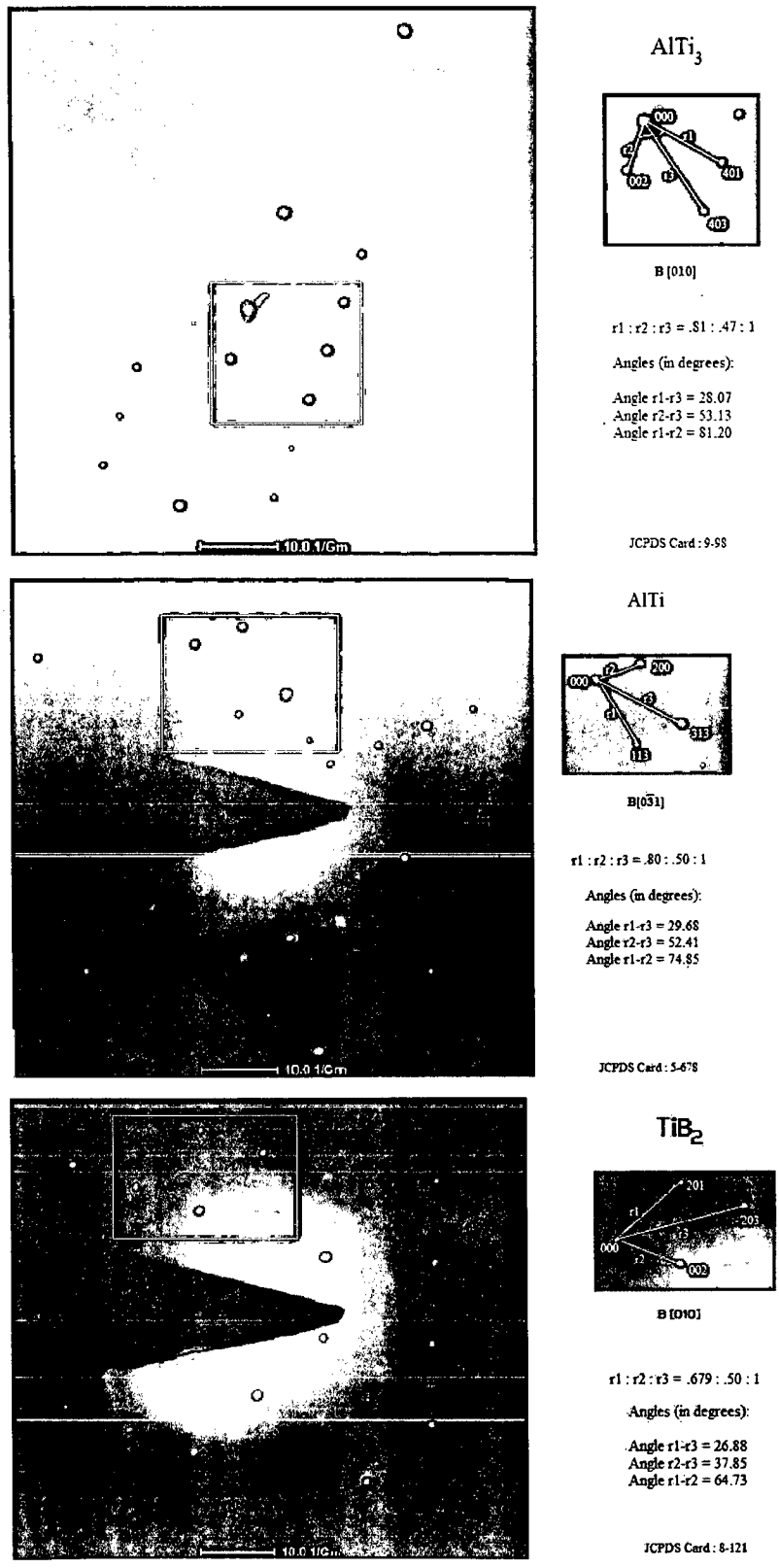

Fig.6.17: SAD pattern of TEM micrograph (RS sample) from a region shown in Fig. 6.16 (lamellar phases) confirming presence of $AlTi_3$, TiAl and TiB_2 in different projections

The width of γ lamellae in the alloy is found to be about ~140 nm whereas α_2 lamellae has width of about ~80 nm as seen from Fig. 6.16. In comparison, the α_2 lamellae width for sample is 150 nm and width of γ lamellae is about 180 nm for binary alloy *[87]*. Thus, it is observed that lamellar width for the present sample is finer as compared to the binary sample *[87]*. This lamellar refinement is attributed to lowering of the α to lamellar transformation temperature due to Cr addition *[129, 176]*. Similar observations have been obtained in homogenized samples.

6.4.7 Homogeneity analysis of billets (Microhardness and Phase distribution through optical and SEM/EDAX)

This study is carried out to ascertain the homogeneity of larger samples as the cross section of the RS billet under study (dia. 75 mm) is relatively larger than normal laboratory scale samples. The locations of hardness measurement (points marked at an interval of 7 mm starting from one edge of the billet) are shown in Fig. 6.18. Micrograph showing microhardness impression is shown in Fig. 6.19. Hardness and microhardness results are presented in Table-6.8 and 6.9.

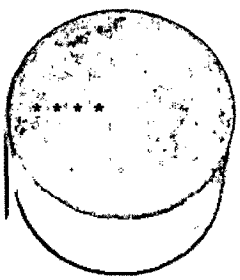

Fig. 6.18: Location of hardness measurement in RS and homogenized samples

It is observed from Table 6.8 that, Vickers hardness varies from 138 to 180 Hv for the alloy billets in RS condition and 160-240 Hv in homogenized condition. However, for the specific alloy, the variation of hardness is found to be in a quite narrow band, where higher hardness is derived from the regions containing more lamellar phase whereas lower band of hardness is due to γ phase rich regions.

Fig. 6.19: Microhardness of RS and homogenized samples, (a) RS alloy *A1*, (b) RS alloy *A2*, (c) homogenized alloy *A1*, (d) homogenized alloy *A2*, (e) RS alloy *A5*, (f) homogenized alloy *A5*

However, this range of hardness is very low for the aluminides even the hardness of individual phases are high (Table 6.9), as obtained in microhardness results. This is due to presence of porosity in the alloy in RS as well as in homogenized condition. In the later case, some improvements in the hardness is noted, which is due to formation of Ti rich phases containing lamellar phase of ($\alpha_2+\gamma$).

Table 6.8: Hardness of RS and homogenized sample phases

Alloy	Hardness, Hv	
	RS	Homogenized
A1	138-156	160-180
A2	146-160	172-200
A3	142-158	180-210
A4	160-180	210-240
A5	160-175	220-240

The microhardness measurement carried out at different points in a region of optical microstructure show, hardness of RS alloy *A1-A3* in different locations has marginal difference with highest microhardness for location 1 (Fig. 6.18 a, b). This indicates presence of Ti rich compounds at the centre of the grain. Along the periphery of the particles porosity is present, which reduces the microhardness of the peripheral phases. However, RS alloy *A4-A5* has relatively higher microhardness as compared to the alloy *A1-A3*. This is due to use of smaller Ti particle in RS, where diffusion of aluminium to the cross section makes Ti rich aluminides during RS process itself.

Significant increase in microhardness at all the locations has been noted after homogenization, which indicates the presence of Ti rich phases (Table 6.9). Again, maximum microhardness is obtained in location 1 (homogenized condition), which is for Ti rich aluminide regions (α_2 and γ). In location 2 i.e. periphery of particles, microhardness is marginally low, which is partly due to presence of porosity. Higher microhardness i.e. of the level of ~600 Hv indicates formation of α_2 phases, hardness ~500Hv indicates lamellar

phases and 450-500 Hv indicates presence of γ phase regions *[166, 167]*. Similar observation made by Lee at al. showed that the microhardness of α_2 is always higher than that of either γ or α_2/γ lamellae *[64]*. Therefore, from the above, it is clear that after homogenization, aluminide consists of mainly two phases γ and α_2.

Table 6.9: Microhardness of RS and homogenized sample phases

Alloy	Microhardness, Hv in Location				
	RS			Homogenized	
	1	2	3	1	2
A1	240	220	200	550	418
A2	275	210	190	650*	500
A3	200	--	180	560	480
A4	300	400	--	680*	520
A5	340	250	320	640	580

1: Inside the grain/ particle, 2: Inner Boundary of grain/ particle, 3: Intergranular area
*lamellar grains

6.4.8 DSC evaluation of homogenized alloys

The homogenized alloy samples were analyzed through DSC technique to confirm the completion of aluminide reactions and to evaluate the transition temperatures of aluminides. The DSC results of alloy samples taken are shown in Fig. 6.20.

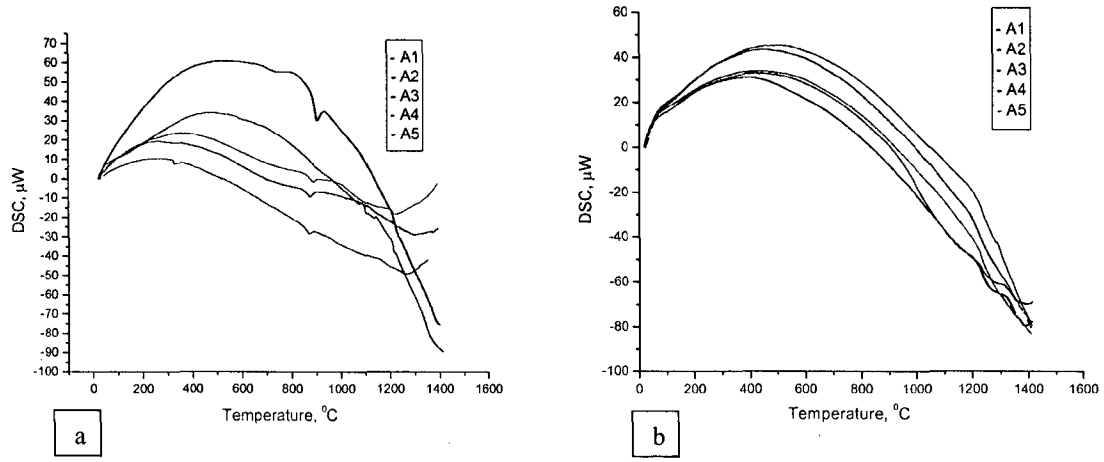

Fig. 6.20: DSC plots for samples taken from two different conditions of billet, (a) as reaction synthesized and (b) after homogenization.

As seen from Fig. 6.20, the endothermic reaction point of the RS sample is ~875^{0}C. It indicates transformation of alloy is not completed. Although this temperature range is for transformation of Ti element from α phase to β phase, small traces of low melting compound rich in Al cannot be ruled out. And, this is the reason for incorporating two stage homogenization (section 6.3). It means after RS, alloy contains some amount of Ti in element form. The same has been confirmed through XRD also. On comparing the DSC plots for RS and homogenized sample, it is observed that such endothermic point is not present in DSC of homogenized alloy. Second peak in RS sample is seen at temperatures ~1277^{0}C in alloy samples *A1*, *A2* and *A4*. This endothermic peak indicates phase transformation of (α+γ) phase to α phase *[232, 290]*. But for alloy *A3* and *A5* endothermic peak is observed at higher temperatures i.e. ~1375^{0}C. Since this temperature is near to upper limit of instrument, clear indication of peak is not seen. These alloys contain very small amount of Ni (as coating on boron powder). Therefore, two possibilities arise for this temperature. One is formation of some intermetallics of Ni alongwith aluminides and second is formation of β phase (from α phase). XRD also could not detect clearly the Ni containing phases since Ni content in alloy is too low to be detected by XRD. It requires further study with more number of samples to confirm the phase formation. However, present results indicate that alloy *A3* and *A5*, which contain some amount of Ni-P has definite role in affecting the transition temperatures.

In case of homogenized alloy, only single endothermic reaction is seen at ~1375^{0}C. In this case also, due to limitation of instruments, exact transition temperature could not be obtained. But it confirms that, there in no melting till this temperature and therefore alloy is in desired phase which can be utilized for high temperature applications. XRD of samples after DSC (RS and homogenized samples of all the alloys) have shown only TiAl and Ti_3Al phases. This is in expected lines, since samples were (RS as well as homogenized) heated beyond single phase α region and after cooling the alloy transformed to Ti rich aluminides.

6. 5 DISCUSSION

6.5.1 Selection of process parameters

From the above results, it is inferred that, material in reaction synthesized condition is inhomogeneous, porous, with less theoretical density and has predominantly aluminium rich phases. Swelling observed during RS is also closely related with porosity. Some of these are improved during homogenization treatment, where Ti rich phases form. However, porosity and density of alloy does not change by homogenization treatment.

Understanding the pore formation is very important to minimize it. Its generation sequence is proposed as follows. The first solid state reaction during heating occurs between pure Ti and aluminium powder particles. From this reaction, layers of transient phases form at the contact area of particles. The chemical composition of the major transient phase is $TiAl_3$. Simultaneously, some particles of pure aluminium away from the solid reaction zone melt as the temperature increases during continuous heating and initiate liquid solid reaction. The solid-solid reaction as well as liquid solid reaction both yields the transient phases, which are the main exothermic reaction between pure Ti and aluminium. As the temperature is raised to the T_{peak}, the major exothermic reaction is two-fold, between pure Ti and aluminium powder particles and between the transient phases and pure Ti. During the latter mode of reaction, pure Ti is embedded inside the layers of the transient phases. In this configuration, aluminium, having greater mobility, diffuses towards Ti in the core, faster than Ti in the opposite direction, leaving pores in the transient phases.

It has been observed in the present study that, pores are mainly present around the Ti particles i.e. at the previous aluminium sites (Fig. 6.4-6.8). The phenomenon of pore formation is due to the difference in physical properties of Ti and aluminium, and their interaction with each other *[5, 199, 211]*, unbalanced diffusion rates and solubility. Even though interdiffusion between the two reactive elements is quite rapid, it is still slower than

the self diffusion of the aluminium in liquid. As a result, excess vacancies will accumulate at the grain boundaries on the aluminium side. It has been reported that, $TiAl_3$ formation is extremely exothermic, which can heat the local material above the melting point of $TiAl_3$. At this point the remaining Ti react as $2Ti+TiAl_3$ 3TiAl. This reaction is also exothermic. Thus, the local temperature could be above 1460^0C, the melting point of TiAl *[63]*. However, due to heat loss to the surroundings, melting of aluminides is limited. Simultaneously, the compact is expected to densify during reactive sintering due to enhanced diffusion in the liquid, and because of liquid pulling all the particles together in a capillary action (regrouping) *[292]*. However, it does not densify, but swells during this process, due to Kirkendall effect. Also, the difference in CTE of the intermetallics causes stresses to be set up between each intermetallic, resulting in cracking, which increases swelling. Also, for Ti-Al system, heat of reaction increases monotonically with aluminium content (from 0.2 to 0.6 atomic fraction) *[253]*.

Using small powder particles, improvement in sintering process has been observed but, swelling of compacts still occurred. Pearl Lee Sullivan (1993) *[293]* and Savitski *[205, 206]*, reported that larger particle size of powders increase the amount of swelling during reactive sintering. When the particle size is large, the resultant pore size is also significant. Effect of aluminium particle size is not as significant as those of Ti. Liquid aluminium makes good contact with reactant particles *[252]*. Larger particles requires high ignition temperatures and result in lower peak temperatures, because of increased heat loss due to lower heating rate and in some cases due to incomplete reaction. Particle size also affects the volume change between the reactant and the product. Ti of 76 to 106 μm mixed with aluminium particles of ~45μm gave the max volume shrinkage. Change in Ti particle size affects combustion temperature also. For example, from smaller than 45 to 150μm combustion temperature decreases significantly. This is due to larger particle size results in more heat dissipation and hence greater deviation from an adiabatic reaction *[294, 295]*. Concentration of gases increases with the powder particle size (Ti aluminide produced by gas atomization of the melt). Therefore, use of small size powder particle is very important from this point of view also. From Fig. 6.12, it is observed that relatively more amount of porosity is present in alloys made with larger size of Ti particles (Fig. 6.12a) as compared to the alloy with smaller size Ti particles (Fig. 6.12b).

Oddone and German (1989) *[292]* reported, other than aluminium melting at 660^0C followed by aluminide formation, another exothermic reaction is observed at 1340^0C, where

$TiAl_3$ becomes unstable, reacts with Ti rich TiAl and Ti_3Al and transform to TiAl. Also, one more reaction is seen at 880^0C, which correspond to alpha to beta phase transition of Ti. The dilatometer results show that the compact begins to swell at 660^0C and remains steady upto ~850^0C.

As per another explanation, after reaction of the molten aluminium with Ti, diffusion is inhibited by the intermetallic shell and homogenization of the compact is prevented. The reaction involving the transformation of Ti from hcp to bcc structure apparently increases the diffusion in the compact and, thus, contributes to greater homogenization. Unfortunately, when Ti transforms into a bcc, the molten aluminium reacting with the Ti is already complete. Therefore, the increase in diffusion after the transformation of Ti into BCC is only a solid state reaction and is slow. In an effort to combine both of these reactions to benefit from the increased diffusion rate of the bcc Ti during a liquid state reaction, beta stabilized Ti is used and noted that reaction was more complete and diffusion barrier was not established. Increased rate of densification is also attributed to hcp to bcc reaction where drop in activation energy for volume diffusion in TiAl was seen *[292]*.

To minimize the porosity, two methods i.e. heating rate control and extended soaking treatment were suggested *[64]*. Slow heating allows longer heating reaction time, resulting in greater amounts of transient phases. In the slow heating regime T_{onset} increases more sensitively with heating rate than T_{peak}, which widens the gap between these two temperatures. Fast heating rate increases the amount of TiAl and Ti_3Al but decreases that of $TiAl_3$ and pure Ti. Thus, fast heating minimizes the amount of transient phases because it reduces the extent of the solid reaction prior to the main exothermic reaction. Another heat treatment method effective for reducing the amount of transient phases is to soak for a sufficient time above the T_{peak}. In an experiment of Ti46.6Al1.4Mn2Mo heat treated to 1000^0C, amount of transient phases decreased steadily with holding time *[216]*. Increasing the soaking temperature removed the transient phases at higher rate. Effect of soaking treatment on porosity was also encouraging. Samples heated to 1000^0C at a rate of 5^0C/ min, held for more than 160 min. showed decreased porosity significantly *[216]*. Considering the fact that fast heating rate produces large quantity of liquid aluminium and also process control is complex, slow heating rate of 10^0C/ min was selected, which was followed by holding at reaction temperature.

Similarly, sintering temperature also alters the Ti_3Al microstructure. The higher the temperature, the greater the amount of TiAl. At the lower temperatures, large voids occurs in

the centre of Ti_3Al regions. As the sintering temperature increases, these voids are closed. The density increases with increasing sintering time approach to full density *[63]*.

Complete elimination of porosity in RS/ homogenization stage is not possible; however, it can be controlled by selection of optimum process parameters like heating rate, soaking time, heating temperatures, powder particle size, use of β stabilizer etc.

Application of pressure like, hot isostatic pressing is another important factor, which has been used successfully to densify the TiAl compound. By controlling the RS hot pressure conditions, it is possible to control the sample density and TiAl/ Ti_3Al phase ratio. Density can be increased with increasing maximum temperature and pressure and or/ sintering time *[63]*. It has been reported *[296]* that, the molar volume change during the reaction to form Al_3Ti from aluminium and Ti to be 5.6% (estimated from their theoretical densities). Thus, external pressure would help to densify the synthesized Al_3Ti at high temperature *[296]*. The pressure applied during the reactive sintering, i.e. the hot pressing, produces a nearly fully dense net-shape product consisting of TiAl and Ti_3Al. However, simultaneous application of load may also reduce the onset temperature and faster ram speed reduces the heat loss to the tooling, which results in increase in the likelihood of melting. It is therefore necessary to know for the formation of a critical quantity of liquid before application of load *[33]*.

In the present work, moderate heating rate 10^0C/ min, use of pressure before and after the reaction (around hcp to bcc transformation temperature), use of Nb (β stabilizer), use of appropriate Ti particle size etc. has been considered to obtain the cumulative best results of RS. However, porosity could not be brought down due to relatively lower heating rate, lower pressure for compaction (post reaction synthesis) and relatively larger Ti particle size (in alloy *A1-A3*). This study brings out that there is a definite role of all these parameters irrespective of amount of pressure. Nb is helpful in the diffusion of Ti during RS. Cr and B do not have any significant role during RS, however they form compounds like Cr_2Ti and TiB_2 useful for grain refinement in further processing. Very small amount of Ni-P (as coating over boron) has some important role in densification, which makes the alloy to follow the polynomial characteristics during subsequent HIPing and hot isothermal working. This may be due to formation of Ni based intermetallics alongwith boron helping in densification through grain boundary cohesion *[297]*. Also, application of pressure during this transformation reaction will further enhance the reaction kinetics. Therefore, pressure application should be around this temperature and the same has been followed in the present work.

In presence of boron, the process of aluminide formation at reaction is modified. Smaller size of boron present in the interstices of Ti-Al also participates in reaction and simultaneously forms borides alongwith aluminides and decreases the diffusion process during RS and homogenization. This can be schematically represented by Fig. 6.21. Also, simultaneous application of pressure has been envisaged to accelerate the kinetics of reaction by increased interface contact. However, application of pressure, before and after the reaction contributes to some extent.

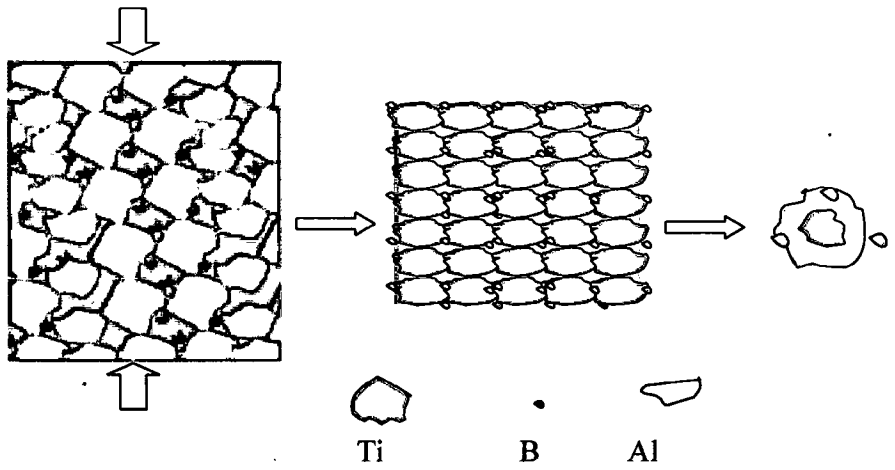

Fig. 6.21: Schematic diagram showing role of boron during reaction synthesis

6.5.2 Chemistry, Microstructure and property correlation

Although the present experimentation was carried out after considering all the factors mentioned in section 6.5.1, loss of alloying elements were noted by spillage of viscous reaction product, which also governed the microstructure, properties and homogenization response of the alloys. Alloys were aimed to have aluminium between 46-48 at%, which has been achieved, but loss of Nb has been noted (which was aimed to have near 2 at%). Also, gases content has been very high. This level of gas content has also contributed in increasing the porosity. Although compounds with gases have not been detected in XRD, gases at this level shall be forming oxides and nitrides, which will have negative effect on ductility of alloys. This level of gas content could have come partly from processing atmosphere and partly from the initial powder. Although high purity powders and vacuum processing were used, it was found to be insufficient to control the gases.

Present experimental cycle (loading and heating) cycle has been found to be optimum to control the spillage of viscous products. Further, it has been observed that, microstructures are also a function of processing parameters. Most of the porosities were found to be present in the intergranular region. It is also noted clearly through SEM that, larger Ti particle size alloys have higher porosity as compared to smaller Ti particle size alloy (Fig. 6.12). Cumulative effect of gas porosity and Kirkendall porosity is responsible for the density achieved in the present work. The alloys made through this method, can be used only after further processing like, after hot isothermal pressing, which shall bring down the porosity level.

Microstructure clearly reveals the presence of duplex type structure ($\alpha_2+\gamma$) after homogenization. It is an important microstructure, however, content of individual phase is also important, which can be achieved after further processing and heat treatment. Observations made through optical microscopy, SEM, EDAX, TEM, XRD etc. are all complimentary, which confirms the sequence of aluminide phase formation as discussed in section 6.5.1. Microhardness measurement made on the homogenized sample also confirms the presence of various phases and homogeneity of the alloys. Elemental mapping has been very useful in confirming the homogeneity of the alloy and optimizing the homogenization cycle. Vickers hardness results are indicative only, which confirms that property variation across the cross section of the billet is not present. Further processing is required to evaluate the mechanical properties since porosity level needs to be brought down to obtain the reliable properties. DSC studies of RS and homogenized alloys show the transformation temperatures and confirm the absence of elemental content in the alloys after homogenization.

6.6 SUMMARY

Reaction synthesis of Ti48Al2Cr2Nb, ($\alpha_2+\gamma$) alloy has been carried out with minor addition of boron and Ni-P coated boron alongwith using two sizes of Ti powder (200μm and 50μm average). Optimum heating and loading cycle has been selected after trial experiments and using guidelines of DSC studies. Only minor loss of alloying elements (1-2%) has been observed in reaction synthesis (RS) due to spillage of viscous reaction products. Chemistry of the alloys is found to be within the aimed composition. Gas content was found to be higher, which can be partly due to processing/ handling and partly due to purity of initial powder. Alloy products near to full theoretical density have been obtained.

The RS samples were found to be inhomogeneous and contain Al_3Ti as the major phase as seen by microscopy and XRD characterisation. Diffusion of aluminium from periphery of Ti particles to center of Ti particles has been observed through microscopy, making annular type pattern of aluminium rich aluminide at outer periphery of Ti particles and Ti rich regions at the centre of Ti particles. Width of aluminium rich annular region is found to be between 15-30μm, where boron containing alloys have relatively lesser width. Grain size of homogenized alloys is found to be according to grain size at RS stage as well as according to use of Ti particle size. Marginal growth of grain is seen in case of boron free alloy (*A1*).

RS samples were homogenized at 1250^0C for different soaking times (12-20 hrs.) depending on the alloys. Stable phases like TiAl and Ti_3Al were observed in the homogenized samples through XRD. Microstructures consisting of lamellar (γ plus α_2) and γ grains has been observed for all the alloys through optical microscopy and TEM.

Average Vickers hardness values for alloys produced by RS are found to be 138-180, which increased to 160-240 Hv after homogenization. Lower hardness is due to porosity content in the alloy at this stage. After homogenization, homogeneity of chemistry, properties and microstructures across the cross section of billet (dia 75mm) were confirmed. Homogenized alloys have shown transformation temperature ($\alpha+\gamma$ to α) around 1375^0C as obtained through DSC of homogenized samples.

Significant effect of boron addition (0.1 at%) and Ni-P coated boron addition (0.1 at%) on reaction synthesis characteristics were not found. However, it has been noted that it inhibits grain coarsening during homogenization. Boron containing phases Ni_2B (through XRD) and TiB_2 (through TEM) has been detected. It has been observed that, boron containing alloys took longer time and alloys made with smaller Ti particle took lesser time in homogenization. Formation of TiB_2 phase is observed to be forming in RS stage simultaneous to aluminide formation as confirmed through TEM.

Effect of Ti particle size on reaction synthesis is clearly seen by the presence of Ti rich aluminides (TiAl) in the RS stage itself for alloys (*A4-A5*) where smaller size of Ti powder particles are used. Use of smaller size Ti particle resulted in relatively higher density in RS due to better compaction.

Ni-P coated alloys (*A3* and *A5*) shows polynomial relation in increasing density of alloy from RS to hot deformation stage whereas all other alloys (*A1, A2, A4*) shows linear increase in density.

Chapter-7

DEFORMATION STUDIES – I
HOT WORKING AND FLOW CURVE

7.1 INTRODUCTION

The understanding of deformation behaviour of Ti aluminide alloy processed through powder metallurgy (PM) route has great importance to design the hot working parameters to obtain desired microstructure and properties. Only a limited studies have been reported on hot workability of PM alloys; Nieh et al. (1999) studied superplastic deformation behaviour of a powder metallurgy TiAl alloy with metastable microstructure *[298]*; Wegmann et al. (2002) examined high temperature mechanical properties of hot isostatic pressed and forged alloy powder *[299]*; Gerling (2004) et al. analyzed the structural characterization and tensile properties of a high niobium containing TiAl sheet obtained by powder metallurgy processing *[300]*. These studies have indicated that, flow behaviour of Ti aluminide is complex, and the hardening and softening mechanisms are significantly affected by the temperature and stain rate.

Since, the intermetallic TiAl compound has poor ductility, conventional thermomechanical processing is extremely difficult. Therefore, isothermal and near isothermal (near conventional) working are usually adopted. Isothermal deformation is an effective method of working in plastic zone of materials under low flow stress and without abrupt cooling, where material can be worked at specific strain rates to impart the desired amount of deformation. Several studies have been reported in hot isothermal deformation of intermetallics *[26, 75-79, 223]*. However, there are no reported works on the deformation studies of γ Ti aluminides made through reaction synthesis route. This chapter aims to investigate the deformation behaviour of reaction synthesized alloys processed in the present study. Also, this study attempts to bring out the mechanisms of deformation of Ti aluminide under varying strain rate and temperatures. Studies with more practical approach were also conducted like, near isothermal forging in air to demonstrate the forgeability of the reaction synthesized alloys.

7.2 HOT DEFORMATION OF BILLETS

7.2.1 *HOT ISOSTATIC PRESSING (HIP)*

HIP was carried out under argon pressure of 100MPa at 1200^{0}C. Primary aim was to improve the density of reaction synthesized billets for further secondary processing. Photographs of HIPed billets are shown in Fig. 7.1. The billet shows outer layers have been oxidized, which may be due to small amount of oxygen present in argon used for HIPing. Improvement in density of various alloys is discussed in previous chapter (section 6.4.2), where improvement in density (upto ~ 2%) were observed. Microstructural study of the HIPed billets is presented in subsequent sections.

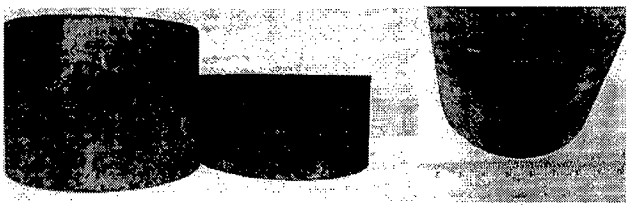

Fig. 7.1: Photograph of HIPed billets.

7.2.2 HOT ISOTHERMAL FORGING (HIF)

HIF, (described as isothermal forging process) was carried out under vacuum of 10^{-4}mbar at 1250^{0}C on the reaction synthesized plus homogenized billets. It was limited to upset forging only, where 50% deformation was imparted on each billets. Half of the billet was taken for HIF and other half was taken for other studies. Forged billets were furnace cooled under vacuum. Photograph of HIFed billets is presented in Fig. 7.2. Microstructural study of the HIFed billets is presented in subsequent sections.

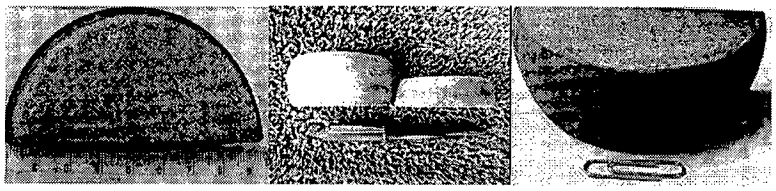

Fig. 7.2: Photograph of HIFed billets

7.2.3 HOT NEAR-ISOTHERMAL FORGING

The alloy has poor workability, therefore it can be best deformed under isothermal conditions. However, this limits the industrial processing of the alloy and its wider applications. Therefore, an attempt has been made to study the deformation of this alloy under near isothermal conditions. For this, two types of processes have been followed. One is through generation of near isothermal condition by pack forging in a capsule of Ti alloy and the other is through forging in ambient atmosphere with insulation of ceramic blanket. Effective deformation of 50% was imparted under the similar forging conditions. Photograph of the pack forged and ambient forged samples are presented in Fig. 7.3.

Fig. 7.3: Photographs showing (a) packed capsule for forging, (b) pack forged aluminides (arrow showing cracking at the edge), (c) near isothermal forged billet samples

Packing capsule was made in such a way as to avoid oxidation of the alloy through leak proof packing using electron beam welding. As homogenized billet samples were used for pack forging. The packed capsule was preheated at 1250^{0}C for 1hr. and upset forging was carried out using a 500 ton hydraulic press. After forging, packing was removed to get the forged aluminide. Cracks towards edges were seen (Fig. 7.3b), which are attributed to formation of brittle oxides at the edges during forging due to localized breaking of weld. In the case of open die forging, wrapped billets with ceramic blankets were preheated and were upset forged using 500 ton hydraulic press. In this case also, edges were found to get oxidized which again resulted in surface cracks. Pack forged material and open die forged samples were cleaned and edges were trimmed before taking samples for microstructural examination.

7.3 DETERMINATION OF FLOW CURVE

In the metalworking processes, load required for deformation is a function of strain, temperature and strain rate. Hot tensile test has limited utility because necking limits uniform deformation to true strains of less than 0.5 and therefore hot isothermal compression test is a preferred method for flow curve determination at high temperatures under constant strain rate conditions.

7.3.1 HOT ISOTHERMAL COMPRESSION TEST

Uniaxial hot compression test was conducted at different temperatures and at three different strain rates to obtain flow stress in various combinations of temperature and strain rates. Three alloys were tested in a Gleeble 3500C thermo-mechanical simulator under isothermal and constant strain rate conditions. Specimens were heated at the rate of 3^0C/sec and soaked for 60 sec. at the test temperature. Photograph of the tested specimens is presented in Fig. 7.4. It is noted that, some of the specimens failed during testing when the test temperature was low and strain rate was high. This indicates that, those specimens were tested below the brittle to ductile transformation temperature (BDTT) for specified strain rates. A detailed observation of individual specimens during hot compression test is presented in Table 7.1.

To accurately measure the temperature of the specimen, a thermocouple was welded to the surface of the specimen and temperature was recorded. At slow strain rates of deformation, most of the heat escapes through the anvils and to the environment, but at high strain rates time will be insufficient for heat to flow and so specimen temperature rises. Rise in temperature of specimen due to deformation heating at the studied strain rate 0.001 to 0.1/sec has not been observed, so temperature correction has not been incorporated in the present work.

It has been noted that, material at low temperature and higher strain rates could not sustain its integrity and developed cracks at the outer surface. Also, at very high temperatures cracking, is observed in few samples at 1250^0C (Fig. 7.4).

Retesting was carried out at the same temperature and strain rates to confirm the reasons of cracking as observed in some of the specimens. Similar result was obtained. This confirms the important role of temperature and strain rate for successful deformation. From this observation, 1050-1150^0C temperature and 0.001-0.01/sec. strain rates are found to be safer hot working parameters. Based on these results, hot workability maps have been derived and are discussed in section 7.3.3. Further, a detailed analysis on temperature, strain rate and deformation stress has been carried out through processing map approach, which is discussed in next chapter.

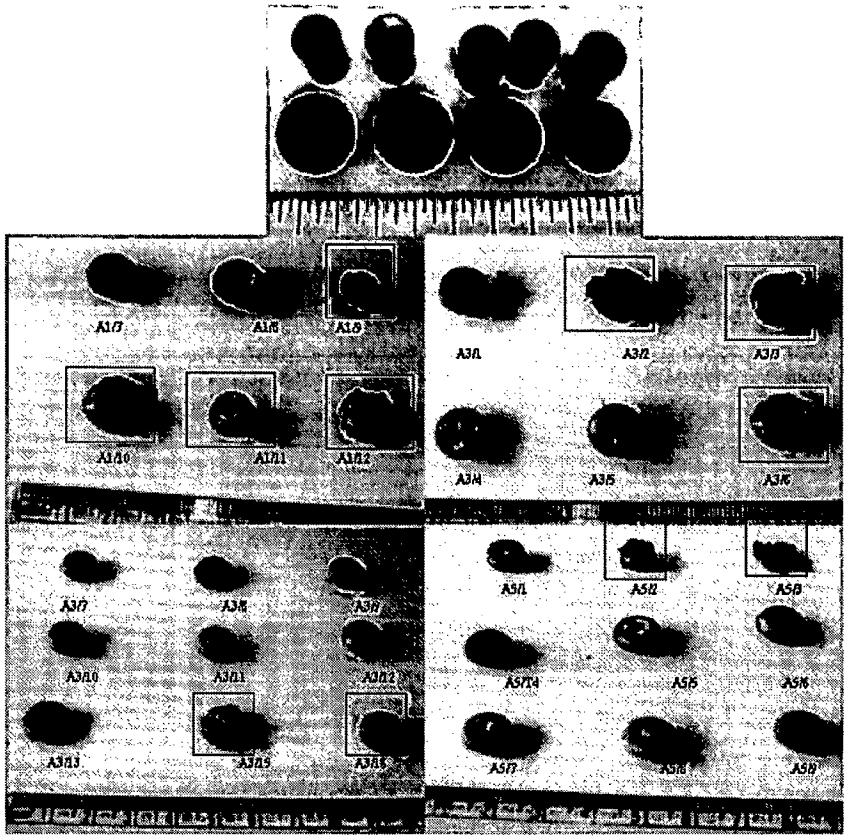

Fig. 7.4: Photograph of some of the hot compression tested specimens (cracked/ surface cracks during testing are shown in box).

7.3.2 EVALUATION OF FLOW CURVE

The true stress- true strain curves of the isothermal hot compression tested specimens under different temperatures and strain rates are shown in Fig. 7.5. The curves initially exhibit the peak stresses (around 0.1-0.2 strain), then the flow stresses decrease with increasing strain. The curves can be divided into three stages, i.e. strain-hardening (stage-I), steady state- strain stages (stage-II) and strain-softening (stage-III). These stages depend on the type of alloys, temperatures and strain rates.

It is observed that, at lower temperature and high strain rates, decrease in flow stress is rapid, whereas, decrease in flow stress is gradual at lower strain rates (0.001/sec.) at the same temperature. It shows mainly strain hardening and softening stages, where steady state stage is very low at lower temperature and higher strain rate. Precisely the softening stage called for low temperature- higher strain rate deformation is not a softening process instead it is a microcracking process, since dynamic recrystallization is very low at this temperature and strain rate range. Therefore, it is attributed to deformation instability due to cracking at lower temperature and higher strain rates where flow localization leads to premature failure.

Table 7.1: Details of specimens and visual observations

Specimen No.	Test Details : Alloy, T (^{0}C)/ $\dot{\varepsilon}$ (sec^{-1})	Remarks
A1/1	*A1, 1050, 0.001*	Tested specimens were found to be free of surface cracks except some microcracks seen for specimen of 0.1 $\dot{\varepsilon}$
A1/2	*A1, 1050, 0.01*	
A1/3	*A1, 1050, 0.1*	
A1/4	*A1, 1150, 0.001*	Tested specimens were found to be free of surface cracks
A1/5	*A1, 1150, 0.01*	
A1/6	*A1, 1150, 0.1*	
A1/7	*A1, 950, 0.001*	Surface microcracks seen for specimens tested at 0.1 and 0.01 $\dot{\varepsilon}$
A1/8	*A1, 950, 0.01*	
A1/9	*A1, 950, 0.1*	
A1/10	*A1, 1250, 0.001*	Specimens tested at this temperature were cracking during testing. Repeat test confirmed the same
A1/11	*A1, 1250, 0.01*	
A1/12	*A1, 1250, 0.1*	
A3/1	*A3, 850, 0.001*	Surface cracks were noticed for specimens tested at 0.1 and 0.01 $\dot{\varepsilon}$
A3/2	*A3, 850, 0.01*	
A3/3	*A3, 850, 0.1*	
A3/4	*A3, 950, 0.001*	Tested specimens were found to be free of surface cracks except some microcracks seen for specimen of 0.1 $\dot{\varepsilon}$
A3/5	*A3, 950, 0.01*	
A3/6	*A3, 950, 0.1*	
A3/7	*A3, 1050, 0.001*	Tested specimens were found to be free of surface cracks
A3/8	*A3, 1050, 0.01*	
A3/9	*A3, 1050, 0.1*	
A3/10	*A3, 1150, 0.001*	Tested specimens were found to be free of surface cracks. However some unusual increase in load was seen during test for specimen of 0.1 $\dot{\varepsilon}$
A3/11	*A3, 1150, 0.01*	
A3/12	*A3, 1150, 0.1*	
A3/13	*A3, 1250, 0.001*	Deep cracks were noticed for specimens tested at 0.1 and 0.01 $\dot{\varepsilon}$. some unusual increase in load was seen during test for specimen of 0.1 $\dot{\varepsilon}$
A3/14	*A3, 1250, 0.01*	
A3/15	*A3, 1250, 0.1*	
A5/1	*A5, 750, 0.001*	Cracks were found for specimens tested at 0.1 and 0.01 $\dot{\varepsilon}$.
A5/2	*A5, 750, 0.01*	
A5/3	*A5, 750, 0.1*	
A5/4	*A5, 950, 0.001*	Tested specimens were found to be free of surface cracks
A5/5	*A5, 950, 0.01*	
A5/6	*A5, 950, 0.1*	
A5/7	*A5, 1150, 0.001*	Tested specimens were found to be free of surface cracks
A5/8	*A5, 1150, 0.01*	
A5/9	*A5, 1150, 0.1*	

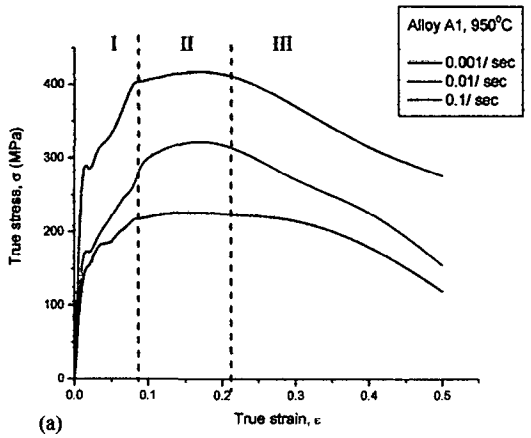
Alloy A1, 950°C
0.001/ sec
0.01/ sec
0.1/ sec
I
II
III
True stress, σ (MPa)
True strain, ε

(a)

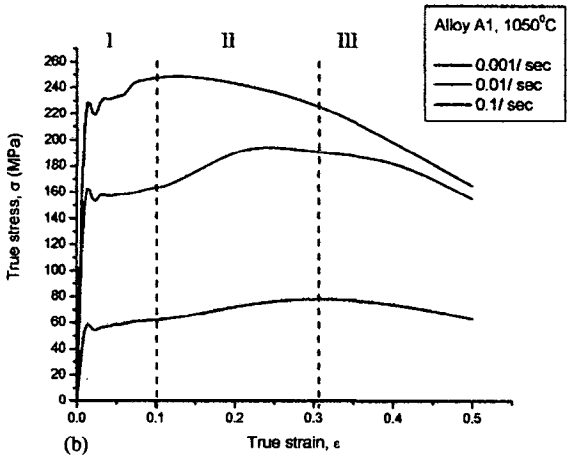
Alloy A1, 1050°C
0.001/ sec
0.01/ sec
0.1/ sec
I
II
III
True stress, σ (MPa)
True strain, ε

(b)

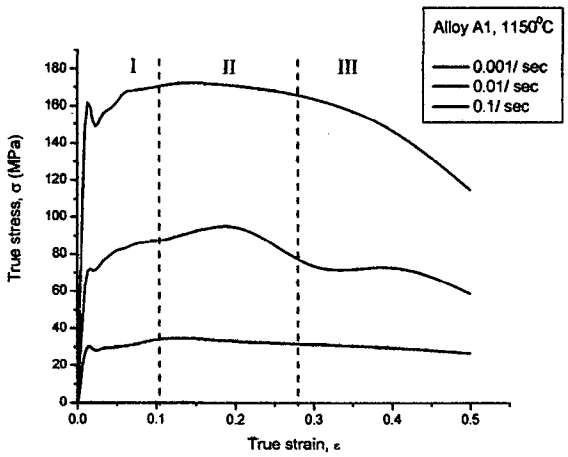
Alloy A1, 1150°C
0.001/ sec
0.01/ sec
0.1/ sec
I
II
III
True stress, σ (MPa)
True strain, ε

(c)

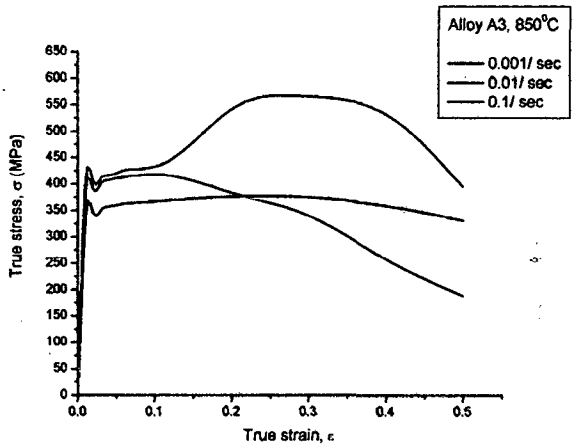
Alloy A3, 850°C
0.001/ sec
0.01/ sec
0.1/ sec
True stress, σ (MPa)
True strain, ε

(d)

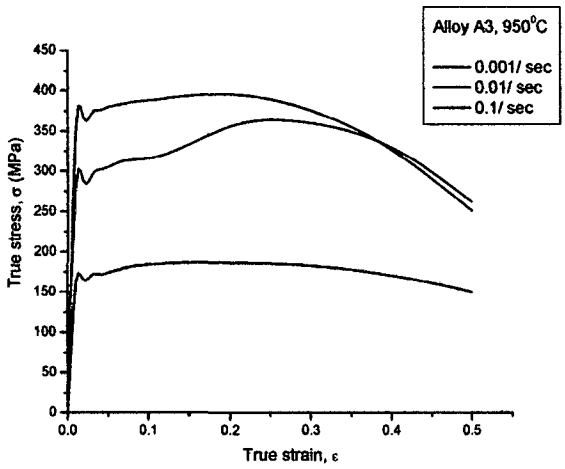
Alloy A3, 950°C
0.001/ sec
0.01/ sec
0.1/ sec
True stress, σ (MPa)
True strain, ε

(e)

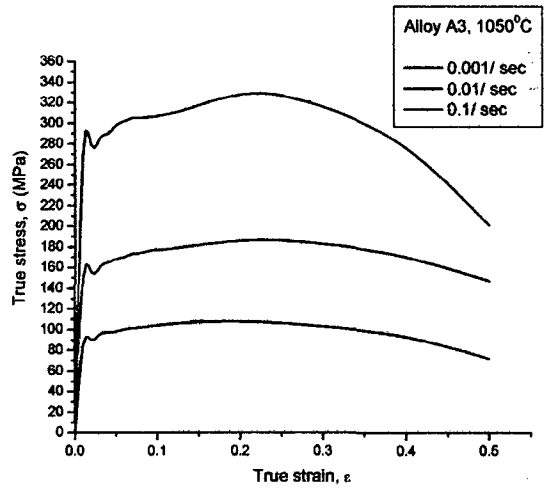
Alloy A3, 1050°C
0.001/ sec
0.01/ sec
0.1/ sec
True stress, σ (MPa)
True strain, ε

(f)

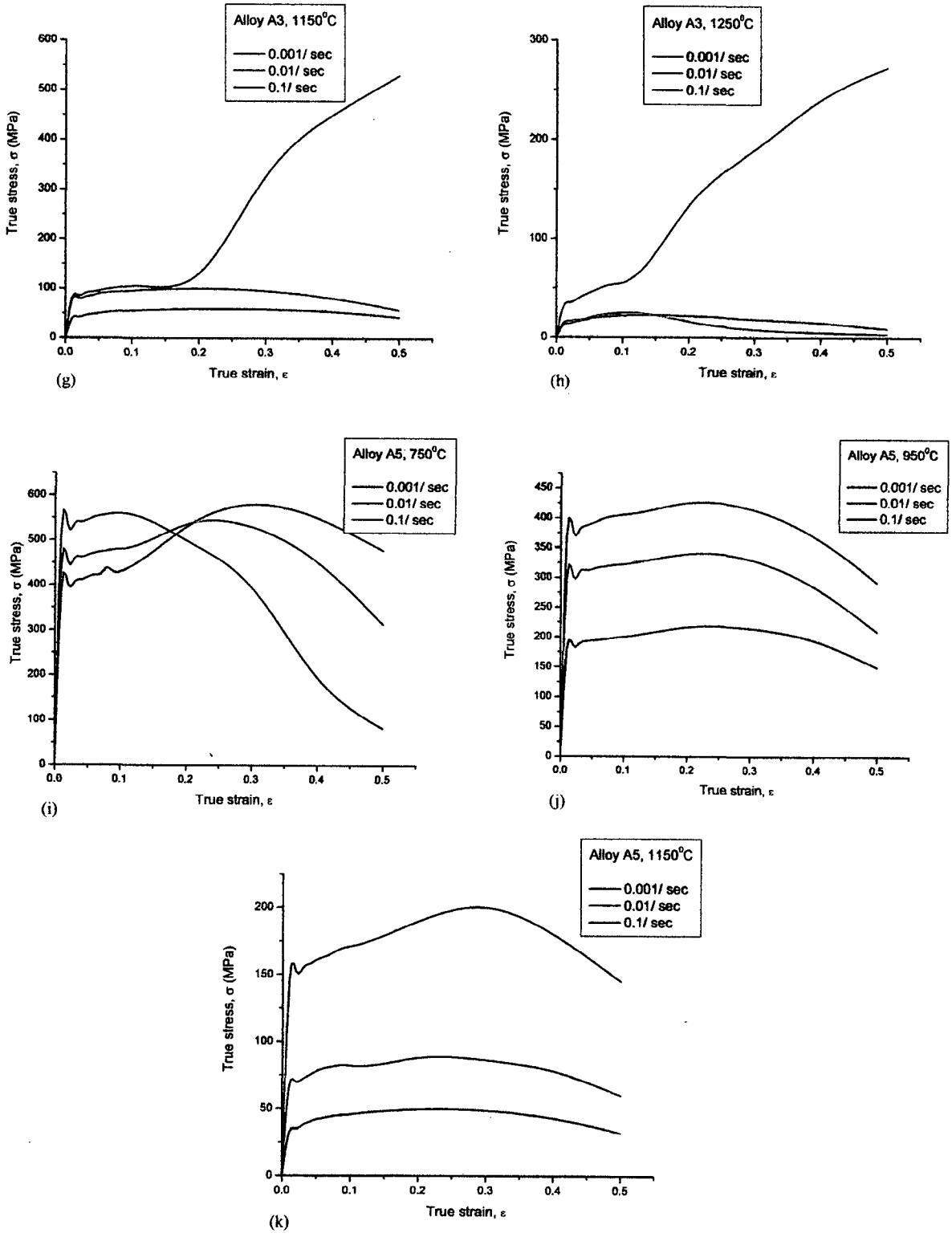

Fig. 7. 5 : Flow curve of various alloys at different temperatures and strain rates, (a-c) alloy *A1*, (d-h) alloy *A3*, (i-k) alloy *A5*

However, at higher temperature, flow curve characteristics are different where steady state-strain stage is clearly present. In this case also, flow stress decreases with strain but at slower rates as compared to earlier case. This indicates flow softening instead of cracking (as observed in low temperature high strain rate deformation). Similar to previous case, steady state strain region starts early for slow strain rate condition and is higher than the higher strain rate condition. Such behaviors have been known to be typical of dynamic recrystallization under hot deformation *[301]*. On the other hand, flow curves obtained under low strain rate conditions show relatively low work hardening behaviour also. This may be due to effect of dynamic recrystallization counter balancing the strain hardening effect. All these indicate that the alloy is very sensitive to deformation temperature and the strain rate.

The proposed three stages of flow curve showed similar trend for all the three alloys (*A1*, *A3*, *A5*) at different temperatures and strain rates as shown in Fig. 7.5. For a typical example, various stages are attempted to mark in stress- strain plot (Fig. 7.5 a-c). Only variation in stage width (strain range for each stage) depending upon hardening and softening phenomena were noticed. Generally it can be observed that stage-II (steady state stage) increases with decreasing strain rate at the same temperature. Minor fluctuation in flow stress within the stage (stage-II) is observed, which can be due to small variation in local chemistry of specimen affecting the hardening/ softening phenomena through dynamic recrystallization. Specimen tested at 750 and 850^{0}C at 0.1/sec strain rate for alloys *A3* and *A5* respectively, does not show steady state, which is seen as point of inflection due to rapid decrease in flow stress. This is explained in previous paragraphs, where microcracking phenomena may be working instead of softening, due to less temperature and high strain rate. This can be the limiting condition for deformation and here comes the role of brittle to ductile transition, which has been reported to be in this range of temperatures *[146, 147]*.

Generally it is observed that, specimens tested at low strain rates show extensive strain hardening while the specimens tested at higher strain rates show flow softening with rise in temperature. The degree of flow softening is high at high strain rates and low temperatures. This can be due to deformation heating, grain refinement/ breakdown and solutionising of second phase and/ or redistribution of solute. But, in the present study this phenomenon is reverse, as explained earlier that, strain hardening is not predominant at slower strain rates. Similarly, flow softening is not predominant at higher strain rates. This clearly indicates absence of deformation heating (at this level of strain rate). The result shows that mainly extent of dynamic recrystallization, which is function of temperature and strain rates, is governing the hardening and softening phenomena.

One important characteristics of flow curve (as seen from Fig. 7.5) noted in the present work is, the presence of small peak at flow stress below 0.1 strain (~0.05) value. It is similar to mild steels, where it is attributed to yield point phenomenon. All the three alloys show this characteristic to some extent at all the temperatures and strain rates. But at very high temperature (>1150^{0}C), this characteristics gradually disappears. It can be attributed to presence of interstitials like nitrogen, oxygen, boron etc., which act at lower temperatures, like yield point phenomenon and does not act at higher temperatures due to higher diffusivity of these interstitials. Such diffusion process is enhanced at elevated temperature through dislocation climb also.

Another important characteristic in true stress-true strain plot was observed at 1150 and 1250^{0}C at 0.1 strain rate in alloy *A3* (Fig. 7.5 g, h). Here, the flow stress continuously increased with increasing strain. The test was repeated and similar result was observed. This indicates continuous strain hardening and absence of strain softening phenomenon. Similar type of anomalous observation at high temperature was reported *[151, 302]* and noted due to dislocation core structure and flow localization. Since, this phenomenon has been observed in only alloy *A3* at 1150^{0}C under 0.1/sec strain rate, not even in alloy *A5* (where difference in these alloys are only in size of Ti particles used in alloy making). However, alloy *A5* has been tested upto 1150^{0}C only, so observation of alloy *A3* (with repeat test) can not be ignored.

Three possible reasons have been proposed to explain this phenomenon. (i) This phenomena can be attributed to absence of global flow softening. However, presence of localized flow softening due to lower recrystallization temperature or inhomogeneous deformation can not be ruled out. Presence of deformation band in the specimen deformed at higher temperature and higher strain rates (section 7.4.1.3) supports this reason. (ii) Occurrences of precipitation are possible at higher temperature under higher strain rate, which may act as a source of microcrack formation. Presence of local softening area and interaction with intermetallic precipitates (due to boron and Ni-P content) at >1150^{0}C under 0.1/sec strain rate can be lead to crack initiation. (iii) Another reason can be deformation heating and resulting in temperature rise. But, this process, even increases the temperature, it will not be reaching to the level where phase transformation from α+γ to α starts (Tα for alloy *A3* ~1300^{0}C). Probability of such temperature rise is less in this experimentation (isothermal compression test) to this level of strain rate (0.1/sec). But, localized structural changes due to phase transformation may possible in creating local flow softening.

Strain rate has significant role in this phenomenon, since alloy tested with lower strain rates at the same temperature does not show this phenomenon. Therefore, higher strain rate (0.1/sec) also indicate availability of less time for growth of nucleated recrystallized grains (globally) and so global flow softening is not available. Also, it has been reported that covalent bond of gamma TiAl would evolve towards a metallic bond as aluminium content decreases *[111]* and in localized area, this can also result in local softening. However, to establish the exact reasons for this continuous hardening phenomenon, more experimentation and submicroscopic analysis is required. From these results it can be inferred that, hot deformation at temperature higher than 1150^0C and at higher strain rates ≥0.1/sec should to be avoided.

Alloy *A1*, tested at 1250^0C, has not shown this behaviour, however cracking of specimens took place during testing and test could not be completed at any strain rate. This observation is although different than that observed in case of alloy *A3*, it can also be due to similar reasons as stated above.

Peak flow stress values for each alloy at various temperatures and strain rates are presented in Table 7.2. It is observed from Table 7.2 that, peak flow stress decreases with increase in temperature and decrease in strain rates. It shows a very strong dependence on strain rate and temperature. This dependence is analogous to that found in conventional Ti alloys. Strain hardening is found to be predominant in alloy *A1* upto strain value of 0.1-0.2, whereas, it is predominant upto 0.3 strain for the alloys *A3* and *A5*. This indicates relatively higher ductility for alloy *A3* and *A5*, which may be attributed to addition of small amount of boron where microstructure is modified as seen in section 7.4.

From the flow curve, it can be clearly seen that deformation resistance of the alloy is low at higher temperature and at low strain rates. However, this level of strain rates is too low for practical forging process. Also, long forging time at high temperature shortens the life of forging dies/press and leads to the decrease in forging temperature of the billet, which in turn increases the deformation resistance of the material. Therefore, isothermal forging is recommended, which is although not economical for larger billets for practical purpose. However, optimum selection of strain rate and forging temperature using near isothermal process, hot working of Ti aluminides can be carried out.

Table 7.2 : Peak flow stress of various alloys at different strain rates and temperatures

Alloy	Strain rate, sec^{-1}	Peak Flow stress (MPa) at different temperatures, (^0C)					
		750	850	950	1050	1150	1250
A1	0.001	Not tested*	Not tested*	225	78	33.7	Tested but failed prematurely
	0.01			314	191	95	
	0.1			414	247	171	
A3	0.001		376	187	108	59	22.3
	0.01		418	360	186	100	25
	0.1		565	396	328	530	272
A5	0.001	580	Not tested*	217	Not tested*	49.6	Not tested*
	0.01	535		339		88	
	0.1	560		425		200	

* due to non-availability of specimens

7.3.3 HOT WORKABILITY MAPS/ OPTIMIZATION OF HOT WORKABILITY

From the testing details and surface observations of the tested samples, hot workability maps have been generated, which provide processing windows for the alloys at different temperatures and strain rates. The hot workability maps are presented in Fig. 7.6.

It is clearly seen from the hot workability maps (Fig. 7.6) that sound deformation has very narrow zone mostly at low strain rates and in the temperature range of 950-1150^{0}C. At higher temperatures (i.e. 1250^{0}C), cracking has been observed (Table 7.1). Hot workability map seen in combination with stress-strain curve clearly shows that at 1250^{0}C some instability occurs. Factor discussed in section 7.3.2 may be leading to occurrence of instability and cracking. From all the three alloys (Fig. 7.6), it is found that; 950-1150^{0}C is the zone of sound deformation with maximum strain rate of 0.01/ sec.

7.4 MICROSTRUCTURE EVALUATION

All the hot worked billets and compression tested samples were analyzed microscopically. Representative samples from the core of deformed zone were drawn from the forged billets and hot compression tested samples. Conventional polishing methods were followed for specimen preparation. Microstructures were observed using optical microscope, SEM and TEM.

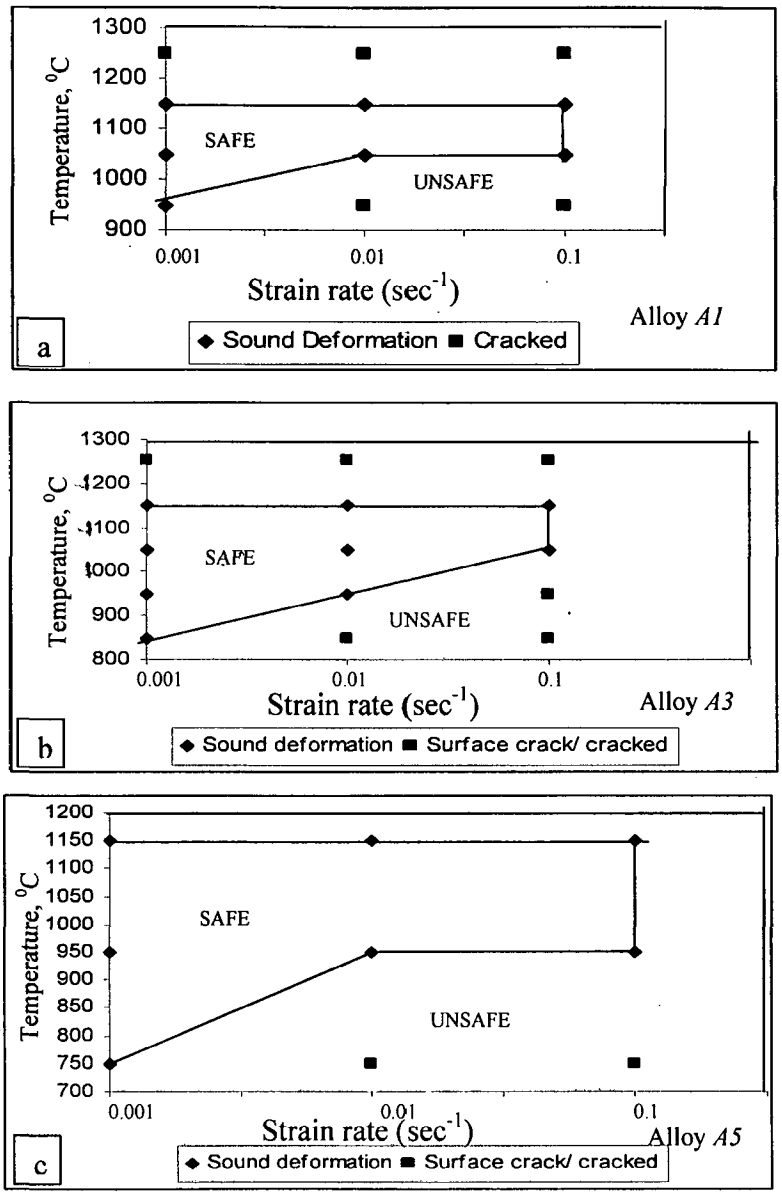

Fig. 7.6: Hot workability maps based on hot isothermal compression test, for alloys *A1*, *A3* and *A5* (a, b, c respectively).

7.4.1 OPTICAL MICROSCOPY

In general, microstructures of all the alloys showed grain refinement after isothermal and near isothermal hot deformation. However, some specific features were also observed in various alloys in specific conditions. Representative optical microstructure of alloys after hot deformation is shown in Fig. 7.7. It clearly shows the grain refinement and generation of lamellar and γ phase with recrystallized grains. Optical photomicrographs representing the specific forging condition and hot compression tested specimens with important features are presented in Figs. 7.8-7.11 and Figs. 7.11-7.14 respectively.

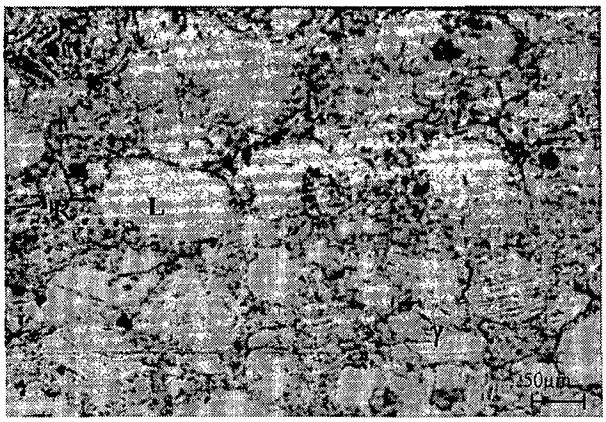

Fig. 7.7: Representative optical photomicrographs of hot worked samples (*A5*), showing deformed grains, lamellar phase (L), γ phase and recrystallized grains (R)

7.4.1.1 Microstructure of HIPed and hot isothermal forged billets

HIPed microstructure of alloy *A1* (parent metal) shows two phase refined microstructure (Fig. 7.8a) whereas, well developed lamellar structure is observed for alloy *A2* (Fig. 7.8b) alongwith γ phase. Similarly, pack forged alloy *A2* under near isothermal condition (Fig. 7.8 c-d) shows fine lamellar structure. It shows orientation difference within the grains.

This indicates multiple nucleation sites exists within the grain along the grain boundary for lamellar phase transformation. Presence of annealing twins are also noted in Fig. 7.8d, which may be attributed to slow cooling from the deformation temperature, due to encapsulation in the Ti blocks.

Further, the alloy *A2* after hot isostatic pressing shows formation of recrystallized grains along the intergranular boundary (Fig. 7.8 e-f), with lamellar structures. Development of lamellar structure with different lamellae thickness is also observed in alloys (Fig. 7.8g). It shows growth of different types of lamellae having different interlamellar spacing. It may be attributed to local variation in chemistry *[303]*.

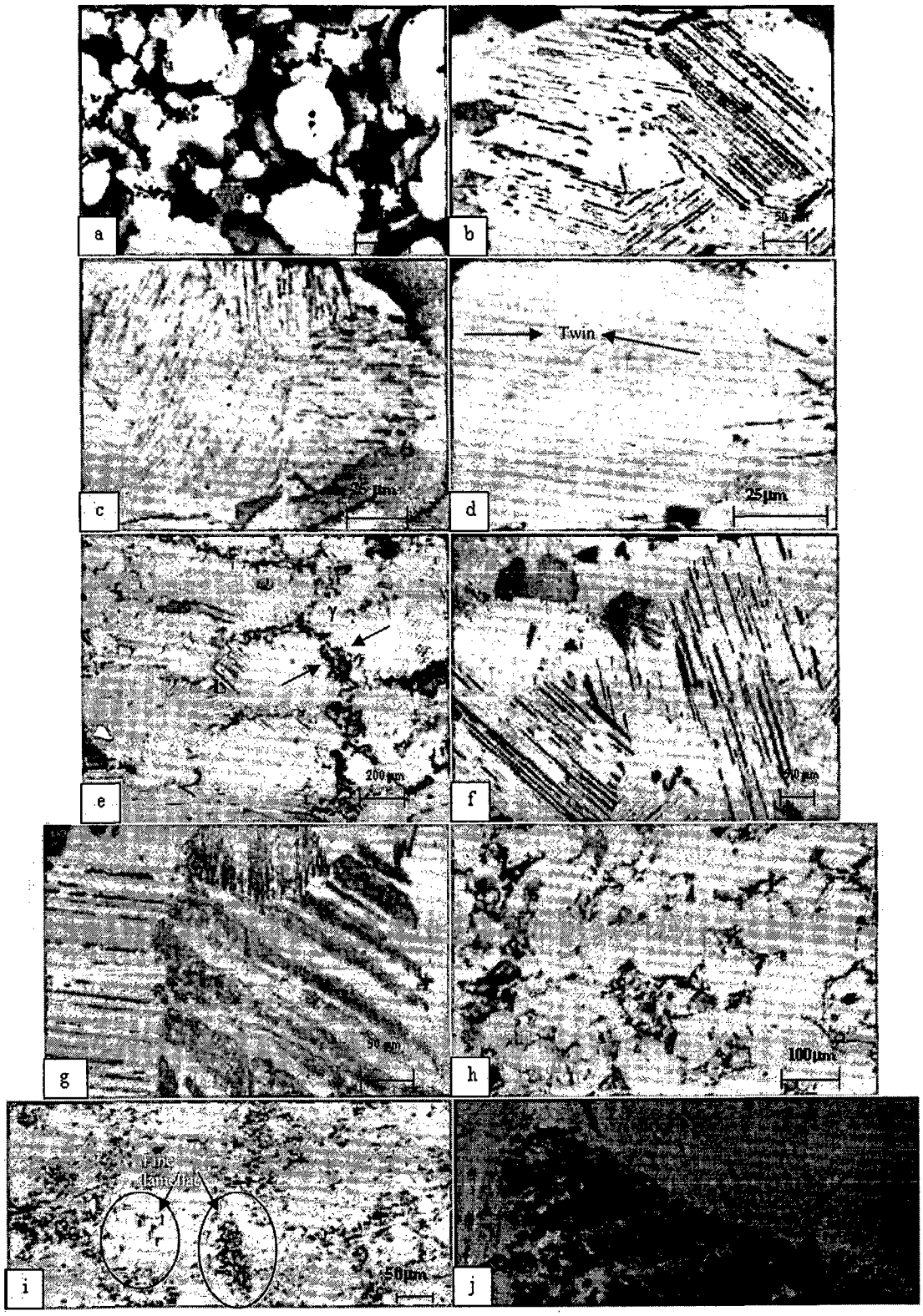

Fig. 7.8: Typical optical photomicrographs of hot worked samples (a) Hp*A1*, (b) Hp*A2*, (c-d) Pf*A2*, (e-f) HpIf*A2*, (g) HpIf*A3*, (h) Hp*A5*, (i-j) HpIf*A2*

It is also seen that, lamellae are nucleated from many places and joining the other group with various angles. Large growth of lamellae (in Fig. 7.8 g) can be attributed to isothermal working of material where cooling process after hot working was very slow due to vacuum processing. This is observed to be similar to discontinuous coarsening/ thickening of lamellae, which is reported to be due to variation in composition, *[102]* and it is possible in the alloy in localized area. Also, use of coated boron could not contribute to grain refinement to the extent as seen for alloy *A2* (Fig. 7.8f).

Under identical conditions of deformation, alloy *A5* (Fig. 7.8 h) shows relatively finer microstructure with smaller grain size than alloy *A2* (Fig. 7.8e). In this case also, formation of recrystallized fine grains along the intergranular area is noticed. Further, at higher magnification, alloy *A2* in HIPed and isothermal forged condition shows (Fig. 7.8 i, j) variety of microstructural zones where new features are found to be generated including packets of fine lamellar (secondary) grains.

7.4.1.2 Microstructure of Open die forged (near isothermal worked) billets

For more practical approach towards mechanical working, some samples were open die forged (in air). Typical microstructures are shown in Fig. 7.9.

It is observed that fine recrystallized grains with regular boundaries are present in the intergranular area. Similar observations were made in case of alloy *A5*, where recrystallized grains were found to be finer with predominantly lamellar structure. Presence of twins is also observed in open die forged alloy *A3* (Fig. 7.9a). This is possible due to higher strain rates *[160]*. Bending of lamellae is seen in specific cases (Fig. 7.9, c-e), where higher amount of working (~30-60%) was imparted. Higher amount of working (~60%) also generates finer recrystallized grains (Fig. 7.9e) as compared to (Fig. 7.9c).

7.4.1.3 Microstructure of isothermal hot compression tested samples

As observed earlier, HIPed (parent) material shows (Fig. 7.8a and 7.10a) presence of two phase structure (Ti_3Al and TiAl), where small amount of recrystallized grains are also present. Optical microstructure of compression tested specimens shows that grains are elongated perpendicular to the compression direction. Microstructure after hot compression at $950^0C/0.001s^{-1}$ $\dot{\varepsilon}$ shows presence of recrystallized grains, which have developed due to slow strain rate (Fig. 7.10b). At 0.01/ sec $\dot{\varepsilon}$ also similar features are observed except the formation of intergranular cracks (Fig. 7.10d). Small amount of recrystallized grains (section 7.4.4) were also observed.

Fig. 7.9 : Typical optical photomicrographs of hot worked samples (a) Af*A3*-50% worked, (b) Af*A5*-50% worked, (c) Af*A2*- 10% worked, (d) Af*A2*-30% worked, (e) Af*A2*-60% worked

It indicates that at high strain rates recrystallization has started but time was insufficient for its growth. At 1050°C, growth of DRX grains is observed (Fig. 7.10 e-g), which is finer at higher strain rates (0.01 & 0.1/ sec). In this case also, DRX took place mainly on the intergranular site indicating nucleation sites are at the grain boundary. Further growth of DRX grains at 1150°C are seen on the similar lines, where it is seen throughout the grains at this temperature at all the strain rates. Further, at 1250°C (0.1/sec, $\dot{\varepsilon}$) a different phenomenon has been observed along the grain boundary leading to cracking (Fig. 7.10k). This is supporting the flow curve characteristics as explained in section 7.3.2.

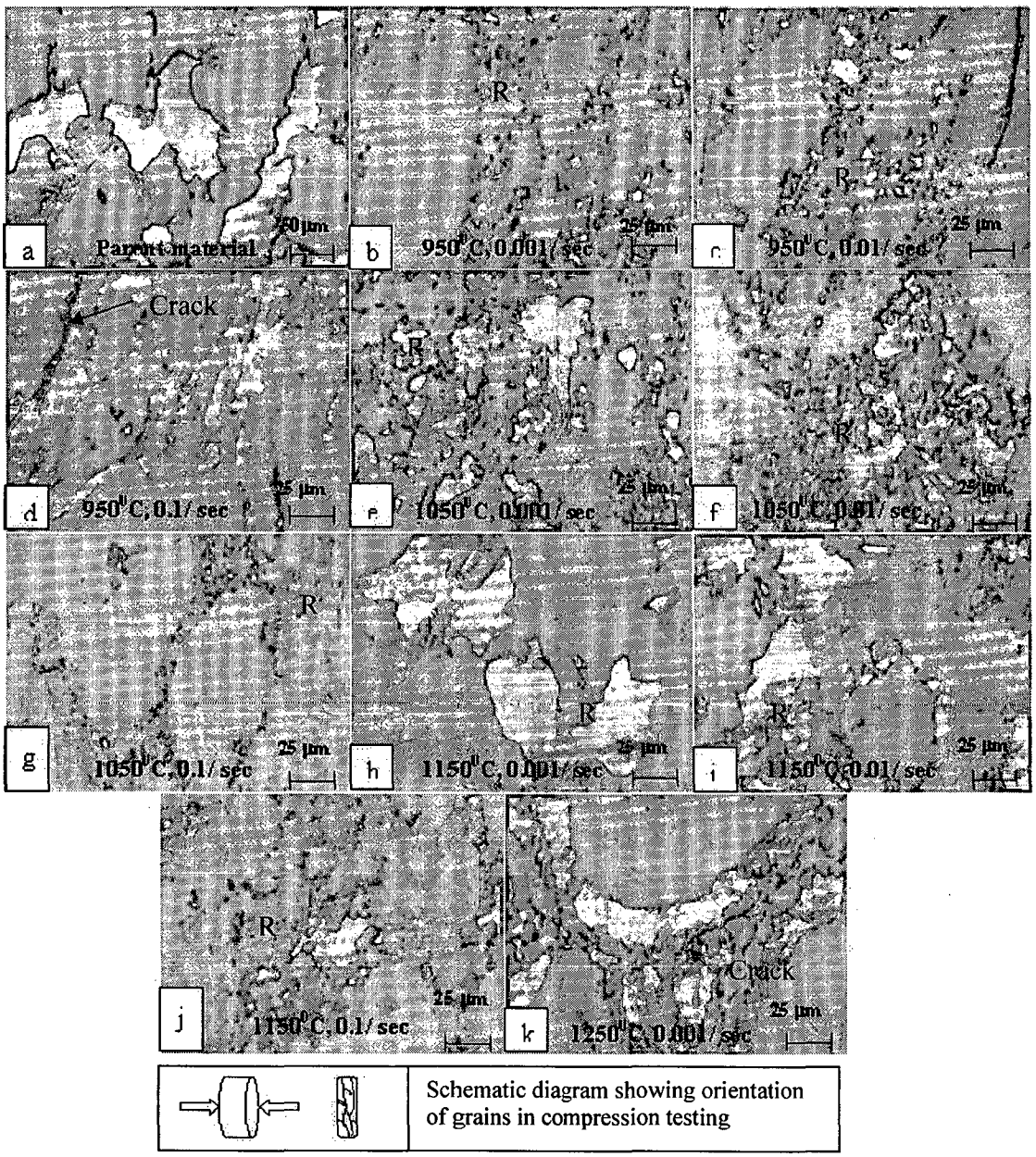

Fig. 7.10: Optical photomicrographs of alloy *A1* at various temperatures and strain rates, showing recrystallized grains (R) and cracks (in Fig. d and k)

Response of alloy *A3* (Fig. 7.11) with respect to deformation is found to be different from alloy *A1*. In this case, DRX as well as lamellar structures are seen at 850°C/0.001 s^{-1} $\dot{\varepsilon}$ (Fig. 7.11 b-d). Since temperature was too low to accommodate the deformation strain, cracks generated at 0.01 & 0.1/ sec $\dot{\varepsilon}$.

Microstructures at 950°C shows good amount of DRX grains along with lamellar transformed grains (Fig. 7.11 e-g). Size of DRX grains is found to decrease with increase in $\dot{\varepsilon}$. This may be due to insufficient time available for growth of nucleated DRX grains. Growth of DRX with refined lamellar structure is seen having similar trend with varying $\dot{\varepsilon}$ at 1050°C also (Fig. 7.11 h-j).

However, at a temperature of 1150°C, recrystallized grains have sufficiently grown and structure consists of mainly lamellar and recrystallized grains. At 1150°C/0.1 s^{-1} strain rate localized formation of deformation bands are seen (Fig. 7.11m and 7.12g), which may be due to localized flow softening. Further, at 1250°C (Fig. 7.11 n-p), flow softening and thickening of plate boundaries/ grain boundaries are seen, which may led to intergranular microcrack formation.

At higher magnification (Fig. 7.12), a variety of fine morphologies consisting of variety of fine lamellar and recrystallized grains are seen. Especially lamellar structure is clearly noticed alongwith dynamically recrystallized grains. Interlamellar spacing and lamellar packet sizes are found to be varying within the alloy microstructure. This indicates the presence of several nucleation sites for lamellar transformation and depending on the localized chemistry, stress condition and temperature, morphologies have been varying.

Response of alloy *A5* with respect to deformation is more similar to alloy *A3* than alloy *A1* (Figs. 7.13-7.14). Parent metal microstructure shows recrystallized and lamellar structure (Fig. 7.13 a). One distinct observation is found in alloy *A3* and *A5* is, microstructure displays lamellar structure at all the deformation temperatures and $\dot{\varepsilon}$. This may be due to the presence of boron in alloy *A3* and *A5 [304]*. At 750°C/0.001s^{-1} $\dot{\varepsilon}$, deformation is observed to be in restricted manner where high stress was required to deform the material. But, microstructure is found to have DRX grains and lamellar structure (Fig. 7.13 b, c) as seen for alloy *A3* at 850°C. Finally, at higher strain rates microstructure reveals formation of cracks (Fig. 7.13 d).

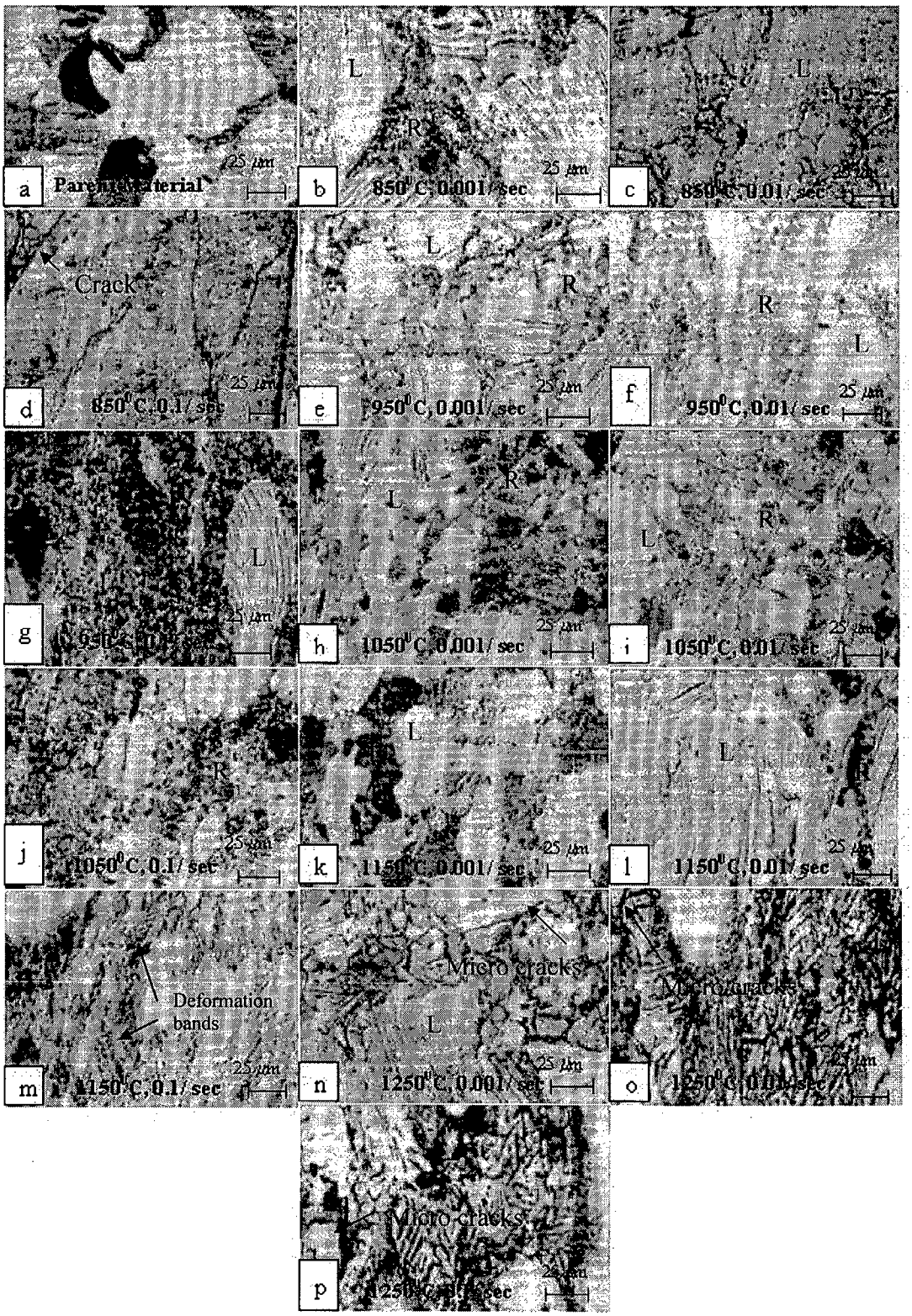

Fig. 7.11: Optical photomicrographs of alloy *A3* at various temperatures and strain rates showing recrystallized grains (R), Lamellar grains (L) and microcracks (in Fig. d, n, o and p)

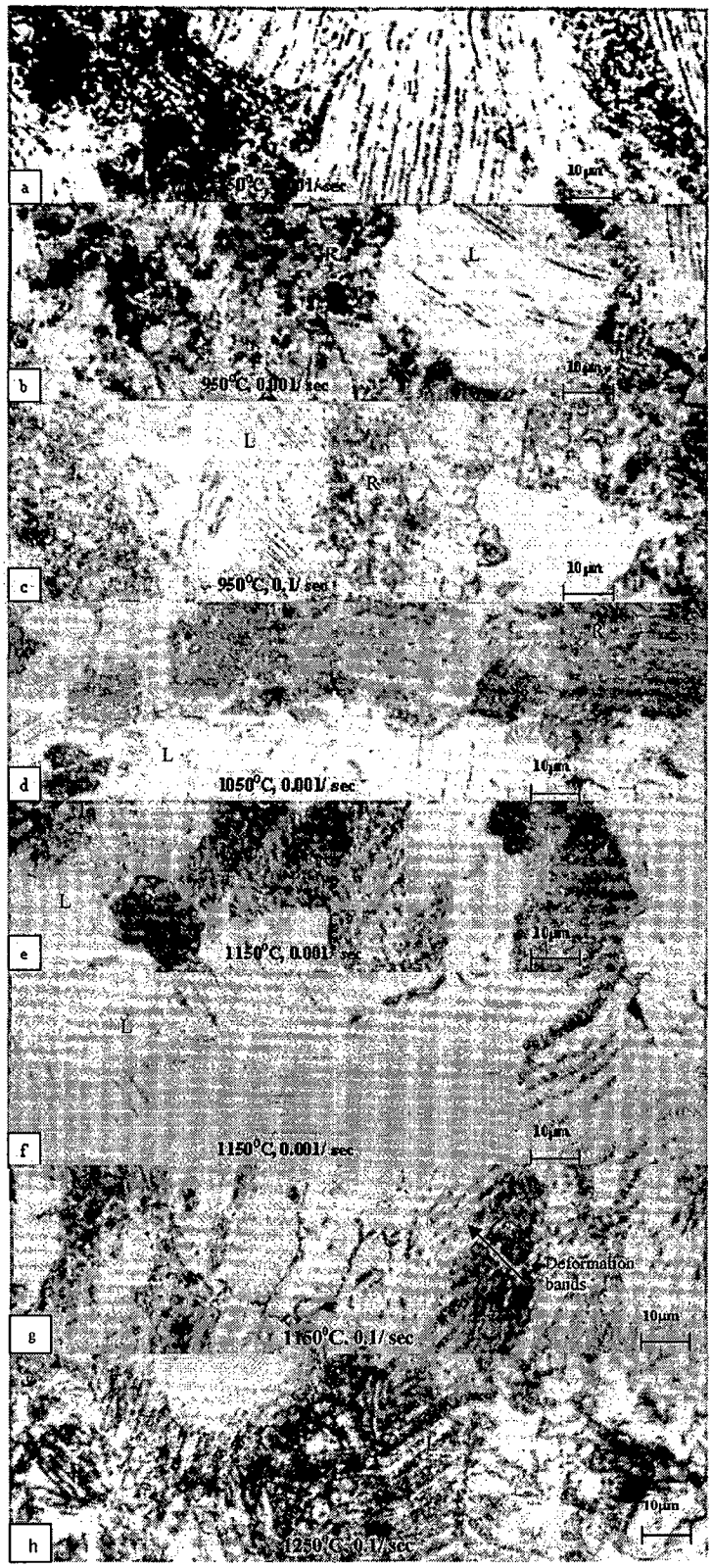

Fig. 7.12: Optical photomicrographs of alloy *A3* at various temperatures and strain rates showing recrystallized grains (R), Lamellar grains (L) and deformation band

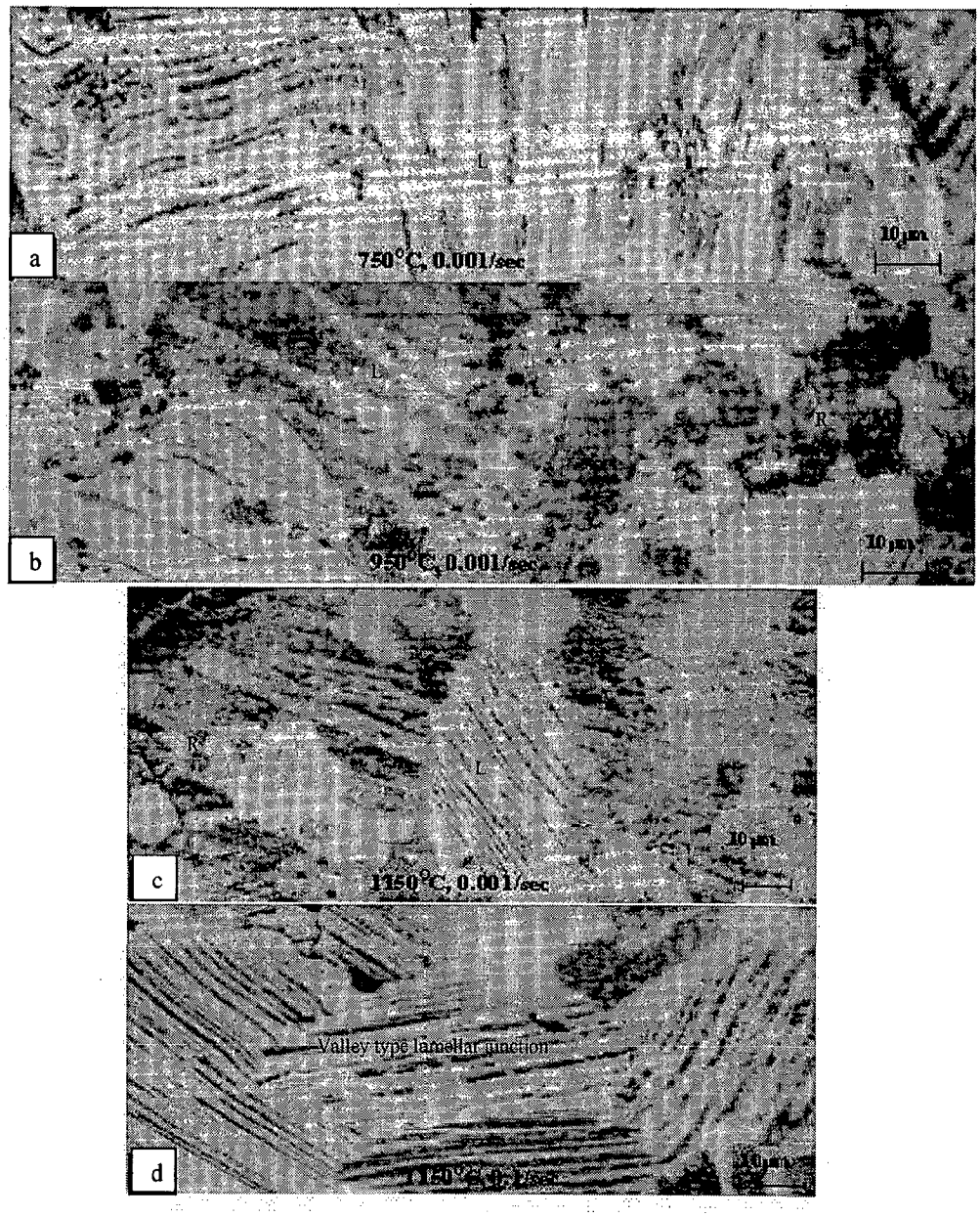

Fig. 7.14: Optical photomicrographs of alloy *A5* at various temperatures and strain rates showing recrystallized grains (R), Lamellar grains (L)

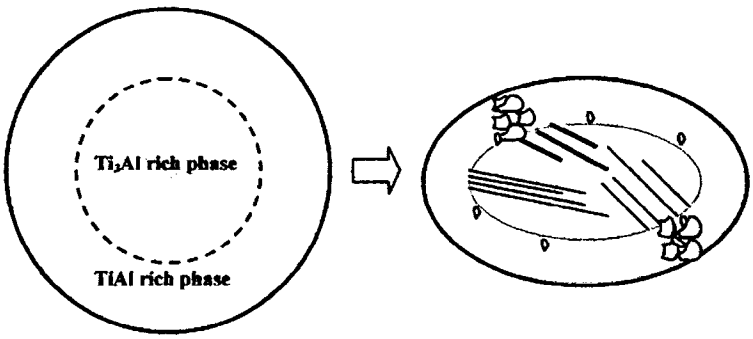

Fig. 7. 15 : Schematic diagram of a grain (originated from Ti particle) showing evolution of DRX grains and lamellar grains

SEM microstructure after hot working is presented in Fig. 7.17. It is found that, after hot isostatic pressing, some amount of porosity is still present in the alloy (Fig. 7.17 a) as confirmed through elemental mapping. Two phase (γ and isolated α_2) phase structure is seen for alloy *A1* (Fig. 7.17a), whereas other alloys (*A2-A5*) contain two phase lamellar structure (Fig. 7.17 b-h). Packets of lamellar zones with different interlamellar spacing have been observed. This can be attributed to local variation in aluminium content due to presence of TiAl and Ti_3Al adjacent to grain boundary, leading to differential deformation and generation of zonal microstructure. Fine lamellar structure is seen in Fig. 7.17b with formation of localized serrated microstructure. At higher magnification (Fig.7.17c), presence of interlamellar microcracks is also seen. Under heavy deformation, micropores led to elongated porosity and sometime such confined elongated pore results in generation of microcracks.

Similar to OM observations, morphology of lamellar phase is found to be varying, making angular boundaries at the meeting points of different lamellae groups. It indicates that nucleation of lamellar phase is heterogeneous and depends on local chemistry, temperature, stress and cooling rate etc., lamellar spacings have been varying (Fig. 7.17 d-f). In the case of open die forged samples, presence of massive phase regions are also seen (Fig. 7.17 g-h). This can be due to faster cooling from the forging temperature.

Scanning electron microscopy of the compression tested samples is presented in Fig. 7.18. It also confirms that alloy *A1* does not show any significant amount of lamellar structure, which has been estimated to be around 5% (section 7.4.4). Whereas, alloy *A3* and *A5* have large amount of lamellar phase (Fig. 7.18 b-l and section 7.4.4) of varying interlamellar spacing. At various magnifications, specimens were observed under SEM to

bring out the finer microscopic features present in the specimen. It is also observed that, very fine lamellae packets are growing in multiple numbers and finally with increase in temperature such lamellar packets cover the entire grain (Fig. 7.18 b and e) at constant (same) strain rates. It is also observed that, as the strain rate increases at constant deformation temperature, lamellae start bending, which either merges with another lamellae packet or progresses with easy path (Fig. 7.18b, c, d/ g, i/j, l). Although, varieties of lamellar structures were found to be growing with different spacing and orientations, presence of single phase was also noted in the microstructure at high temperature deformed sample (Fig. 7.18 f, h). Formation of subsidiary lamellae has been observed with very fine features growing perpendicular to lamellae (Fig. 7.18k).

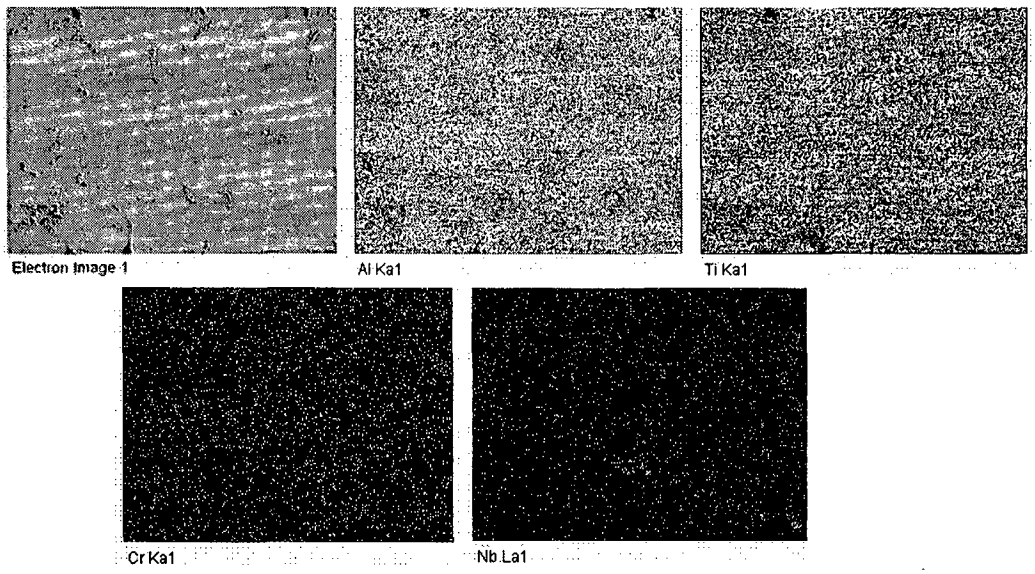

Fig. 7.16 : X-ray elemental mapping of homogenized plus isoforged sample If*A3* showing distribution of alloy constituents

7.4.3 TRANSMISSION ELECTRON MICROSCOPY

Selected samples from hot deformation were also studied under transmission electron microscope to confirm the presence of various phases evolved during deformation. Photomicrographs of representative two samples Af*A2* (open die forged alloy *A2*) and *A3*/10 (Alloy *A3* compression tested at 1150^0C/0.001s^{-1} $\dot{\varepsilon}$) are included in Fig. 7.19 with corresponding SAD pattern. Presence of α_2 phase, γ phase, twins, lamellar phase etc. has been confirmed through TEM (Fig. 7.19).

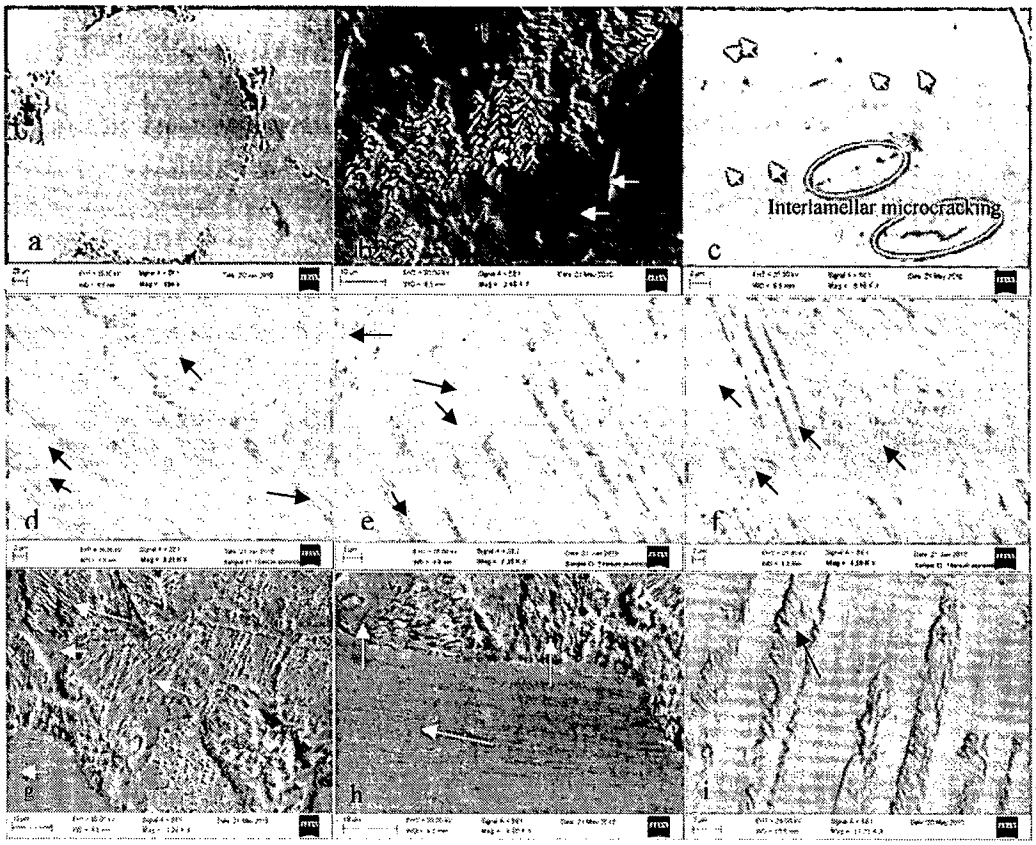

Fig. 7.17: Typical SEM photomicrograph of (a) Hp*A1*, (b-c) HpIf*A2*, (d-f) If*A3*, (g-h) Af*A3* showing various phases. Arrows marked in the photomicrographs indicates packets of specific type of lamellar morphologies.

Fig. 7.19a shows α_2 phase, which has been confirmed through diffraction pattern (Fig. 7.19b). Further long platelets of α_2 and γ phase is noticed with moderate dislocation density (Fig. 7.19c) and recrystallized grains. In another location alternate plates of α_2 and γ phase with twining (Fig. 7.19 d) has been observed. Presence of well developed twins were confirmed through TEM (Fig. 7.19 d-e) in the deformed specimen indicating twining as a mode of deformation, which is acting for the alloy deformed even at high temperature ~1250^{0}C (in open die forging). Long plates of α_2 phase in lamellar structure are seen clearly in another location (Fig. 7.19f-g) which has been confirmed by SAD pattern (Fig. 7.19 h).

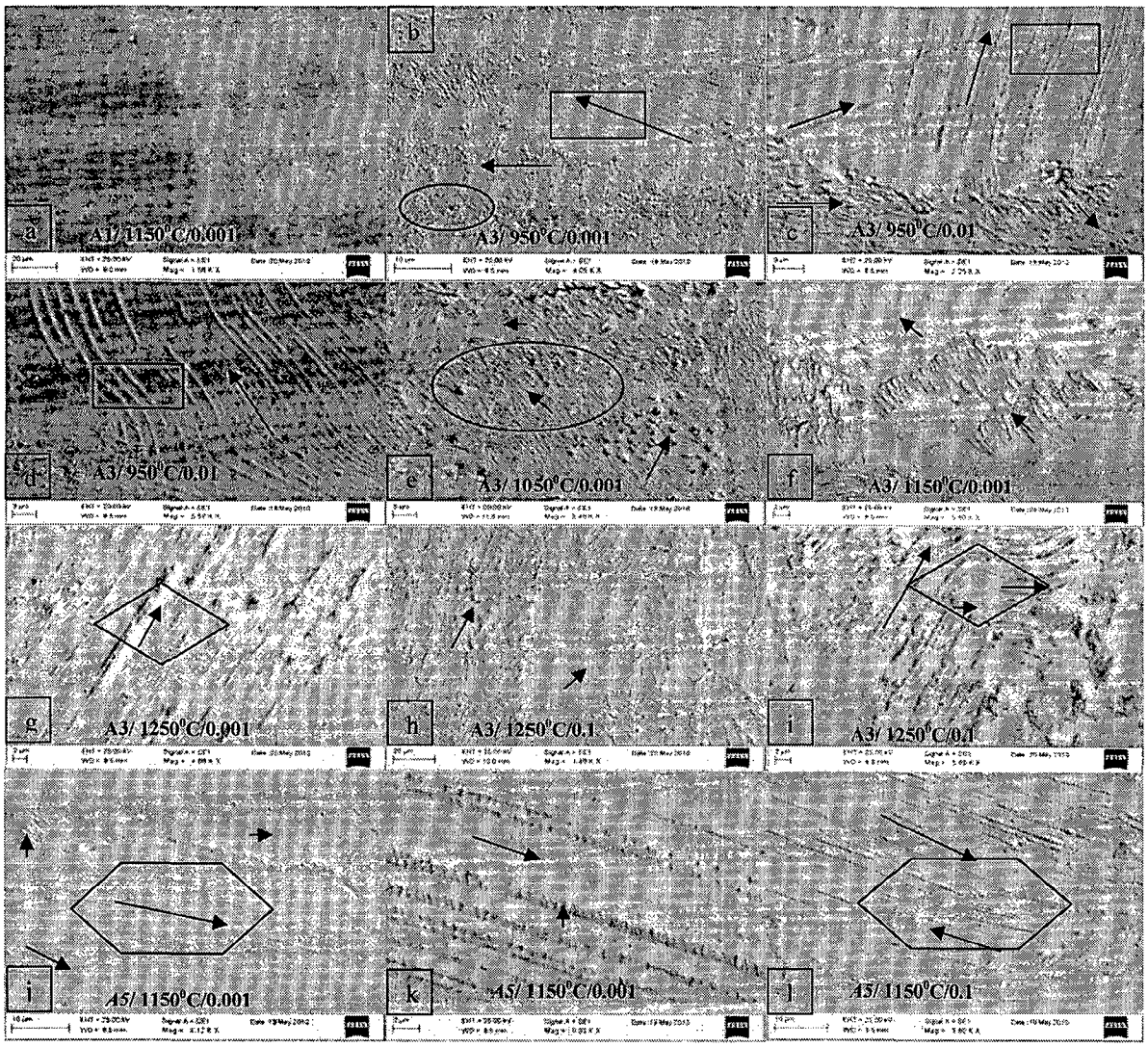

Fig. 7.18: Typical SEM photomicrographs of compression tested alloys at various temperature and strain rates showing different phases, morphologies and lamellae orientation. Four types of lamellar morphologies are indicated with four specific type of geometrical boundaries and arrows showing the lamellar orientation

In another specimen of hot isothermal compression tested sample, large grains with moderate dislocation density are observed (Fig. 7.19 i). Here thickness fringes are also seen, and presence of γ phase has been confirmed through SAD pattern (Fig. 7.19 j).

Low density dislocations as well as superdislocations were also observed under TEM for the samples deformed at relatively lower temperatures (750-850^{0}C). However, such features were not observed in the samples deformed at higher temperatures (>950^{0}C). This indicates, dislocations have been annihilated in high temperature working and resulted in fine recrystallized grains.

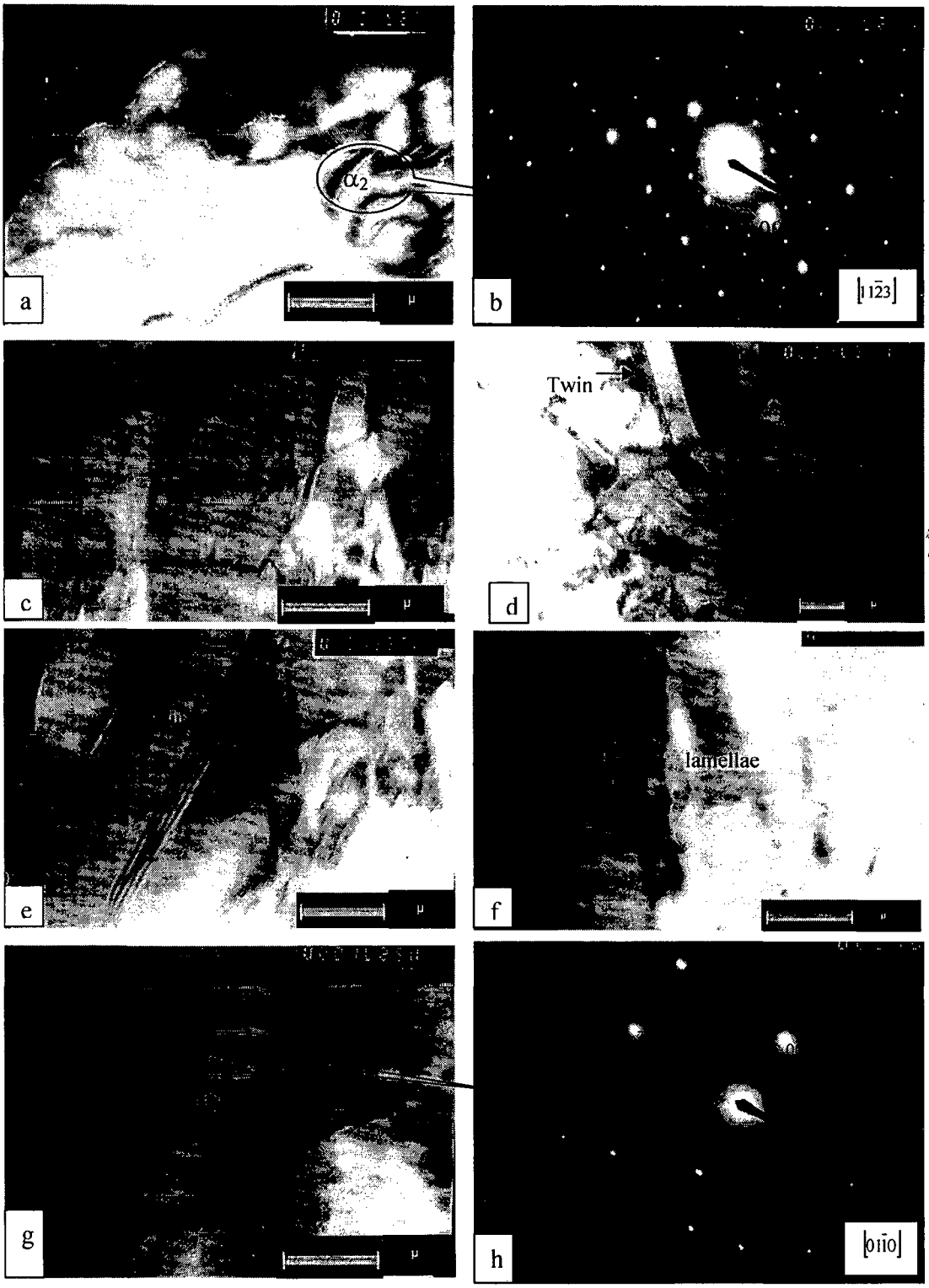
a
α_2
b
$[1\bar{1}23]$
c
Twin
d
e
lamellae
f
g
h
$[0\bar{1}\bar{1}0]$

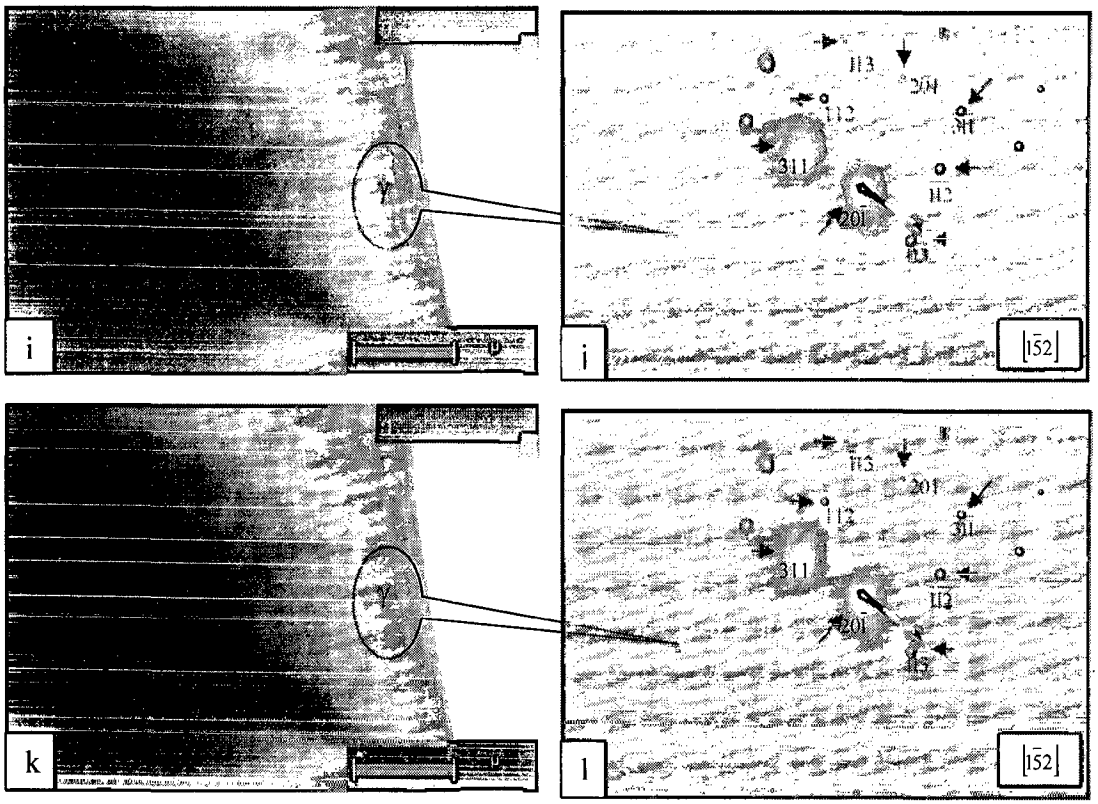

Fig. 7.19: TEM photomicrograph and SAD patterns of different alloys, a-h. Af (60%) *A2*, i-l. *A3*/10, showing presence of α_2 and γ phases, lamellar structure and twins.

7.4.4 QUANTITATIVE ANALYSIS OF MICROSTRUCTURAL FEATURES

For a given percentage of deformation (~50%), lamellar spacing and volume fraction of lamellar phase has been estimated from the 10 different locations of the specimens covering the representative microstructures. Results of hot worked microstructural analysis are tabulated in Table 7.3. From this table, it is noted that, grain size of the alloys after isothermal/ near isothermal deformation has significant amount of refinement from the homogenized stage (section 6.4.3) of the alloys. However, grain size is governed by the Ti particles used during RS. As noted earlier, alloy *A1* mainly contains DRX grains and lamellar phase is observed only in alloys *A2-A5*. It indicates the role of minor amount of boron (0.1 at. %) added in the alloys (*A2-A5*).

Table 7.3: Quantification of microstructural features in hot worked material of various alloys.

Alloy	Method of processing	Grain size, μm	Lamellae packet size, μm	% lamellar phase	Interlamellar Spacing, μm	Recrystallised grain size, μm	% Recrystallized grains
A1	Homogenized	200-220	20-25	-	-	-	-
	HIPed	150-180	30-32	4-6	0.5-1	-	-
	Pack forged	100-120	25-30	6-9	0.8-1	5-8	12-15
	HIPed+ isoforged	100-125	30-40	9-11	2-2.5	10-12	25-30
	Open die forged	80-100	30-35	14-16	<0.5	5-10	50-60
A2	Homogenized	180-200	80-100	-	-	-	-
	HIPed	150-180	80-100	5-8	1-1.4	-	-
	Pack forged	80-100	60-70	18-21	0.8-1.2	4-8	15-20
	HIPed+ isoforged	100-110	60-80	42-48	2-2.4	10-15	28-30
	Open die forged	80-100	40-50	55-60	<0.5	5-7	40-45
A3	Homogenized	180-200	80-120	-	-	-	-
	HIPed	150-180	80-100	18-20	1.8-2.5	-	-
	Pack forged	100-120	60-80	28-35	0.8-1	5-10	15-18
	HIPed+ isoforged	100-110	60-80	35-38	1-1.5	10-12	30-32
	Open die forged	80-100	40-50	60-65	0.4-07	5-10	40-45
A4	Homogenized	40-50	30-40	-	-	-	-
	HIPed	40-50	40-50	30-34	1.5-2	-	-
	Pack forged	45-50	30-40	25-30	0.8-1	3-5	15-18
	HIPed+ isoforged	40-50	30-40	55-60	2-2.5	8-10	30-35
	Open die forged	30-40	25-30	70-80	<0.5	2-5	30-35
A5	Homogenized	40-50	30-40	-	-	-	-
	HIPed	40-50	40-50	28-35	1.5-2	-	-
	Pack forged	45-50	30-40	30-35	0.8-1	3-5	18-20
	HIPed+ isoforged	40-50	30-40	55-65	2-2.4	812	3-35
	Open die forged	30-40	25-30	70-80	<0.5	2-5	30-35

Higher content of recrystallized grains with lower grain size (recrystallized) has been observed, as the rate of deformation increases from isothermal to open die forging, where strain rate of ~0.01/ sec. to ~0.1/sec respectively was imparted with temperature gradients (as normally present in open die forging). This can be due to generation of large number of nucleation sites resulting in higher % of DRX grains but of smaller size due to insufficient

time for growth of nuclei at higher strain rates. Similar trend is seen for interlamellar spacing with respect to various processes. Interlamellar spacing has been observed to be upto 2.5 μm depending on the rate of loading. Also, content of lamellar phase was found to be higher for open die forged specimens, indicating deformation under stress gradient and temperature gradients favours such type of microstructures. Similar observations on preferential growth of one phase have been reported on α-β Ti alloy *[305]*.

In pack forged alloy, % DRX grain is lower than HIP+Isoforged as well as open die forged material. It may be due to use of as homogenized material in pack forging where porosity content was relatively more as compared to HIPed material. Because of this porosity, material could not deform uniformly with effective load transfer across the aluminide section

Quantitative estimation of microstructural features of compression tested samples was also carried out, which is presented in Table 7.4 and plotted in Fig. 7.20. Grain refinement of primary grains has taken place, which is around 60-100μm against initial homogenized grain size (section 6.4.3) of 220-240μm in case of alloy *A1*. Similarly, in case of alloy *A3*, it is the lamellar packets (colony) of the size 35-45μm instead of equiaxed grains, against the initial homogenized grain size of 180-200μm and it is 40-50μm against initial homogenized grain size of 45-50μm in case of alloy *A5*.

Very fine DRX (dynamically recrystallized) grains were observed which are mostly found to be present between the primary grains. It indicates these DRX grains are the transformation products of aluminium rich aluminide (first formed) during reaction synthesis, which was converted to TiAl subsequently during homogenization. Aluminium rich aluminides (TiAl) favour recrystallization as compared to Ti rich Ti_3Al due to lower recrystallization temperature. At deformation temperature under lower strain rate compression, all the generated lattice defects (like dislocations) appear to have been transformed to recrystallized grains through dynamic recrystallization.

Size of DRX grains is found to vary between 5-20μm. It depends on the amount of working, alloy chemistry, strain rate and deformation temperature. Since all the compression tests were performed for 50% deformation, other factors have played role in these specimens. At lower temperature and higher strain rates finer DRX grains (Fig. 7.11 c, d) were observed and vice versa. Sometime these grains were too fine to be measured in an optical microscope for the specimen deformed at low temperature (850^0C) and at higher strain rates (0.01-0.1/sec.).

Table 7.4: Microstructure characteristics in compression tested specimens

Alloy	Grain size, μm	Lamellae packet size, μm	% lamellar phase	Interlamellar Spacing, μm	Recrystallised grain size, μm	% Recrystallized grains
A1/1	50-75	Primary two phase structure	≤ 5%		7-9	30-40
A1/2					8-9	25-35
A1/3	60-70				6-8	25-30
A1/4	50-60				8-12	30-40
A1/5					6-9	25-30
A1/6	40-50				6-9	15-22
A1/7	75-100				6-8	30-35
A1/8					5-9	18-22
A1/9	60-70				5-8	18-25
A1/10	100-120				12-18	cracked
A1/11					10-15	cracked
A1/12					8-12	15-20 (cracked)
A3/1	Lamellar packets	20-25	50-55	1-1.5	4-6	30-40
A3/2		35-40	60-65	05-1	4-8	cracked
A3/3		-	Cracked	0.5-1	-	25-30
A3/4		25-28	60-68	1.5-2	6-8	35-40
A3/5		35-40	50-55	1.5-2	6-9	30-38
A3/6		32-38	60-65	1-1.5	6-8	30-35
A3/7		35-40	50-55	1.8-2	8-12	35-40
A3/8		25-28	55-65	1.5-2	8-10	35-42
A3/9		25-30	50-60	1-1.4	6-10	35-45
A3/10		40-45	60-65	2.4-1.6	8-11	38-45
A3/11		35-38	85-90	2-2.5	7-9	L
A3/12		35-40	70-75	1.2-1.5	4-6	35-40
A3/13		40-45	-	2.8-3	12-18	28-35
A3/14		38-45	-	2.2-2.5	9-11	cracked
A3/15		35-40	-	2-2.5	5-7	-
A5/1		30-35	40-45	-	3-5	cracked
A5/2		30-35	45-50	-	2-3	8-12
A5/3		-	-	-	-	cracked
A5/4		40-45	58-65	2-2.5	5-7	35-45
A5/5		38-45	62-70	1-1.5	3-5	35-40
A5/6		40-45	65-70	1-1.5	3-5	35-40
A5/7		45-50	58-65	2-2.5	18-20	40-45
A5/8		40-45	60-70	1.7-2.2	10-15	40-45
A5/9		40-45	90-95	1.6-2	5-8	L

At relatively higher temperatures (1150^{0}C) and lower strain rates (0.001/ sec.), DRX grains of sizes 10-20μm were observed. It is due to sufficient time and temperature available for nucleation and growth of DRX grains *[159]*. Increasing trends of recrystallized grain size and % recrystallized grains with increasing temperature are observed due to the same reasons. Here, in this case, % DRX grain is marginally higher at lower strain rate at the same temperature and it is marginally lower at higher strain rate *[159]*. The first observation is found to be reverse to that observed in case of hot working of billets (Table 7.3) where increased strain rate (in open die forging) has increased the content of recrystallized grains. This clearly indicates role of temperature gradient also, even at constant strain rates. Since in open die forging such temperature gradients are normally present. But, in case of isothermal condition, all the nucleated DRX grains mostly grow to somewhat similar size. Also, nucleation of DRX grain itself shall be low in isothermal deformation condition as compared to open die forging. This is expected, since temperature as well as stress gradient helps in nucleation of DRX grains in open die forging. In HIPed + isoforged condition, % DRX grain as well as grain size shows very minor difference from the compression tested samples. This confirms the similarity in DRX grain development in terms of its content and its size in isothermal condition for the materials processed through two different routes.

An unusual phenomenon was observed at 1250^{0}C, where compression load was found to be increasing and microstructure is entirely different from the specimens deformed at lower temperatures. This has been explained in section 7.3.2 and it should be taken in consideration while deciding the process parameters.

Amount of DRX grains in isothermal forging for alloy *A1* was found to be similar to other alloys (*A2-A5*), whereas it is higher for open die forging (Table 7.3 and 7.4). Marginal change in % recrystallized grain is seen in isothermal compression with change in strain rates (Table 7.4). In near isothermal forging (open die forging) role of strain rate is predominant (~0.1/sec. for open die forging and ~0.01/sec for isothermal forging) as well as cooling rate (faster in open die forging) in obtaining the % recrystallized grains.

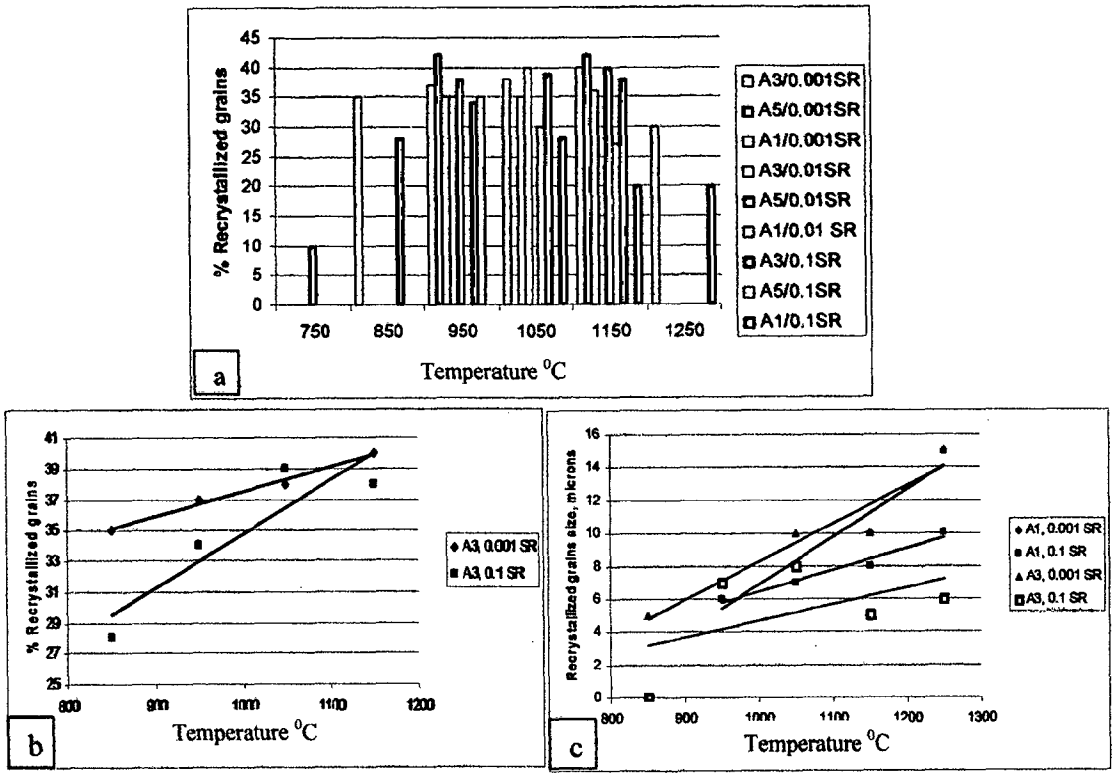

Fig. 7.20: DRX grains obtained in compression tested specimens at various temperatures and strain rates (a) Bar chart showing the % recrystallized grains (b-c) typical trend of % recrystallized grains (plotted with average data of Table 7.4)

Lamellar volume fraction in alloy A3 and *A5* is found to be significantly high. It is in the range of 50-60% for the alloys tested at temperature above 850^{0}C, 40-50% for the alloy tested at 750^{0}C and ~90% for the alloys tested at higher temperature nearer to α transus (>1150^{0}C). This indicates that alloys containing small amount of boron (*A3* and *A5*) transforms to lamellar phase, the content of which increases with temperature. However, minor change in volume fraction of lamellar phase in noted for the changes in the strain rates in both the alloys. Role of oxygen has also been reported in assisting the lamellar phase formation *[281, 306, 307]*. However, in the present study, although oxygen is high in all the alloys (Table 6.3), predominant lamellar structure is observed in alloys *A2-A5* with minor content in alloy *A1*. This indicates that, oxygen is playing significant role in boron containing alloys. It can be inferred that presence of oxygen alone (without boron) has limited role in formation of lamellar structure. Also, contribution of oxygen in formation of lamellar structure in alloys *A2-A5* in presence of boron needs to be further investigated.

Interlamellar spacing has shown similar trends as noted in case of hot working of alloys. At higher temperature and slow strain rates (comparing between HIPed + isoforge and open die forge) interlamellar spacing is higher and vice versa (Table 7.3).

7.5 MICROHARDNESS MEASUREMENT

Mainly three types of features are found to be present in the microstructure noted as, recrystallized grains (R), single phase (S) and lamellar phase (L). Microhardness values of these phases in different alloys are tabulated in Table 7.5 and corresponding microstructure with indentation is presented in Fig. 7.21.

In general, it is observed that, microhardness of different phases varies with morphological changes. Microhardness of single phase is found to be between 520 to 668Hv. Recrystallized grains also showed a wide variation in microhardness from 214 to 380 Hv depending on morphology and grain size. Microhardness of lamellar packets is found to be varying from 388 to 573 Hv.

Table 7.5: Microhardness values of various phases in different alloys.

Sl. No.		1	2	3	4	5	6	7	8	9	10	11	12	13	14	15
Microhardness Hv*	L	429	435	440	415	453	497	548	388	403	469	573	410	522	456	405
	S	668	520	558	576	553	646	*at 300gm load, R (Recrystallized grains),								
	R	295	220	214	350	315	380	S (Single phase), L (Lamellar phase)								

On an average lamellar phase has microhardness of ~430 Hv. However, for some cases it has shown very high microhardness (L6, 7, 10, 11, 13, 14 of Fig. 7.21). On closer observation, they reveal very fine lamellae which can be attributed to higher microhardness. Further it is noted that, these samples have undergone deformation at higher strain rates (0.1 and 0.01/ sec.) which has resulted in fine lamellae. Also, higher microhardness (Sl. No. S6, R6 and L15) is noted in case of alloy *A1* at 1250^{0}C testing, which can be attributed to precipitation of some new intermetallics at that temperature due to boron or impurity content. Microhardness of single phase is noted as very high, which indicates presence of α_2 phase, microhardness of recrystallized grains indicates presence of γ phase as well as α_2 phase and microhardness of lamellar phase indicates alternate layer of α_2 and γ phase *[166, 167]*. Presence of these phases has also been confirmed by TEM.

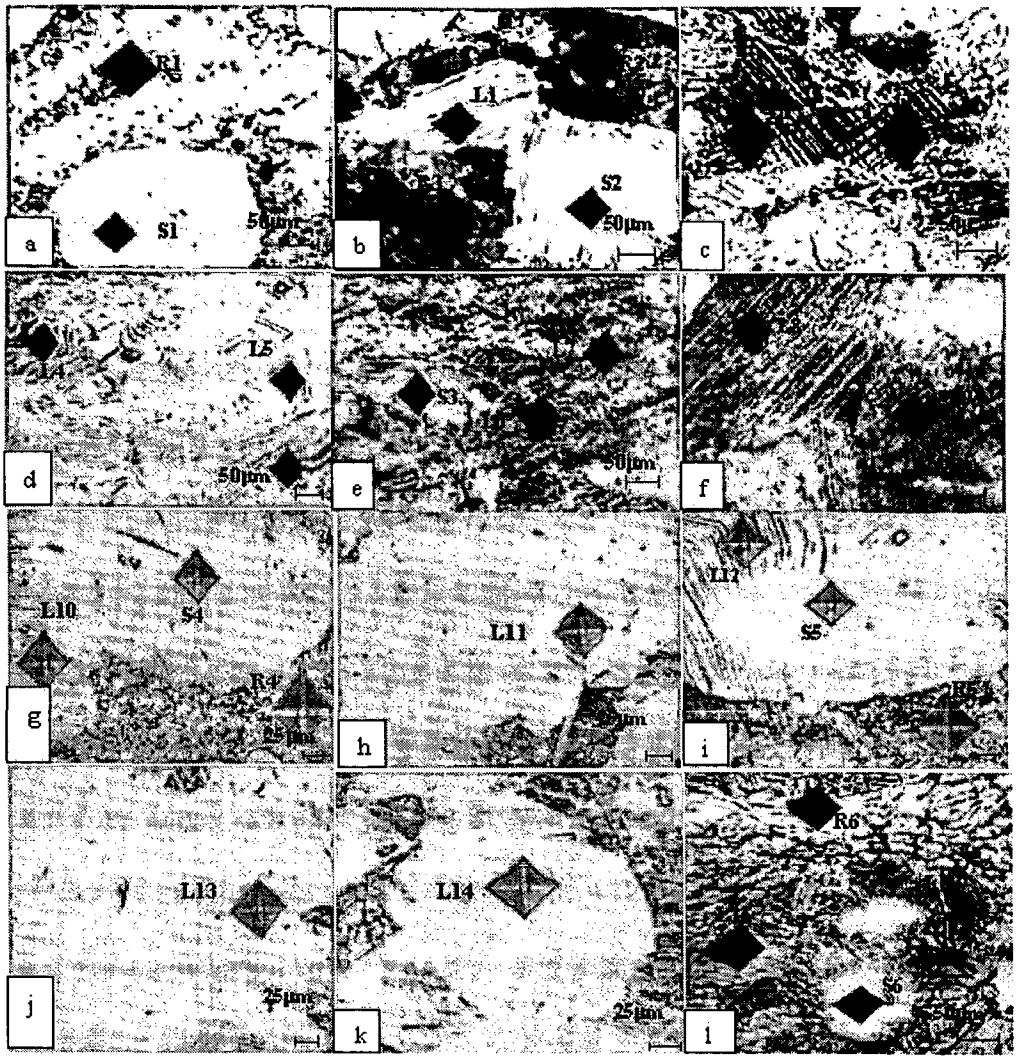

Fig. 7.21: Microhardness of some typical compression tested samples (a) *A1*/2, (b) *A3*/10, (c) *A1*/12, (d) *A3*/11, (e) *A3*/12, (f) *A3*/13, (g) *A3*/6, (h) *A3*/12, (i) *A5*/ 8, (j) *A5*/9, (k) *A1*/6, (l) *A1*/13

7.6 DISCUSSION

7.6.1 ANALYSIS OF HOT DEFORMATION RESULTS

Hot deformation of $\alpha_2+\gamma$ titanium aluminides processed through reaction synthesis route showed many important characteristics during processing and also resulted in variety of microstructural features. Being a brittle material, only hot isothermal and near isothermal working is possible under controlled strain rate conditions. It has been observed that, isothermal processing is best for this alloy, which also helps in closing the remnant

microporosity present in the PM processed alloy. Selection of temperature, strain rate and accordingly hot working process is very important *[309, 310]*. In the present work, hot deformation was imparted by compression using a hydraulic press, which is found to be safe, where, rate of compression (strain rate) needs to be very slow (<0.1/ sec strain rate). It is found that, isothermal vacuum hot pressing gives best results where material has been successfully deformed without any surface cracks. However, industrial practice may not always allow this process. Therefore, near isothermal working using pack forging route and thermally insulated ambient working can be followed under very slow rate of compression effecting strain rate of ~0.1/sec. Surface cracks at the edges are noted in forging through these methods, which can be removed by local machining. Important point noted during near isothermal working is that, forging should be carried out with minimum loss of time i.e. the time when the forge stock comes out of preheating furnace and till it goes back to furnace or completion of the forging process.

Through the uniaxial isothermal compression testing of cylindrical specimens of three different alloys, it has been demonstrated that, flow behaviour of aluminides is very sensitive to deformation temperature as well as strain rate. Many a times cracking of specimen took place either due to lower temperature (750-850^{0}C) or/ and due to use of higher strain rates (0.1/sec). In most of the cases it has been observed that, such cracks are mainly present in the bulged area of the specimen and direction of cracks is parallel to the compression axis (Fig. 7.4 and 7.22). It confirms that such cracks originate due to the tensile hoop stresses acting radially during compression, which is normally seen in forging of brittle materials.

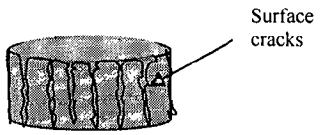

Fig. 7.22 : Schematic diagram of hot compression tested specimen showing peripheral cracks

Characteristic flow curves are similar to other materials where strain hardening increases the flow stress in the initial period of upto 0.2-0.3 strain and then flow softening becomes predominant and brings down the flow stress with increasing strain. Flow softening is caused mainly by dynamic recrystallization during high temperature deformation in TiAl

base alloys *[308]*. Degree of these phenomena depends on the alloy chemistry, strain rate and temperature. It has been observed that, strain hardening was marginally extended to strain of a 0.3 in case of alloy *A3* and *A5* as compared to alloy *A1* where it was upto 0.2. The reason behind this may be presence of boron containing phases in alloy *A3* and *A5*, which provide additional deformation resistance, either by the presence of refined microstructure or by presence of very fine borides. Peak stress of all the alloys at different strain rates and temperatures is found to be in line with other Ti alloys, where it increases with decreasing temperature and increasing strain rates and vice versa.

Steady state phenomenon is seen at higher temperature (1050-1150^{0}C) under lower strain rates. On the other hand, steady state condition is less prevailing at lower temperatures and higher strain rates where flow stress decreases very fast. This indicates significant role of time and temperature in deciding the steady state. At higher strain rates, time is insufficient to equalize the strain hardening process and probably localized softening brings down the flow stress rapidly. Similarly, in case of lower temperatures, strain hardening continues with increasing strain and as soon as localized flow softening/ inhomogeneity interacts, flow stress falls rapidly. Whereas in case of high temperature and slow strain rates, both these phenomena get sufficient time and temperature and maintain flow stress where decrease in flow stress is low with strain and longer steady state is seen. Therefore, this is the best situation for deformation of brittle materials like Ti aluminides *[309, 310]*.

Flow curve has been divided into three stages based on change in flow stress with strain. Continuous rise in flow stress is denoted as strain hardening stage (I) followed by steady state stage (II), where flow stress is not increasing with strain and then flow softening stage (III) leading to continuous decrease in flow stress with strain. Steady state is the most useful stage for plastic deformation where strain hardening is counter balanced by the strain softening and large amount of deformation can be imparted in the material. It has been observed that, degree of dynamic recrystallization is playing significant role in governing this stage (II). Accordingly, strain rate and temperature is selected to obtain maximum width of this stage. Among the alloys *A1-A5*, most of the alloys have shown wider steady state stage in the cases, where alloys have been deformed between 950-1150^{0}C at slower strain rates (<0.01/ sec.). This also indicates the zone of plastic deformation.

However, another important phenomenon has been noted during hot compression testing of alloy *A3* at 1250^{0}C, especially when strain rate was 0.1/sec, i.e. continuous strain hardening followed by cracking of the specimen. This is a very interesting situation where strain hardening continues upto failure/ cracking. It means flow softening is not taking place.

This has been explained in detail in section 7.3.2. It may be due to higher strain rates or presence of some new harder phases at this temperature. Since such phenomenon is not observed at lower strain rates (0.01 and 0.001/ sec.), it indicates strain rate assisted high temperature phenomenon, triggering the formation of some intermetallics. Since, specimen crumbled every time after the completion of testing, intensive microstructural analysis could not be carried out. However, optical microstructure study of crumbled pieces confirms thickened grain boundaries (Fig. 7.12), which may be due to precipitation/ diffusion at higher temperature under higher strain rate and this could have became source of crack initiation. It calls for further detailed submicrostructural analysis.

For microstructure observation, specimens from the central part of deformed billet were taken, since it has the maximum deformation. Upon isothermal hot working, dynamic recrystallization occurs and results in a mixture of fine equiaxed grains and deformed elongated grains. DRX grains are mostly present at the original grain boundaries decorated with a narrow region, giving the appearance of a necklace type structure. This has been noted in all the alloys.

Microstructure of the alloys after deformation is found to have γ + lamellar phase in varying amount. It is due to cooling rate from hot deformation, presence of boron *[92, 135, 138, 304]*. Morphology of lamellar grain boundary also changes with localized aluminium content. While the lamellar grain boundary of Ti44Al is straight, that of Ti48Al alloy is serrated. Linearity of the LGB increases as aluminium content decreases *[311, 312]*. This difference is mainly caused by the different α to γ transformation temperature. The mechanism of the formation of serrated LGB is not clear but the high diffusivity of atoms at the high temperature seems to be an important factor *[301]*.The hardness of the alloys also increase with decreasing Al content *[312]*. Since the alloy in the present work contains 48 at% aluminium, presence of lamellar as well as γ grains were found. Especially when the alloy contained small amount of boron (0.1 at%) i.e. alloy *A3* and *A5*, significant amount of lamellar phase were noted, since boron helps to form lamellar phase *[304]*.

Lamellar content also depends on the rate of cooling from the elevated temperatures [92], like cooling during and after mechanical working *[304]*. In many cases boron free alloys develop lamellar structure at slow cooling [92]. Microstructure also varies from the central and peripheral regions of the ingot with respect to the volume fraction of the lamellar grains, it decreases from the surface to the centre of the ingot. This has attributed to the difference in cooling rates. Considering this, microstructural analysis was carried out on the samples drawn from the core of deformed samples.

7.6.2 DEFORMATION MECHANISMS

Strength and ductility of γ-TiAl alloys are affected by different parameters like stoichiometry, heat treatment, deformation temperature, impurity content, grain size and alloying additions. Some of these parameters have also been observed to affect the microstructural mechanisms of deformation. At room temperature, deformations mechanisms of single phase γ alloys have been reported as superdislocations, stacking faults and twins associated with partial dislocations. However, the mechanism of hot deformation is rather complex and vary considerably from alloy to alloy. Dynamic processes (recovery and recrystallization) occur during hot deformation. Dynamic recovery results from the annihilation of dislocations due to ease of cross slip, climb, and dislocation unpinning at the hot working temperatures, whereas in dynamic recrystallization, dislocation annihilation only occurs, when the dislocation density reaches a critical levels that strain free recrystallized grains are nucleated. The stress-strain curve for a metal undergoing dynamic recovery shows an increase in flow stress upto to a steady state value that corresponds to the development of a steady state substructure. But in dynamic recrystallization, the rate of strain hardening is high until recrystallization occurs then flow stress drops rapidly as recrystallization progresses. Characteristic stress strain curves representing dynamic recovery (DRY) and dynamic recrystallization (DRX) is presented in Fig. 7.23.

From the flow curves obtained for different alloys, it is clearly seen that, flow stress increases first with strain and reaches to maximum, which is similar to typical curve shown in Fig. 7.23 for dynamic recrystallization. It is also observed that, microstructure obtained in hot deformation of all the alloys under different conditions, mainly consists of fine recrystallized grains and lamellar packets. There were few cases where twinned structures were observed. These are found to be in near isothermal working (like pack forging, open die forging, Fig. 7.8d, Fig. 7.9a, Fig. 7.19). It can be attributed to lowering of deformation temperature or presence of thermal gradient across the specimen.

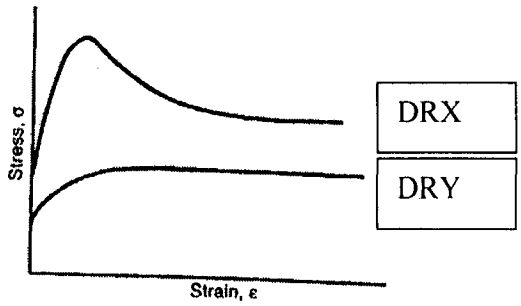

Fig. 7.23: Characteristic curve for dynamic recovery and dynamic recrystallization *[313]*

Also may be due to relatively higher strain rate in open die forging/ pack forging *[159]*, which was carried out under hydraulic press at strain rate ≥0.1/ sec. Also, there was no evidence of presence of high density dislocation and fault, which are typical of deformation assisted by dynamic recovery process. In only one specimen (alloy *A5*, deformed at 750^{0}C), superdislocations have been observed. It indicates lower temperature deformation may be assisted by dynamic recovery process. Also, flow stress variation is found to be varying significantly with temperature, which is also an indication of dynamic recrystallization process. Therefore, it can be summarized that dynamic recrystallization is the predominant mechanism of hot deformation of these alloys and dynamic recovery may also be operative alongwith dynamic recrystallization below certain temperature (for alloy *A5*, ≤750^{0}C).

7.7 SUMMARY

Hot isostatic pressing (under argon), hot isothermal forging (under vacuum) and hot near isothermal forging (ambient) of all the alloys has been carried out in the temperature range of 1200-1350^{0}C. Surface cracks were observed only in the case of near isothermal forging (open die forging). Hot isothermal compression testing of three alloys (*A1*, *A3* and *A5*) was carried out at temperature ranging from 750-1250^{0}C and with strain rate of 0.001 to 0.1/ sec under vacuum. In this case, surface crack/ were observed only in case of specimens tested at high strain rate (0.1/ sec) and low temperatures (750-850^{0}C).

Peak flow stress is found to decrease with increase in temperature and decrease in strain rate. Peak stress is found in the range of 0.1-0.3 strain. Also, anomalous behaviour at very high temperature, >1150^{0}C and at high strain rate (0.1/sec) was observed in alloy *A3*, where increase in flow stress was observed.

Stress-strain curve have been divided in three stages. Flow hardening, steady state stage and flow softening stage. Steady state stage, useful for deformation is found be more in the deformation at strain rate of <0.01/sec. Among the alloys *A1-A5*, most of the alloys have shown wider steady state stage for the alloys deformed between 950-1150^{0}C at slower strain rates (<0.01/ sec.). This also indicates the zone of plastic deformation. Hot workability maps based on observations of hot compression tested samples show 950-1150^{0}C is the zone of sound deformation with maximum strain rate of 0.01/ sec.

Microstructures of all the alloys were found to be refined after isothermal and near isothermal hot deformation. Microstructure of boron free alloy (*A1*) showed two phase (α_2 and γ), whereas boron containing alloys (*A2-A5*) showed lamellar structure alongwith single phase γ. This indicates role of boron in formation of lamellar structure. Alloys made with smaller size of Ti particle showed relatively finer microstructure than alloy made with larger grain size, indicating role of initial Ti particles (used in reaction synthesis) even after deformation.

Content of lamellar phase in boron containing alloys, is found to be increasing with increase in temperature. Lamellar phase volume fraction in alloy *A3* and *A5* is found to be upto ~90% for the alloys tested at higher temperature near to α transus (>1150^{0}C). Also, interlamellar spacing has similar trends as noted in hot working of alloys i.e. at higher temperature and slow strain rates, spacing is higher and vice versa.

Presence of twins has been noted in alloy (*A2*) deformed with relatively higher strain rate (≥0.1/sec, through pack forging and open die forging) indicating role of strain rate and temperature gradient.

Higher content of recrystallized grains with smaller size have been observed as the rate of deformation increases (from isothermal to open die forging) in presence of temperature gradients (in open die forging). Similar trend is seen for interlamellar spacing in various processes. Interlamellar spacing has been estimated <2.5μm depending on the rate of loading. Also, content of lamellar phase was found to be higher for open die forged specimens, indicating deformation under stress gradient and temperature gradients favours such type of microstructures. Amount of DRX grains in isothermal forging for all the alloys was found to be nearly same.

Two different phenomenon have been observed with respect to generation of DRX grains. Percentage DRX grains is higher in open die forging than isothermal pressing at same temperature, indicating content of DRX grains are higher in case of higher strain rates.

Whereas, it is reverse in case of isothermal forging. In this case, percentage DRX grain decreases with increasing strain rate. However, size of DRX grains is found to be increasing with decreasing strain rate and vice versa in both the cases.

DRX grains are found to be present between the primary grains. It indicates these DRX are the transformation products of aluminium rich aluminide (first formed) during reaction synthesis, which was converted to TiAl subsequently during homogenization. Grain size of DRX is found to vary between 5-20μm. Size and volume fraction of DRX grain is found to decrease with increase in strain rates. Growth of dynamically recrystallized grains was observed with increasing temperature and decreasing strain rate and vice versa. Formation of DRX at 750°C indicates that, it may be the minimum temperature of deformation to trigger recrystallization.

Lamellae orientation difference within the grain indicated multiple nucleation sites along the grain boundary for lamellar phase transformation. Bending of lamellae is specifically seen in cases, where higher amount of working (~50%) was imparted.

At higher temperature (>1150°C), localized flow softening and deformation band (at 0.1/sec $\dot{\varepsilon}$) formation are seen, which would have lead to inter granular micro crack formation along with thickening of plate boundaries/ grain boundaries.

Presence of α_2 phase, γ phase, twins, lamellar phase etc. has been confirmed through TEM. Long platelets of α_2 and γ phase is observed with moderate dislocation density for the samples deformed at relatively lower temperatures (750-850^{0}C). This indicates, dislocations are annihilated in high temperature working and resulted in fine recrystallized grains.

Microhardness of recrystallized grains (R), single phase (S) and lamellar phase (L) was found to be between 214-380Hv, 520-668Hv and 388-497Hv respectively. On an average lamellar phase has microhardness of ~430Hv. Observing the microstructure closely, it shows presence of very fine lamellae could have attributed to higher microhardness.

Dynamic recrystallization is found to be the restoration processes of γ-TiAl base alloys during high temperature deformation. The easiness of dynamic recrystallization in TiAl probably results from lower stacking fault energy (SFE) and poor mobility of the dislocations. Presence of twins confirms the twinning as a mode of deformation in hot deformation of titanium aluminides.

Chapter-8

DEFORMATION STUDIES – II
HOT WORKABILITY, DEVELOPMENT AND VALIDATION OF CONSTITUTIVE EQUATIONS

8.1 INTRODUCTION

Ductility is a general way to compare the deformation resistance of material. However, ductility alone is insufficient in the evaluation of workability, because it depends on several factors besides fracture susceptibility of material. Workability is not merely a property of a material but a characteristic of the material/ process system, where, specific stress-state conditions of a particular metalworking process is also important. For example, the tensile elongation of a material may be enhanced (or necking may be delayed) by the application of an external hydrostatic compression or by slow speed deformation of a specimen with a stable fine grained structure at higher temperatures. In other words workability consists of two independent parts: 'state-of-stress' (SOS) workability and intrinsic workability. SOS workability depends upon the geometry of the deformation zone in which the workpiece is subjected to a three dimensional stress state consisting of shear stress components (contribute to plastic flow) and hydrostatic component, which decide workability. Hydrostatic component should be essentially compressive for higher workability. The 'state-of-stress' workability is specific to the mechanical working process and is independent of the material behaviour. The present work is carried out to understand the material behaviour and therefore 'state-of-stress' is not discussed in the present work in detail.

The intrinsic workability depends upon the initial microstructure as decided by the alloy chemistry and prior processing history, and its response to the temperature, strain rate and strain in the processing. This response is embedded implicitly in the flow stress variation with temperature, strain rate and strain and is represented mathematically as a constitutive equation. However, as a part of the explicit response of the material to the imposed process parameters, certain microstructural changes occur within the material in terms of microstructural damage as the flow may be unstable or localized. Alternately, the

microstructure may undergo a favorable reconstitution like dynamic recrystallization. Therefore, both the aspects are considered in material process modeling to obtain safe working zone.

Workability problems can arise when metal deformation is localized in a narrow zone. This results in a region of different structures and properties that can be the site of failure in the deformation process or in the service. It is commonly caused by the formation of a dead metal zone between the workpiece and the tooling. This can arise when the workpiece is constrained from sliding at the interface, it barrels, and the friction-hill pressure distribution is created over the interface. A similar situation can arise, when the processing tools are at a lower temperature than the workpiece *[313]*. However, flow localization may occur during hot working in the absence of frictional or chilling effects. In this case, localization of metal flow results from flow softening. It arises during hot working as a result of deformation heating or microstructural instability, such as the generation of a softer texture during deformation.

Workability also depends on grain size and grain structure. When grain size is large, workability is lower, because cracks may initiate and propagate easily along the grain boundaries. Moreover, in cast structures, impurities are frequently segregated, creating regions of low workability. Workability also decreases with increase in alloy content due to formation of precipitates and low melting compounds *[313]*.

Considering the above explicit responses (microstructural changes) and implicit responses (strain rate, temperature dependence on flow stresses), processing maps and constitutive equations are developed, which represent deformation behaviour of the material. Using the data obtained through hot isothermal compression test of different alloys, processing maps have been generated and constitutive equations have been derived.

Processing maps developed earlier on the basis of deformation mechanisms and fracture mechanisms have limited usefulness and are applicable for pure metals and simple alloys. It does not apply for complex alloys where strain rate sensitivity varies as a function of strain rate and temperature. Therefore, approach based on macroscopic determination of flow stress as a function of temperature and strain rates has been adopted in the present study. It applies criteria of instability to identify the regions of temperature and strain rates that should be avoided during processing. Microscopic studies identify the nature of instability during hot deformation of the materials. This method maps the power efficiency of the

deformation of the material in a strain rate/ temperature space, known as Dynamic Material Modeling (DMM). This methodology describes the dynamic path in response to an instantaneous change in strain rate at a given temperature and strain rate. As such, it describes how workpiece material dissipates applied power by various metallurgical processes, depending on the instantaneous change in strain rate at a given temperature and strain. In its general form, DMM is considered to be a generalized concept of workability that plays a role in unifying the relationships among constitutive behaviour, hot workability and microstructure development. This concept has been applied in the present work to determine the safe working zone for alloys *A1*, *A3* and *A5* through processing map approach.

8.2 HOT WORKABILITY AND MICROSTRUCTURE CONTROL: PROCESSING MAP APPROACH

8.2.1 STRESS AT DIFFERENT TEMPERATURES AND AT DIFFERENT STRAIN FOR VARIOUS ALLOYS

Different metals have different workability limits, which change with chemistry, grain size, temperature, second phase content and with strain rate. Several tests have been evolved for various purposes. Hot isothermal compression test has been found to be simple and useful test and the same has been used in the present study. Flow stress values at various compressive strains in hot isothermal compression test have been obtained from stress-strain curves (Fig. 7.5) and are presented in Table 8.1-8.3 for alloy *A1*, A3 and *A5* respectively. It has been noted from Table 8.1-8.3 that, flow stress varies with temperature and strain. Peak stress obtained at various true strains at respective temperatures for all the three alloys are given in Table 7.2.

From the Tables 8.1-8.3 and Fig. 8.1, variation in flow stress with temperature is clearly seen. It is noted that flow stress decreases with increase in temperature. But reduction in flow stress with temperature is not at a constant rate. It is clear from Fig. 8.1a that slope changes at 1050^0C, where rate of decrease in flow stress is similar in most of the conditions except 0.4 strain ($0.001 s^{-1}$ $\dot{\varepsilon}$), 0.5 strain ($0.1\ s^{-1}$ and $0.01\ s^{-1}$ $\dot{\varepsilon}$). For these cases, marginal increase in rate of change of flow stress is seen maintaining similar trend of decreasing flow stress with increase in temperature.

Table 8.1: Flow stress values as a function of T and $\dot{\varepsilon}$ for alloy *A1*

Strain	Strain rate	Stress (MPa), at different temperatures		
		950, ^{0}C	1050, ^{0}C	1150, ^{0}C
0.1	0.001	220	62	33.7
	0.01	299	163	87
	0.1	406	247	170
0.2	0.001	225	72	33.2
	0.01	314	190	95
	0.1	414	243	171
0.3	0.001	215	78	31.7
	0.01	271	191	74
	0.1	370	227	164
0.4	0.001	180	74	29.8
	0.01	226	182	70
	0.1	315	198	147
0.5	0.001	120	63	27
	0.01	175	155	59
	0.1	276	165	115

Table 8.3: Flow stress values as a function of T and $\dot{\varepsilon}$ for alloy *A5*

Strain	Strain rate	Stress (MPa), at different temperatures		
		750, ^{0}C	950, ^{0}C	1150, ^{0}C
0.1	0.001	430	200	46
	0.01	480	322	82
	0.1	560	405	171
0.2	0.001	530	217	49.6
	0.01	535	339	88
	0.1	500	425	190
0.3	0.001	580	215	48.7
	0.01	530	330	86
	0.1	395	415	200
0.4	0.001	550	195	43
	0.01	452	285	78
	0.1	195	370	180
0.5	0.001	478	150	32
	0.01	313	210	60
	0.1	82	292	145

Table 8.2: Flow stress values as a function of T and $\dot{\varepsilon}$ for alloy *A3*

Strain	Strain rate	Stress (MPa), at different temperatures				
		850, ^{0}C	950, ^{0}C	1050, ^{0}C	1150, ^{0}C	1250, ^{0}C
0.1	0.001	367	184	104	55	22.3
	0.01	418	316	177	95	25
	0.1	432	388	307	105	55
0.2	0.001	376	187	108	59	22
	0.01	383	356	186	100	16
	0.1	541	396	328	130	133
0.3	0.001	375	183	103	58.5	18.6
	0.01	330	360	183	95.3	8
	0.1	565	376	316	327	190
0.4	0.001	360	171	93	54	15
	0.01	258	330	170	81	5
	0.1	533	327	276	450	240
0.5	0.001	331	150	72	43	9
	0.01	189	262	147	57	3.4
	0.1	395	251	201	530	272

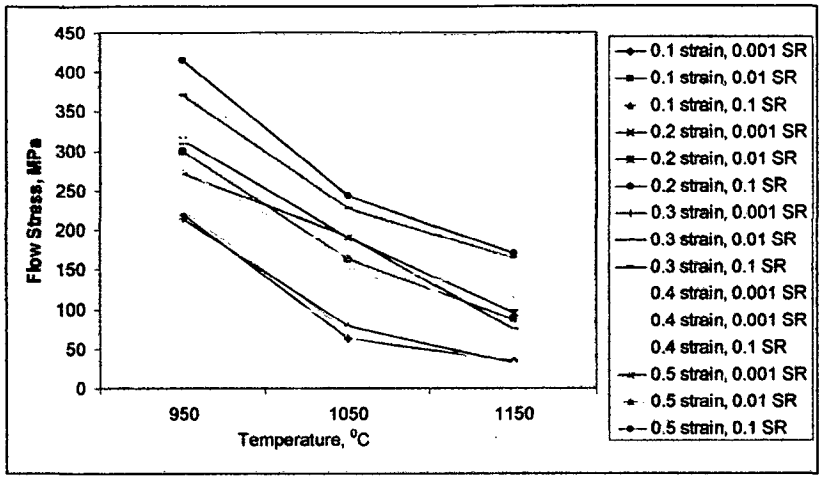

(a)

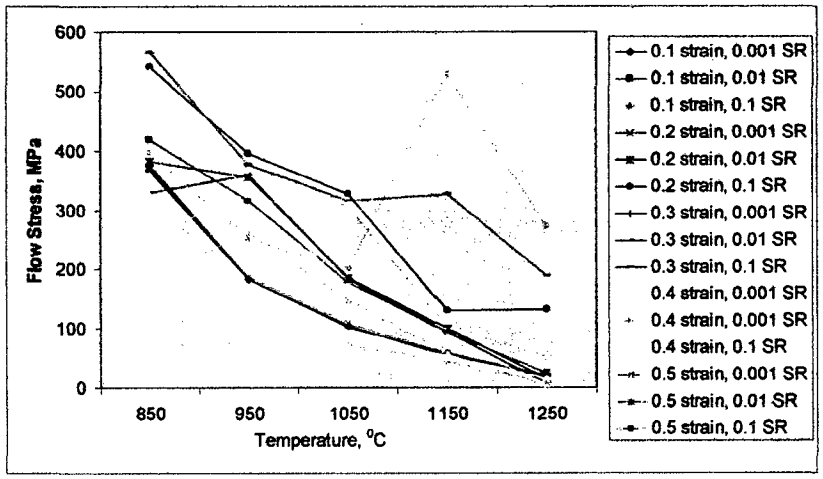

(b)

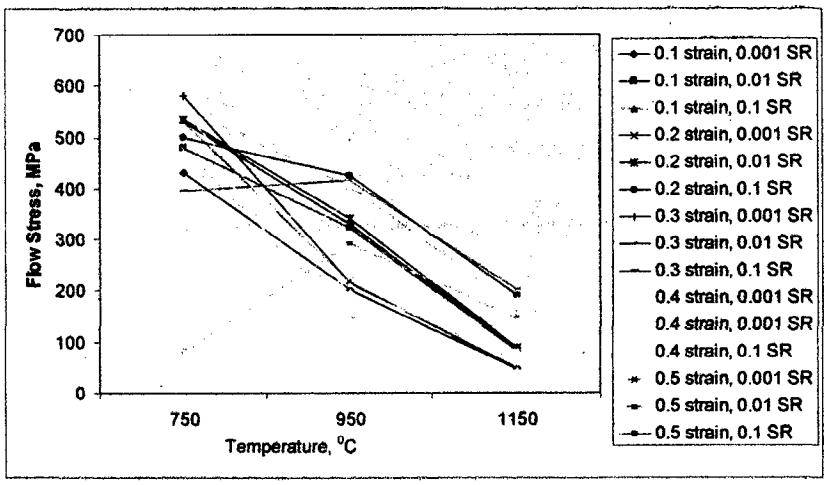

(c)

Fig. 8.1 : Variation of flow stress with temperature at different strain and strain rates, (a) alloy *A1*, (b) alloy *A3*, (c) alloy *A5* (SR denoted in plots corresponds to 'strain rate per sec.')

Decrease in slope (in most of the cases) after 1050^0C means, rate of decrease in flow stress was higher between 950^0C to 1050^0C and the same (rate of decrease) has come down after 1050^0C. This is due to pronounced effect of dynamic recrystallization at 950-1050^0C. After 1050^0C, flow softening and growth of dynamically recrystallized grains makes relatively smaller difference in flow stress and therefore slope decreases. Flow stress is found to be higher at higher strain rate i.e. at $0.1s^{-1}$ strain rate and 0.01 s^{-1} strain rate at all the temperatures and strain. At higher strain rate, grains (dynamically recrystallized) shall be fine, which results in higher flow stresses. Also, flow softening is not predominant due to non availability of sufficient time for rearrangement of strain free recrystallized grains.

In Fig. 8.1b, it is observed that flow stress changes differently (than Fig. 8.1a) with increase in strain. This is all due to role of strain hardening and flow softening. Initially, strain hardening is predominant upto 0.3 strain, so flow stress increases then it decreases from 0.4 strain onwards due to predominance of flow softening. This trend is seen for 0.1 s^{-1} $\dot{\varepsilon}$ at all the temperatures. However, at 1150^0C and 1250^0C (only at $0.1s^{-1}$ $\dot{\varepsilon}$), different behaviour is seen, where flow stress start increasing with strain. This has been explained in section 7.3.2. Flow stress is found to be increasing at 850^0C to 950^0C test temperatures. It is due to premature failure seen in case of 850^0C, where only strain hardening plays major role followed by failure of specimen. Therefore, from these results and results of alloy *A5* at 750^0C, it can be said that, upto 850^0C, alloy strength is not truly flow stress but it shows only max. stress before failure. It means flow stress can be marked for the maximum stress at a specific strain rate for the alloy tested from 950^0C onwards at specific strain. In all other tested specimens, general trend of decreasing flow stress with increasing temperature is observed with marginal change in slope. Even flow stress decreases in case of 0.1 s^{-1} $\dot{\varepsilon}$ from 1150^0C to 1250^0C at all the strain. Peak flow stress is noted at 0.2 strain in all the cases except at 850^0C (0.1 s^{-1} $\dot{\varepsilon}$) where peak stress is found to be at 0.3 strain, showing strain hardening is continued to be predominant upto 0.3 strain due to relatively higher strain rate and lower temperature.

In the Fig. 8.1c, a distinct trend is seen with respect to variation in flow stress with temperature for different strain rates. It is noted that slope changes at 950^0C. But change is different for different strain rates at a specific strain. For 0.001 s^{-1} $\dot{\varepsilon}$, slope is decreasing at 950^0C, whereas it is marginally increased at 950^0C (for 0.01 s^{-1} $\dot{\varepsilon}$). A very unique trend is

seen in case of 750^{0}C to 950^{0}C for 0.1 s^{-1} $\dot{\varepsilon}$ at 0.3 to 0.5 strains where flow stress is increasing with temperature, whereas it is similar to 0.01 s^{-1} $\dot{\varepsilon}$ slope for 0.1 s^{-1} $\dot{\varepsilon}$ at 0.1 and 0.2 strain. This is due to formation of large amount of microcracks at 750^{0}C deformation temperature due to lack of flow softening, which grows after 0.3 strains and results in premature failure showing less flow stress. In true sense, it is not the flow stress, instead it is fracture stress at that temperature. Flow stress is found to be higher at higher strain rate i.e. at 0.1 strain rate and 0.01 strain rate at all the temperatures and strains except at 750^{0}C (0.1 s^{-1} $\dot{\varepsilon}$ and 0.3-0.5 strain). High flow stress at higher strain rates are due to similar reasons noted for alloy *Al* and lower flow stress at 0.1 s^{-1} $\dot{\varepsilon}$ (0.3-0.5 strain) is due to premature failure of specimen.

8.2.2 PROCESSING MAPS

Processing map is an explicit representation of the response of a material, in terms of microstructural evolution, to the applied process parameters. It consists of superimposition of power dissipation map and an instability map. These maps have been developed for all the three alloys at three different strains 0.1, 0.3 and 0.5 and are presented in Figs 8.2-8.5. The input to generate a processing map is the experimental data of flow stress as a function of temperature, strain rate and strain. Since maps generated will be only as good as the input data, accurate and reliable technique for generating data has been used (isothermal hot compression test in a Gleeble thermomechanical simulator).

The map exhibits several efficiency 'hills' which appear as 'domains' with successively increasing isoefficiency contours. The efficiency of power dissipation represents the relative rate of entropy production, the highest being that for a linear dissipator. If the material system does not produce entropy constitutively at a rate that at least matches the rate of entropy input through imposed process parameters, the flow becomes localized and causes flow instability. The regions of stability correspond to areas on a map where the energy dissipation process of the material is in a steady state. Stability criteria are

$0 < m \leq 1$

$\partial m / \partial(\log \dot{\varepsilon}) < 0$

Further, the stability is represented by dimensionless parameter $\xi(\dot{\varepsilon})$, which is evaluated as a function of temperature and strain rate. Metallurgical instability during plastic

flow occurs in regimes where $\xi(\dot{\bar{\varepsilon}})$ is negative. Instability can be due to adiabatic shear bands, flow localization, dynamic strain aging (Luder's band), kink bands, mechanical twinning and flow rotations. The presence of these instabilities in the microstructure of the component will have to be avoided by keeping away from the processing conditions of such unstable regimes.

The value of strain rate sensitivity (m), efficiency of power dissipation (η) and instability parameter $\xi(\dot{\bar{\varepsilon}})$ values were computed using equations (8.1-8.3) and are plotted in the temperature-strain rate plane to obtain 'm' (strain rate sensitivity) maps, η (power efficiency) maps and instability maps respectively (Figs.8.2-8.5).

The deformation behaviour at high temperature has been dealt with by many forming theories. Prasad and Seshacharyulu (1998) *[314]* have developed the dynamic material model (DMM) under which the work piece is considered as a disspator of power. This model is very effective in describing the deformation behaviour at high strain levels, where dynamic processes such as dynamic recovery and dynamic recrystallization can occur, which is used to construct processing map to identify the deformation mechanism and to predict the deformation defect. Power dissipation occurs by two complementary processes: a large part as heat through plastic deformation and the other part in bringing about microstructural changes. The total power dissipated can be calculated as :

$$P = \sigma\dot{\varepsilon} = \int_0^{\dot{\varepsilon}} \sigma d\dot{\varepsilon} + \int_0^{\sigma} \dot{\varepsilon} d\sigma = G + J \qquad (8.1)$$

The first integral is defined as G content and represents the main power input dissipated in the form of a temperature rise. The second integral is defined as J co-content and is related to the power dissipated by metallurgical processes. The power partitioning between G and J is given through the following equation,

$$\frac{dJ}{dG} = \frac{\dot{\varepsilon} d\sigma}{\sigma d\dot{\varepsilon}} = \frac{d(\ln \sigma)}{d(\ln \dot{\varepsilon})} = m \text{ (strain rate sensitivity)} \qquad (8.2)$$

At a given deformation temperature and strain

$$J = \frac{m}{m+1}\sigma\dot{\varepsilon}$$

The efficiency of dissipation η is obtained by comparing its dissipation through the microstructural changes with that occurred in an ideal dissipation, and is given by:

$$\eta = \frac{J}{J\max} = \frac{2m}{m+1} \tag{8.3}$$

where $J\max = \frac{\overline{\sigma\dot{\varepsilon}}}{2}$ when m=1

Deformation processing should be focused on the regions of maximum efficiency of power dissipation, unless structural instabilities like flow localization etc. occur. The location of regions of microstructural instability is based on principles of maximum rate of entropy production (Ziegler 1965) *[315]* and is found by mapping the instability parameter, $\xi(\dot{\varepsilon})$, where:

$$\xi(\dot{\varepsilon}) = \frac{\partial \ln[m/(m+1)]}{\partial \ln \dot{\varepsilon}} + m < 0 \tag{8.4}$$

In the regions where the material undergoes flow instability, the value of the instability parameter $\xi(\dot{\varepsilon})$ is negative. In fact, the efficiency of power dissipation (η) given in Eq.(8.3) explicitly in terms of the strain rate sensitivity parameter (m), is valid only when the flow stress (σ) - strain rate ($\dot{\varepsilon}$) curve at any strain and temperature obeys the power law:

$$\sigma = K\,\dot{\varepsilon}^{m} \tag{8.5}$$

For this case, the parameter, m is independent of $\dot{\varepsilon}$ and the flow instability condition given by Eq.(8.4) reduces to $m<0$. For complicated alloy systems, the flow stress with respect to $\dot{\varepsilon}$ does not obey the power law and the computation of η in terms of m from Eq.(8.3) and the flow instability condition given in Eq.(8.4) become erroneous.

Therefore, instability criterion has been modified by Murty et al. *[316]* to take care of alloy systems which do not follow the power law. This criterion is applicable for any type of flow stress-strain behaviour. Condition for the metallurgical instability is given as (Appendix A),

$$2m < \eta \tag{8.6}$$

For ideally plastic flow, one half of the power is dissipated in material flow and the other half is dissipated in viscous heat ($G_{max} = J_{max} = P/2$). The behavior of superplastic materials approaches this extreme. The other extreme occurs for materials which are strain rate insensitive, i.e., $m \rightarrow 0$ or $J = 0$. When $J = 0$, $G = P$ and all the power would be dissipated by heat which leads to plastic instability by a continuum process such as adiabatic shearing. Hence,

$$J = 0 \Rightarrow \eta = 0 \tag{8.7}$$

From Eqs. (8.6) and (8.7), the condition for metallurgical instability for any flow stress distribution can be written as

$$2m < \eta \leq 0 \tag{8.8}$$

Thus for stable material flow, $0 < \eta < 2m$ and the range of m values ($0<m\leq 1$) is derived from theoretical considerations of the maximum rate of power dissipation by material systems and experimental observations. The instability criterion (8.8) is valid for any type of σ-ε curve. If σ-ε curve obeys the power law, then $\eta = 2m/(m+1)$ which is always less than 2m for $0<m\leq 1$ and hence the material flow is stable.

Following this criteria, the instability map is generated, which is superimposed on the dissipation map to obtain a processing map. The processing maps are generated using the procedure described by Prasad and Sasidhara (1997) *[317]*.

Fig. 8.2-8.4 (*m* maps) does not specifically identify regions where failure/ instability will occur; it does highlight regions of high strain rate sensitivity. These regions represent where damage is less likely because 'necks' tend to push deformation to other nonnecking areas, thus diffusing the necking mechanism. Strain rate sensitivity about 0.2 to 0.3 is considered quite satisfactory for most typical forming operations where necking is a concern. Very high strains than those experienced during forming operations can be achieved with materials having high strain-rate sensitivity without failure (by necking). For example, *m* reaches values above 0.5 and as high as 0.9 in so called superplastic materials, such as Ti6Al4V or Aluminum 7475. Interestingly, failure of these materials under these conditions is not typically through necking but through cavitation *[318]*. The cavitation, which is the nucleation and growth of tiny cavities, probably occurs at the intersection of surfaces of grain boundary sliding or cooperative grain boundary sliding within the material.

As shown in Fig. 8.2-8.4 (*m* plots) strain rate sensitivity is found to vary in the range of 0-0.55 for alloy *A1*, 0-0.9 for alloy *A3* and 0-0.4 for alloy *A5* depending on strain rates and temperature. This indicates superplastic capability of alloys under various conditions. Alloy *A3* shows maximum strain rate sensitivity among these three alloys upto 0.9. However, it needs to be seen alongwith microstructural damage/ instability due to some other phenomenon like cavitation, which occurs under fine grained, high temperature and high

strain rate conditions. From the plot 8.3 (*m* plots), such condition is seen under high strain rate and high temperature conditions (top right at 0.5 strain, *m* plot Fig. 8.3c). Therefore, grain size shall be playing important role in this case to avoid the cavitation. Alloys *A1* shows highest '*m*' in strain rate and temperature range of 10^{-2}-10^{-3}/ sec with 1000-1100^{0}C whereas alloy A3 shows highest *m* in strain rate and temperature range of 10^{-2}-10^{-3}/ sec with 950-1050^{0}C and at ~10^{-1}/ sec with ~1150^{0}C. This indicates alloy A3 has higher superplastic forming capability and large regions for superplastic deformation. It means small content of boron added in alloy *A3* is definitely helping to improve strain rate sensitivity and correspondingly superplastic forming capability of alloy. This may be through grain refinement and accelerated dynamic recrystallization resulting in fine grains (as noted in previous chapter). For alloy *A5*, *m* plot is indicative only, since testing temperatures have wide gap covering different failure mechanism regimes like at 750^{0}C (failure by cracking in absence of sufficient and uniform flow softening) and 1150^{0}C (failure by flow softening/ cavitation). Therefore, superplastic regime can not be demarcated clearly.

It is also noted from the *m* plots of the alloys that, there is marginal increase with increase in strain except alloy *A1*, where it has similar character for 0.1, 0.3 and 0.5 strain values. This can be due to presence of small amount of boron in alloy *A3* and *A5*, which is affecting the *m* value through its presence as a fine particle of borides helping in dynamic recrystallization and grain refinement during testing (high temperature). Whereas grain refinement in alloy *A1* through dynamic recrystallization does not takes place to the extent as in case of alloy *A3* and *A5* (as noted in previous chapter).

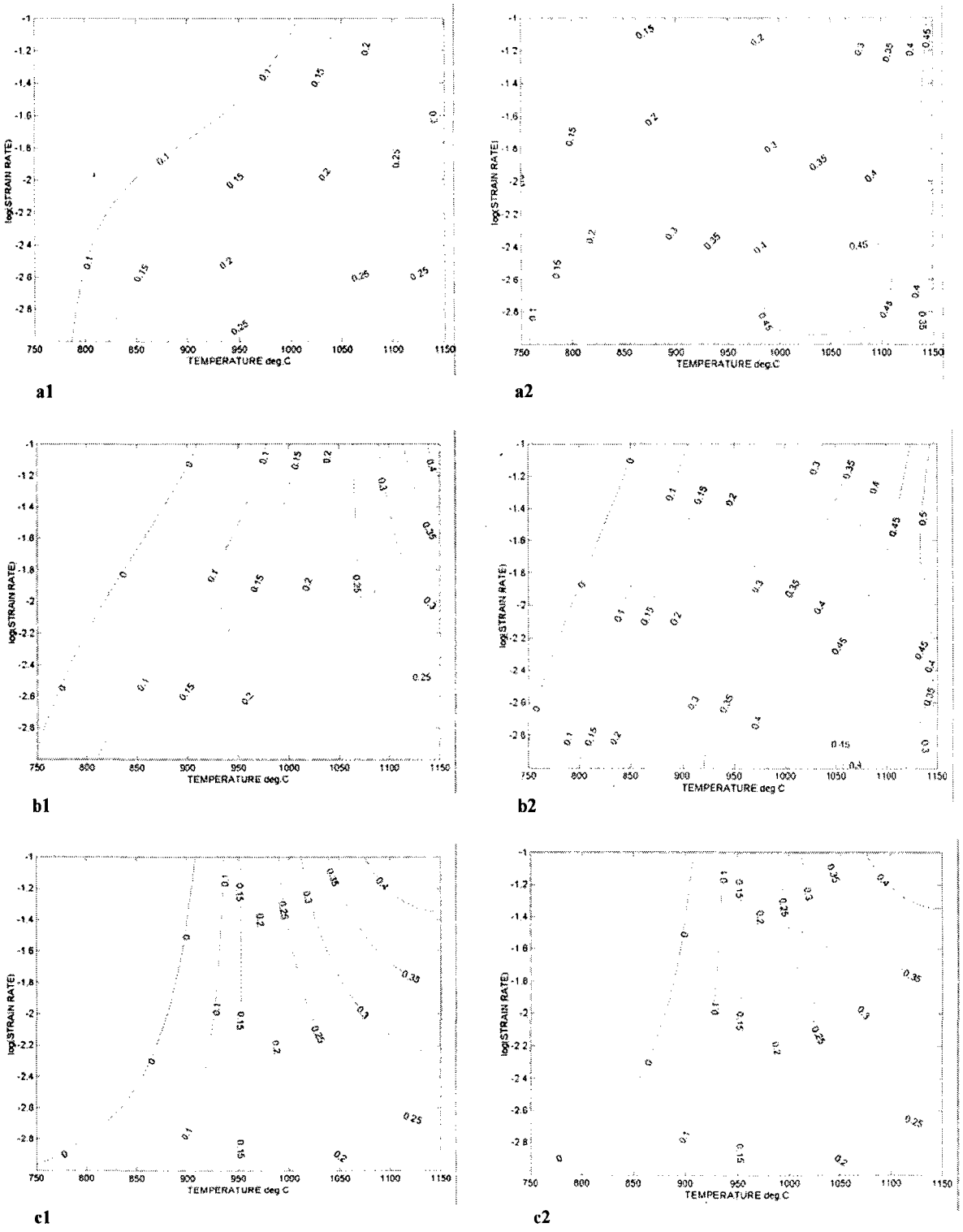

Fig. 8.4: [illegible] contour maps of strain rate sensitivity (a1, b1, c1) and efficiency of power dissipation maps (respectively a2, b2, c2) for alloy *A5*, (a1 & a2) 0.1 strain, (b1 & b2) 0.3 strain, (c1 & c2) 0.5 strain values.

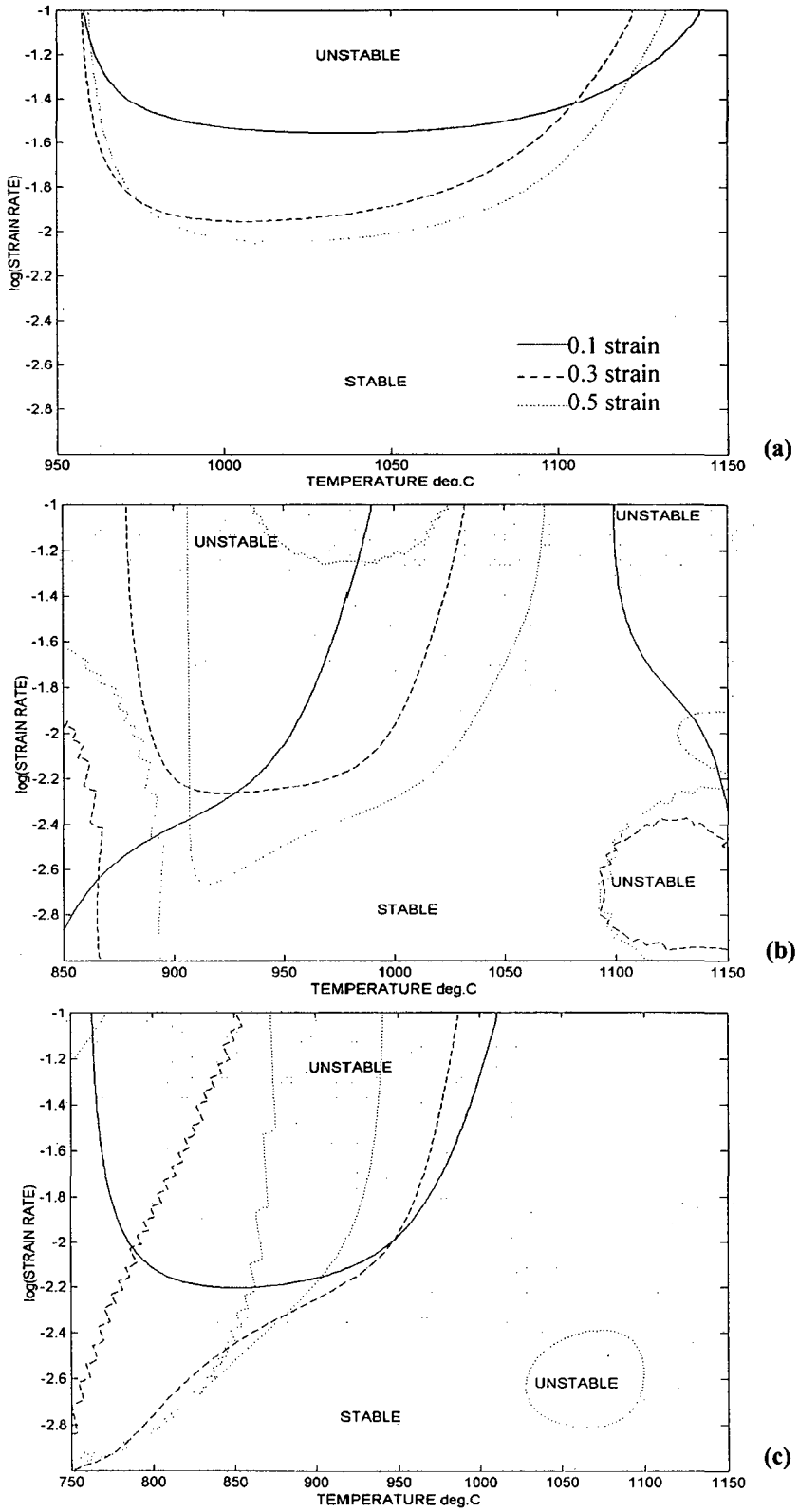

Fig. 8.5: Instability maps for the alloys showing stable (safe) and unstable (unsafe) working zone, (a) alloy *A1*, (b) alloy *A3*, (c) alloy *A5*

Efficiency of power dissipation maps are presented in Fig. 8.2-8.4. The contours in the map represent constant efficiency of power dissipation. It is directly related to the relative rate of entropy production in the system caused by change in microstructure. The map consists of variation of efficiency of power dissipation (η) as a function of temperature and strain rate. Power efficiency upto 0.75 is observed in case of alloy *A1* and *A3* and upto 0.45 in case of alloy *A5*. Mainly three domains are generally seen in power efficiency maps, viz. DRX domain, superplasticity/ wedge cracking domain and ductile fracture domain. However, in the present map mainly two domains viz DRX domain and superplastic domain can be seen. In the present study boundary of these domains is difficult to mark clearly, since microstructure consist of mainly recrystallized grains and lamellar packets with marginal variation only in its content.

DRX domain is found to be in the temperature and strain rate regime of 950-1150^{0}C and 10^{-1}-10^{-2}/sec respectively, which is in the homologous temperature range 0.7-0.8 and at lower than intermediate strain rates (0.1-1 s^{-1}) in the maps (being a low stacking fault energy materials) *[319]*. The maximum efficiency of power dissipation in the DRX domain is found to be 0.45 for alloy *A1*, 0.75 for alloy *A3* and 0.45 for alloy *A5*. Higher efficiency of power dissipation indicates favourable situation for hot deformation of the alloy. The contours in the DRX domain are widely spaced representing a less steep hill and present a fairly wide window, as seen in most of the materials.

Superplastic / wedge cracking domain is found to be in the temperature range of 1050-1150^{0}C under strain rates lower than 0.01s^{-1} for alloy *A1* whereas this domain is in the temperature range of 950-1050^{0}C at strain rates lower than 0.01s^{-1} for alloy *A3*. It shows alloy *A3* can be superplastically deformed at marginally lower temperature than alloy *A1*. Many of the grain boundaries are found to be oriented at >60^0 angles with respect to compression axis. Tensile ductility will be abnormally high in this domain, which becomes poor if wedge cracking occurs. Wedge cracks have not been observed, which occur at grain boundary triple junctions and mostly it gets repaired in compressive state of stress. It is not possible to obtain microstructural evidences of wedge cracks in compression tested specimens. It is normally confirmed through tension test under peak conditions of this domain.

The void formation or ductile fracture domain occurs at lower temperatures and higher strain rates and is characterized by a steep increase in the efficiency with increasing strain rate and decreasing temperature. This domain has not been found in the present work,

which is mainly relevant to metal matrix composites deformed at higher strain rates. The microstructures exhibit interface debonding and/or particle failure.

Based on the *m* maps and power efficiency maps (η), stable regions can be identified. However, for better clarity, processing maps have been generated in line with *m* and η maps. This clearly shows the stable regions where deformation processing is recommended after considering the practical feasibility. From Fig. 8.5, it is clear that stable region lies in the slow strain rate regime, which increases with increase in temperature. But, again at very high temperature, unstable region is seen where microstructural damage occurs by excessive flow softening and cavitation.

Safe working range for the alloy *A1* is found to be wider as compared to other two alloys *A3* and *A5*, i.e. 950-1150^{0}C under strain rate of 10^{-2}/sec. At higher temperature (1150^{0}C), the alloy can be worked safely at a strain rate of 10^{-1}/sec also, indicating uniform flow softening and absence of microstructural damage. For alloys *A3* and *A5*, safe working zone lies in the similar temperature zone at slower strain rates (10^{-2}-10^{-3}/ sec.). However, small instability region is also noted in case of alloy *A3* and *A5* at higher temperature (1050-1150^{0}C) and slow strain rate (10^{-3}/sec.). This can be due to interaction of hard boride particles with flow softened matrix. Also, another instability region is noted in alloy *A3* at higher temperature and higher strain rate. The possible reasons for this phenomenon have been explained in section 7.3.2. Similar observation of surface cracking was reported by Ha et al. (2007) at higher temperature (1300^{0}C) and higher strain rate (>0.3/sec) *[302]*. High temperature instability region in case of alloy *A5* is relatively lower in alloy *A3*, where Ni-P electroless coated boron particles were used indicating presence of Ni may be helping to minimize the interaction between boron/ borides and matrix. Further investigation needs to be carried out to confirm this phenomenon.

It is also noted that, safe working zone decreases with increase in strain, as seen from Fig. 8.5. This is because increase in strain, brings a mixture of microstructure (partially recrystallized, lamellar and single phase), where stable and unstable phases are present, which oppose further recrystallization. However, this effect is different for different alloys. It is more pronounced in case of alloy *A3* and *A5*, which may be due to presence of additional boride phases. It indicates that, in multicomponent system, as the number of component increases, safe working zone shrinks due presence of more number of phases.

8.3 MODELLING OF FLOW STRESS STRAIN CURVE: DEVELOPMENT AND VALIDATION OF CONSTITUTIVE EQUATIONS

For a given material, the relations between stress components and strain components are presented by a equation known as constitutive equation representing the behaviour of that material. The simplest example of a constitutive equation is well known Hooke's law in elastic regime. During plastic deformation of most of the metallic materials, the stress-strain curve becomes non-linear because hardening (or softening) of the material. The strain rate can also influence the hardening or softening of material. Therefore general form of constitutive equation for deformation processing is,

$$\sigma \equiv f(\varepsilon, \dot{\varepsilon}, T)$$

where σ is the equivalent (effective) stress, ε is equivalent (effective) true strain, $\dot{\varepsilon}$ is strain rate and T is processing temperature.

8.3.1 BASIC CONSTITUTIVE EQUATION

The most frequently used constitutive equation is

$$\sigma \equiv K\varepsilon^n \dot{\varepsilon}^m + Y \tag{8.9}$$

Where 'n' is strain hardening exponent, *m* is the strain rate sensitivity, and Y and K are coefficients. Strain rate sensitivity is important at elevated temperatures, while it has little influence at room temperature for most metallic materials. In contrast, strain hardening exponent becomes more significant with decreasing temperature. But, this equation does not reflect the effect of temperature. A more fundamentally sound equation for the relationship between the flow stress and the deformation parameters has been proposed by Sellers (1990) *[320]* by assuming materials flow during deformation as a thermally activated process. They pointed out that there exists a universal hyperbolic sine function description of the flow behaviour, as indicated in eq. (8.10):

$$\dot{\varepsilon} = A[\sinh(\alpha\sigma)]^n \exp\left[-\frac{Q}{RT}\right] \tag{8.10}$$

At low stresses ($\alpha\sigma<0.8$), the equation reduces to a power law:

$$\dot{\varepsilon} = A_1\sigma^n \exp\left[-\frac{Q}{RT}\right]$$

At high stresses ($\alpha\sigma>1.2$), the equation becomes exponential

$$\dot{\varepsilon} = A_2 \exp(\beta\sigma)\exp\left[-\frac{Q}{RT}\right]$$

where, $\beta=\alpha n$, $\dot{\varepsilon}$ is the strain rate, σ is the flow stress, Q is the activation energy of hot deformation, R is universal gas constant, T is the absolute temperature, A, A_1 and A_2 are the constants independent of the deformation temperature and α is experimentally determined constant.

In order to employ Eq. (8.10) for the powder metallurgy TiAl alloy, a numerical curve-fitting method was used to obtain values of the kinetic parameters *[321]*. The Q is an important physical parameter indicating the plastic deformability, and can be calculated as follows :

$$Q = R\left\{\frac{\partial \ln \dot{\varepsilon}}{\partial \ln[\sinh(\alpha\sigma)]}\right\}_T \left\{\frac{\partial \ln[\sinh(\alpha\sigma)]}{\partial(1/T)}\right\}_{\dot{\varepsilon}} \tag{8.11}$$

The first term on the right-hand side of Eq. (8.11), $\partial \ln \dot{\varepsilon} / \partial \ln[\sinh(\alpha\sigma)]$, refers to the slope of $\ln\dot{\varepsilon}$ versus $\ln[\sinh(\alpha\sigma)]$ at different deformation temperatures, and the second term $\partial \ln[\sinh(\alpha\sigma)]/\partial (1/T)$ refers to the slope of $\ln[\sinh(\alpha\sigma)]$ versus the reciprocal of temperature 1/T at different strain rates.

Combined strain rate and temperature dependence of the flow stress during deformation can be represented by:

$$Z = \dot{\varepsilon} \exp(Q/RT) = A\,[\sinh(\alpha\sigma)]^n \tag{8.12}$$

The Zener-Hollomon parameter, the physical meaning of which is the so-called temperature compensated strain rate parameter. Generally, Z can be used to characterize the combined effect of strain rate and temperature on the deformation process, especially the deformation resistivity.

When $\alpha\sigma<0.8$ (in the low stress regime), then Eq. (8.12) reduces to

$$Z = \dot{\varepsilon} \exp(Q/RT) = A_1\sigma^n \tag{8.13}$$

When $\alpha\sigma>1.2$ (in the high stress regime), then Eq. (8.12) reduces to

$$Z = \dot{\varepsilon} \exp(Q/RT) = A_2 \exp \alpha\sigma \tag{8.14}$$

Assuming the hot deformation of the present alloy comes under high stress regime, from Eq. (8.14), $\dot{\varepsilon} \exp(Q/RT) = A_2 \exp \alpha\sigma$

$$\ln \dot{\varepsilon} + (Q/RT) = \ln A_2 + \alpha\sigma \quad (8.15)$$

at constant temperature, $\ln \dot{\varepsilon} = \ln A_2 + \alpha\sigma$ (8.16)

From Eq. (8.15) and (8.16), by linear regression of the relation of $\ln \dot{\varepsilon}$ vs σ at different temperatures, an optimum value of α is determined.

Substituting the values of α and flow stress and utilizing Eq. (8.11), activation energy Q is determined (slopes of Figs. 8.6, 8.7 a-b and 8.8). Value of Q is found to be varying (marginally) with temperature (due to change in α, σ, $\dot{\varepsilon}$ and T in eq. 8.11). Maximum value of Q has been taken for further calculation, since highest activation energy is the practical condition for deformation. Although minimum value of Q indicates the initial feasibility of deformation, highest value of Q shall ensure the continuation of deformation of material.

Taking the natural logarithm each side of Eq. (8.12),

$$\ln Z = \ln A + n \ln[\sinh(\alpha\sigma)] \quad (8.17)$$

Substituting Q and strain rates at different temperatures into Eq. (8.12), the values of Z and ln Z of alloy under different conditions are obtained. Based on the peak stresses, the relationship between ln Z and $\ln[\sinh(\alpha\sigma)]$ is plotted. The slope of the plot corresponding to the value of stress exponent 'n' in Eq. (8.13) is determined and the intercept corresponding to ln A is determined. Therefore, under the deformation conditions over a specific temperature range the hot deformation equation of alloy can be expressed as :

$$\dot{\varepsilon} = A [\sinh(\alpha\sigma)]^n \exp[-Q/RT] \quad (8.18)$$

The proposed deformation constitutive equation gives an estimate of the flow stress for the alloy and can be used to analyze the hot working process.

8.3.2 DEVELOPMENT OF CONSTITUTIVE EQUATIONS

From Table 8.1-8.3, values of ln $\dot{\varepsilon}$, ln σ, α, Q, ln[sinh($\alpha\sigma$)], n, A have been calculated using equation 8.10 to 8.18 and respective plots have been made, which are presented in Figs. 8.6-8.10. Since tested data at 750^{0}C comes under premature failure due to cracking, this data has large variation than the data at other temperatures (Fig. 8.5 for alloy *A5*) and so it has not been considered for further calculation. Therefore, data available for alloy *A5* was found to be insufficient (only at two temperatures 950 and 1150^{0}C), constitutive equations has not been derived for alloy *A5*.

Q for alloy *A1* and alloy *A3* is found to be 335 and 387.5 kJ/ mole respectively. This value is near to the range of that for volume diffusion (290-343kJ/mol) measured by Imayev et al. (2001) *[322]* in TiAl alloy with a typical duplex microstructure, but lower than that reported by Wegmann et al. (2002) *[299]* for other PM TiAl alloy. It is also comparable to the reported values for high temperature deformation of TiAl- base alloys showing softening behaviour, such as 410kJ/ mol for Ti-47Al-1V alloy *[223]*, 465kJ/ mol for Ti-47Al-2V alloy *[323]*, 402kJ/ mol for Ti-45Al-5.4V-3.6Nb-0.3Y alloy *[324]*, 355kJ/mol for Ti-48Al-2Cr-2Nb alloy *[56]* and 327kJ/ mol for Ti-49.5Al-2.5Nb-1.1Mn alloy *[325]*. Work of Liu et al. showed Q as 353kJ/ mol for Ti-46Al-8.5Nb-0.2W *[319]*. Q of 260kJ/ mol was reported by Bertels et al. 2002 for Ti-47Al-2Cr-0.2Si *[326]*, which is slightly lower than Q of Ti-tracer diffusion in single phase TiAl alloys *[244]*. Q for another PM alloy Ti-48Al-2Cr-2Nb is reported to be 385kJ/ mol [308], which is also comparable. High activation energy requirement has also been reported to overcome the high Peierls stress in TiAl *[147, 148]*. Hence, activation energy for hot deformation indicates that, deformation may be through volume diffusion process, where dislocation shall be playing important role.

Value of n (stress component) for alloy *A1* and alloy *A3* is found to be 1.004 and 1.029 respectively. Constant parameter for alloy *A1* and alloy *A3* is found to be 2.22X10^9 and 8.34X10^{11} respectively. Value of α varies for different processing temperature and is given in Table 8.4. General trend of α value in alloy *A1* is seen as increasing with temperature. However, some mixed trend is seen in alloy *A3* and alloy *A5*, where it is higher at lower temperature (750 and 850^{0}C) and is very low at higher temperature (>1150^{0}C, alloy *A3*). This comes under unstable region of deformation, which may be due to premature cracking of alloys at lower and higher temperature (alloy *A3* at 850, 1150 and 1250^{0}C and alloy *A5* at 750^{0}C). Using these values, constitutive equation for alloy *A1* and alloy *A3* has been developed through Eq. 8.10, which is given below as C-1 and C-2 respectively. Under deformations over a temperature range of 950-1150^{0}C, these equations have been derived and the same has been tested for the alloys at different temperatures, which is presented in Table 8.5.

$$\dot{\varepsilon} = 2.22X10^{9} [\sinh(\alpha\sigma)]^{1.004} \exp[-335/RT] \quad (C1)$$

$$\dot{\varepsilon} = 8.34X10^{11} [\sinh(\alpha\sigma)]^{1.029} \exp[-387/RT] \quad (C2)$$

Table 8.4 : α value calculated using equation 8.16 and Fig. 8.6 (at constant temperature)

Temperatures, ^{0}C	α value		
	Alloy *A1*	Alloy *A3*	Alloy *A5*
750	-	-	0.055
850	-	0.0221	-
950	0.0243	0.0193	0.0219
1050	0.0263	0.0204	-
1150	0.033	0.008	0.0284
1250	-	0.014	-

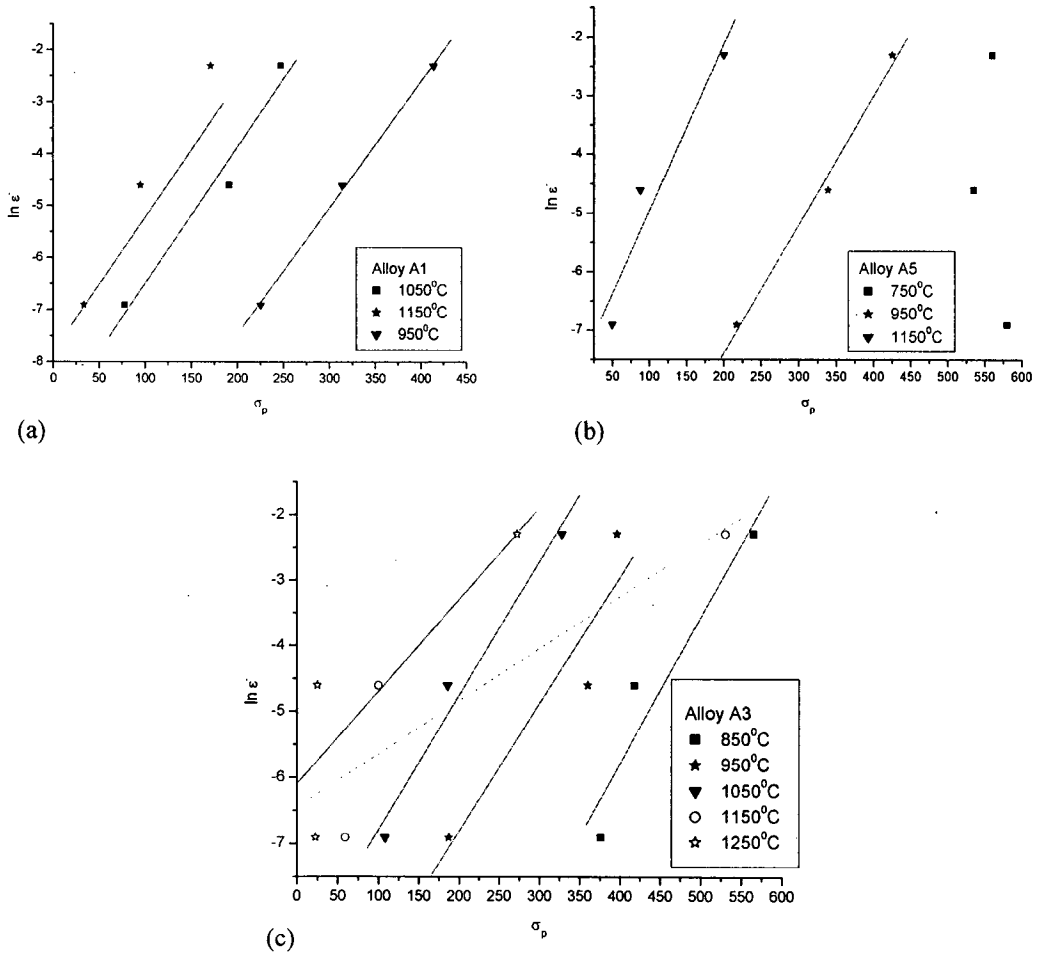

Fig. 8.6 : Plot of ln $\dot{\varepsilon}$ *vs.* σ_p for various alloys where slope of individual plot gives α for that alloy at that temperature,(a,b,c corresponds to plots of alloy *A1*, *A3*, *A5* respectively)

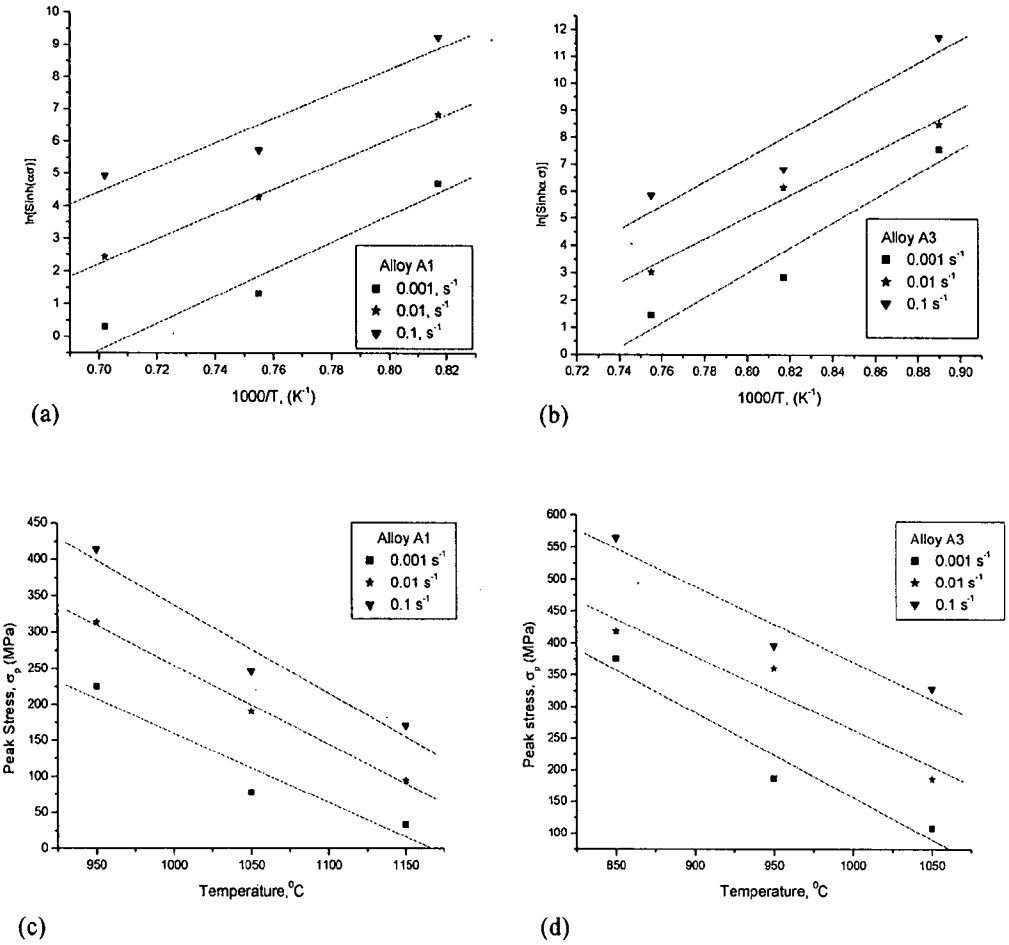

Fig. 8.7 : Relationship between peak stress and temperature in various forms used in determination of Q, (a and c corresponds for alloy *A1*, b and d corresponds to alloy *A3*)

Flow stress/ peak stress relation with temperature have been plotted with various parameters (Fig. 8.7) to obtain the value of variables and constants for constitutive equations. Peak stress observed in alloys at different deformation temperature clearly show the decrease in deformation stress with increase in temperature (Fig. 8.7 c,d). It is in line with general deformation behavior of metallic materials. However, this is found to be followed in the temperature range of 950-1150^{0}C (in strain rate of 0.001-0.01/sec.) indicating it as a safe working range. Similarly, flow stress is found to increase with increase in strain rate (Fig. 8.8). It is also similar to metallic materials where higher strain rate does not have sufficient

time to accommodate the dynamic softening processes and finally strain hardening become predominant. Zener-Hollomon parameter is found to have very close linearity with the peak stress (Fig. 8.9). This confirms the difficulty in processing with increasing peak stress, which is due to lower temperature or due to higher strain rate as represented by increasing Zener-Hollomon parameter.

Strain rate sensitivity (m) is the increase in stress needed to cause a certain increase in plastic strain rate at a given level of plastic strain and at a given temperature. From Fig. 8.10, it is seen that 'm' varies with strain mainly at low strain level (0.1-0.2) and at higher strain level (0.5). At intermediate strain (0-0.4) change in 'm' is marginal. This is due to predominance of strain hardening at initial strain and predominance of flow softening at later stage. At intermediate level, strain hardening and flow softening are balancing each other and therefore changes in 'm' are marginal. It is also observed that 'm' is higher in all the cases with increase in temperature. This is in line with general observations in metallic materials, where 'm' is very low at room temperature and it increases with increase in temperature.

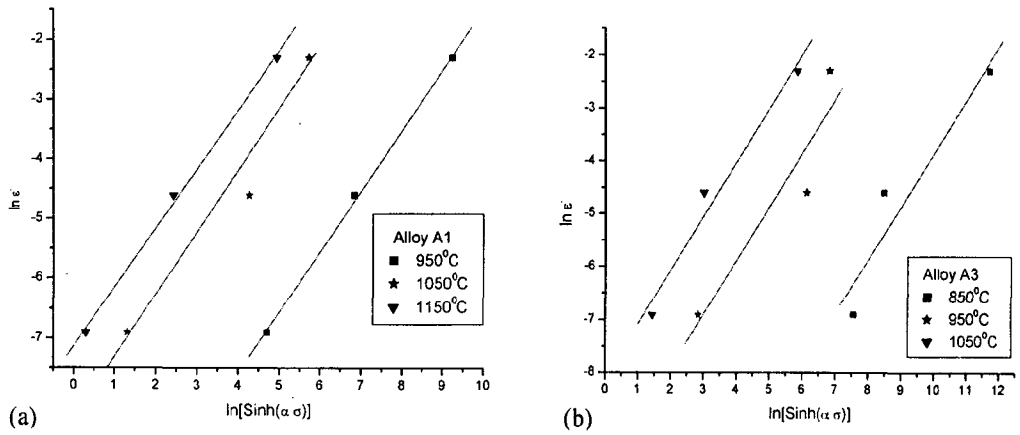

Fig. 8.8 : Relationship between peak stress and strain rate for (a) alloy *A1*, (b) alloy *A3*

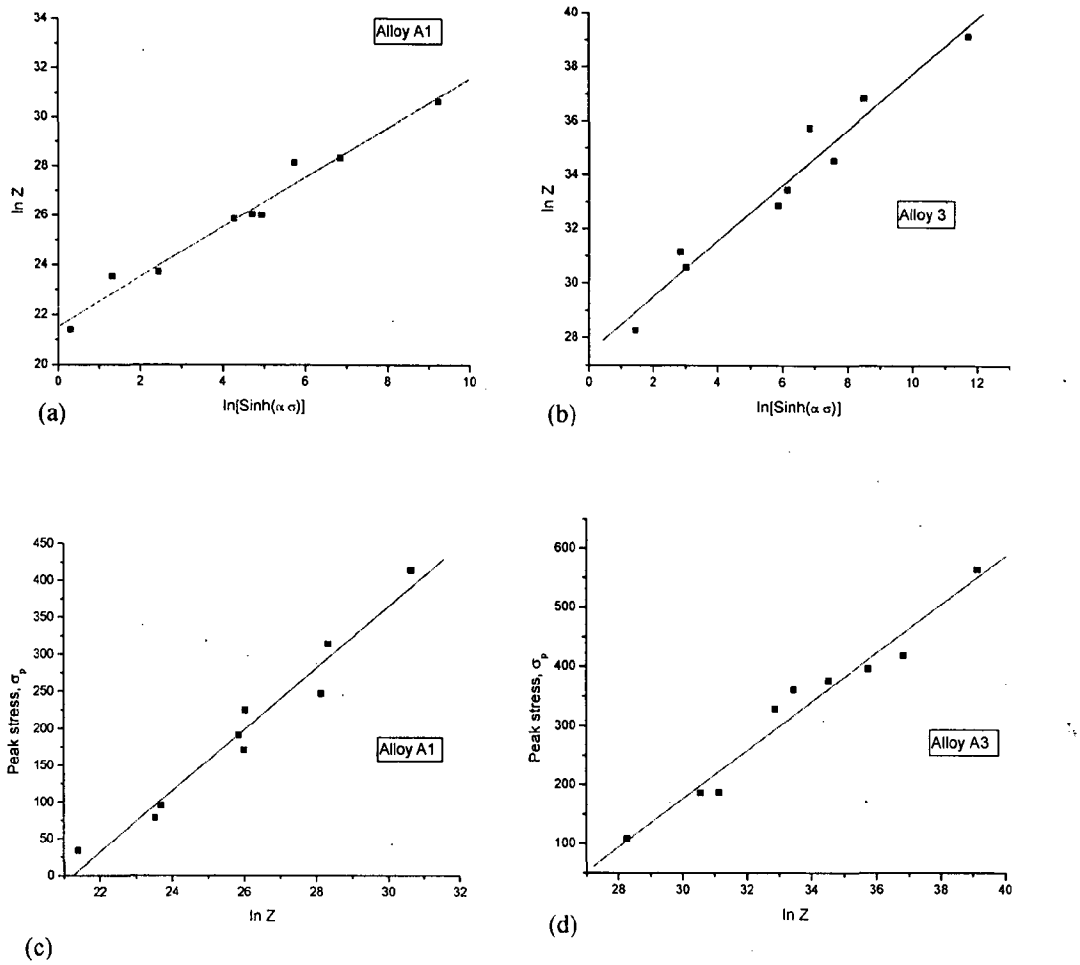

Fig. 8.9: Relationship between peak stress and Zener Hollomon parameter, (a,c) for alloy *A1*, (b,d) for alloy *A3*

It is observed that the changes in microstructural evolution that occurred with decreasing temperature at a fixed strain rate were almost similar to those that occurred with increasing strain rate at a fixed temperature (Fig. 7.10-7.14). Degradation of lamellae and recrystallization of γ phase during high temperature deformation have been observed. The recrystallized grain size (D_{DRX}) developed in the TiAl alloy was dependent on the deformation temperature and strain rate. For the present TiAl alloys, this dependence was found to be ln D_{DRX} = = 2.95-0.038lnZ (for alloy *A1*) and ln D_{DRX} = 4.58-0.080lnZ (for alloy *A3*), as shown in Fig. 8.11.

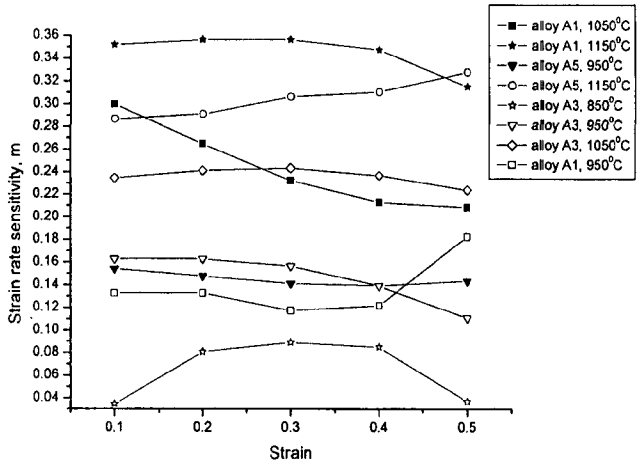

Fig. 8.10 : Variation in strain rate sensitivity with strain at different temperatures

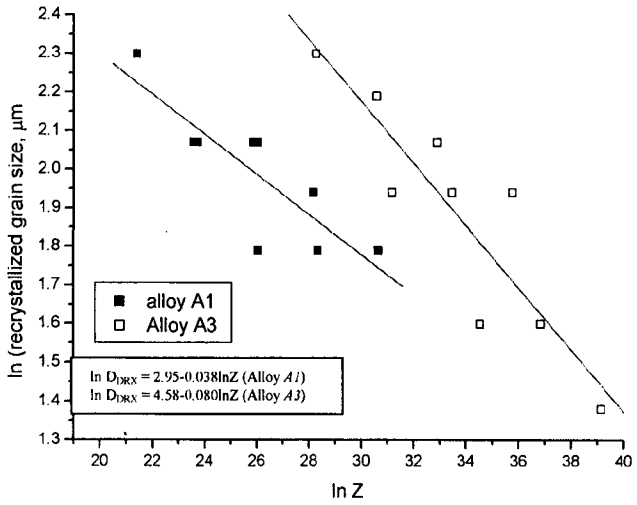

Fig. 8.11 : The variation of recrystallized grain size of alloys with Zener Hollomon parameter

Marginal increase in the recrystallized grain size with increasing the temperature and with decreasing the strain rate, i.e. with decreasing Z is observed. This may be due to availability of time for growth of DRX nuclei as discussed in previous chapter. It means, increase in Z, help in generation of DRX grains i.e. nucleation of DRX grains. It is through decreasing temperature and increase in strain rate (higher Z), resulting in finer DRX grains, which grows at lower strain rates and higher temperature (lower Z). So, it can be stated clearly that, increase in Z help in nucleation and decrease in Z help in its growth. This is due to the fact that, increase in Zener Hollomon parameter results in a larger driving force for

recrystallization, which could be due to increased dislocation density under such conditions. Therefore, it is important to control the deformation parameters in order to obtain the uniform optimum microstructure alongwith successful operation.

8.3.3 PREDICTION OF STRESS-STRAIN CURVES AND VALIDATION OF CONSTITUTIVE EQUATIONS

Using the constitutive equations developed for the alloys, flow stress values for different strain rates and at different temperatures have been calculated and are compared with the experimental values for the same alloy. Constitutive equations developed for alloy *A1* and alloy *A3* has also been applied to alloy *A5* and flow stress has been calculated. Also, these two constitutive equations have been applied to alloys on each of the other alloys to know the universal applicability of the equations. Calculated and experimental values are presented in Table 8.5 and compared through plot shown in Fig. 8.12. From the Table 8.5 and Fig. 8.12, it is observed that flow stress calculated using constitutive equation derived for alloy *A1* and alloy *A3* are very near to experimental value for the same alloy in the intermediate temperature and strain rate i.e. at 950^0C with strain rate of 0.01/sec.

Error range of 10% on the calculated value has been shown in Fig. 8.12 alongwith experimental value. Percentage error is max. upto 9% except three cases i.e. at very low strain rates (0.001/sec) at temperature $>1050^0$C, and high strain rate (0.1) at temperature 1050^0C.

Later case is marginally higher, which can be considered within acceptable range of calculation/ experimental error. Whereas, former case clearly shows equation has not been able to predict the flow stress correctly. This is due to higher flow softening, where time available for dynamic process is sufficient and even higher. This nullifies not only the effect of strain hardening, but also, brings predominance of flow softening. All these indicate that constitutive equation should be applied in sound deformation regime of intermediate strain rate and temperatures.

Similar results were observed for alloy *A3* using constitutive equation C-2. Here also, % error is marginally higher for lower strain rates and for 0.1/ sec strain rate at 950^0C. It indicates the error which was for 1050^0C at 0.1/sec strain rate is seen in case of alloy *A3* at 950^0C at 0.1/sec strain rate. This shows alloy *A3* containing small amount of boron would have acted to decrease the temperature from 1050^0C to 950^0C for this alloy for the similar phenomenon acting for alloy *A1*.

Table 8.5: Calculated and experimental flow stress for alloys at different temperature and strain rates

$\dot{\varepsilon}$	Flow stress and % Error from calculated value using constitutive eq.									Alloy	Remarks
	Cal*, MPa	Exp*, MPa	% Error#	Cal*, MPa	Exp*, MPa	% Error#	Cal*, MPa	Exp*, MPa	% Error#		
	950^{0}C			**1050^{0}C**			**1150^{0}C**				Using
0.001	213.7	225	-5.2	103.35	78	24.49	24.37	33.7	-38.2	*A1*	constitutive
0.01	308	314	-1.9	190.35	191	-0.34	87.19	95	-8.9		eq. derived
0.1	402.6	414	-2.8	277.55	247	11	156.6	171	-9.19		for *A1* (C1)
0.001	176.6	225	-27.38	58.67	78	-32.9	6.63	33.7	-454		Using
0.01	268.7	314	-16.8	141.99	191	-34.5	50.78	95	-124		constitutive
0.1	360.79	414	-14.75	227	247	-8.78	124.1	171	-58		eq. derived for *A3* (C2)
	850^{0}C			**950^{0}C**			**1050^{0}C**			*A3*	Using
0.001	343.2	376	-9.54	225.9	187	17.2	75.6	108	-42.7		constitutive
0.01	444.49	418	5.96	343.6	360	-4.75	183	186	-1.6		eq. derived
0.1	545.7	565	-3.52	461.43	396	14.18	292.72	328	-12.04		for *A3* (C2)
0.001	367.2	376	-2.39	273.32	187	31.58	133.1	108	18.9		Using
0.01	470.9	418	11.24	394	360	8.6	245.4	186	24.2		constitutive
0.1	574.7	565	1.69	514.7.4	396	23	357.8	328	8.33		eq. derived for *A1* (C1)
	750^{0}C			**950^{0}C**			**1150^{0}C**			*A5*	Using
0.001	211	430	-103	237.1	217	8.48	28.32	49.6	-75.14		constitutive
0.01	258.7	480	-89.3	341.85	339	0.83	101.3	88	13.14.2		eq. derived
0.1	294.46	560	-90.1	446.57	425	4.83	181.96	200	-9.91		for *A1* (C1)
0.001	209.5	430	-105.2	195.9	217	-16.7	7.06	49.6	-602		Using
0.01	250.19	480	-91.8	298.16	339	-13.9	60	49.1	-79.2		constitutive
0.1	290.885	560	-92.5	400.33	425	-6.16	146.4	125.69	-59.12		eq. derived for *A3* (C2)

*Cal : Calculated flow stress through constitutive equation, *Exp : Flow stress determined experimentally through hot isothermal compression test, # % error in calculated flow stress from the experimental value

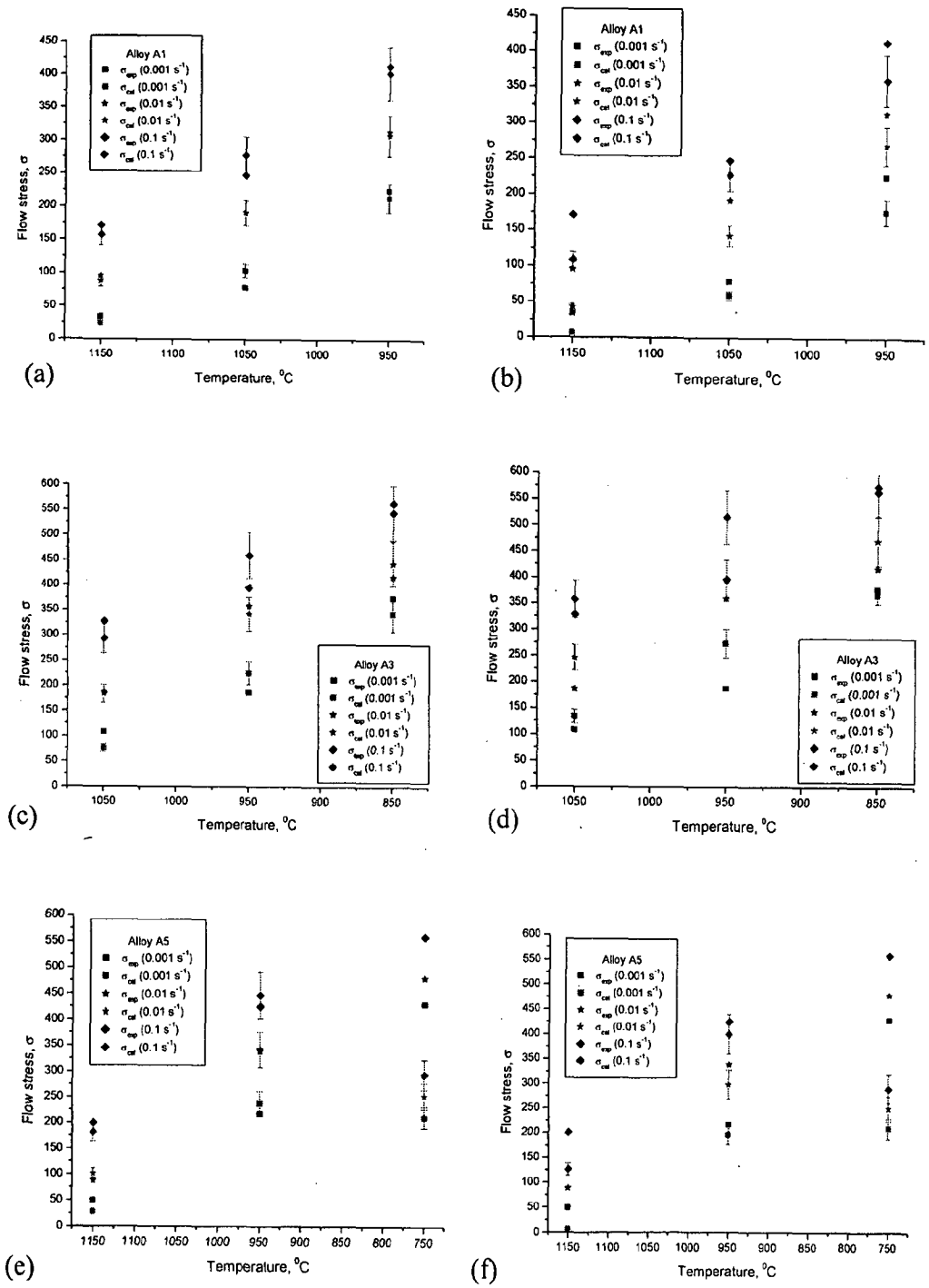

Fig. 8.12: Comparison of flow stress calculated using constitutive equation (with error bars) and experimental values, (a) For alloy *A1* using eq. C1, (b) For alloy *A1* using eq. C2, (c) For alloy *A3* using eq. C2, (d) For alloy *A3* using eq. C1, (e) For alloy *A5* using eq. C1, (f) For alloy *A1* using eq. C2

Both the constitutive equations (C1 and C2) were applied on alloy *A5* for checking its applicability to other alloy. It is observed that, the equation C1 is predicting flow stress very near to experimental flow stress at 950^0C at all the strain rates.

Applicability of respective constitutive equations for other alloys has limitations due to change in values of equation parameters. However, universal applicability of constitutive equation C1 (with very small error) is observed in sound deformation regime where behavior of alloys is mostly similar, i.e. at 950^0C at stain rate of 0.01/sec.

8.4 DISCUSSION

Flow stress certainly depends on the alloy chemistry, which influences the deformation behaviour through phase transformation of the alloy. In the present work, deformation behaviour of three alloys *A1*, *A3* and *A5* show small variation with temperature and strain rates. Boron containing alloys *A3* and *A5* have shown higher flow stress as compared to alloy *A1*. This is due to presence of boron containing intermetallic phase stable upto the processing temperature. Change in flow stress of different alloys with temperature at a specific strain has been clearly observed. It indicates that, the alloys have important effect of small variation in chemistry, which finally affects the safe working zone.

DRX and superplastic deformation are "safe" mechanisms for hot working while dynamic recovery is preferred for warm working. All other mechanisms either cause microstructural damage or inhomogeneity and hence are to be avoided. The processing maps containing all such information are a useful guide in designing hot working process such that, the process parameters are selected and controlled within the "safe" processing domains. The DRX domain is a mostly chosen domain for bulk metal working in industrial process due to its advantages over superplastic deformation.

Strain hardening and flow softening are the two important phenomena, which control the deformation behaviour of titanium aluminides. It depends on the deformation temperature and strain rate. It has been reported that the stress (flow) softening is caused by dynamic recrystallization during high temperature deformation in TiAl-base alloys *[327, 328]*, which is due to low SFE of the alloy system and poor mobility of the dislocations. Several researchers have reported that the significant flow stress softening is observed at the temperatures ranging from 1000-1250^0C due to occurrence of dynamic recrystallization, Seetharaman and Lombard *[325]*, Nobuki et al. *[323]*, Fujitsuna et al. *[223]* and Shih [56] in TiAl alloys.

Hot workability regime i.e. safe working zone of these intermetallic alloys have been carefully derived considering various factors. Although large amount of studies have been

made on titanium aluminides and many suggestions have been reported but the same is not applied in the practical situation either because of minor change is chemistry or due to processing methods. When all the processing parameters are one and same then, it is the minor change in chemistry which governs microstructural distribution, phase transformation and transition temperatures. Therefore, a process designed for an alloy is not applied to another alloy in total. But, it has definite trends to take a clue from the deformation behavior of one alloy to another alloy where change in chemistry is minor.

In Processing map approach, strain rate sensitivity and power efficiency maps are very important, which shows the plastic working capability of material and working zone utilizing the maximum power in deformation. In the present work, value of strain rate sensitivity, α value, n value etc. have minor difference among the alloys. Strain rate sensitivity for alloys are found upto 0.55 for alloy *A1*, upto 0.9 for alloy *A3* and upto 0.4 for alloy *A5* depending on strain rates and temperature. This clearly indicates a very good to moderate capability of alloys for high temperature deformation under controlled strain rate. Power efficiency upto 0.75 is observed in case of alloy *A1* and *A3* and upto 0.45 in case of alloy *A5* has been observed. This level of power efficiency indicates availability of a very good working domain in the alloys. Power efficiency for alloy *A5* is found to be lower. This can be due to wider range of test temperature where 750^0C comes in the regime of premature failure. More test data in closer intervals of max. 100^0C are required to provide more accurate results, which is not available. Therefore, this alloy (*A5*) has not been discussed here.

Like deformation maps of other metallic materials, mainly three domains are seen in power efficiency maps, viz. DRX domain, superplasticity/ wedge cracking domain and ductile fracture domain. Superimposing the strain rate sensitivity map and power efficiency map, a combined map (called processing map) has been generated where DRX domain is identified for safe working zone avoiding wedge cracking or cavitation. This zone is different for different alloys as discussed in section 8.2.2. However, a common working zone of 950-1050^0C with 0.01/ sec strain rate is found to be safe for all the three alloys. Also, deformation with these parameters is practically possible at industry level. It has been observed that upto 0.1/ sec strain rate, material can be deformed at 950-1050^0C but it is specific to alloy *A1*, where additional intermetallic phase of boron is not present. Some unusual behaviour of increasing flow stress and cracking of sample is also seen in alloy *A3* at higher temperatures (>1150^0C) and higher strain rates (0.1/sec.), which limits the working of material at higher temperatures. This is creating instability in the deformation of alloy.

Activation energy for deformation of the alloy is found to be in line with the reported values. Strain rate sensitivity is observed to be increasing with increase in temperature for all

the three alloys. However, with increasing strain, it has three zones. Initially it increases (upto 0.1 strain) then almost stable (0.1-0.4) then decreases (>0.4 strain). This indicates, at a specific temperature (in near isothermal working), an alloy should be given 30-40% deformation avoiding change in strain rate sensitivity of the alloy at that temperature. Then the alloy should be again preheated before further deformation. Zener Hollomon parameter is found to be increasing with increase in strain rates and with decrease in temperature, which is in agreement with the reported works. It has shown very close linearity with increasing peak stress, indicating the processing difficulty with increasing flow stress. It also shows near linear relation with recrystallized grains, which is line with the reported literature *[321]*. Both the alloys *A1* and *A3* show the similar trend. Constitutive equations were found to be applicable for the respective alloys and equation C-1 is predicting more accurately. Prediction is more precise in sound deformation regime i.e. 950-1050^{0}C range at 0.01/ sec. strain rate.

8.5 SUMMARY

Effect of dynamic recrystallization has been clearly noted in the temperature range of 950-1050^{0}C, which modifies the flow stress with temperature. Change in flow stress is also observed with strain at constant temperature through change in deformation characteristics.

Deformation studies of TiAl alloys based on macroscopic determination approach of flow stress as a function of temperature and strain rates has been carried out. Zones corresponding to flow instabilities have been identified. It is noted that flow instabilities are either due to lower temperature (where formation of microcracks leads to premature failure of material) or due to higher temperature and higher strain rates (where localized flow softening leads to failure).

Power efficiency upto 0.75 is observed in case of alloy *A1* and *A3* and upto 0.45 in case of alloy *A5*. Mainly two domains are seen in power efficiency maps, viz. DRX domain and superplasticity/ wedge cracking domain. DRX domain is found to be in the temperature and strain rate regime of 950-1150^{0}C and 10^{-1}-10^{-2}/sec respectively, which is in the homologous temperature range 0.7-0.8 and at lower than intermediate strain rates (0.1-1 s^{-1}) in the maps. Superplastic / wedge cracking domain is found to be in the temperature range of 1000-1150^{0}C under strain rates lower than 0.01s^{-1} for alloy *A1*, whereas, it is 950-1050^{0}C under strain rates lower than 0.01s^{-1} for alloy *A3*. It shows alloy *A3* can be superplastically deformed at marginally lower temperature than alloy *A1*. Ductile fracture zone is not clearly noted in the present work.

Safe working range for the alloy *A1* is found to be wider as compared to other two alloys *A3* and *A5*, i.e. 950-1150^{0}C under strain rate of 10^{-2}/sec. At higher temperature

(1150^{0}C), the alloy can be worked safely at a strain rate of 10^{-1}/sec also. For alloys *A3* and *A5*, safe working zone lies in the similar temperature zone at slower strain rates (10^{-2}-10^{-3}/ sec). However, small instability region is also noted in case of alloy *A3* and *A5* at higher temperatures (1050 to 1150^{0}C) and slow strain rate (10^{-3}/sec.).

It is also noted that, safe working zone decreases with increase in strain. It is more pronounced in case of alloy *A3* and *A5*, which ay be due to presence of additional phases based on boron. It indicates, in multicomponent system, as the number of component increases, safe working zone shrinks due presence of more number of phases.

Strain rate sensitivity is found to be upto 0.55 for alloy *A1*, upto 0.9 for alloy *A3* and upto 0.4 for alloy *A5* depending on strain rates and temperature. It is also seen that '*m*' varies with strain mainly at low strain level (0.1-0.2) and at higher strain level (0.5). At intermediate strain change in '*m*' is marginal.

Activation energy for alloy *A1* and alloy *A3* are found to be 335 and 387.5 kJ/ mole respectively. Value of n (stress component) for alloy *A1* and alloy *A3* are found to be 1.004 and 1.029 respectively. Constant parameter for alloy *A1* and alloy *A3* are found to be $2.22X10^9$ and $8.34X10^{11}$ respectively. Value of α varies for different processing temperature and is found to be in the range of 0.019-0.055. Zener Hollomon parameter is found to have very close linearity with the peak stress. This confirms the difficulty in processing with increasing peak stress, which is due to lower temperature or due to higher strain rate. Constitutive equations (C1 and C2) have been derived for alloy *A1* and *A3* respectively.

$$\dot{\varepsilon} = 2.22X10^9 [\sinh(\alpha\sigma)]^{1.004} \exp[-335/RT] \quad (C1)$$

$$\dot{\varepsilon} = 8.34X10^{11} [\sinh(\alpha\sigma)]^{1.029} \exp[-387/RT] \quad (C2)$$

These equations were found to be applicable for the respective alloys and equation C1 is predicting more accurately. Prediction is more precise in sound deformation regime i.e. 950-1050^{0}C range at 0.01/ sec. strain rate. Universal applicability of equation C1 is noted at 950^{0}C at intermediate strain rates

The recrystallized grain size (D_{DRX}) developed in the TiAl alloy was dependent on the deformation temperature and strain rate. For the present TiAl alloys, this dependence was found to be $\ln D_{DRX} = 3.26-0.052\ln Z$ (for Alloy *A1*) and $\ln D_{DRX} = 4.27-0.084\ln Z$ (for Alloy *A3*).

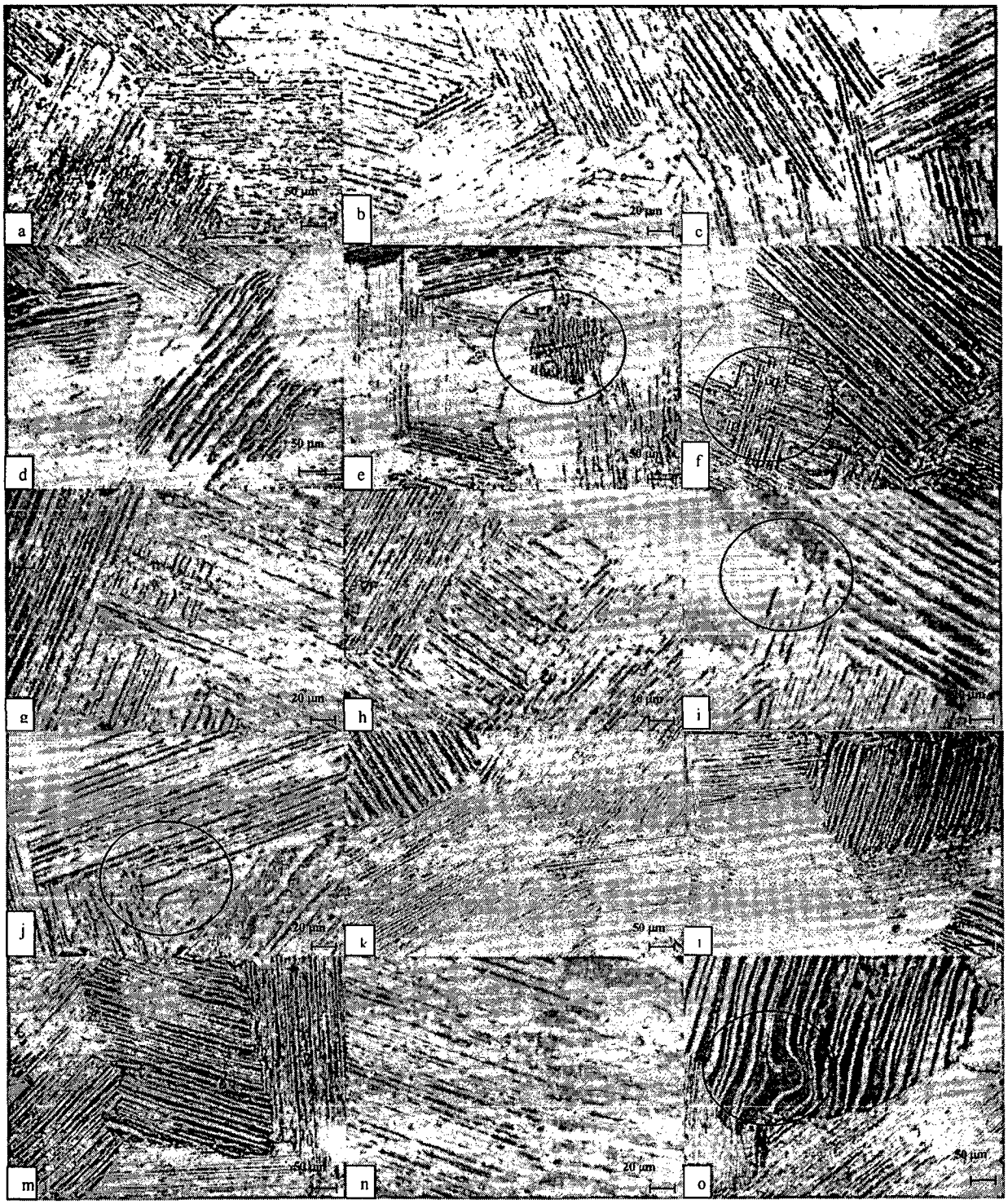

Fig. 9.2: Photomicrographs showing different type of lamellar microstructure developed during heat treatment of aluminides Af*A2*, where specific morphologies are circled.

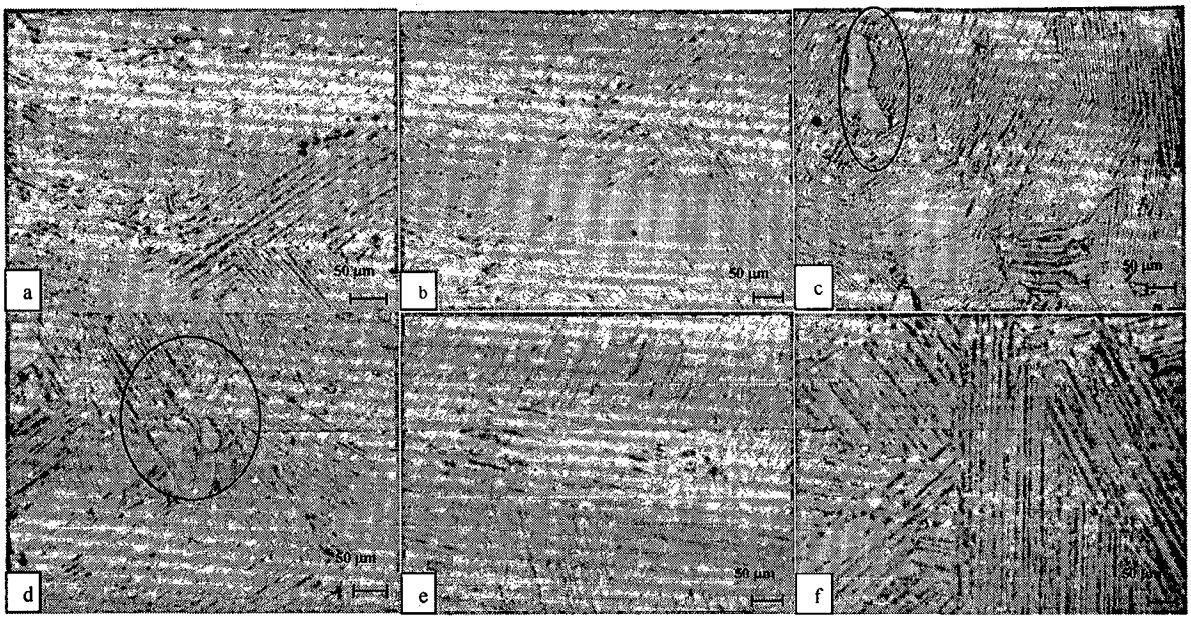

Fig. 9.3: Photomicrographs showing evolution of microstructure during heat treatment of compression tested specimens *A3*, (a-b) showing lamellar structure with finer spacing and smaller colony size after single annealing, (c-d) showing presence of γ phase after double annealing and (e-f) showing lamellar structure like 'a-b' after double annealing

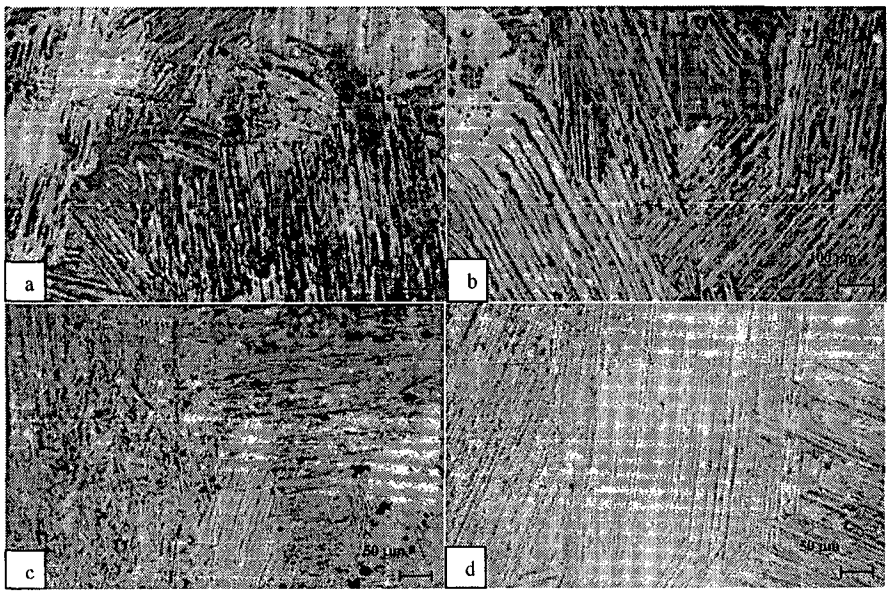

Fig. 9.4: Photomicrographs showing evolution of different lamellae morphologies during heat treatment of compression tested specimens *A5*, (a-b) as quenched specimen, (c-d) after annealing

Microstructure of heat treated (annealed) samples of alloy *A5* shows (Fig. 9.4c, d) finer colony sizes as compared to alloy *A1* and *A3* (Table 9.2). This may be due to smaller colony size in hot deformed structure (Table 7.4), which are available as nucleation sites even after heating above T_α and also presence of boron in the alloy helps in creating more nucleation sites for phase transformation. Preferential growth of α_2 lamellae is also observed (Fig. 9.4c), which can be attributed to growth of undissolved deformed structure, noted in the case of higher temperature and slow stain rate deformation (Fig. 7.8g).

Table 9.2 : Colony size of heat treated alloys.

Sample No.	Colony size, μm
A1	100-300
A2	90-250
A3	100-250
A4	75-200
A5	100-200

9.3.2 SCANNING ELECTRON MICROSCOPY

Scanning electron microscopy was also used to observe the microstructure of heat treated specimens. It also showed typical lamellar structure with different orientations. Representative photomicrographs are presented in Fig. 9.5. Lamellar spacing and colony sizes were measured through SEM. Here also, lamellar spacing and colony size are found to be finer for alloys *A2-A5* as compared to alloy *A1* (Table 9.2). Minor variation in chemistry of the alloy was noted from place to place with respect to aluminium content (44-47 at. %) as measured through EBSD (SEM).

9.3.3 TRANSMISSION ELECTRON MICROSCOPY

Transmission electron microscopy of selected heat treated specimens was carried out to confirm the presence of various phases.

Presence of lamellar structure was confirmed in all the alloy samples. Representative photomicrograph for alloy *A2* and alloy *A4* showing presence of γ phase with corresponding SAD pattern in many locations of lamellar structure is shown in Fig. 9.6. SAD pattern shows the presence of γ phase with variants of family of planes [110], [112], [114].

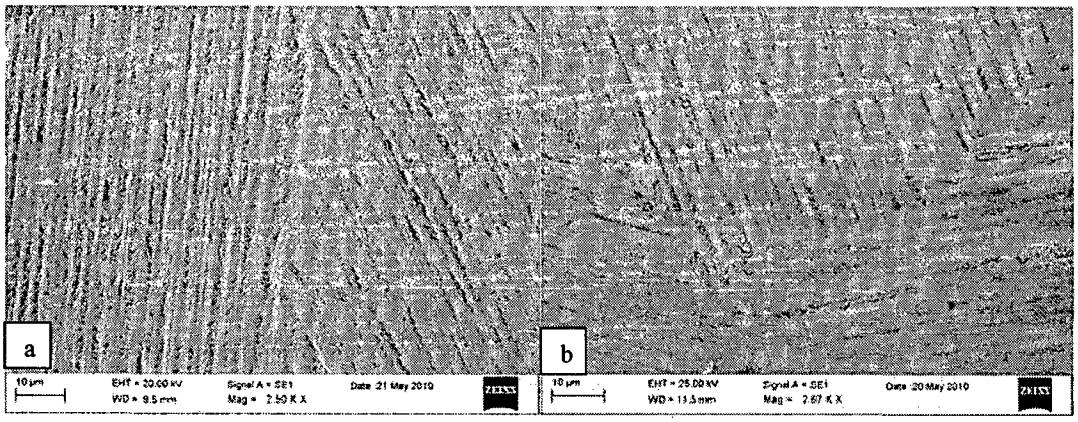

Fig. 9.5: Representative SEM photomicrographs of alloys *A2-A5* showing lamellar microstructure after heat treatment

9.4 ESTIMATION OF TENSILE STRENGTH USING EMPIRICAL RELATIONS WITH HARDNESS

Unfortunately tensile properties at room temperature could not be measured since the samples produced were too small for making a tensile specimen. The yield strength (YS) has been estimated (Table 9.3) through hardness using Kim et al. equation (2009) *[332]* which describes the relationship as;

$$\text{Log (YS)} = 0.00239\ (\text{Hv}) + 1.969 \qquad (9.1)$$

Table 9.3 : Calculated yield strength of Ti aluminides after heat treatment.

Sample No.	Hardness (Av.), Hv	Yield strength, MPa
A1	292	464.38
A2	311	515.57
A3	284	444.38
A4	355	656.82
A5	300	485.28

Table 9.3 shows that yield strength varies between 444-656 MPa, which is found to be in similar lines of reported values *[78,122, 123,163, 165]*. Highest strength of alloy *A4* is mainly due to fine lamellar structure (Table 9.2) and presence of boron.

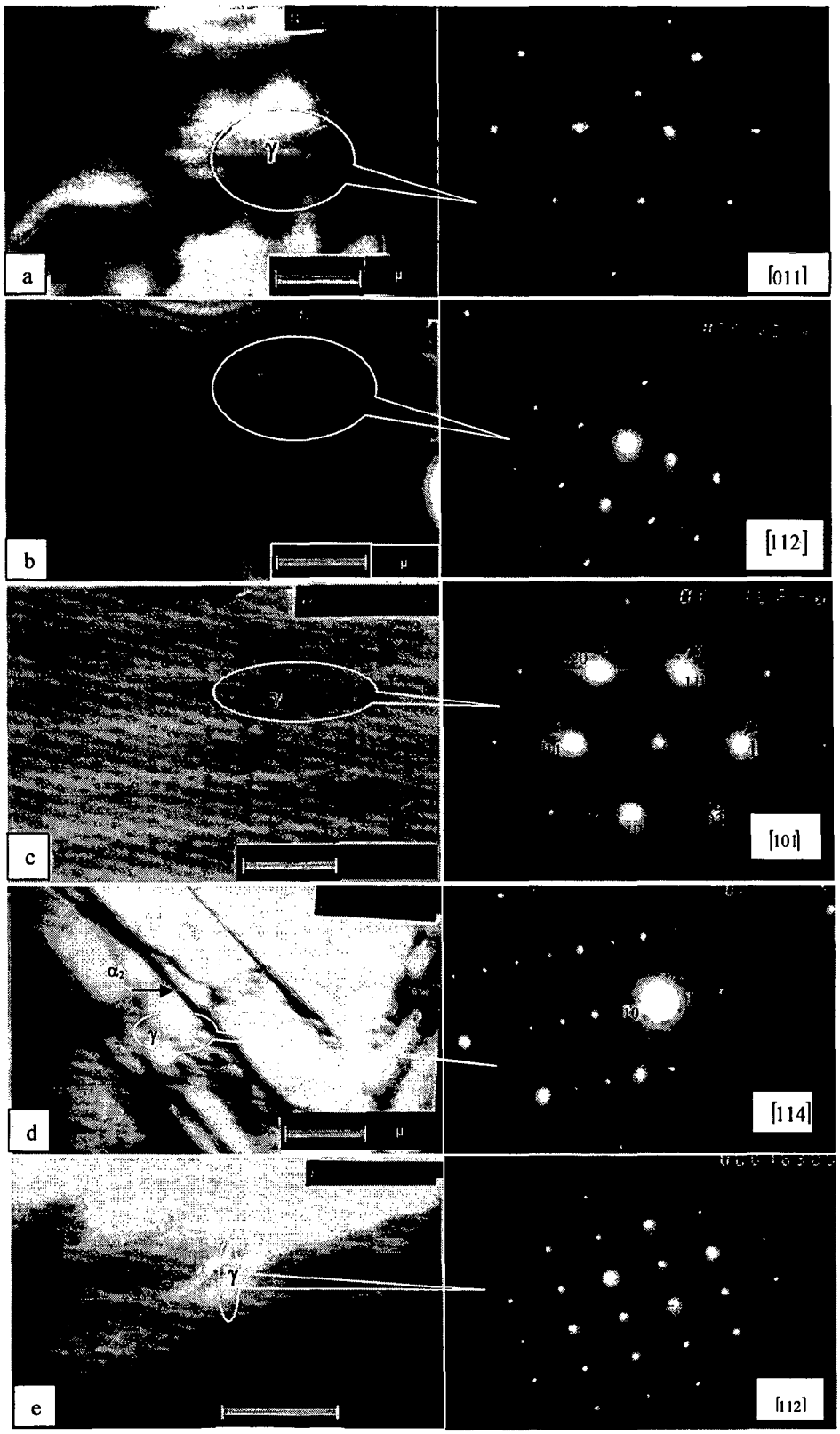

Fig. 9.6: TEM photomicrographs (Bright field) showing (γ grain) in lamellar microstructure with corresponding SAD pattern of the heat treated samples of alloy *A2* (a-d) and alloy *A4* (e).

9.5 DISCUSSION

9.5.1 DESIGN OF HEAT TREATMENT CYCLE

Need of keeping a relatively smaller grain size (<350μm) and fully lamellar microstructure with controlled lamellar spacing has always been suggested *[139]* where refined grain size (colony size) limit the fast growth of cracks. Fully lamellar microstructure with very fine lamellar spacing and small colony sizes has been found to be most promising ones for high temperature properties such as creep and stress rupture strength *[333, 334]*. To obtain fine grained (colony size) microstructure following options are present.

-Heat treatment in the α-β phase field where coexistence of two phases leads to small grain sizes of both the phases by competition of nuclei *[248]*. Then, controlled cooling (faster) to α phase, limiting α grain size followed by cooling (faster) below Tα to obtain lamellar structure *[227, 335]*, avoiding coarsening of grains.

-Cyclic heat treatment (rapid heating and cooling) where more number of cycles, results in smaller grains. Rapid heating, rapid cooling and short holding time at T>Tα results in significant grain refinement. By this treatment grain refinement from 500μm to 10μm has been achieved *[227]*.

-Long holding time below Tα *[227, 335]* and short incursion in α phase field helps in formation of refined microstructure.

-Small amount of boron (~0.2 at%) *[336]* refines the grain and improves ductility at room temperature. It provides similar effect of controlled cooling (in boron free material) to obtain lamellar structure.

When two phase alloys are heated or hot worked at temperatures higher than 1150^0C in the α-γ region, the initial structure is destroyed and a new structure is formed. It promotes both recrystallization of γ and lamellar microconstituents. However, annealing below the eutectoid temperature in the two phase region (α_2+γ) did not result in significant change in structure. However, reduction in volume fraction of lamellar content only has been reported by redistribution of constituent elements through diffusion. Similarly, finer lath morphology can be obtained after recrystallization in the (α-γ) phase field followed by annealing (stabilization) in the (α_2+γ) field *[337]*.

Here, cooling rate from α-γ transformation kinetics *[338]*, show very significant influence on the phase transformation from α phase *[339]*. Alloy cooled at the rate of 20^0C/min showed fully lamellar structure with colony size of 280-330μm with lamellar

spacing of 170nm (Ti46Al9Nb) without boron *[340]*. Similar observation has been noted in the present work. Increase of annealing temperature and a decrease of cooling rate result in the formation of lamellar structure *[35]*.

Chemistry also plays an important role in determining the microstructure in heat treatment. As the aluminium content decreases, equiaxed γ grains decreases and disappear and the microstructures consists of only α_2/γ lamellar grains. Linearity of the lamellar grain boundary (LGB) increases as aluminium content decreases. It is confirmed that, while the lamellar grain boundary of Ti44Al is straight, that of Ti48Al alloy is serrated. This difference is mainly caused by the different α to γ transformation temperature *[312]*. Similarly, small content of boron (~0.2 at%) makes significant change in microstructure. It has been reported that, alloy containing boron was transformed to refined fully lamellar microstructure having colony size of 30-65μm and extremely fine lamellar spacing 30-40nm *[231]*. Boron addition improves the thermal stability of lamellar structure by suppressing formation of feathery and Widmanstatten microstructure *[135]*. It broadens the cooling rate range of fully lamellar structure formation making the way for lamellar structure even in fast cooling (air cooling). Alloys containing $\leq$ 1000wt. ppm oxygen do not exhibit fully lamellar microstructure whereas it shows fully lamellar when oxygen is > 1000 wt. ppm *[341]*.

Considering the above and requirement of lamellar structure, heat treatment cycle has been designed and applied in the present work.

9.5.2 HEAT TREATMENT

In the heat treatment of all the alloys, one common observation is noted i.e. presence of lamellar structure. It may be due to presence of oxygen in the alloys and small content of boron in alloys *A2-A5*, which helped in getting lamellar structure with finer interlamellar spacing and colony sizes *[281]*. In double annealing of an alloy (*A3*), presence of γ phase was seen. It indicates role of cyclic annealing in activating the transformation towards growth of γ phase leading towards duplex structure.

Lamellar colony size and interlamellar spacing is found to be varying from location to location indicating variation in microconsituents. In many cases serrated grain boundaries are observed, which indicates that, aluminium is in lower amount *[312]*. Gas content especially oxygen has prominent role which suppresses the effect of other elements and result in lamellar structure. Oxygen content has played important role in the present study in helping in lamellar structure formation, since it is >1000wt. ppm in all the alloys. It has been

observed that, alloy *A1* also has shown similar behaviour to alloys *A2-A5* in lamellar structure formation. But interlamellar spacing and colony size (Table 9.2) is higher indicating lack of boron in the material as compared to other alloys (*A2-A5*).

In many cases it is observed that, deformation structure prior to heat treatment has an important role in evolution of microstructure after heat treatment. In case of alloy *A1* effect of previous working (hot deformation) is found to be acting to some extent in controlling the colony sizes, whereas in all other alloys, presence of boron also played a role in transformation. It indicates, time given in heat treatment above Tα was insufficient and therefore it can be optimized considering the avoidance of grain coarsening.

Hardness of the alloy is found to be in the range of 292-355 Hv, where highest is for alloy *A4*. This can be attributed to presence of refined structure. Similarly, yield strength estimated through Kim et al. equation suggests the role of refined lamellar structure in obtaining the higher strength (alloy *A4*).

9.6 SUMMARY

Heat treatment cycle is designed and carried out to obtain refined fully lamellar microstructure. Fast cooling from just above the α transus followed by reheating and soaking at two phase region is followed. Hardness of the alloys is found to vary between 284 to 355 Hv in heat treated condition. Variation in hardness in an alloy is found to be within a very close range indicating homogeneity of the alloy. Higher hardness for alloy *A2* and alloy *A4* from alloy *A1* indicates the role of boron. Similarly, yield strength estimated through Kim et al. equation *[332]* suggests the role of refined structure in obtaining the higher strength (alloy *A4*).

Microstructure in most of the cases is seen to be lamellar type. However, minor variation in morphology of lamellar microstructure is observed among the alloys. As-quenched alloy microstructure showed feathery structure with fine lamellar colonies. Interlamellar spacing of all the heat treated samples of the same alloy is found to be nearly same. Lamellar colony size is found to be varying. Lamellar colony size of alloy *A1* is found to be relatively higher (100-300μm) than alloys *A2-A5* (75-200μm) since alloy *A1* do not have any grain refiner. This also indicates that previous history of deformation has been present partially, in governing the microstructure morphology. This can be attributed to insufficient time available only (10 mins) to completely dissolve the structure (developed

during hot deformation) and remnant (of deformed structure) would have acted as nucleation sites for new lamellar structure.

Local variation in morphology of lamellar structure is observed. In open die forged and heat treated sample of alloy *A2*, many localized phenomenon like presence of serrated lamellar boundaries, lamellae resembling bamboo-clusters boundary (zig-zag uneven boundary), small isolated lamellar colony, straight cross boundary, secondary lamellar colony, localized lamellae coarsening, differential lamellae, discontinuous coarsening, bending of lamellae etc. are seen. This indicates, differential nucleation and growth of lamellae, which can be attributed to localized variation in constituents of the alloy (as confirmed by SEM) and differential hot deformation in open die forging.

In double annealing treatment presence of γ phase is observed. It indicates single annealing cycle is insufficient to nucleate γ precipitate. It means, if this cycle is repeated γ phase can be obtained with desired volume fraction. In double annealing lamellar spacing and colony size is found to be similar to single annealing. Also, addition of a small amount of Ni to TiAl alloy promote single γ phase matrix with a small volume fraction of precipitates.

It can be summarized that, alloys made through RS method and deformed isothermally and near isothermally have shown desired response in heat treatment.

Chapter-10

CONCLUSIONS

Deformation studies of γ+ α_2 Ti aluminide has been carried out through reaction synthesis (RS) process. Ti48Al2Cr2Nb (at%) was selected as the base alloy and with minor addition of boron (0.1 at%) and Ni-P coated boron, alloys were made. Also, two sizes of Ti powder particles (200μm and 50μm average) were used in alloy making. In this way, total five alloys (A1-A5) were made with these variations. Reaction kinetics of Ti aluminide formation was studied through differential scanning calorimetry (DSC) for eight different powder mixtures, which include binary (Ti48Al) and ternary (Ti48Al2Cr, Ti48Al2Nb) alongwith alloy mixtures of A1-A5. Based on reaction kinetics studies, trial experimentations and reported works, reaction synthesis parameters were established. Homogenization was carried out to obtain homogenous TiAl and Ti_3Al phases. Alloys made through RS were studied for isothermal and near isothermal deformation through isothermal pressing, open die forging, pack forging and hot isothermal compression testing. Workability maps were generated on the basis of hot isothermal compression test observations. Further, processing maps have been generated and constitutive equations have been derived on the basis of hot isothermal compression testing data. Deformed samples were studied for heat treatment response also to obtain lamellar microstructure. Following conclusions are drawn from the above studies.

1. Formation of Al_3Ti phase alongwith Ti rich phases like, Al_2Ti and AlTi were found after DSC of alloy powder mixtures.
2. Onset temperature of reactions for all the alloys are found to be just after endothermic peak of aluminium melting and it is found to be nearly same for different alloys at lower heating rates. Minor increase in onset temperature is noted for all the alloys with increase in heating rates. Exothermic completion temperature also varies in the similar way for various alloys and at different heating rates. Peak temperature is found to be increasing with increase in heating rates in all the cases. No significant effect of boron of the level of 0.1 at% is observed in the reaction temperatures.
3. Additions of Cr and Nb bring down the reaction enthalpy, whereas addition of boron as well as use of smaller size Ti particles increase the enthalpy. But diminishing effect of Cr

and Nb on enthalpy from the binary alloy is not compensated by using 0.1 (at%) boron and also with use of smaller size Ti particle size.

4. Using Johnson – Mehl – Avrami equation, activation energies (E) for different alloys are found to be in the range of 169.5 to 234.4 kJ/ mol. By alloying addition, E decreases from that of the binary alloy. The value of Avrami parameter 'n' for exothermic reaction is found to be in the range of 0.946 to 4.62 for various alloys. Binary alloy and ternary alloy (TiAlNb) showed value of n <2 whereas ternary alloy (TiAlCr) and quaternary alloys (*A1-A5*) showed value of n>2, indicating addition of Cr is helping additionally in multidimensional growth of reaction products.
5. Effect of particle size of Ti has been noted in changing the enthalpy, reaction temperature and reaction transformation mechanisms. Similarly, role of Ni-P coating over boron has been observed in retarding the reaction kinetics of the alloy. It shows that, although alloying additions are bringing down the enthalpy, but helping in phase transformation by multidimensional growth (higher n value) and through lowering of activation energy.
6. In RS, smaller size Ti particle resulted in relatively higher density due to better compaction. Also, effect of Ti particle size on reaction synthesis is clearly seen by the presence of Ti rich aluminides (TiAl) in the RS stage itself for alloys (*A4-A5*) where smaller size of Ti powder particles are used.
7. Boron containing alloys took longer time and alloys made with smaller Ti particle took lesser time in homogenization.
8. No significant effect of boron addition (0.1 at%) and Ni-P coated boron addition (0.1 at%) on reaction synthesis characteristics were noted. However, it has been found that it inhibits grain coarsening during homogenization.
9. Homogenized alloys have shown transformation temperature ($\alpha+\gamma$ to α) around 1375^0C.
10. In hot deformation, surface cracks are observed at high strain rate (0.1/ sec) with low temperatures ($750\text{-}850^0$C).
11. Alloys have shown wider steady state stage when deformed between $950\text{-}1150^0$C at slower strain rates (<0.01/ sec.) indicating useful zone of plastic deformation. Hot workability maps also show this is the zone of sound deformation.
12. Microstructure of boron free alloy (*A1*) showed two phase (α_2 and γ), whereas boron containing alloys (*A2-A5*) showed lamellar structure (> 40%) alongwith single phase γ.
13. Presence of twins has been noted in alloy (*A2*) deformed with relatively higher strain rate (≥0.1/sec.).

14. Percentage of DRX grains is higher in open die forging (≥0.1/ sec.), indicating content of DRX grains are higher in case of higher strain rates. Whereas, it is reverse in case of isothermal forging. In this case, percentage DRX grain decreases with increasing strain rate. However, sizes of DRX grains are found to be increasing with decreasing strain rate and vice versa in both the cases.
15. DRX grains (5-15μm) are found to be present between the primary grains.
16. Formation of DRX grains at 750°C indicates that, it may be the minimum temperature of deformation to start recrystallization.
17. Lamellae orientation difference within the grain indicated multiple nucleation sites along the grain boundary for lamellar phase transformation.
18. Dynamic recrystallization is found to be the restoration process of γ-TiAl base alloys during high temperature deformation.
19. Flow instabilities are found to be either due to lower temperature where formation of microcracks leads to premature failure of material or due to flow softening (at higher strain rates and higher temperature).
20. Mainly two overlapping domains are seen in power efficiency maps. DRX domain is found to be in the temperature and strain rate regime of 950-1150^{0}C and 10^{-1}-10^{-2}/sec respectively, which is in the homologous temperature range 0.7-0.8. Superplastic domain is found to be in the similar temperature range at lower strain rates.
21. For Boron containing alloys, superplastic domain is 950-1050^{0}C under strain rates lower than 0.01s^{-1}.
22. Safe working range for boron free alloy *(A1)* is found to be wider as compared to other two alloys *A3* and *A5*.
23. Strain rate sensitivity is found to be upto 0.55 for boron free alloy *(A1) and upto* 0.9 for boron containing alloy *(A3). 'm' is found to be* varying with strain mainly at low strain level (0.1-0.2) and at higher strain level (0.5). At intermediate strain change in *'m'* is marginal.
24. Activation energy for deformation of boron free alloy *A1* is found to be 335kJ/ mole and of boron containing alloy, it is 387.5 kJ/ mole.
25. Constitutive equations (C1 and C2) have been derived for alloy *A1* and *A3* respectively.

$$\dot{\varepsilon} = 2.22X109\ [\sinh(\sigma\alpha)]1.004\ \exp[-335/RT] \qquad (C1)$$

$$\dot{\varepsilon} = 8.34X1011\ [\sinh(\sigma\alpha)]1.029\ \exp[-387/RT] \qquad (C2)$$

26. These equations were found to be applicable for the respective alloys, where equation C1 predict more accurately. Prediction is more precise in sound deformation regime i.e. 950-1050^{0}C range at 0.01/ sec. strain rate. Universal applicability of equation C1 is noted at 9500C at intermediate strain rates.
27. The recrystallized grain (DRX) size developed in the TiAl alloy was dependent on the deformation temperature and strain rate. For the present TiAl alloys, this dependence was found to be ln DRX = 3.26-0.052lnZ (for Alloy *A1*) and ln DRX = 4.27-0.084lnZ (for Alloy *A3*).
28. Increasing Z (at low temperature and higher strain rate) help in nucleation of DRX grains (in open die forging), whereas decreasing Z helps in growth of nuclei with increasing temperature and decreasing strain rate (in isothermal working).
29. In heat treatment, hardness of the alloys is found to be varying between 284 to 355Hv in heat treated condition. Higher hardness for alloy *A2* and alloy *A4* from alloy *A1* indicates the role of boron.
30. Microstructure after heat treatment in most of the cases is seen to be lamellar type.
31. In double annealing treatment presence of γ phase is observed. Lamellar spacing and colony size is found to be similar to single annealing.
32. From the present study, it can be concluded that, reaction synthesized Ti aluminide alloy can be hot worked using safe working parameters, where alloy results in refined microstructure. Also, desired microstructure can be obtained through heat treatment. This route of processing can be adapted and should be explored for realization of useful components.

Chapter-11

SUGGESTIONS FOR FUTURE WORK

The Ti aluminide alloy has very promising properties and it is a wonderful invention, which needs to be applied to system level. As on date, research in this field has been mainly focusing in the area of alloy design, development and microstructure property correlations. Now, focus towards process development is the demand of time.

In this direction following suggestions are provided.

1. Development of process technology for processing of alloy at industrial scale.
2. Study on the homogeneity aspects of alloy in large billets.
3. Design of desirable microstructure through thermomechanical treatment on large size ingots.
4. Component design, test and qualification methods.

APPENDIX-A

ANALYSIS OF INSTABILITY CRITERIA

The mechanical behavior of materials under processing is generally characterized by the constitutive equations which relate the flow stress(σ) to the strain (ε), strain rate ($\dot{\varepsilon}$) and temperature (T). According to DMM, the power P (per unit volume) absorbed by the work piece during plastic flow is given by

$$P = G + J \tag{A1}$$

or

$$\sigma\ \dot{\varepsilon} = \int_0^{\dot{\varepsilon}} \sigma\ d\dot{\varepsilon} + \int_0^{\sigma} \dot{\varepsilon}\ d\sigma \tag{A2}$$

The G term represents the power dissipated by plastic work, most of which is converted into viscoplastic heat, the little remaining power is stored as lattice defects. The dissipator power cocontent J is related to the metallurgical mechanisms which occur dynamically to dissipate power. In variational procedure, the G content is the work function and the J cocontent is a complimentary set. Metallurgical processes such as dynamic recovery, dynamic recrystallisation, internal fracture (void formation or wedge cracking), dissolution or growth of particles or phases under dynamic conditions, dynamic spheroidization of acicular structures and deformation induced phase transformation or precipitation under dynamic conditions contribute to the changes in the dissipator power cocontent J. The dynamic material behavior is modeled explicitly in terms of variation of power cocontent J with the process parameters.

The rate of change of stress, σ with $\dot{\varepsilon}$ at constant ε and T is known as the strain rate sensitivity parameter

$$m = \frac{dJ}{dG} = \left[\frac{\partial\ (\ln\sigma)}{\partial\ (\ln\dot{\varepsilon})} \right]_{\varepsilon,\,T} \tag{A3}$$

For an ideal dissipator,

$$J = J_{max} = \sigma\dot{\varepsilon} / 2 \tag{A4}$$

The variation of efficiency parameter,

$$\eta = \frac{J}{J_{max}}, \tag{A5}$$

as a function of ε, $\dot{\varepsilon}$ and T represents the power dissipation characteristics of the work piece material. Srinivasan and Prasad [2] have used equation (8.2) for the computation of the efficiency parameter, η.

Strictly speaking, the strain rate sensitivity parameter, m at constant ε and T varies with $\dot{\varepsilon}$ and it becomes independent of $\dot{\varepsilon}$ if σ versus $\dot{\varepsilon}$ curve follows power law,

$$\sigma = K \dot{\varepsilon}^{m}, \tag{A6}$$

where K and m are material constants.

Using Eq. (A6), one can obtain G and J defined in Eqs. (A1) and (A2) as,

$$G = \frac{\sigma\dot{\varepsilon}}{1 + m} \tag{A7}$$

$$J = \frac{m\,\sigma\dot{\varepsilon}}{1 + m} \tag{A8}$$

The efficiency of power dissipation, η for the power law stress distribution using Eqs.(A4), (A5) and (A8) can be written explicitly in terms of 'm' as in Eq. (8.2).

From Equations (A1), (A4) and (A5), the efficiency parameter for any flow stress distribution can be written as,

$$\eta = \frac{J}{J_{max}} = \frac{(P - G)}{J_{max}} = 2 - \frac{G}{J_{max}} \tag{A9}$$

The test values of σ at any ε and T are reported in literature for $\dot{\varepsilon} > \dot{\varepsilon}_{min} = 10^{-3}$,whereas the integration for G in equation (A9) needs the input from $\dot{\varepsilon} = 0$. To overcome this difficulty, the integral for G is split as [15],

$$G = \left[\frac{\sigma\dot{\varepsilon}}{m+1}\right]_{\dot{\varepsilon}=\dot{\varepsilon}_{min}} + \int_{\dot{\varepsilon}_{min}}^{\dot{\varepsilon}} \sigma \, d\dot{\varepsilon} \qquad \text{(A10)}$$

and it can be evaluated by numerical quadrature from the test data through a cubic spline fit which is well established in accuracy.

Kumar[13] and Prasad[14] have developed a criterion for evaluating the regimes of flow instabilities. The criterion is based on the continuum principles as applied to large plastic flow proposed by Ziegler[12] according to which instabilities occur when,

$$\frac{dD}{d\dot{\varepsilon}} < \frac{D}{\dot{\varepsilon}} \qquad \text{(A11)}$$

where $D(\dot{\varepsilon})$ is the dissipation function at a given temperature. According to DMM, $D(\dot{\varepsilon})$ is equivalent to J co-content and therefore the above equation becomes

$$\frac{dJ}{d\dot{\varepsilon}} < \frac{J}{\dot{\varepsilon}} \qquad \text{(A12)}$$

They used J cocontent (10) which is obtained from the power law stress distribution (8) in Eq. (A12) for getting the flow instability condition (Eq. 8.3) in terms of 'm'. The details on the derivation of the Eq. (8.3), are briefly described here.

By taking logarithm on both sides of Eq. (A8), one obtains

$$\ln J = \ln\left(\frac{m}{m+1}\right) + \ln\sigma + \ln\dot{\varepsilon} \qquad \text{(A13)}$$

Differentiating equation (A13) with respect to $\ln\dot{\varepsilon}$, one gets,

$$\frac{\partial \ln J}{\partial \ln\dot{\varepsilon}} = \frac{\partial \ln\left(\frac{m}{m+1}\right)}{\partial \ln\dot{\varepsilon}} + \frac{\partial \ln\sigma}{\partial \ln\dot{\varepsilon}} + 1 \qquad \text{(A14)}$$

Equation (A12) can be written in the form

$$\frac{\partial \ln J}{\partial \ln\dot{\varepsilon}} < 1 \qquad \text{(A15)}$$

Using equations (A3) and (A14) in (A15), they get the criterion for instability given by equation (8.3). It should be noted that equation (A8) in terms of m, σ and $\dot{\varepsilon}$ is obtained

by assuming the constitutive relation (A6) in which m is independent of $\dot{\varepsilon}$. Then equation (8.3) reduces to m<0 for the metallurgical instability. Hence, equation (8.3) becomes erroneous if the flow stress (σ) versus strain rate ($\dot{\varepsilon}$) curve does not obey the power law. In such a situation, a simple condition for the metallurgical instability is obtained here from equation (A12) in terms of η and m as follows.

We know that

$$J = \int_0^{\sigma} \dot{\varepsilon}\, d\sigma, \tag{A16}$$

which implies that

$$\frac{\partial J}{\partial \dot{\varepsilon}} = \frac{\partial \sigma}{\partial \dot{\varepsilon}}\,\dot{\varepsilon} = \sigma \frac{\partial \ln \sigma}{\partial \ln \dot{\varepsilon}} = m\,\sigma \tag{A17}$$

From equations (A4) and (A5), the efficiency parameter, η can be written in the form,

$$\eta = \frac{J}{J_{max}} = \frac{2J}{\sigma\dot{\varepsilon}} \tag{A18}$$

which implies

$$\frac{J}{\dot{\varepsilon}} = \frac{1}{2}\,\eta\,\sigma \tag{A19}$$

Using equations (A17) and (A19) in equation (A12), one obtains the condition for the metallurgical instability as

$$2m < \eta \tag{A20}$$

For ideally plastic flow, one half of the power is dissipated in material flow and the other half is dissipated in viscous heat ($G_{max} = J_{max} = P/2$). The behavior of superplastic materials approaches this extreme. The other extreme occurs for materials which are strain rate insensitive, i.e, $m \to 0$ or J = 0. When J = 0, G = P and all the power would be dissipated by heat which leads to plastic instability by a continuum process such as adiabatic shearing. Hence,

$$J = 0 \Rightarrow \eta = 0 \tag{A21}$$

From Eqs. (A20) and (A21), the condition for metallurgical instability for any flow stress distribution can be written as

$$2m < \eta \leq 0 \qquad \text{(A22)}$$

Thus for stable material flow, $0 < \eta < 2m$ and the range of m values ($0<m\leq 1$) is derived from theoretical considerations of the maximum rate of power dissipation by material systems and experimental observations. The instability criterion (A22) is valid for any type of σ-ε curve. If σ-ε curve obeys the power law as in equation (A6), then $\eta = 2m/(m+1)$ which is always less than 2m for $0<m\leq 1$ and hence the material flow is stable.

REFERENCES

1. Kim Y.W., *JOM.* 47(7) (1995) 39-41.
2. Kim. Y.W., *JOM.* 46(7) (1994) 30-39.
3. Appel F. and Wagner R., *Mater. Sci. Eng A* 22(5) (1998) 187-268.
4. Clemens H. and Kestler H., *Advanced Engineering Materials*. 2(9) (2000) 551-570.
5. Kim J. K., Kin T.K., Lee TK., Hwang S.K., Nam S.W. and Kim N.J., The Minerals, Metals and Material Society, (1999) 231-238.
6. Kim Y.W., *JOM.* 41(7) (1989) 24-30.
7. Huang S.C. and Siemers P.A., *Met Trans A.* 20 (1989) 1899.
8. Semiatin S. L. and Mcquay P.A., *Met Trans A.* 23 (1992) 149.
9. Ibrahim I.A., Mohammed F. A. and Lavernia, *J Mater Sci,* 26 (1991) 1137-1156.
10. Semiatin S.L., Vollmer D.C ., El-Soudani S. and Su C., *Scripta Mater.* 53 (1990) 1409-1413.
11. Semiatin S.L., Lark K.A., Barker D.A., Seetharaman V. and Marquardt B., *Met Trans A.* 23 (1992) 295-305.
12. Imayev R.M., Imayev V.M. and Salishchev G.A., *J Mater. Sci*. 27 (1992) 4465-4471.
13. Imayev R.M., Kaibyshev O.A. and Salishchev G.A., *Acta Met.* 40(3) (1992) 581-588.
14. Imayev R.M., Gabdullin N.K., Salishchev G.A., Senkov O.N., Imayev V.M. and Froes F. H., *Acta Mater*. 47 (6) (1999) 1809-1821.
15. Clemens H., Kestler H., Eberhardt N. and Knabl W., *Gamma Titanium Aluminides, Eds.* Kim Y.W., Dimiduk D.M., and Loretto M.H., TMS: Warrendale, PA (1999) 209-222.
16. Lipsitt H. A., High Temp Ordered Intermetallic Alloys, Eds. Koch C. C., Liu C. T. and Stolloff N. S., MRS, 39 (1985) 351-364.
17. Huang S. C. and Chesnutt J. C., Intermetallic Compounds, Eds. Westbrook J. H. and Fleisher R. L., John Wiley and Sons, 2 (1994) 73 - 90.
18. Austin C.M., Kelly T. J., McAllistor K. G. and Chesnutt J. C., Structural Intermetallics, Eds. Nathal M. V., Darolia R., Liu C. T. Martin P. L., Miracle D. B., Wagner R. and Yamaguchi M., The Minerals, Metals and Mater Society, (1997) 413-425.
19. Venskutonis A. and Kibacher K., European Space Agency Bulletin: Preparing for the future, 10 (2000) 2-3.
20. Tetsui T., *Intermetallics*. 10 (2002) 239–245.
21. Tetsui Toshimitsu, *Mater. Sci. Eng A* 582 (2002) 329-331,
22. Taub A. I. and Fleischer R. L., *Science*. 243 (1989) 616-621.
23. Westbrook J.H., *Met Trans A* 8 (1977) 1327-1360.
24. Sauthoff G., Intermetallics, VCH Verlagsgesellchaft mbH, Germany (1995).
25. Zhao J.C. and Westbrook J. H., Ultrahigh-Temp Mater for Jet Engines and Westbrook, MRS Bulletin (2003), 622-630, www.mrs.org/publications/bulletin.
26. Appel F., Oehring V. and Wagner V., *Intermetallic.*, 8 (2000) 1283-1312.
27. Appel F., Paul J.D.H., Ochring M., Frobel U. and Lorenz U. *Met Mater Trans A.* 34A (2003) 2149.
28. Kattener U.R., Lin J.C. and Chang Y.A., *Met Trans A.* 23A (1992) 2081.

29. Dimiduk D. M. *Mater Sci Eng A* 263 (1999), 281-288.
30. Djanarthany S., Viala J. and Bouix J., *Mater Chemistry and Physics.* 72 (2001) 301–319
31. Das Gopal, Kestler H., Clemens H. and Bartolotta P.A., *JOM.* 56(11) (2004) 42-45.
32. Zhang W. J., Reddy B. V. and Deevi S. , *Scripta Mater.* 45 (2001) 645-651.
33. McQuay Paul and Larsen Don, Structural Intermetallics, Eds. Nathal M. V., Darolia R., Liu C. T. Martin P. L., Miracle D. B., Wagner R. and Yamaguchi M. The Minerals, Metals and Mater Society, (1997) 523-529.
34. Kuang J.P., Harding R.A.and Campbell J., *Mater Sci Eng A.* 329–331 (2002) 31–37.
35. Chraponski J. Szkliniarz W., Koscielna A. and Serek B., *Mater Chemistry and Physics*, 81(2003) 438–442.
36. Skrotzki W., Kegler K., Tamm R., and Oertel C.G., Cryst Res Technol, 40(2005) 90 – 94.
37. Springgate Mark Edwin, Nikolas Douglas Gene, Sturgis, David H. and Yasrebi Mehrdad, United States Patent No. 6,024,163, February, 2000.
38. Dimcic B, Vilotizevic M., Bozic D., Rajnovic D. and Jovanovic M. T., *Mater Sci Forum.* 494 (2005) 211-216.
39. Mei B., Lin J., Miyamoto Y. and Iwasa M., SIJ Int, 40 (2000), S77-S81.
40. Zhao I., Beddo J., Morphy D. and Wallace W., *Mater Sci Eng A.* 192/193 (1995) 957-964.
41. Kumaran S., Chantaiah B., Srinivasa Rao T., *Mater Chemistry and Physics*, 108 (2008) 97-101.
42. Bouodina M., Guo Z.X., *Mater Sci and Eng A* 332 (2002) 210-222.
43. Oehring M., Appel F., Pfullmann Th., Borrmann R., *Appl. Phy. Lett.* 66 (8) (1995) 941-943.
44. Suryanarayana C., *Progress in Mater Sci* 46 (2001) 1-184.
45. Suryanarayana C., *Int J of Non-equilibrium Processing.* 11(2002) 325-345.
46. Froes F. H., Suryanarayana C., Russel K. and Li C.G., *Mater Sci Eng A* 192/193 (1995) 612-623.
47. Bertolino N., Monagheddu M., Tacca A., Giuliani P., Zanotti C. and Tamburini A. U., *Intermetallics.* 11 (2003) 41–49.
48. Zhenbin Ge, Kexin Chen, Junming Guo, Heping Zhou and Ferreira Jose M.F., *J European Ceramic Soc.* 23(2003) 567–574.
49. Minay EJ, McShane HB and Rawlings R.D., *Intermetallics.* 12 (2004) 75 – 84.
50. Pant Bhanu, Agarwala Vijaya, Agarwala R. C. and Sinha P. P., *Trans IIM,* 60(4) (2007) 407-416.
51. Yamaguchi M., Inui H. and Ito K. *Acta Mater*. 48 (2000) 307-322.
52. Pather R., Mitten W.A., Holdway P., Ubhi H.S., Wisbey A., Bzooks J.W., *Intermetallics*. 11 (2003) 1015-1027.
53. Perkins R. A., Chiang K. T. and Meier G. H., *Scr Met.* 21 (1987) 1505.
54. Shemet V., Tyagi A. K., Singheiser L., Breuer K. U. and Quadakkers W. J., *Proc of Int Symp on Mater Ageing and Life Management (ISOMALM – 2000)*, Kalpakkam, India, Eds. Baldev Raj, Bhanu Sankara Rao, Jayakumar T. and Dayal R.K., (2000) 809-814.
55. Teng Lidong, Nakatoni Daisuke and Seetharaman Sebhadri, *Metall. Mater. Trans.* 38B (2007) 477-484.
56. Shih D.S. and Scar G. K., High Temp Ordered Intermetallic Alloys IV, Mater Res Soc Symp Proc, 213 (1991), 727.
57. London B. and Kelly T. J., Microstructure/ Property Relationships in Ti Aluminides and Alloys, Eds. Kim Y. W. and Boyer R.R., TMS, Warrandale, (1991) 285.

58. Kim Y. W. and Froes F. H., High Temp Aluminides and Intermetallics, Eds. Whang S. H. , Liu C. T., Pope D. P., (1990) 465-492.
59. Rowe R. G., High Temp Aluminides and Intermetallics, Eds. Whang S. H., Liu C. T., Pope D. P. and Stiegler J. O., TMS, Warrandale(1990) 465-492.
60. Blackburn M. J. and Smith M. P., Technical report no. AFWAL-TR82- 4086, U.S. Air Force Wright Laboratories (1982).
61. Kumar Vikas, Germann L and Studel Jean-Loup, Annual Report SNECMA/ARMINE/TUBOMECA No. 940937, Lot2 (1999).
62. Tetsui T., Structural Intermetallics, Eds. Nathal M. V., Darolia R., Martin P. L., Miracle D. B., Wagner R. and Yamaguchi M., The Minerals, Metals and Mater Society (1997) 489-493.
63. Rawers J.C. and Wrzesinky, W.R., *J Mater Sci.* 27 (1992) 2877-2886.
64. Lee Byeong Joo and N. Saunders, *Z Met.* 88 (1997) 152-161.
65. Kim Y.W. and Dimiduk D.M., *JOM.* 43 (1991) 40.
66. Huang S. C. and Hall E. L., High Temp Ordered Intermetallic Alloys IV, Eds. Johnson L. A., Pope D. P. and Stiegler J. O., Mater Res Soc Symp Proc, 213, (1991) 827-832.
67. Semiatin S.L., Lark K.A., Barker D.A., Seetharaman V. and Marquardt B., *Met Trans.* 23A (1992) 295-305.
68. Mutoh Y., Moriya T., Zhu S. J. and Mizuhara Nagaoka Y., Third Pacific Rim Int. Conference on Advanced Mater and Processing, Honolulu, Hawaii, 1998.
69. Yamaguchi M., *Mater Sci Tech.* 8 (1992) 299.
70. Du H.L., Aljarany A., Datta P.K., Burnell-Gray J.S., *Corrosion Science,* 47 (2005), 1706-1723.
71. Datta P.K. and Burnell-Gray J.S., *Journal of Applied Electrochemistry,* 30 (10) 1191, DOI: 10.1023/A:1004164521182.
72. Du H.L., Datta P.K., Lewis D.B. and J.S. Burnell-Gray, *Corrosion Science.* 36(4) (1994) 631-642.
73. Hu D., Jiang H., Wu X., Intermetallics 17 (2009) 744-748.
74. Bondarev B., Anoshkin N., Molotkov A., Notkin A. and Elagin D., Intermetallic Compounds- Structure and Properties, Eds. Izumi O., The Japan Inst of Metals, Sendai, (1991)1009.
75. Imayev R. M., Imayev V. M. and Salischev G., *Scr ipta Met Mater*. 29 (1993) 713-718.
76. Imayev R. M., Imayev V. M. and Salischev G., *Scr ipta Met Mater*. 29 (1993) 719-724.
77. Imayev V.M., Salischev G.A., Imayev R.M., Shagiev M.R., Gabdullin N.K., and Kuznestov A.V., Structural Intermetallics, Eds. Nathal M.V., Darolia R., Liu C. T., Martin P. L., Miracle D. B., Wagnor R. and Yamaguchi M., Minerals Metals and Mater Soc Conf Proc, (1997) 505-514.
78. Salischev G., Imayev R M., Senkov O. N., and Froes F. H., *JOM.* 52 (12) (2000) 46-48.
79. Salischev G., Imayev R M., Senkov O. N., Imayev V. M., Gabdullin N. K., Shagiev M. R., Kuznestov A. V. and Froes F. H. *Mater Sci Eng*. A. 286 (2000b) 236-243.
80. Shagiev M.R., Salischev G., Imayev R.M., Imayev V.M. and Kuznestov A.V., *Mater Sci Forum,* 447-448 (2004) 317-322.
81. Baczewska Karwan J., Dymkoski T. and Seetharaman S., *Adv in PM and Particulate Mater.* 4(1996), Part 15, 15-3.

82. Baczewska Karwan J, Dymkowski T. and Seetharaman S., Proc Int Conf on Non Ferrous Metals and alloys 99, Archives of Metallurgy, No.3 (2000).
83. Zhang P., Baczewska Karwan J., Du S. and Seetharaman S., *Met Mater Trans A.* 27A (1996) 2978-2984.
84. Dogan B., Wagner R. and Beaven P. A.,*Scripta Met*, 25 (1991) 773-778.
85. Dahms M., Seeger J., Smarsly W. and Wildhagen B., *ISIJ Int.* 31 (1991) 1093-1099.
86. Banerjee D., Intermetallic Compounds, Eds J. H. Westbrook and R. L. Fleisher, John Wiley and Sons Ltd., 2, (1994) 91-131.
87. Bhanu Pant, PhD Thesis, Synthesis and characterization of Ti aluminides for space applications, Indian Institute of Technology Roorkee, 2005.
88. Bhanu Sankar Rao K., Sadhana 28, 3 & 4 (2003), 695-708.
89. Bhanu Sankara Rao K, Lerch BA, Noebe RD, HITEMP Review. NASA CP-10146:53.1-53.11, 1994
90. Hansson T., Kamaraj M., Mutoh Y. and Pettersson B., ASTM STP 1367 (1999), 65-79.
91. Banerjee S., Mukhopadhyay P., Phase Transformations : Examples from Ti and Zr alloys, *Elsevier* (2007) 442-459.
92. Hu D., Botten R.R, *Intermetallics*. 10 (2002) 701-715.
93. Dimiduk D. M., Vasudevan V.K., Gamma titanium aluminides, Eds. Kim Y.W., Dimiduk D.M., Loretto M.H., Warrendale (PA), TMS, (1999) 239.
94. Zhang Z., Leonard K.J., Dimiduk D.M., Vasudevan V.K., Structural intermetallics, Eds. Hemkar K.J., et al., Warrendale (PA), TMS, (2001) 515.
95. Rotherflue L.L., Lipsitt H.A., Titanium 95, Eds. Blenkinsop PA, Evans W.J., Flower H.M., London, IOM, (1996)176.
96. Krishnan M., Natrajan B., Vasudevan V.J., Dimiduk D.M., Structural intermetallics, Eds. Nathal M.V., Darolia R., Liu C.T., Martin P.L., Miracle D.B., Wagner R., Yamguchi M., Warrendale, PA, TMS, (1997) 235.
97. Prasad U., Xu Q., Chatuvedi M.C., Structural intermetallics 2001, Eds. Hemkar K.J., et al., Warrendale PA, TMS, (2001) 615.
98. Takeyama M, Kikuchi M., *Intermetallics.*, 6 (1998) 573.
99. Denquin A., Naka S., *Acta mater.* 44(1) (1996) 343-352.
100. Kad B.K., Hazzledine P.M., *Phil. Mag. Lett.* 66 (1992) 133.
101. Inui H., Oh M.H., Nakamura A., Yamguchi M., *Phil. Mag.* A. 66 (1992) 539.
102. Denquin.A., Naka S., *Acta mater.* 44(1) (1996) 353-365.
103. Shong D.S., Kim Y.W., *Scripta metal.* 23 (1989) 254.
104. Mcquay P.A., Dimiduk D.M., Semiatin S.L., *Scripta metal. Mater.* 25 (1991) 1689.
105. Wang P., Wiswanathan G.B., Vasudevan V.K., *Metall. Trans.* 23A (1992) 690.
106. Wang P., Vasudevan V.K., *Scripta metall.* 27 (1992) 89.
107. Wang P., Vasudevan V.K., Mater Res. Soc. Symp. Proc. 288 (1993) 229.
108. Zhang X.D., Loretto M.H., *Phil. Mag. Lett.* 68 (1993) 289.
109. Jones S.A., Kaufman M.J., *Acta metal.* 41 (1993) 387.
110. Denquin.A., Naka S., Khan T., Titanium 92, Science and technology, Eds. F.H. Froes and I.L. Caplan, TMS Warrendale PA (1992), 1017.

111. Tsujimoto T., Hashimoto K., MRS Symp. Proc. 133 (1989) 391.

112. Hu D., Huang A.J., Wu X., *Intermetallics.* 15 (2007) 327-332.

113. Kim Y.W., Dimiduk D.M., *J. Met.* 43 (1991) 40.

114. Yamaguchi.M., Nishitani.S.R., Shirai Y., High temperature Aluminides & Intermetallics, Eds. Whang S.H., Liu C.T, Pope D.P. & Stiegler J.O., The minerals, Metals & materials society, (1990) 63-110.

115. Tsuzimoto T. and Hashimoto K., High Temp Ordered Intermetallic Alloys III, Eds. Liu C. T., Taub A.I., Stollof N. S. and Koch C. C., Mater Research Society, 133 (1989) 391-396.

116. Hanamura T., Ikematsu Y., Morikawa H., Tanino M. and Takamura J., Proc Int Symp on Intermetallic Compounds, Eds. Isumi O., Sendai, Japan, (1991)179-183.

117. Ramaseshan R., PhD Thesis on Synthesis and characterization of γ-TiAl/ Ti_2AlC intermetallic composites made by reactive processing of electroless Coated Ti Powders, Indian Institute of Technology Madras, Chennai, India (1998).

118. Kawabata T., Tamura T. and Izumi O., High Temp ordered Intermetallic Alloys III, Eds. Liu C. T., Taub A. I., Stollof N. S. and Koch C. C., Mater Research Society, (1989) 329-334.

119. Morinaga M., Saito J., Yukawa N., Adachi H., *Acta Met.* 38 (1990) 25.

120. Song A., Yang R., Li D., Hu Z. Q., Guo Z. X., *Intermetallics.* 8 (2000) 563-568.

121. Hao Y. L., Yang R., Cui Y. Y., Li D., *Intermetallics* 8 (2000) 633-636.

122. Perdrix F., Trichet M. F., Bonnentien J. L., Cornet M., Bigot J., *Intermetallics,* 9 (2001) 807-815.

123. Tian W. H., Nemoto M., *Intermetallics.* 5 (1997) 237-244.

124. Wu X., Intermetallics 14 (2006) 1114-1122

125. Li Z. X., Cao C. C., *Intermetallics.* 13 (2005) 251.

126. Hu D., *Intermetallics* 10 (2002) 851-858.

127. Hanamura T., Uemori R., Tanino M., *J. Mater. Res.,* 3 (1988) 656.

128. Kawabata T., Tamura T., Izumi O., *Metall. Trans. A.* 24 (1993) 141.

129. Huang S.C., Hall E.L., *Metall. Trans. A* 22 (1991) 2619.

130. Beddoes J., Wallace W., L. Zhao, *Int. Mater. Rev.* 40 (1995) 197.

131. Martin P.L.,. Mendiratta M.G, Lipsitt H.A., *Metall. Trans. A.* 14 (1983) 2170.

132. Martin P.L., Lipsitt H.A., Proceedings of the International Conference on Creep and Fracture of Engineering Materials and Structures, Vol. 4, Eds. Wilshire B., et al., Institute of Metals, London, (1990) 255.

133. Beddoes J., Zhao L., P. AU, W. Wallace, *Mater. Sci. Eng. A.*192/193 (1995) 324.

134. Kim Y.W., *JOM.* 41(7) (1989) 24.

135. Li Z.X., Cao CC., *Intermetallics.* 13 (2005) 251-256.

136. Hecht U., Witusiewicz V., Drevermann A., Zollinger J., *Intermetallics.* 16 (2008) 969-978.

137. Cheng T.T., *Intermetallics.* 8 (2000) 29-37.

138. Zhang W.J., Deevi S.C., *Mater. Sci and Engg. A* 337 (2002) 17-20.

139. Kim Y.-W., Dimiduk D.M., Structural Intermetallics, Eds. Nathal M.V., et al., The Minerals, Metals and Materials Society, TMS, Warrendale, PA, 1997, p. 531.

140.Taniguchi S., Shibata T., *Intermetallics.* 4 (1996) 885

141. Huang S.-C., Shih D.S., Microstructure/ Property Relationships in Titanium Aluminides and Alloys, Eds. Kim Y.-W., Boyer R.R., TMS, Warrendale, PA, (1990) 105.
142. Austin C., Gamma Titanium Aluminides, Eds. Kim Y.-W., et al., TMS, Warrendale, PA, (1995) 21.
143. Kim Y.W., Acta Metall. Mater. 40 (1992) 1121.
144. Shih D.S., Huang S.-C., et al., Microstructure/Property Relationships in Titanium Aluminides and Alloys, Eds. Kim Y.-W., Boyer R.R., TMS, Warrendale, PA, (1990) 135.
145. Naka S., Thomas M., Sanchez C., Khan T., Structural Intermetallics, Eds. Nathal M.V., et al., The Minerals, Metals and Materials Society, TMS, Warrendale, PA, (1997) 313.
146. Wagner R., Appel F., *Mater Sci. Eng R.* 22 (1998) 187.
147. Dahms M., Pfullmann.T., Seeger.J., Wildhanger, Microstructure/property relationships in Titanium Aluminides & alloys, Eds. Kim Y.W.,. Boyer R, R., The minerals, metals & materials society (1991) 337-344.
148. Kim Y.W., *Mater. Sci. Eng. A.* 192/193 (1995) 519.
149. You M.H. and Fu C.E., *ISIJ international*, 31 (10) (1991) 1049-1062.
150. Kumpfert J., Kim Y.W., Dimiduk D.M., *Mater. Sci. Eng. A* 192/193 (1995) 465.
151. Appel F., Paul J. D. H., Ochring M., Frobel U. and Lorenz U, *Met Mater Trans A.* 34A (2003), 2149.
152. Lin J.P., Xu X.J., Wang Y.L., He S.F., Zhang Y., Song X.P., Chen G.L., *Intermetallics.* 15 (2007) 668-674.
153. SI J.-Y., Han P.-B. , Zhang J., J. of Iron and Steel Research, Int. 2010, 17(8) 67-73.
154. Hug G., Loiseau A. and Veyssiere P., *Phil. Mag. A.* 57 (1988) 499-523.
155. Hug G., Loiseau A. and Lasalmonie A., *Phil. Mag. A.* 54 (1986) 47-65.
156. Huang S.C., *Scripta Metall.* 22 (1988) 1885-1888.
157. Lipsitt, Schectman D., and Schafrik R.E., *Metall. Trans. A.* 6A (1975) 1991-96
158. Chaudhari G. P., Viola L. A., Intermetallics 18 (2010) 472–478.
159. Usta M., Wolfe H., Duquette D.J., Stoloff N.S., Wright R.N., *Mater Sci and Engg. A.* 359 (2003) 168-177.
160. Rong T.S., Joaes I.P., SMallman R.E., *Acta Mater.* 46 (13) (1998) 4507-4517.
161. Heshmati-Manesh S., Nili Ahmadabad M., Ghasemiarmaki H., Jafarian H.R., *J. of alloys and comp.* 436 (2007) 200-203.
162. Takahashi T., Nagai H. and Oikawa H., *Mater Sci Eng A.* 128A (1990), 195.
163. Seetharaman V.and Semiatin S. L, *Met Mater Trans A.* 29A (1998) 1991.
164. Imayev R.M., Imayev V.M. and Salischev G., *Scripta Met Mater*, 29 (1993) 713-718..
165. Denquin A., Ph.D. Thesis, University of Orsay, France, 1994.
166. Wang G. X. and Dahms M., *Scripta Met Mater*, 26 (1992) 717-722.
167. Hamada S., Hamada H., Suzuki H. and Nozue A. J., *J Mater Sci.* 37 (2002) 1107-1113.
168. Chan K. S, *JOM*, 44 (1992) 30.
169. Chan K.S., *Metall. Trans. A.* 23 (1992) 183.
170. Chan K., Kim Y.W., *Metall. Trans. A.* 24 (1993) 113.
171. Enoki M., Kishi T., *Mater. Sci. Eng. A.* 192/193 (1995) 420.
172. Huang S. C., Met Trans A. 23A (1992) 375.

173. Schwenker S., Kim Y.-W., Gamma Titanium Aluminides, Eds. Kim Y. W. et al., TMS, Warrendale, PA, (1995) 985.

174. Morris M.A., Li Y.G., Leboeuf M., *Scripta Metall. Mater.* 31 (1994) 499.

175. Vasudevan V.K., Stucke M.A.,. Court S.A, Fraser H.L., *Phil. Mag. Lett.* 59 (1989) 299.

176. Huang S. C. and Shih Donald S, Micro–Property Relationships in Ti Aluminides and Alloys, Eds. Kim Y. W. and Boyer Rodney R., TMS, (1991) 105-121.

177. Austin C. M. and Kelly T. J., Proc Int Symp on Structural Intermetallics, Eds Darolia R., Lewandowski J. J., Liu C. T., Martin P. L., Miracle D. B. and Nachal M. V., TMS, Warrandale, PA, (1993) 143.

178. Suryanarayana C., Froes F. H. and Riowe R. G., , Int Mater Rev, 9 (11), (1990) 948-957.

179. Cantor B., Proc 22nd Risoe Int Symp Mat Sci: Sci of Metastable and NanocrystallineAlloys, Eds. Dinesen A. R., Eldrup M., Juul Jensen D. and Linderoth S., Risoe National Laboratory, Denmark 2001.

180. Shechtman D., Blackburn M. J. and Lipsitt H. A., *Met Trans.* 5 (1974) 1373.

181. Koch C. C., *Int Mater Rev.* 33(4) (1988) 201-219.

182. Vujic D., Li Z.and Wang S. H., *Met Trans A,* 19A (1988) 2445- 2455.

183. Mckamey C. G., Whang S. H., and CT Liu, *Scripta Met Mater.* 32(3) (1995) 383-388.

184. Inui H., Oh M. H., Nakamura A., Yamguchi M., *Acta Met.* 40 (1992) 3095-3104.

185. Hiroyuki Y. Yasuda, Takayoshi Nakano, Jun Nakazawa and Yukichi Umakoshi, *ISIJ Int.* 37(12) (1997) 1210-1217.

186. Wei Zhao and David E. L., Symposium on Influences of Interface and Dislocation Behavior on Microstructure Evolution; http://www.mrs.org/ members/ proceedings/ fall2000/y/Y10_4.pdf, 2000

187. Wegmann Gerhard, Maruyama Kouichi, *Phil Mag A.* 80 (2000) 2283 – 2298.

188. Whittenberger J. D., Solid State Powder Processing, Eds Clauer A. H. and Barbadillo J. J., The Minerals, Metals and Mater Society, (1990) 137-155.

189. Pillai Suresh C., Kelly John M., McCormack Declan E., O'Brien Paul and Raghavendra Ramesh, J Mater Chemistry 13(10) (2003) 2586 – 2590.

190. Srinivasan S., Desch P. B. and Schwartz R. B., *Scripta Met Mater.* 25 (1991) 2513.

191. Christman T.and Jain M, *Scripta Met Mater,* 25(1991) 767.

192. Fuchs G. E., Titanium 92, Science and Technology II, Eds. Froes F. H. and Chaplan I. L., TMS, (1993) 1275.

193. Paransky E., Gutmanas E.Y., Gotman I., Koczak M., *Metall. Mater. Trans. A.* 27(8) (1996) 2130–2139.

194. Munir Z. A. and Anselmi Tamburini, *Mater Sci Rep.,* 3(1989) 277.

195. German R. M., *Advances in P M,* 2(1990) 115.

196. Yi H. C. and Moore J. J., *J Mater Sci.* 25 (1990) 1159.

197. Yi H. C. and Moore J. J., *Scr Met.* 22 (1988) 1889-1892.

198. Wen C. E., Yasue K. and Yamada Y., *J Mater Sci.* 36 (2001) 1741-1745.

199. German R.M., Bose A., and Stolloff N.S., High Temp Ordered Intermetallic Alloys III, Eds. Liu C. T., Taub A.I., Stoloff N.S. and Koch C. C., MRS Proc, 133 (1989) 403-414.

200. Westwood A. R. C., *Met Trans A.* 19A (1988) 749-758.

201. Bose A., Rabin B. H. and German R. M., *P M Int,* 20 (1988) 25.

202. Nishimura C. and Liu C. T., *Acta Met et Mater.* 41 (1993) 113-120

203. Guo J. T. and Cui C. Y., *Key Eng Mater*, 217 (2002) 117-128.
204. Gedevanishvili S. And Deevi S. C., *Mater Sci and Eng. A.* 325 (2002), 163-176.
205. Savitski A. P, *Soviet P M Metal Ceramics.* 19 (1980) 488.
206. Savitskii A. P. and Brutsev N. N., *Soviet P M Metal Ceramics.* 20 (1981) 621-681.
207. Hahn Y. D. and Lee Y. T., *Adv in P M and Particulate Mater.* 9 (1992), 309-318.
208. Naidich Y. V., Lavrinenko I. A. and Evdokmov V. A., *Sov. Powder Met Metal. Ceram.* 13 (1974) 26-30.
209. Qian Wang, Zhengming Sun, Hitoshi Hashimoto, Shuji tada, Yong-ho Park, Se-Hyun Ko and Toshiko Abe, *Mater Trans JIM,* 41(5) (2000), 551-554.
210. Martin P. L. and Hardwick D. A., Intermetallic Compounds, Eds, Westbrook J. H. and Fleisher R. L., John Wiley and Sons, 1 (1994) 637-660.
211. German R. M., Liquid Phase Sintering, Plenum Press, NY, 1985.
212. Babaghorbani P. and Gupta M., Processing and Fabrication of Advanced Materials XVI (PFAM XVI), Eds. Gupta M., Srivatsan T. S. and Thakur S. K., Int. Conf. PFAM- XVI, Singapore, 2007
213. Wong W. L. E. and Gupta M., Processing and Fabrication of Advanced Materials XVI (PFAM XVI), Eds. Gupta M., Srivatsan T. S. and Thakur S. K., Int. Conf. PFAM- XVI, Singapore, 2007.
214. Pathak J.P., Singh J.K. and Mohan S., *Indian Journal of Engineering and Material Sciences,* June (2006) 238-246.
215. Pathak J.P., Mohan S., Sahoo K.K. and Gupta R.C., Proc. Int. Conf. on Recent Advances in Composite Materials, Mech. Engg. Dept., Banaras Hindu University, India, Dec. (2004) 410.
216. Lee T.K., Mosunov E.I., Hwang S.K., *Mater. Sci. and Engg. A.* 239-240 (1997) 540-545
217. Adeli M., Seyedein S.H., Aboutalebi M.R., Kobashi M., Kanetake N., *J. of Alloys and Compounds* 497 (2010) 100–104.
218. Kingery W.D., Woulbourn J. M. and Charvat F. R., *J. Amer. Ceramic Soc.* 46 (1963) 391-395.
219. Salishchev G. A., Imayev R. M., Senkov O. N., Imayev V. M., Gabdullin N. K., Shagiev M. R., Kuznetsov A. V., Froes F. H., *Mater. Sci. and Engg. A.* 286 (2000) 236-243.
220. Nobuki M., Hashimoto K., Tsujimoto T., Asai Y., *J. Jpn. Inst. Met.* 50 (1986) 840-844.
221. Nobuki M., Tsujimoto T., *Iron Steel Inst. Jpn. Int.* 31 (1991) 931-937.
222. Singh J. P., Tuval E., Weiss I. Srinivasan R., γ Titanium Aluminides, Eds. Kim Y. W., Wagner R., Yamaguchi M., TMS, Warrendale, PA (1995) 547-554.
223. Fujitsunah N., Ohyama I., Miyamoto O., Ashida Y., *ISIJ International*, 31(10) (1991) 1147-1153
224. Semiatin S. L., Seetharaman V., *Metall. Mater. Trans. A*, 26A (1995) 371-381.
225. Tetjukhin V.V., Levin I.V., Kozlov A.N., Poljanskij S.N., US Patent No. 2179899, Apr 2002.
226. Wang L., Liu Y., Zhang W., Wang H., Li Q., *Intermetallics,* 19 (2011) 68-74.
227. Wang. J.N., Xie.K., *Intermetallics.* 8 (2000) 545-548.
228. Seetharaman V., Semiatin S. L., *Mater.Sci. and Engg. A.* 299 (2001) 195-209.
229. Beschliesser M., Chatterjee A., Lorich A., Knabl W., Kestler H., Dehm G., Clemens H., *Mater.Sci. and Engg. A.* 329-331 (2002) 124-129.
230. Imayev V., Imayev R., Kuznetsov A., *Scripta Mater.* 49 (2003) 1047-1052.
231. Clemens H., Bartels A., Bystrzanowski S., Chladil H., Leitner H., Dehm G., Gerling R., Schimansky F. P., *Intermetallics.* 14 (2006) 1380-1385.

232. Perez Bravo M., Madariaga I., Estolaza K., Tello M., *Scripta Mater. 53* (2005) 1141-1146.
233. Wang J. N., Yang J., Wang Y., *Scripta Mater.* 52 (2005) 329-334.
234. Zhang W.J., Francesconi L., Evangelista E., *Mater Lett.* 27 (1996) 135.
235. Zhao L., Au P., Beddoes J.C., Wallace W., US patent US5653828, 1995.
236. Kikuchi M., Nakamura H., Yamabe Y., Japanese patent JP6116691, 1994
237. Wang J.N., Xie K., *Intermetallics*. 8 (2000) 545.
238. Wu X, Hu D., *Scripta Mater.* 52 (2005) 731.
239. Clemens H., Bertel A., Bystrzanowski S., Chladil H., Leitner H., Dehm G. et al., *Intermetallics*. 14 (2006) 1380.
240. Kumagai T., Abe E., Takeyama M., Nakamura M., *Scripta mater.* 36 (1997) 523.
241. Dimiduk D.M., Vasudevan V.K., Gamma titanium aluminides, Eds. Kim Y.W., Dimiduk D.M., Loretto M.H., Warrendale, PA, TMS (1999) 239.
242. Prasad U., Chaturvedi M.C., *Metall. Trans.* 34A (2003) 2053.
243. Herzig Chr, Prezeorski T., Friesel M., Hisker F., Divinski S., *Intermetallics*. 9 (2001) 461.
244. Mishin Y., Herzig Chr., *Acta Mater*. 48 (2000) 589
245. Hu.D, Huang A.J., Wu.X., *Intermetallics*. 13 (2005) 211-216.
246. Dey S.R. , Hazotte A., Bouzty E, Naka.S, *Acta materialia.* 53 (2005) 3783-3794.
247. Sujata M., Sastry D. H. and Ramachandra C., *Intermetallics.* 12 (2004) 691–697.
248. Novoselova T., Malinov S., Sha W., Intermetallics, 11 (2003) 491 –499.
249. Sujata M., Bhargava S., Suwas.S., Sangal.S, *Journal of Mater. Sci letters.* 20 (2001) 2207-2209.
250. Stein F, Zhang L.C., Sauthoff G, Palm M, *Acta mater*. 49 (2001) 2919-2932.
251. Jewett T.J. Ahrens B., Dahms M., *Mater. Sci & Engg A.* 225 (1997) 29-37.
252. Sohn H. Y. and Wang X., *J. Mater Sci.* 31 (1996) 3281.
253. Wang X., Sohn H. Y. and Schlesinger M. E., *Mater Sci Eng A.* 186 (1994) 151.
254. Wang T., Liu R. Y., Zhu M. L. and Zhang J. S., *J. of Therm. Anal. Cal.* 70 (2002) 507.
255. Friedman H., *J. Polym. Sci.* 6C (1963) 183.
256. Pant Bhanu, Agarwala Vijaya, Agarwala R. C. and Sinha P. P., *Trans. IIM,* 60(1) (2007) 925-930.
257. Akhtar N., Janes R.and Parker M. J., *J. Mater. Sci.* 31 (1996) 3053.
258. Knyazik V.A., Shteinberg A.S. and Goroveko V. I., *J. Therm. Anal.* 40 (1993) 363.
259. He X., Xu X., Han J. and Wood J. V., *J. Mater Sci. Lett.* 18 (1999) 1201.
260. Dumead S.D, Readey D.W., Semler C.E. and Holt J.B, *J. Am. Ceram. Soc.* 72 (1989) 2318.
261. Holt J. B., Kingman D.D.and Bianchini G.M., *Mater. Sci. Eng.* 71 (1985) 321.
262. Dumead S.D. and Munir Z.A., *J. Am ericanCeram. Soc.* 75 (1992) 180.
263. Wang L. L. and Munir Z.A., *Metall Mater Trans. B*. 26B (1995) 595.
264. Agarwala, R.C., Agarwala, V. and Sharma, R., Metal-Organic, and Nano-Metal Chemistry (SRINMC), Taylor & Francis Group, LLC, 36,(2006) 493–515.
265. Yang D., Hodgson P., Wen C., *Intermetallics*. 17 (2009) 727-732.
266. Lucadamo G., Barmak K., Lavoie C., Cabral Jr C, Michaelsen C., *J. Appl. Phys.* 91 (2002) 9575.
267. Bormann R., *Mater Res Soc. Symp Proc.* 343 (1994) 169.

268. Nassik M., Chrifi-Alaoui F.Z., Mahdouk K., Gachon J.C., *J. of Alloys and Compounds.* 350 (2003) 151-154.

269. Kubaschewski O., Dench W.A., *Acta Met.* 3(1955) 339.

270. Ramos A.S., Vieira M.T., *Surf. & Coat. Techno.* 200 (2005) 326-329.

271. Bohnenkamp U., Diploma thesis, University of Hamberg, 1993.

272. Divinski S, Hisker F., Klinkenberg C., Herzig C., *Intermetallics* 14 (2006) 792-799.

273. Kasahara K., Hashimoto K., Doi H. and Tsujimoto T., *JIM,* 53 (1989) 58.

274. Meier G. H., Appalonia D., Perkins R.A. and Cheng K.T., Intermetallics, Eds. Grobstein T. and Doychak J., TMS Warrendale PA (1988) 185.

275. Huang M., Li X., Yi H., Ma N., Wang H., *J. Alloy and Comp.* 389 (2005) 275.

276. Criado J. M. and Ortega A., *Acta Metal.* 35 (1987) 1715.

277. Joraid A. A., *Themochimica Acta.* 436 (2005) 78.

278. Holubova J., Cernosek Z. and Cernoskova E., *J. of Therm. Anal. Cal.* 62 (2000) 715.

279. Henderson D.W., *J. Therm. Anal.* 15 (1979) 325.

280. Doyle C. D., *J. of Appl. Polym. Sci.* 6 (1962) 639.

281. Lamirand M., Bonnentien J.L., Ferriere G., Guerin S. and Chevalier J.P., *Scripta Mater.* 56 (2007) 325-328.

282. Michaelsen C., Wohlert S., Bormann R., Barmak K., *Mater. Res. Soc. Symp.* 398 (1996) 245.

283. Ma E., Thompson C V., *J. Appl Phys.* 69 (1991) 2211.

284. Gupta R. K., Pant Bhanu, Agarwala Vijaya, Ramkumar P., Sinha P. P., *Trans. IIM.,* 63 (4) (2010) 715-718.

285. Gupta R. K., Pant Bhanu, Agarwala Vijaya, Agarwala R. C. and Sinha P. P., High *Temperature Mater. And Processes,* 28 (3) (2009) 121-132.

286. Wu Yinjiang, Zhang Xiaoming, Li Ying guan, Yin Weihong, Zhon lian , Jin Zhihao, *Key Engg Mater.,* 217 (2002) 111-116.

287. Palm M. and Inden G., Structural Intermetallics, Eds Nathal M. V., Darolia R., Liu C. T., Martin P. L., Miracle D. B., Wagner R. and Yamaguchi M. The Minerals, Metals and Mater Society, (1997) 73-82.

288. Breur J., Wilger T., Friesel M. and Herzig Chr., Intermetallics, 7 (1999) 381.

289. Ghosh Dulal C. and Biswas Raka, *Int J Mol Sci.* 3 (2002), 87-113.

290. Nekkanti R. M., McQuay P.A., and Semiatin S.L., *Scripta Met. et mater.* 26 (1992) 1089-1094

291. Gupta R. K., Niraj Nayan, Ghosh B. R., *Metal Science and heat treatment,*47(11-12) (2005) 522-525.

292. Oddone Robert R, German Randall M., Advances in powder Metallurgy, Eds. Thomas G Gastasve & William F., Jandeska, Proceedings of the 1989 powder Metallurgy conference & Exhibition San Diego, California USA , (1989) 475-488.

293. Pearl Lee Sullivan, *J. of Mater Process Techno.* 38 (1993) 1-14.

294. Wegmann G., Gerling R., Schimansky F.P., *Acta Materialia.* 51 (2003) 741-752.

295. Yi H.C., Petric A, & Moore J.I., *Solid state phenomena,* 25&26 (1992) 225-232.

296. Matsubara Tpshio, Venishi Keisuke, Kobayashi Kojiro F., *Mater Transactions. JIM,* 41(5) (2000) 631-634.

297. Liu C.T and Pope D.P., Intermetallic Compounds, Eds Westbrook J. H.and Fleischer R.L, John Wiley and Sons, 2, (1994) 17-51.

298. Nieh TG, Hsiung LM, Wadsworth J., *Intermetallics.* 7 (1999) 163.

299. Wegmann G., Gerling R., Schimansky F. P., Clemens H., Bartels A., *Intermetallics* 10(2002) 511-517.

300. Gerling R., Bartels A., Clemens H., Kestler H., Schimansky F.P., *Intermetallics,* 12 (2004) 275-280.

301. Sakai, T., Jonas J.J., *Acta Metallurgica* 32 (1984), 189–209.

302. Ha Tae kwon, Jung Jae young, *Mater Sci & Engg A*. 449-451 (2007) 139-143.

303. Hu D., *Intermetallics* (2001) 1037-1043.

304. Hu D., Huang A.J., Novovic D., Wu X., *Intermetallics,* 14 (2006) 818-825

305. Gupta R. K., Arumugam M., Karthikeyan M. K., Bhanu Pant, Ghosh B. R., *Engineering Failure Analysis*, 14 (2007) 1286-1293.

306. Huang A., Loretto M.H., Hu D., Liu K., Wu X., *Intermetallics* . 14 (2006) 838-847.

307. Uemori R., Manamura T., Morikawa H., *Scripta metall. et Materials* . 26 (1992) 969-974.

308. Semiatin S.L., Cornish G.R., Eylon D., *Mater. Sci and Engg. A*. 185 (1994) 45-53.

309. Zhang W., Liu Y., Liu B., Li H.-Z., Tang B., *Trans. Nonferrous Met. Soc. China,* 20 (2010) 547-552.

310. Liu B., Liua Y., Zhang W., Huang J.S., *Intermetallics*, 19 (2011) 154-159.

311. Mitao S., Isawa T., Tsuyama S., *Scripta Met. et Mater.*, 26 (1992) 1405-1410.

312. Tsuyama S., Mitao S., Minakawa K., Microstructure property relationships in Ti aluminides and alloys, Eds. Kim Y.W., Boyer R.R., The Minerals, Metals and Materials (1991) 213-226.

313. Dieter G.E., Kuhn H.A., Semiatin S.L., Handbook of workability and process design, ASM Int. (2003) 27-29.

314. P rasad, Y.V.R.K., Seshacharyulu, T., *International Materials Reviews* 43 (1998) 243–258.

315. Ziegler, H., *Progress in Solid Mechanics,* vol. 4. Wiley, New York, (1965) 91–193.

316. Narayana Murty S.V.S., Nageswara Rao, Kashyap B.P., *J. of Mater. Sci.* 37 (2002) 1197-1201.

317. Prasad, Y.V.R.K., Sasidhara, S., HotWorking Guide – A Compendium of Processing Maps, ASM International, 1997.

318. Chokshi A.H., Mukharjee A.K., Langdon T.G., *Mater. Sci Eng. Res.*, 10 (1993) 237-274.

319. Liu Z.C., Lin J.P, Wang Y.L., in. Z., Chen G.L., Chang K.M., *Materials letters* . 58 (2004) 948-952.

320. Sellars, C.M., Modeling an interdisciplinary activity. Eds. Yue, S., Proceedings of the International Conference on Mathematical Modelling of Hot Rolling of Steel. CIMM, Hamilton, 1990.

321. Zhang W., Liu Y., Li H.Z., Wang H., Liu B., *J. of Mater. Process techno.*, 209 (2009) 5363-5370.

322. Imayev R.M., Salishchev G.A., Senkov O.N., Imayev V.M., Shagiev M.R., Gabdullin N.K., Kuznetsov A.V., Froes F.H., *Mater. Sci. Eng. A.*, 300 (2001) 263–277.

323. Nobuki M., Hashimoto K., Takahashi J., Tsujimoto T., *Mater. Trans., JIM*, 31 (1990) 814.

324. Chen Y., Yang F., Kong F., Xiao S., Constitution modeling and deformation behavior of yttrium bearing TiAl alloy, *Journal of Rare Earths,* 29, (2) (2011)114.

325. Seetharaman V., Lombard C.M., Microstructure/Mechanical Properties Relationships in Titanium Aluminides and Alloys, Eds. Kim Y.W., Boyer R.R., TMS (1991) 237.

326. Bartels Arno, Kestler Heinrich, Clemans Helmut, *Materials Sci Engg A*. 329-331 (2002) 153-162.

327. Millet J.C.F., Brooks J.W., Jones I.P., *Mater. Des.* 14 (1993) 61.

328. Beddoes J., Zhao L., Immarigeon J.P., Wallace W., *Mater. Sci. Eng. A.* 183 (1994) 211.

329. Fantao K., Yuyong C., Fei Y., *Intermetallics*, 19 (2011) 212-216.

330. Gupta R. K., Rama Mehta, Vijaya Agarwala, Bhanu Pant, Sinha P.P., *Trans. IIM,* 63(6) 2010 833-839.

331. Whang S.H., Kim J. Y., Chen G.C., Li Z.X., *Scripta Met et. Mater.*, 27 (1992) 699-704.

332. Kim Y. W., Rosenberger A., Dimiduk D.M., *Intermetallics*, 17 (2009) 1017-1027.

333. Cao Guoxin, Fu lianfeng, Lin Jianguo, Zhang Yonggang, Chen changgia, *Intermetallics*, 8 (2000) 647-653.

334. Schillinger W., Clemens H., Dehm G., Bartels A., *Intermetallics*, 10 (2002) 459.

335. Yang Jie, Wang J.N., Wang Yong, Xia Qiang fei, Zhang Bin, *Intermetallics*, 9 (2001) 369 – 372.

336. Larsen D.E., Christodoulou L., Kampe S.L., Sadler P., *Mater Sci Eng*, 144 (1991) 45.

337. Soboyejo W.O., Midea S.J., Schwartz D.S., Parzuchowski M.J., Microstructure property relationships in Ti aluminides and alloys, Eds. Kim Y.W., Boyer R.R., The Minerals, Metals and Materials (1991) 197-211.

338. Jones S.A., Kaufman M.J., *Acta metal. Mater.* 41 (1993) 387-398.

339. Zheng R.T., Zhang Y.G., Chen C.Q., Cheng G.A., Liang C.L., Lix.J., *J. of Mater process. Techno.* 184 (2007) 217-223.

340. Bystrzanowski S., Bartels A., Clemens H., Gerling r., Schimansky F.P., Dehm G., et al., *Intermetallics*, 13 (2005)515.

341. Perdrix F., Cornet M., Bigot J., Chevalier J.P., *J. Phys. IV*, 6 (2000) 15.